Femtosecond Molecular Dynamics of Complex Reactions

Thesis by

Dongping Zhong

In Partial Fulfillment of the Requirements for the Degree of Doctor of Philosophy

California Institute of Technology
Pasadena, California
1999

(submitted May 5, 1999)

Acknowledgments

Many people deserve to be acknowledged for their essential intellectual and emotional support during my graduate studies at Caltech. Foremost amongst these is my advisor, Professor Ahmed H. Zewail, who brought me into this stimulating field, Femtochemistry. His guidance, encouragement, example, friendship, and, most of all, belief in my ability to do good science has carried me through much of my graduate career. I thank him for the opportunity to let me play in Femtoland IV and work in a number of exciting projects. His incredible enthusiasm for ultrafast reaction dynamics has been inspiring and contagious through numerous fruitful scientific discussions (even until the dawn!). He gave me a well-balanced combination of intellectual freedom and guidance that helped me to develop creativity and high scientific standards. All of those are very memorable in my life and will continue to guide me in my future scientific career. I would also like to thank my another mentor, Professor Donald W. Setser of Kansas State University; without his initial support and encouragement I would likely not have had the opportunity to study in the United States.

I would like to thank the members of my examining committee: Prof. B. Vincent McKoy (Chairman), Porf. John H. Richards, and Prof. Mitchio Okumura for their encouragement and friendship. Sometimes they do not have an easy task and I appreciate their effort.

I am grateful to all of my colleagues over the years for providing a cordial atmosphere in Femtoland. Dr. Po-Yuan Cheng deserves special recognition for more than two-year collaboration. I truly enjoyed the day and night experiments, scientific

arguments and discussions. On the early stage of my Caltech time, thank Juen-Kai Wang and Søren Pederson for teaching me the ins and outs of the femtosecond laser. The collaborations with Thorsten M. Bernhardt and Saqib Ahmad were both stimulating and enjoyable. I also would like to thank Spencer Baskin, Sang Kyu Kim, Chaozhi Wan, Marcus Motzkus, Jim Cao, Hyotcherl Ihee, Eric Diau, Steven De Feyter, Mirianas Chachisvilis, Torsten Fiebig, Klaus Möller, Lobastov Vladimir, and Udo Gomez for many stimulating interactions and their friendships. Sing Chong is a good friend and officemate and I would like to thank him for always being there. Good luck to him in the environment science.

Words would fail if I try to thank the moral support of my parents, brother and sister since my birth. Without their love and unending support and encouragement, I would not have reached as far as I have. Finally, behind every married graduate student there is a loving, understanding and beautiful wife, to Lijuan I am extremely grateful. Her presents to me of our wonderful sons, Frank and Randy, were extremely joyous occasions and I thank her for these. To my sons, I promise to be home for supper together more often and "not to go" after that.

Financial support for this research was made available through the National Science Foundation, the Air Force Office of Scientific Research, and the Office of Naval Research. I thank the Division of Chemistry and Chemical Engineering at Caltech for giving me the Herbert Newby McCoy Award.

Abstract

The exploring of complex reactions within femtosecond resolution provides new challenges because the reactions evolve along multiple pathways. New techniques are needed to dissect these complex systems into the elementary reactions. In this thesis, femtosecond-resolved mass spectrometry is successfully developed to achieve *temporal, speed, angular* and *state* resolution(s) of the reaction dynamics. With these capabilities, the mechanism and dynamics of the complex reactions are able to be microscopically elucidated for each elementary step by monitoring the temporal evolution of the transition state and final products, measuring the energy deposition among the translational and internal motions of the final products, and resolving the correlation between the structural changes and the energy release.

The complex reactions studied range from unimolecular dissociation, to bimolecular reactions, to cluster solvation, and to nonradiative dynamics. For unimolecular reactions, the level of complexity varies from diatomics to polyatomics, from direct-mode to complex-mode, from one-bond breakage to multi-bond fission. The six different systems were examined and a variety of dynamic behaviors have been revealed, including product rotational and vibrational excitation, electronic and vibrational predissociation, and saddle-point transition-state dynamics.

Many kinds of bimolecular reactions were studied, consisting of the major contributions of this thesis. For the first time, the famous electron-donor-acceptor charge-transfer reactions are fully understood. More than ten systems were examined with the different charge-transfer characters and all elementary steps involved are microscopically resolved. Several concepts have been addressed including the reversibility of electron

transfer, the nonconcertedness of reverse electron transfer and the bond breakage, the energy dissipation, and the reaction coherence. The reversible electron transfer is found as a general reaction mechanism. The system has been considered as a benchmark textbook example and provides insights into biological charge-transfer processes.

The aromatic nucleophilic substitution reaction was studied. The reaction is involved with many elementary steps and the rate-determining step was identified. The first atom-molecule inelastic collision was clocked in fs resolution and a novel method is presented by femtosecond detachment. The collision complexes are observed and quantum resonance may play a role. The first four-center covalent-covalent bimolecular reaction was studied and the cooperative motion of four centers was observed. The method presented is general and very important, and should be applied to study a variety of covalent-covalent bimolecular reactions.

The solvation ultrafast dynamics were systematically studied for many systems from small to lager clusters by monitoring the temporal evolution and translational energy distributions of the escaped solute. Different solvent structures are identified based on the dramatic temporal behaviors of the exited solute. Finally, the nonradiative dynamics of big organic molecules, using azines as examples, were studied. Different isomers of the valance-bond azines are observed. The conical intersection was found to play a key role on the ultrafast nonradiative dynamics and seems to be a general phenomenon, consistent with the recent *ab initio* predictions.

Table of Contents

Chapter 1

Introduction

Femtochemistry, first introduced in 1987 by a series of pioneering pump-probe studies of chemical reactions on the femtosecond time scale with atomic resolution from Zewail's group at Caltech,[1-2] explores the cornerstone of the chemical reactivity, the fleeting transition states, and probes the bond-breaking and bond-making processes of elementary reactions in real time. The experimental foundations (such as femtosecond transition-state spectroscopy) and concepts (such as molecular coherence) have brought to fruition predictions and applications for the entire field, including femtosecond studies in biology and physics. The field has added the dimension of time to structure and a true view of the dynamical changes of the chemical bond is attained. Recent advances in this field can be found in several latest books and review articles.[3-9]

The advent of the femtosecond laser, either the earlier colliding-pulse mode-locking fs dye laser or the later self-mode-locking Ti:Sapphire fs solid laser,[10] provides two key parameters: ultrashort time resolution and ultrahigh laser intensity. The fs laser pulse currently reaches as short as 4 fs[11] and the resulting time resolution is able to resolve all nuclear motions. A lot of fundamental processes are clocked and their dynamics and mechanism are uncovered.[3-9] The intense laser intensity has reached as high as 10^{19}-10^{20} W/cm^2 and a lot of new physical phenomena such as nonlinear processes can be studied.[12] In this thesis, the fs resolution was mainly used to reveal the evolution of molecular events.

In the field of molecular reaction dynamics, the femtosecond methodology has been applied to study all different kinds of reactions in all phases ranging from the simple two-atom dissociation to the big biological system and has brought chemistry and biochemistry to a new level of understanding. Two recent excellent reviews by Zewail

can be found in Reference 8-9. For most molecular systems studied so far, the dynamics are obtained by preparing the molecular system in a specific quantum state with a certain amount of energy and then following the temporal evolution of the state. In this way, the total time evolution of the well-prepared system is obtained. Most research studies follow two directions: using fs resolution to clock the fundamental processes and developing new methods with fs resolution to explore complex reactions.

For most complex systems, the reactions evolve along several exit pathways simultaneously. If all pathways have similar reaction times, experimentally it is very difficult to separate each channel unless the different products are separately monitored. Moreover, if each reaction pathway gives similar reaction products (usually with the different energy disposal), a new experimental method needs to be developed to distinguish the same identities with the different energy content. In this thesis, a femtosecond- and kinetic-energy-resolved time-of-flight (fs-KETOF) mass spectrometry was successfully developed to achieve *temporal*, *speed (kinetic-energy)*, *angular* and *state* resolution of the dynamics. Using this powerful technique, the complex reactions can be dissected into the elementary steps.

Chapter 2 describes the experimental methodology, including the two tunable fs lasers used in the fs pump-probe experiments, the pulsed supersonic molecular beam used to prepare isolated molecular systems in low internal excitation states and the fs-KETOF method. The basic principles of the fs-KETOF method are detailed and the procedure of extracting the energy and spatial (angular) distributions of products is given.

In Chapter 3, a full account of the studies of the elementary steps in complex *unimolecular reactions* is given.[13-15] The level of complexity varies from diatomics to

polyatomics, from direct-mode to complex mode, and from one-bond breakage to multi-bond fission. The systems studied cover six different reactions: iodine (I_2), cyanogen iodide (ICN), methyl iodide (CH_3I), iodobenzene (C_6H_5I), 1,2-diiodotetrafluoroethane ($1,2\text{-}C_2F_4I_2$) and mercury iodide (HgI_2). By resolving the femtosecond dynamics and simultaneously observing the evolution of velocity, angular and state distribution(s) of the reaction, we are able to study multiple reaction paths, the nature of transition-state geometry and dynamics, coherent wave packet motion, evolution of energy disposal and the nonconcerted motion in multi-center reactions. A variety of dynamical behaviors have been revealed and these include product rotational and vibrational excitation, electronic and vibrational predissociation, and saddle-point transition-state dynamics. These findings provide new challenges for the theoretical calculations including the reconstruction of *ab initio* potential energy surfaces. The work is still in progress to generalize the bond-breaking time using the experimental data of the simple one-bond-breakage systems. Dr. P.Y. Cheng was a collaborator and co-author on the experimental studies of iodobenzene dissociation.[15]

Chapters 4-6 present the fs studies of *bimolecular reactions* and are the major contributions of the thesis.[16-21] For all bimolecular systems studied here, we use van der Waals binary complexes as our reaction precursors, produced in a pulsed supersonic molecular beam under carefully controlled conditions. This method, first introduced by Soep and Wittig in the middle of 1980s,[22] provides two advantages: the zero-of-time of the reaction is precisely defined and the impact geometry is well controlled by the structure of the van der Waals complex. Before this work, only three isolated bimolecular reactions were studied in the gas phase with fs resolution: $H+CO_2(N_2O)$, $Br+I_2$ and

$O+CH_4$.[23-25] All three systems are radical atom-molecule reactions. From Chapter 4 to Chapter 6, many different types of bimolecular reactions were studied in great detail.

Chapters 4-5 describe the studies of the important electron-donor-acceptor charger-transfer bimolecular reactions.[16-19] These charge-transfer reactions were heavily studied in solution during 1950s-60s.[26] However, the elementary steps of these reactions are not studied at all in the isolated systems from the later 1960s to the middle of 1980s (a big gap!) although the crossed-beam method had provided great insight into the elementary molecular dynamics of many chemical reactions.[27] The experimental difficulty in the crossed-beam technique is that in order to study these charge-transfer bimolecular reactions three beams (two molecular beams and one pump laser beam) need to be used. With the advent of both the femtosecond spectroscopy and the method of using the van der Waals complex as a reaction precursor nearly at the same time in the middle of 1980s, the important charge-transfer bimolecular reactions should have been studied (probably people already forget it!) and after another ten years, the veil of the elementary steps of the charge-transfer bimolecular reactions was revealed (I was so lucky to have this opportunity!).

In Chapter 4, the famous prototype charge-transfer reaction of benzene (and its deuterated and methyl-substituted species) with iodine, two of the most important molecules in chemistry, was studied in great detail.[16,17] The microscopic elementary dynamics and the structure of the transition states are elucidated by studying (1) the temporal evolution of the transition state and the final products; (2) the product translational-energy and spatial distributions of each channel; (3) the reaction time dependence on the total energy; and (4) the dynamical and structural changes with

varying charge-transfer energy. The reaction mechanism mainly involves two exit channels. The first one is an ionic pathway following the harpoon mechanism and the second one is a major neutral pathway by intermolecular reversible electron transfer occurring on an ultrafast time scale of less than 500 fs. This work is a result of collaboration with Dr. P.Y. Cheng.[16,17]

In Chapter 5, the charge-transfer reaction of benzene with iodide monochloride was first studied and the results perfectly support the dynamics and reaction mechanism proposed in Chapter 4. Then, we extended to study other strong electron-donor-acceptor complexes in general and focused on dissecting the charge-transfer reactions into the different elementary steps.[18,19] The systems studied are diethylsulfide, *p*-dioxane and acetone with iodine. The results are very striking and only the neutral exit channel by reversible electron transfer (RET) was found for all three charge-transfer reactions. Two elementary dynamical processes were elucidated. The first elementary dynamic process includes the energy dissipation to the donor substrate and the searching for the exit channel in the dative-bonding transition state before RET. This process takes less than 1 ps. The second elementary dynamic process is one-molecule caging after RET and takes more than 1 ps. The correlation of the dynamics and the structural evolution during the entire process is also elucidated by measuring the product spatial distributions. The reactions are fully understood by the successful separation of different elementary steps from the temporal evolution, energy partition, and spatial distributions. These studies emphasize several important concepts: (1) the reversibility of electron transfer in general charge-transfer reactions; (2) the nonconcertedness between RET and the chemical bond breakage; (3) the energy dissipation into the donor substrate depending on the time scale

of RET; and (4) the coherence of the reaction trajectories. Dr. T.M. Bernhardt is a collaborator in this project.[19]

Chapter 6 presents several case studies for the different types of bimolecular reactions and demonstrates the powerful fs-KETOF technique.[20,21] Three total different systems are investigated: (1) aromatic nucleophilic substitution reaction, (2) inelastic collision dynamics, and (3) four-center cooperative reaction. The first system is a complicated reaction involving many dynamical processes. By clocking the evolution of the reaction, the rate-determined step is elucidated and an important intermediate, a so-called σ-complex, is identified. The inelastic collision process is first studied in this work by fs resolution and a novel method was proposed by femtosecond detachment of a lighter radical in a short time scale of less than 100 fs, leaving a heavy atom to collide with a molecule with a low collision energy. It should be emphasized here that this method is very general and can be applied to study a variety of atom-molecule inelastic collision processes. The collision complex can be identified and the quantum resonance may play a role. We have studied the inelastic collision of the I-atom with CH_3I, C_6H_5I and ICN molecules and the first two systems are detailed here. The four-center reaction of covalent + covalent molecules was first studied by fs resolution and this is a very important application. A variety of covalent + covalent bimolecular reactions are not well studied yet, such as the famous reactions of H_2+I_2 and O_2+O_2.[28] These reactions are usually forbidden in the ground state and only the vibrational and electronic excitation, not the translational, will enhance the reaction cross sections dramatically. In the system of CH_3I+CH_3I studied here, similar to HI+HI reaction, the I_2 formation was found in less than 500 fs by excitation of one CH_3I moiety into a repulsive electronic state. Clearly, a

cooperative motion of four centers (C, I, I, C) must occur in order to finish the reaction in such a short time. This methodology should be applied to study other covalent + covalent bimolecular reactions by excitation of one moiety to its higher electronic state or higher vibrational ground state.

Chapter 7 presents *solvation dynamics* in clusters by using the fs-KETOF method to monitor the caging exit of the solute, here I-atoms.[29,30] A variety of systems have been studied. These systems include: the I-atom solvated in $(C_5H_6I)_n$, $(CH_3I)_n$, $(ICN)_n$, $(CCl_3H)_n$, $(C_6H_6)_n$, $(C_2H_5SC_2H_5)_n$, $(OC_4H_8O)_n$, $(CH_3COCH_3)_n$. The cluster distributions vary from small sizes (n=1-4) to large ones (n>10). The evolution of kinetic-energy distributions of the exited I-atoms out of the caging was measured following the change of cluster sizes. A correlation between the exit time and the kinetic energy distribution of the exited I-atoms was observed from all systems studied. The longer time the I-atoms take to exit out of the caging, the lower kinetic energy they have. This is a general dynamical picture of inelastic collision processes: more collisions need longer time and lose more translational energy. The temporal evolution of the exited I-atoms exists a bi-exponential behavior from all studied system, which indicates the different caging structures in clusters. The work is still in progress including molecular dynamics simulations and here only the first system, the I-atoms solvated in $(C_5H_6I)_n$, is presented. Partial work of solvation dynamics is from the collaboration with Dr. P.Y. Cheng on the early stage of this project.

Finally, in Chapter 8, we present the first fs studies of *nonradiative dynamics* of big organic molecules in an isolated environment.[31] Recently, more and more theoretical calculations have predicted that many nonradiative dynamics in big organic molecules

are governed by conical intersections.[32] The studies of azines are threefold: (1) solve the puzzle of the fast nonradiative dynamics; (2) test the theoretical prediction on the conical intersections; and (3) observe the valence-bond isomers of azines. The experimental results are very striking and indicate that the conical intersection does play a key role on the fast nonradiative dynamics. The isomerization dynamics of different valence-bond structures have been observed. Recent studies in this group of the nonradiative dynamics of azulene[33] and the photodissociation of many large organic molecules[34] have revealed that the reaction dynamics are indeed controlled by conical intersections, which seems to be a general phenomenon. The photochemistry and photophysics of many large organic molecules need to be re-studied by using the methodology induced by femtochemistry and the dynamics and mechanism should be brought to a new level of understanding. This work is from the collaboration with Drs. E.W. Diau, T.M. Bernhardt and S.D. Feyter, and Professor John D. Roberts.[31]

1.1. References

1. M. Dantus, M.J. Rosker and A.H. Zewail, J. Chem. Phys. **87** (1987) 2395; *ibid.*, **89** (1988) 6128; M.J. Rosker, M. Dantus and A.H. Zewail, *ibid.*, **89** (1988) 6113.
2. A.H. Zewail, Science **242** (1988) 1645; T.S. Rose, M.J. Rosker and A.H. Zewail, J. Chem. Phys. **91** (1989) 7415.
3. A.H. Zewail, *Femtochemistry: Ultrafast Dynamics of the Chemical Bond* (World Scientific, Singapore, 1994).
4. *Femtosecond Chemistry*, eds. J. Manz and L. Wöste (VCH, Weinheim, 1995).
5. *Femtochemistry: Ultrafast Chemical and Physical Processes in Molecular Systems*, ed. M. Chergui (World Scientific, Singapore, 1996).
6. *Femtochemistry and Femtobiology*, ed. V. Sundström (World Scientific, Singapore, 1998).
7. *Chemical Reactions and Their Control on the Femtosecond Time Scale, XXth Solvay Conference on Chemistry*, Adv. Chem. Phys. **101**, eds. P. Gaspard, I. Burghard, I. Prigogine and S.A. Rice (John Wiley & Sons, New York, 1997).
8. A.H. Zewail, J. Phys. Chem. **100** (1996) 12701.
9. A.H. Zewail, Proc. Robert A. Welch Found. Conf. Chem. Res. **41** (1997) 323.
10. C. Rullière, *Femtosecond Laser Pulses* (Springer, Berlin, 1998).
11. A. Baltuška, M.S. Pshenichnikov and D.A. Wiersma, Optics Lett. **23** (1998) 1474.
12. G. Mourou, Appl. Phys. B **65** (1997) 205; Appl. Phys. B **68** (1999) 287-655 (special issue).
13. D. Zhong and A.H. Zewail, J. Phys. Chem. A **102** (1998) 4031.
14. D. Zhong, S. Ahmad and A.H. Zewail, J. Am. Chem. Soc. **119** (1997) 5978.

15. P.Y. Cheng, D. Zhong and A.H. Zewail, Chem. Phys. Lett. **237** (1995) 399.

16. P.Y. Cheng, D. Zhong and A.H. Zewail, J. Chem. Phys. **103** (1995) 5153.

17. P.Y. Cheng, D. Zhong and A.H. Zewail, J. Chem. Phys. **105** (1996) 6216.

18. D. Zhong and A.H. Zewail, Proc. Natl. Acad. Sci. USA **96** (1999) 2602.

19. D. Zhong, T.M. Bernhardt and A.H. Zewail, J. Chem. Phys., *submitted.*

20. D. Zhong, S. Ahmad, P.Y. Cheng and A.H. Zewail, J. Am. Chem. Soc. **119** (1997) 2305.

21. D. Zhong, P.Y. Cheng and A.H. Zewail, J. Chem. Phys. **105** (1996) 7864.

22. C. Jouvet and B. Soep, J. Chem. Phys. **80** (1984) 2229; S. Buelow, G. Radhakrishnan, J. Catanzarite and C. Wittig, J. Chem. Phys. **83** (1985) 444.

23. N.F. Scherer, L.R. Khundker, R.B. Bernstein and A.H. Zewail, J. Chem. Phys. **87** (1987) 451; S.I. Ionov, P.I. Ionov and C. Wittig, Faraday Disc. Chem. Soc. **97** (1994) 379.

24. M. Gruebele, I.R. Sims, E.D. Potter and A.H. Zewail, J. Chem. Phys. **95** (1991) 7763; S.A. Wright, M.F. Tuchler and J.D. McDonald, Chem. Phys. Lett. **226** (1994) 570.

25. R.D. van Zee and J.C. Stephenson, J. Chem. Phys. **102** (1995) 6946.

26. R.S. Mulliken and W.B. Person, *Molecular Complexes* (Wiley-Interscience, New York, 1969).

27. Y.T. Lee, Angew. Chem. Int. Ed. Engl. **26** (1987) 939; J.C. Polanyi, *ibid.*, **26** (1987) 952; D.R. Herschbach, *ibid.*, **26** (1987) 1221.

28. D.C. Clary, Science **279** (1998) 1879.

29. P.Y. Cheng, D. Zhong and A.H. Zewail, J. Phys. Chem. **99** (1995) 15733.

30. P.Y. Cheng, D. Zhong and A.H. Zewail, Chem. Phys. Lett. **242** (1995) 369.

31. D. Zhong, E.W.-G. Diau, T.M. Bernhardt, S.D. Feyter, J.D. Roberts and A.H. Zewail, Chem. Phys. Lett. **208** (1998) 129.

32. M. Klessinger and J. Michl, *Excited States and Photochemistry of Organic Molecules* (VCH, New York, 1995); F. Bernardi, M. Olivucci and M.A. Robb, Pure Appl. Chem. **67** (1995) 17; W. Domcke and G. Stock, Adv. Chem. Phys. **100** (1997) 1; D.R. Yarkony, Acc. Chem. Res. **31** (1998) 511.

33. E.W.-G. Diau, S. De Feyter and A.H. Zewail, J. Chem. Phys., *in press*.

34. E.W.-G. Diau, O.K. Abou-Zied, A.A. Scala and A.H. Zewail, J. Am. Chem. Soc. **120** (1998) 3245; S. De Feyter, E.W.-G. Diau and A.H. Zewail, Chem. Phys. Lett., *in press*.

Chapter 2

Experimental Methodology

2.1. Introduction

The experiments presented in Chapters 3-8 all involved the application of femtosecond pump-probe spectroscopy, or namely femtosecond transition-state spectroscopy (FTS), to gaseous systems prepared in a pulsed supersonic molecular beam. In order to resolve the dynamics and mechanism of complex reactions, the femtosecond kinetic-energy resolved time-of-flight (fs-KETOF) mass spectrometry was successfully developed to achieve the temporal, energy and spatial resolution of dynamics. It is very significant to add another dimension (kinetic-energy) to conventional FTS and to reach the capability of dissecting complex reactions into the elementary steps and mapping out the reaction evolution. Here, we give out the detailed description of the fs laser system, the molecular beam and fs-KETOF method. Specific details relevant to the individual experiments, such as sample preparation, are presented in later Chapters.

2.2. Femtosecond Laser System

All experiments were performed using the synchronously-pumped dye laser with amplifiers except for the high time resolution (~60 fs) of several experiments, a colliding pulse mode-locked (CPM) ring dye laser was used. The description of the CPM fs laser can be found in Ref.1 and here we only describe the workhorse synch-pumped laser system.

The synch-pumped laser system is schematically shown in Figure 2.1. The second harmonic output of a 76 MHz mode-locked Nd:YAG laser (Coherent Antares 76S) was used to synchronously pump an ultrafast dye laser (Coherent Satori) to generate fs laser pulses. The dye laser is of the hybrid mode-locking linear cavity design, employing twin

jets, and dispersion compensated by a prism pair. Solutions of Rhodamine 610 and DODCI laser dyes (Exciton) in ethylene glycol were used as the gain medium and the saturable absorber, respectively, to produce laser radiation around 610 nm. The mode-locking of the dye laser was continuously monitored by a home-made real-time scanning autocorrelator. Typical characteristics of the dye laser output pulses are 200 fs fwhm and 2 nJ/pulse.

The resulting fs laser pulses were amplified through a four-stage pulse dye amplifier pumped by the second harmonic output of a 20 Hz Q-switch Nd:YAG laser (Spectra-Physics DCR-2A). The first three stages were side-pumped and employed SR-640/water as the gain media. The last stage was end-pumped with a double-pass arrangement and used R640/water as the gain medium. The amplified pulses (~ 400 μJ/pulse) were then recompressed through a SF-10 prism pair to compensate for the group velocity dispersion occurring during the amplification. To generate pump pulses between 260-350 nm, 80% of the amplified 610-nm beam was split off by a beamsplitter and was focused into a small quartz cell containing D_2O to generate a white light continuum. Different spectral portions of the continuum were selected by interference filters (10 nm fwhm) centered at the desired wavelengths. The filtered continuum was reamplified in a three-stage dye amplifier pumped by the second or third harmonic output of the same Q-switch Nd:YAG laser used to pump the first dye amplifier. Another SF-10 prism pair is used to compress the pulse width. The resulting pulses were then frequency doubled through a 0.5 mm KDP crystal to produce the pump pulses (~ 5-10 μJ/pulse).

The remaining 20% of the 610-nm light was amplified again through a single-stage dye amplifier (R640/water) with a double-pass arrangement. The resulting pulses

were delayed in time by a retroreflector mounted on a computer controlled translation stage (Dynaoptic Motion), and then frequency-doubled by a 0.5 mm KDP crystal to obtain the probe pulses at around 304 nm (~20 μJ/pulse) for 2+1 resonance-enhanced multiphoton ionization (REMPI) detection of free iodine atoms. The pump and probe beams were recombined collinearly by a dichroic beamsplitter and were focused and spatially overlapped in the extraction region of a time-of-flight mass spectrometer (TOF-MS).

2.3. Molecular Beam Apparatus

The experiments were carried out in a conventional two-chamber molecular beam apparatus schematically shown in Figures 2.2 and 2.3. Briefly, a supersonic molecular beam containing the species of interest was produced in the first chamber through a pulsed valve (General Valve Series 9) with an orifice of 0.5 mm in diameter, skimmed and intersected by the fs laser beams in the extraction region of a two-stage linear TOF-MS housed in the second chamber. Usually, the pure He gas is used as the carrier gas with about ~800 Torr backing pressure. The molecular beam conditions were carefully controlled by two ways for the monomer and cluster studies: (1) controlling the sample pressure by maintaining the liquid samples at different temperatures or adjusting the flow rates for the gas samples; (2) controlling the delay time between the femtosecond laser pulses and the pulsed valve opening. Usually the leading edge of the gas pulse only contains the monomer distribution and the central part is cluster-rich.

The mo0 0 (()A ˝(2)S ˝12.300 0 32 -0.300 0 ())D ˝-0.400 0 (c)A ˝(on)S ˝0.200 0 (t)A ˝-0.300 (

each other. The TOF-MS was also used as a kinetic-energy spectrometer, as described in

Sec. 2.4, to resolve the translational energy distribution of reaction products. A pair of deflection plates was used in the field free region to correct for the drift of ion trajectories due to the molecular beam velocity component perpendicular to the TOF axis. The resulting ions were detected by a dual microchannel plate (MCP) arrangement and the ion signal was fed into a digital oscilloscope (LeCroy 9361, 2.5 GS/s) for recording mass spectra and KETOF distributions.

Time-resolved transients were obtained by monitoring the ion signal of certain mass channel using a boxcar integrator while the pump-probe delay time was scanned. The transients are typically the average of 20-100 scans. For most of the transients reported, the pump laser polarization was parallel or at a magic angle to the TOF-MS axis and orthogonal to the probe laser polarization.

The free iodine atoms produced in the reactions were detected through the 2+1 REMPI scheme. Several two-photon allowed atomic transitions originating from the ground state of iodine atom $^2P_{3/2}$(I, 304.67, 304.55, and 303.69 nm) and the spin-orbit excited state $^2P_{1/2}$(I^*, 305.57 and 304.02 nm) have been reported to lie in the general spectral region of the probe laser. The bandwidth of the probe laser (~2 nm) therefore allows simultaneous detection of both I and I^*. Because of the resonance detection through narrow atomic transitions, the I^+ intensity is very sensitive to the probe wavelength. To ensure resonance detection, the output wavelength of the dye laser was carefully tuned by adjusting a birefrigent filter placed in the dye laser cavity and was measured by a calibrated monochrometer. The dye laser wavelength was tuned to 609.0±1.0 nm. All dye solutions used in the dye amplifiers were kept at the lowest

concentrations possible to minimize spectral broadening and distortion. The probe pulses produced in this manner are centered at about 304.5 nm and have a bandwidth of ~2 nm.

The zero-of-time and the cross-correlation of the pump and probe pulses were determined *in situ* by measuring the transient rise of the aniline or N,N-diethylaniline by 1+1 REMPI signal through its S_1 state immediately after the experiments were done in the molecular beam. Since the S_1 state is long-lived (~ns), therefore the 1+1 REMPI transient rise is equivalent to the convolution of the pump-probe correlation with a step function on the time scales of interest. The typical pump-probe cross-correlation was 450 ±50 fs fwhm. Although a much shorter probe pulse can be easily reached, the resulting broader spectrum leads to a huge I^+ background in most molecules and a loss of tunability for the iodine REMPI detection.

2.4. Femtosecond-resolved KETOF Method

The KETOF technique is basically the mass spectrometric version of the Doppler photofragment spectroscopy implemented by laser-induced fluorescence (LIF).[2] The subject has been extensively reviewed by many authors[3] and the technique without time resolution has been used by many groups.[4-8] Here, we have successfully introduced the fs resolution into the conventional KETOF method and in the following, we describe the basics of the two different methods used in the work.

When a molecule is dissociated through a one-photon excitation by linearly polarized light, the velocity distribution of a fragment can be written as the product of two functions: f(v), the speed distribution, and I(θ), the angular distribution. The speed distribution is determined by its dynamics and mechanism. The c.m. angular distribution

of fragments having the same recoil speed is axially symmetric with respect to the electric vector $\hat{\varepsilon}$ of the light and can be expressed as:[9]

$$I(\theta) = \frac{1}{4\pi}[1 + \beta P_2(\cos\theta)], \tag{2.1}$$

where θ is the angle between the final recoil direction and $\hat{\varepsilon}$, $P_2(x) = (1/2)(3x^2 - 1)$ is the second Legendre polynomial, and β is the recoil anisotropy parameter. If the molecule dissociates instantaneously (much faster than a rotation period), then β is given by

$$\beta = 2P_2(\cos\varphi), \tag{2.2}$$

where φ is a fixed angle between the transition dipole moment (μ) of the molecule and the fragment recoil direction. β can have values between 2 and -1, corresponding to purely parallel (φ=0) and perpendicular (φ=π/2) transitions, respectively. In reality φ can be a range of angles due to rotational and/or vibrational motions which usually reduce the absolute magnitude of β. In these cases, an effective anisotropy parameter, β_{eff}, is more appropriate.

In our experiment, the three-dimensional recoiling distribution is projected onto an axis defined in the laboratory frame, *i.e.*, the TOF-MS axis. By using the coordinate system in Figure 2.4 and $v_z = v\cos\theta_z$ and $\cos\theta = \cos\theta_z\cos\chi + \sin\theta_z\sin\chi\sin\phi_z$, transforming the angular distribution to the laboratory coordinate system in which the z axis is the TOF-MS axis gives the projected distribution as[10]

$$f(v_z,\chi)=\frac{1}{2v}\left[1+\beta P_2(\cos\chi)P_2(\frac{v_z}{v})\right], \qquad v_z \le v\ ,$$

$$f(v_z,\chi)=0\ , \qquad v_z > v, \tag{2.3}$$

where v_z is the velocity component along the z axis, v is the speed of the fragments, and χ is the angle between the z axis and the pump-laser polarization $\hat{\varepsilon}$. The appearances of the v_z distributions thus depend on both χ and β. Figure 2.4 shows some theoretical v_z distributions for a single v at three pump-laser polarization angles.

In cases where the instrumental response function is negligible, the v_z distribution is directly related to the observed KETOF distribution by

$$f(v_z)=h(T)\left|\frac{dT}{dv_z}\right|,$$

$$v_z=-\frac{qE}{m}(T-T_0)\ , \tag{2.4}$$

where $h(T)$ is the observed KETOF distributions, $(dT/dv_z)=-m/qE$ is merely an instrument constant for a given mass m, E is the extraction field strength, q is the ion charge, T_0 is the TOF for $v_z=0$ ions (apart from a small shift), and T is the TOF (Figure 2.3). Strictly speaking, the v_z distribution thus obtained is the laboratory v_z distribution. In our experiment, the c.m. of the dissociating system is traveling with the molecular beam whose z velocity component is negligible. This is because the molecular beam axis is orthogonal to the TOF-MS axis and the molecular beam is skimmed and detected at a far distance from the nozzle (~15 cm). Therefore, the laboratory v_z is equivalent to the $v_{z,cm}$, the iodine atom v_z with respect to the c.m. of the reaction precursor. As mentioned in Sec. 2.3, a pair of deflection plates is used to correct the ion trajectories for the

transverse drift introduced by molecular beam velocity. The force exerted on the ions by the deflection field is perpendicular to the z axis and therefore again do not interfere the $v_{z,cm}$ distribution.

If the reaction results in a distribution of recoil speed f(v), then we have to sum all the single speed v_z distribution, Eq. (2.3), over the entire speed distribution. The v_z distribution becomes

$$f(v_z,\chi) = \int_{|v_z|}^{\infty} \frac{1}{2v}\left[1+\beta(v)P_2(\cos\chi)P_2(\frac{v_z}{v})\right] f(v)v^2 dv\,. \tag{2.5}$$

The observed KETOF distribution is then the convolution of $f(v_z,\chi)$ with some instrumental response functions. The task here is to extract f(v) and $\beta(v)$ from the observed KETOF distribution. An important simplification to the above expression occurs when the KETOF distribution is measured at χ=54.7°, or the "magic angle."[11] At this angle, $P_2(\cos\chi)$=0 and therefore the distribution is independent of β (see Fig. 4.4);

$$f(v_z,54.7°) = \int_{|v_z|}^{\infty} \frac{1}{2v} f(v)v^2 dv\,. \tag{2.6}$$

We measured KETOF distributions at the magic angle with respect to the TOF-MS axis to obtain $f(v_z,54.7°)$. The speed distribution f(v) can then be directly obtained by differentiation:

$$f(v) = -\frac{2}{v}\frac{d}{dv_z} f(v_z,54.7°)\,|_{v_z=v}\,. \tag{2.7}$$

The speed probability distribution in v to v+dv can be obtained:

$$g(v)=v^2 f(v) \quad . \tag{2.8}$$

Experimentally, the v_z distribution measured at the magic angle is smoothed by a Savitzky-Golay numerical filter[12] to remove the high-frequency noise. The resulting data are then differentiated according to Eq. (2.7) to obtain the speed distribution. Only the first half of the KETOF data was used in the analysis. The data smoothing process is necessary because the differentiation significantly amplifies the noise.

The speed distribution thus obtained is the iodine atom speed distribution with respect to the c.m., which can be transformed to the translational energy distribution $P(E_t)$ by $P(E_t)=g(v)(dv/dE_t)$ from the following relations:

$$E_{t,cm}^{total} = \frac{1}{2}\left(\frac{m_I M}{M-m_I}\right)v^2 \quad , \qquad P(E_{t,cm}^{total}) = \frac{g(v)}{v}\left(\frac{M-m_I}{Mm_I}\right), \tag{2.9}$$

where m_I is the mass of the iodine atom (or the mass of the detected ion in general) and M is the parent mass. In some complex reactions, the dissociation kinematics is not as clear as the photodissociation of a simple molecule such as CH_3I (two-body dissociation) and may not even be uniform throughout the entire distribution. In such cases, only the relative translational energy of the iodine atom with respect to the c.m. is evaluated by the following relations:

$$E_{t,cm} = \frac{1}{2}m_I v^2 \quad , \quad P(E_{t,cm}) = \frac{g(v)}{v}\left(\frac{1}{m_I}\right). \tag{2.10}$$

Note that the instrumental response is not included in the above procedure. In our experiment, dissociation and ionization are achieved by fs laser pulses and the resulting

ions are detected by MCP's. As a result, a mass peak originating from a direct ionization of a parent molecule under very low signal level conditions has a width of ~ 4 ns (fwhm) detected by the digital oscilloscope at a sampling rate of 2.5 gigasamples per second. This translates into an instrument-limited speed resolution of ~15-20 m/sec, which is not significant in the present work. Although this instrument-limited resolution is independent of speed, it gives rise to a speed dependent translational energy resolution. Other factors, such as diffraction off the ion optics grids and inhomogeneity of the electric fields, may also affect the resolution.

An important energy resolution limiting factor in the fs-KETOF experiment is the broad bandwidth of the fs lasers. Our pump laser has a bandwidth (fwhm) of ~ 4 nm, or ~ 500 cm^{-1} at 277 nm. This introduces a broad distribution to the available energies for reactions and is probably as important as other instrument-limited factors. However, we believe that the instrument response and laser bandwidth should not affect our interpretation of the data, as tested and demonstrated by many examples in Chapters 3-8.

The anisotropy parameter distribution $\beta(v)$ is obtained by fitting the v_z distributions measured at parallel polarization using the speed distributions derived from the magic angle data. The entire anisotropy distribution is divided into a certain number of "bins." Each bin covers a speed range of 30-100 m/sec and the anisotropy is assumed to be constant within each single bin. The fitting procedure is based on a non-linear least square fitting algorithm,[12] adjusting the value in each bin to obtain a best fit to the parallel (and/or perpendicular) polarization v_z distribution according to Eq. (2.5).

Instead of using the differentiation method to obtain $f(v)$, and the numerical fitting for $\beta(v)$, another approach, which is approximate, may be used and it is often used. It

involves measuring the fs-KETOF distribution by employing a discrimination aperture (or namely the core-sampling condition). Experimentally, a small aperture was placed just before the MCP detector to discriminate against collecting the ions which have v_{xy} components larger than the discrimination value v_d, as illustrated in Figure 2.5. The method has been recently detailed by two other groups[5,13] and here, only relevant points to our experiments are described.

When the molecular dissociation results in two velocity distributions, such as high- and low-velocity components, we are especially able to completely separate the two distributions in this one-dimensional v_z profile. For the high velocity component, the signal only in the small solid angle ($0 \leq \theta \leq \arcsin(v_d / v)$) is collected and the KETOF distribution appears only in the larger v_z region and truncates between v and $(v^2-v_d^2)^{1/2}$ and -v to $-(v^2-v_d^2)^{1/2}$. However, for the low velocity distribution, all ions are detected if the maximum value of v is less than the v_d, and the observed KETOF distribution terminates between v and -v. As shown in Figure 2.5, the higher the recoil speed, the stronger the v_{xy} discrimination and the sharper the observed KETOF distribution. This method was used to study the dissociation of IBz in Chapter 3, a reaction with two-mode excitation, with a 5-mm-diam discrimination aperture to reject ions with high-velocity components of $v_{xy} \geq v_d$=110 m/s under our operating conditions.

2.5. References

1. M.J. Rosker, M. Dantus and A.H. Zewail, J. Chem. Phys. **89** (1988) 6113.

2. J.P. Simon, J. Phys. Chem. **91** (1987) 5378; P.L. Houston, J. Phys. Chem. **91** (1987) 5388.

3. G.E. Hall and P.L. Houston, Annu. Rev. Phys. Chem. **40** (1989) 375, and references therein.

4. G.E. Hall, N. Sivakumar, R. Ogorzalek, G. Chawla, H.P. Haerri, P.L. Houston, I. Burak and J.W. Hepburn, Faraday Discuss. Chem. Soc. **82** (1986) 13.

5. H.J. Hwang, J. Griffiths and M.A. El-Sayed, Int. Mass Spectrom. Ion Processes **131** (1994) 265.

6. S.M. Penn, C.C. Hayden, K.J.C. Muyskens and F.F. Crim, J. Chem. Phys. **89** (1988) 2909.

7. M. Mons and I. Dimicoli, J. Chem. Phys. **90** (1989) 4037.

8. R.A. Hertz and J.A. Syage, J. Chem. Phys. **100** (1994) 9265.

9. R.N. Zare and D.R. Herschbach, Proc. IEEE **51** (1963) 173; R.N. Zare, Mol. Photochem. **4** (1972) 1.

10. R. Vasudev, R.N. Zare and R.N. Dixon, J. Chem. Phys. **80** (1984) 4863.

11. J.L. Kinsey, J. Chem. Phys. **66** (1977) 2560; M. Dubs, U. Bruhlmann and J.R. Huber, *ibid.* **84** (1986) 3106; J.I. Cline, C.A. Taatjes and S.R. Leone, *ibid.* **93** (1990) 6543.

12. W.H. Press, B.P. Flannery, S.A. Teukolsky and W.T. Vetterling, *Numerical Recipes* (Cambridge Univ. Press, New York, 1992).

13. J.A. Syage, J. Chem. Phys. **105** (1996) 1007.

2.6. Figure Captions and Figures

Figure 2.1. Schematic description of the femtosecond laser system. Notice that two tunable femtosecond pulses were utilized and in synchrony.

Figure 2.2. Schematic representation of the molecular beam apparatus integrated with two femtosecond laser beams. The pulsed nozzle and the TOF-MS are located in two separate chambers connected by a skimmer.

Figure 2.3. A diagram showing the "turnaround time" for two ions initially moving parallel to the TOF-MS axis with the same speed but in opposite directions. The time (t_a), which the ion spend in the acceleration region, is about several microseconds in our TOF arrangement.

Figure 2.4. Coordinate system used in describing the fragment angular-velocity distribution in the KETOF experiment. ε_{pu} is the electric vector of the fs pump laser pulse, which was kept in the yz plane. V_{recoil} is the fragment recoil direction. The lower part shows the theoretical predictions of the v_z distributions for some representative β's and χ's for single-speed fragments. Note that the distributions for $\beta=0$ and $\chi=54.7^0$ are identical.

Figure 2.5. A two-dimensional (v_z, v_{xy}) depiction of the v_{xy} discrimination for three recoil speeds given by the circles. The discrimination velocity v_d, which discriminates

against photoions with $v_{xy} \geq v_d$, is also shown. The lower part gives the simulated recoil velocity distributions of the single-speed fragment in the v_z domain without and with the v_{xy} discrimination for $\chi=0^0$ and three typical β's. The higher the recoil speed, the stronger the v_{xy} discrimination.[5,13]

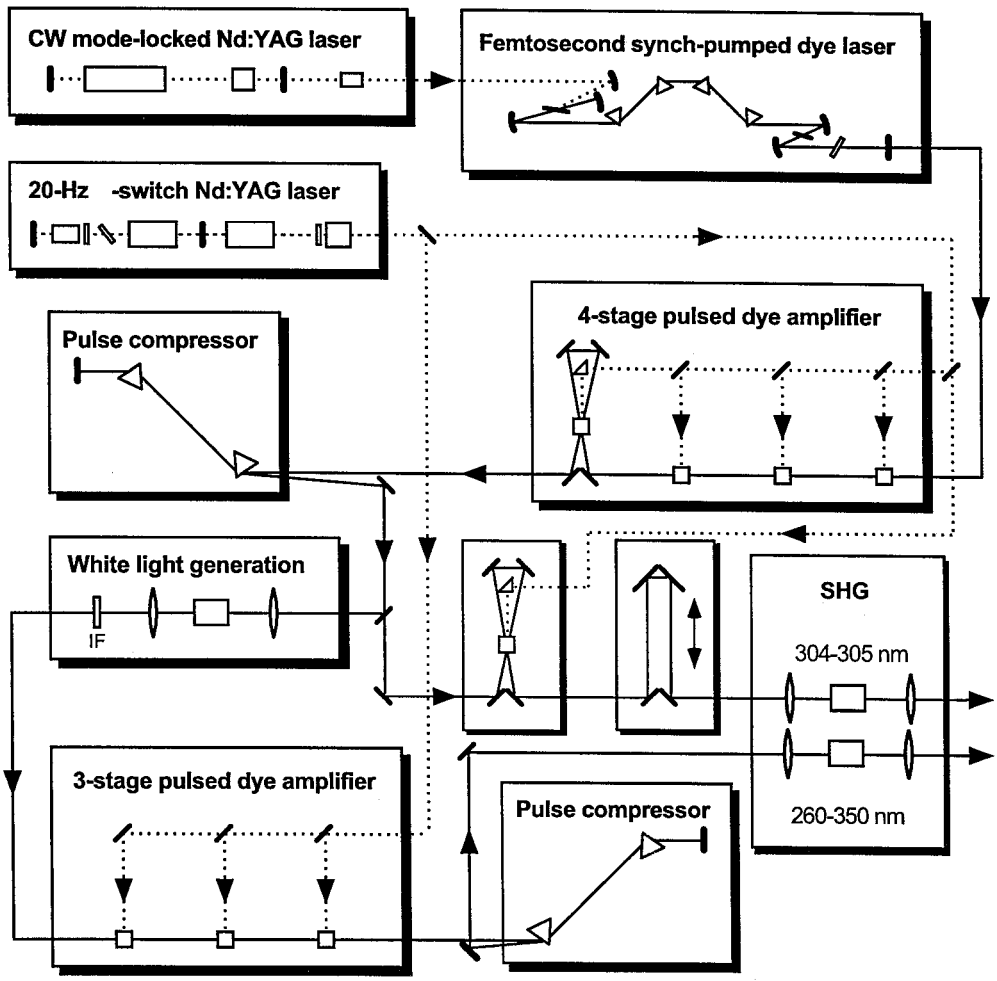
CW mode-locked Nd:YAG laser
Femtosecond synch-pumped dye laser
20-Hz -switch Nd:YAG laser
4-stage pulsed dye amplifier
Pulse compressor
White light generation
IF
SHG
304-305 nm
260-350 nm
3-stage pulsed dye amplifier
Pulse compressor

Figure 2.1

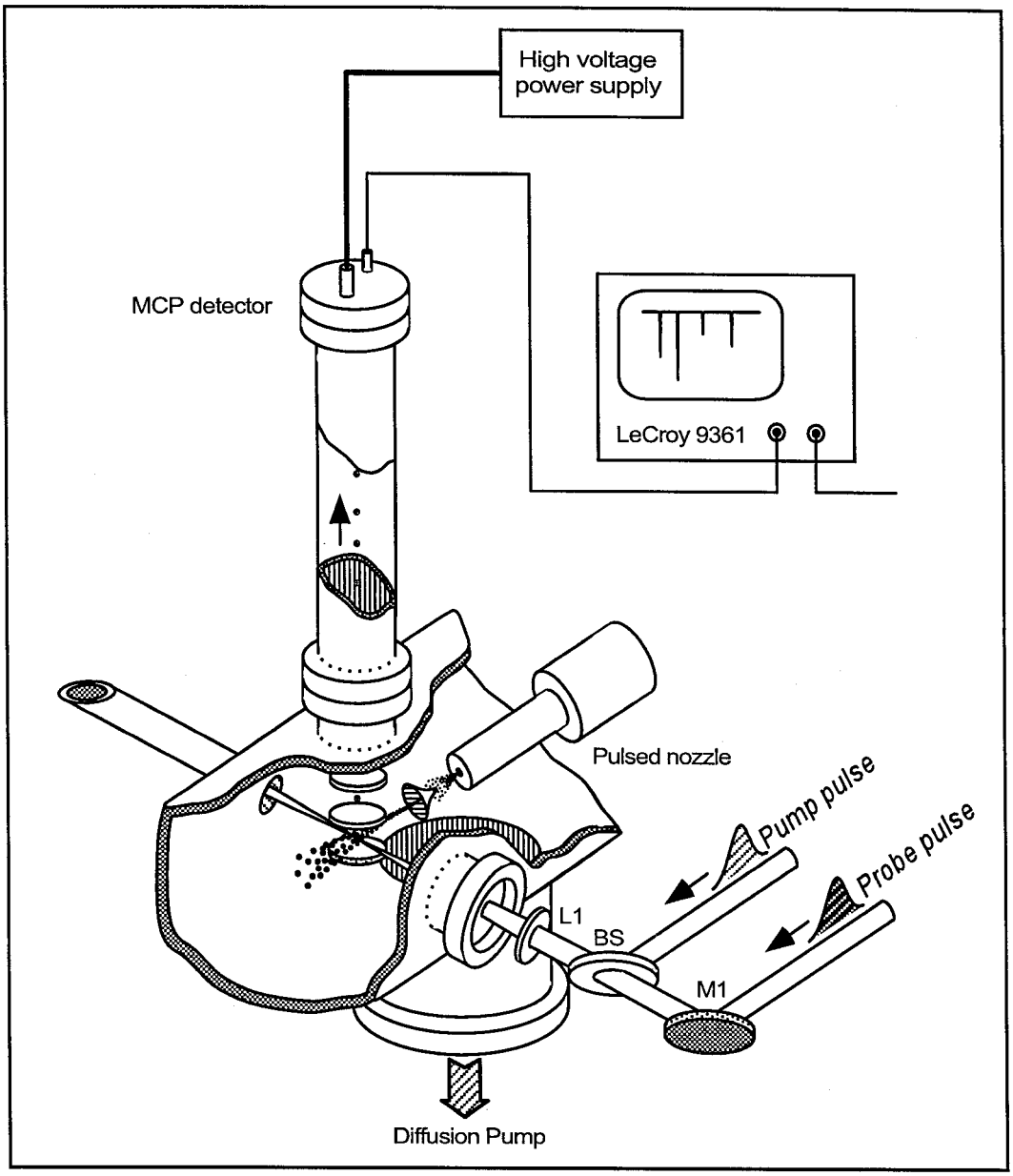
High voltage
power supply
MCP detector
LeCroy 9361
Pulsed nozzle
Pump pulse
Probe pulse
L1
BS
M1
Diffusion Pump

Figure 2.2

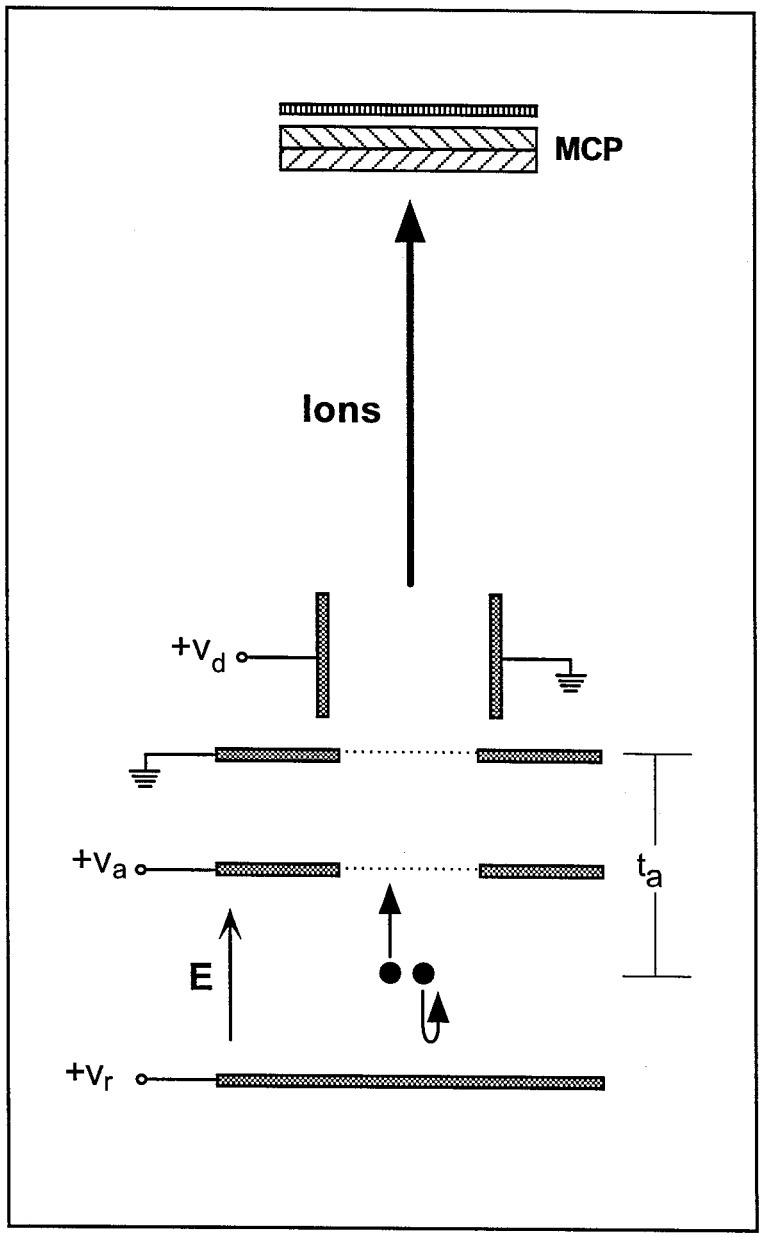

Figure 2.3

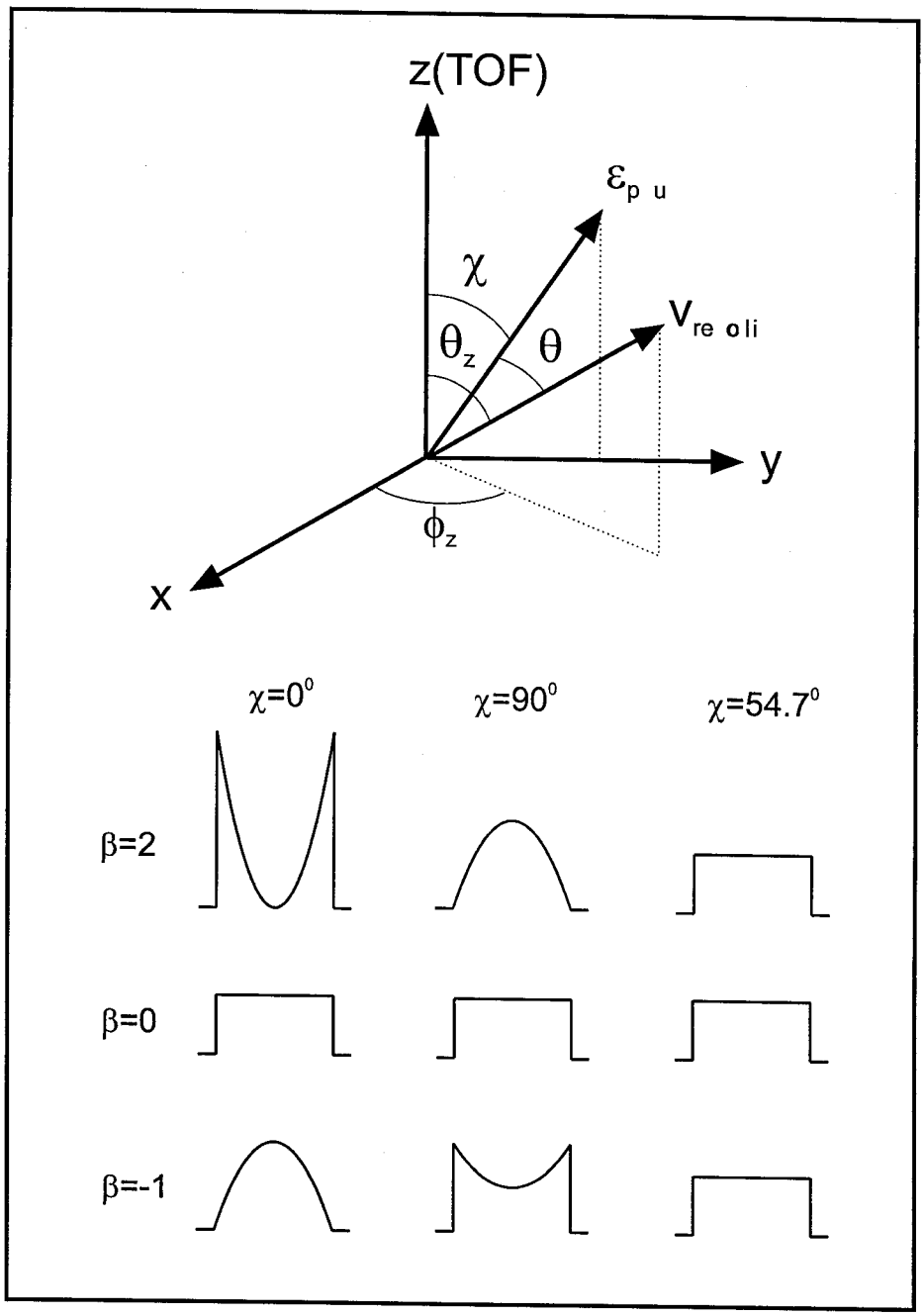
z(TOF)
$\varepsilon_{p\ u}$
χ
θ_z
θ
$V_{re\ oli}$
y
x
ϕ_z
$\chi=0^o$
$\chi=90^o$
$\chi=54.7^o$
β=2
β=0
β=-1

Figure 2.4

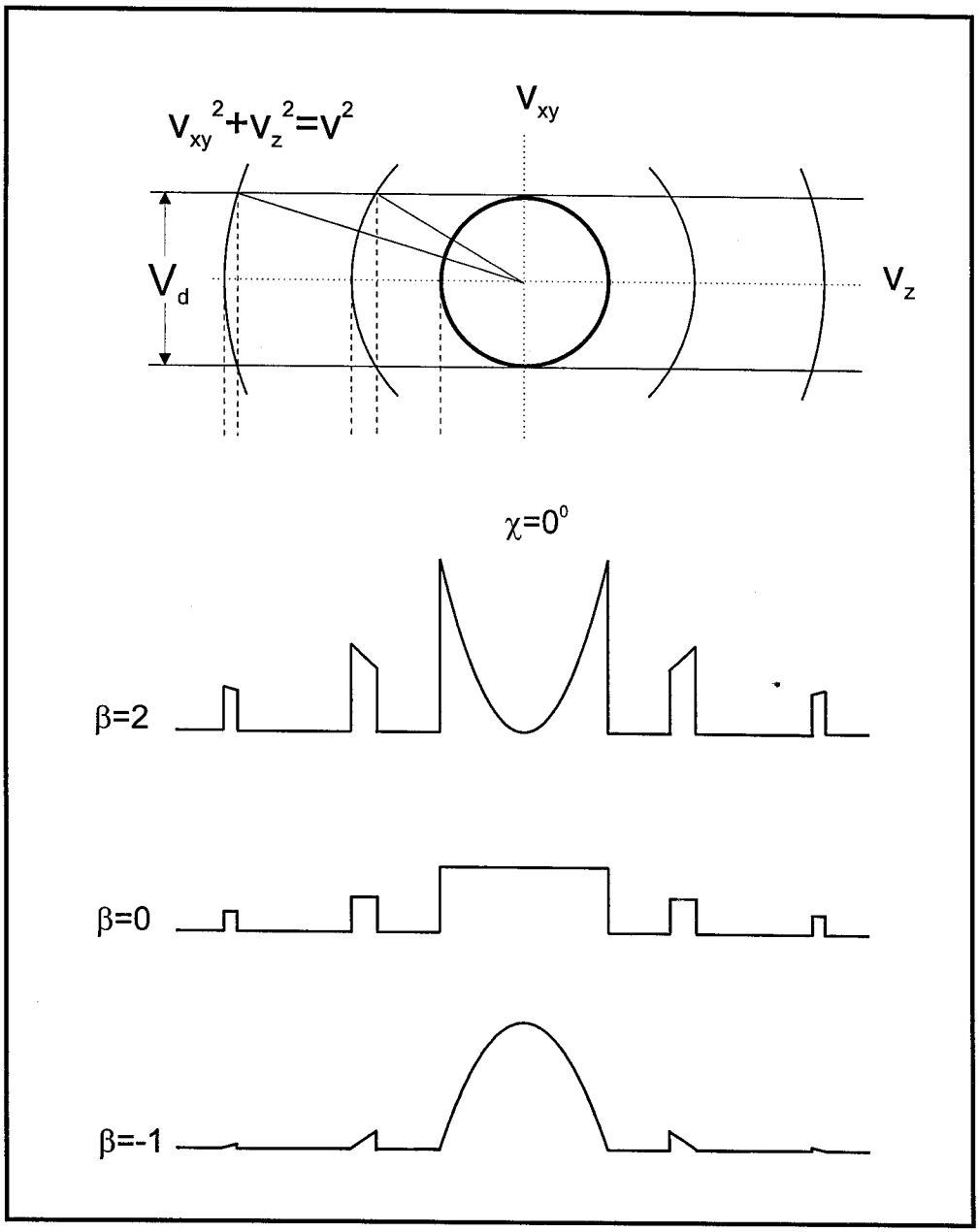

Figure 2.5

Chapter 3

Femtosecond Real-Time Probing of Unimolecular Reactions: Studies of Temporal, Velocity, Angular and State Dynamics from Transition States to Final Products[‡]

[‡] Adapted from: D. Zhong and A.H. Zewail, J. Phys. Chem. A **102** (1998) 4031-4058; D. Zhong, S. Ahmad and A.H. Zewail, J. Am. Chem. Soc. **119** (1997) 5978-5979; P.Y. Cheng, D. Zhong and A.H. Zewail, Chem. Phys. Lett. **237** (1995) 399-405.

3.1. Introduction

Over the past two decades, a variety of detection techniques have been used to probe the ultrafast dynamics of chemical reactions (for recent books see refs. 1-5). These include the use of absorption, laser-induced fluorescence (LIF), multiphoton ionization (MPI), photoelectron spectroscopy, nonlinear degenerate four-wave mixing, stimulated emission pumping, Coulomb explosion, and time-resolved mass spectrometry in molecular beams. One of the techniques used extensively in this laboratory is mass spectrometry with femtosecond (fs), and earlier with picosecond (ps), resolution.

The advantages of fs-resolved mass spectrometry are numerous (see refs. 1-7). First, the mass resolution which identifies reaction constituents. Second, as reported from this laboratory,[8] the kinetic energy distribution(s) can be followed as a function of time, allowing us to map changes in velocities of fragments. Third, by invoking polarized fs pulses, relative to the time-of-flight axis, one is able to study the angular distributions and the nature of the transition(s) involved. Finally, the state of the final fragment could be resolved by selective ionization with the probe fs pulse, using, *e.g.*, resonance-enhanced MPI or REMPI. Thus, for a given velocity or velocity range we can monitor the temporal evolution of the reaction.

With these capabilities of *temporal*, *velocity*, *angular* and *state* resolution of the dynamics, it is possible to study a variety of reactions (for a review see ref. 9), elementary and complex. In this Chapter, we give a full account of the approach with applications to many unimolecular reactions. The level of complexity varies from diatomics to polyatomics, from direct-mode to complex-mode, and from one-center to two-center to four-center reactions. The reactions reported here are those of iodine,

cyanogen iodide, methyl iodide, iodobenzene, 1,2-diiodotetrafluoroethane, and mercury iodide. We systematically study the dynamics in these systems from results of (i) the fs temporal dynamics; (ii) the time- and kinetic-energy-resolved time-of-flight (KETOF) mass spectra; (iii) the angle-resolved KETOF distributions, and (iv) the state-resolved (I and I^*) dynamics.

3.2. Experimental Techniques

3.2.1. Experimental

All experiments were performed in a two-chamber molecular beam apparatus integrated with the tunable femtosecond laser system. Most details have been described in Chapter 2 and only a brief description, related to the work in this Chapter, is given here.

The fs oscillator generates pulses typically with ~200 fs full width at half maximum (FWHM) and 1-2 nJ energy per pulse. The pulse wavelength was tuned to be centered at ~609 nm. These fs pulses were then passed through a home-built four-stage pulsed dye amplifier to reach an energy of 300~400 μJ/pulse. The amplified pulses were compressed through a SF-10 prism pair to compensate for the group velocity dispersion in the amplification process. To generate 277 nm pump pulses, 80% of the beam was split off by a beam splitter and was focused into a small quartz cell containing D_2O solution to generate a white light continuum. An interference filter was used to select a different portion of the continuum at the desired wavelength. This portion was then reamplified through a three-stage pulsed dye amplifier. The resulting pulses were recompressed by

another SF-10 prism pair and then frequency doubled through a 0.5 mm KDP nonlinear crystal to produce the pump beam (277 nm and ~10 μJ/pulse).

Only for the I_2 system was the pump wavelength at 690 nm for the A-state excitation. The remaining 20% of the 609-nm laser beam was sent to a double-passed single-stage dye amplifier and then delayed in time by a retroreflector mounted on a computer-controlled translation stage. A 0.5 mm KDP crystal was used for frequency doubling to obtain the probe beam at around 304.5 nm (~20 μJ/pulse) for 2+1 REMPI detection of free iodine atoms. Finally, the pump and probe pulses were recombined collinearly by a dichroic beam splitter and were focused and spatially overlapped in the extraction region of the TOF mass spectrometer.

A supersonic molecular beam containing the species of interest was generated in the first chamber, skimmed, and intersected by the fs laser beams in the extraction region of a two-stage linear TOF-MS housed in the second chamber. A pair of deflection plates was employed in the field-free region to correct for the drift of ion trajectories due to the molecular beam velocity component perpendicular to the TOF axis (z). The ions were collected by a 25-mm-diam microchannel plate assembly (MCP). The molecular beam, TOF-MS axis, and the fs laser beams were orthogonal to each other. For most results reported here, the pump laser polarization was parallel to the TOF-MS axis and orthogonal to the probe laser polarization. In some magic angle experiments, the pump laser polarization was rotated at an angle of 54.7^0 with respect to the TOF-MS axis by a half-wave plate prior to the frequency doubling. The TOF-MS was also used as a kinetic energy spectrometer, as described in Chapter 2, to resolve the translational energy distribution of reaction products.

The zero-of-time and the cross correlation of the pump and probe pulses were determined by measuring the transient rise of the aniline or n,n-diethyl aniline REMPI signal through their S_1 states immediately after the experiments were done in the molecular beam. Since the S_1 state is long lived, the transient rise is equivalent to the convolution of the pump-probe correlation with a step function on the time scales of interest. The typical pump-probe cross correlation was 450±50 fs FWHM. Although a much shorter probe pulse can be easily reached, the resulting broader spectrum leads to a huge I^+ background in most molecules and a loss of tunability for the iodine REMPI detection. All transients reported here result from one-photon excitation as checked by the power dependence of the observed signal.

Molecules of interest were seeded in ~800 Torr He and were expanded through the pulsed valve. The mixture was made by flowing the He over the sample far away from the nozzle. In order to avoid cluster formation in the expansion, the monomer condition was carefully controlled in two ways: The leading edge of the gas pulse was sampled by varying the delay time between the fs laser pulses and the pulsed valve opening, and the low vapor pressure of samples was used by maintaining the samples at low temperatures.

All samples were purchased from Aldrich except 1,2-$C_2F_4I_2$ which was obtained from PCR. The iodine (I_2, 99.999% pure) was used at room temperature (vapor pressure ~1 Torr). ICN (93%) was further purified through recrystallization followed by vacuum distillation, and used at room temperature (~1 Torr vapor). Methyl iodide (CH_3I, 99.5%) was cooled down to -50^{0}C giving a ~7-8 Torr vapor. $C_2F_4I_2$ (≥97%), without further purification, was maintained at -35^{0}C with a vapor pressure less than 10 Torr. Both

mercury iodide (HgI_2, ~99.999%) and iodobenzene (IBz, ≥98%) were heated to 130^0C and 70^0C, providing vapor pressure less than 1 Torr and ~20 Torr, respectively.

3.2.2. Mass Spectra

The TOF mass spectra are shown in Fig. 3.1a-3.1b. The natural isotope distribution of Hg (196-204) is also presented by the parent HgI_2 mass peak in the insert of Fig. 3b. In contrast to the nanosecond laser experiments, where many parent ions were not observed, most parent ions here are major mass peaks in the TOF mass spectra. Note that no dimer traces were found in Fig. 3a and 3b, and the fragment mass is mostly due to ion fragmentation.

The arrival time of ions from the ionization zone to the detector is in the microsecond (μs) range and this time depends on the ion mass, the applied acceleration electric field (E) and the flight distance. Usually, the time (t_a) the ions spend in the acceleration region is about several microseconds under the conditions used in this laboratory (see Fig. 2.3). When ion fragmentation (AB^{+*} to A^++B) occurs in the different regions during the flight, the ion fragment (A^+) will appear at different positions in the mass spectra. We consider three different cases.

If the molecule AB is ionized at t=0 and then excited AB^+ fragments on the fs to ps time scale, *i.e.,* fragmentation occurs in the ionization zone, then the mass signal is well defined and the mass peaks of A^+ and AB^+ are clearly separated at the normal positions. When the ion has a long lifetime in the μs range, *i.e.,* fragmentation starts after the ion flies out of the acceleration region, A^+ will appear at the same TOF (*i.e.*, mass) as the parent ion AB^+ because the times which ions spend in the field-free region only

depend on the initial velocity, not the mass. If the ion breaks in the acceleration region (~1 μs), the A^+ signal would appear at the normal position, but will have a tail toward AB^+ at longer arrival times of A^+, as observed in the benzene cation fragmentation.[10] However, independent of how long the lifetime of AB^{+*} is, the transient of the fragment A^+ for fs pump-probe experiments should be the same as that of AB^+, because both transients reflect the dynamics of the neutral transition state $AB^{*‡}$ species.

3.3. Methodology

In this section, we describe the approach used in our studies for detecting transition states and final products simultaneously using only one probe fs pulse. The concept is illustrated in Fig. 3.2a, along with the original methodology of femtosecond transition-state spectroscopy,[11] shown in Fig. 3.2b for comparison. For simplicity, we first consider a diatomic molecule, AB, prepared on a repulsive potential energy surface (V_1) by absorbing one-pump photon, and finally dissociates into A+B. In the LIF study,[11] another fs pulse is tuned to be resonant with the transition between the ground-state A and the excited-state A^*. By observing the fluorescence from A^* while varying the pump-probe delay time, the dissociation time is measured. On the other hand, to detect the transition-state evolution of $AB^{*‡}$, the probe wavelength needs to be changed to match the transition between $AB^{*‡}$ and $AB^{**‡}$, *i.e.*, between V_1 and V_2, as shown in Fig. 3.2b. The whole transition-state region can be probed if a continuum tuning is made.

Here, instead of observing the fluorescence by tuning the probe wavelength, we tune the probe laser to ionize A through a single or multiphoton process; typically A is ionized by REMPI. This way, and simultaneously, the complex $AB^{*‡}$ could also absorb

probe photons, through REMPI/MPI, to reach the ion state(s). In Fig. 3.2a, this ion state is sketched as a repulsive state (V_2^+) for an example. The resulting cation AB^{+*} finally fragments into A^++B. By varying the delay time between the probe and the pump, we can observe the dynamics of transition states and final products, at the same time, using one wavelength for the probe and only resolving the kinetic energy.

At the zero delay time, the observed translational energy of A^+ is determined by the total available energy, $E^+_{avl}(t_0)$, on the excited ionic repulsive PES. When the wave packet moves into the transition-state region and is probed at the delay time of $t^‡$, the final A^+ translational energy results from two parts: One contribution is from the available energy, $E_{avl}(t^‡)$, gained by the neutral complex AB^* during the evolution from t_0 to $t^‡$, and the other is from the excited ionic potential contribution, $E^+_{avl}(t^‡)$, as shown in Fig. 3.2a. If the ionic repulsive PES is deeper than the neutral one, the addition of both contributions is smaller than the initial ionic total available energy, $E^+_{avl}(t_0)$, because some part of the photon energy is converted into the electron kinetic energy at $t^‡$, and the observed translational energy of A^+ at $t^‡$ is smaller than that at t_0. When the reaction is complete, the A^+ translational energy is the exact reflection of the A translational energy, which is obtained from the energy release of dissociation of AB^*, *i.e.*, $E_{avl}(t_f)$. This total available energy, $E_{avl}(t_f)$, is the least amount of energy channeled to the translational energy of A^+. *By following the change of the total available energy, i.e., the time evolution of the A^+ translational energy, the dissociation dynamics from the initial transition state to the final products can be studied.*

For example, in our studies of the iodide (RI) molecular dissociation, the probe wavelength was set at ~304.5 nm to ionize the I (and I^*) atoms through 2+1 REMPI (3

photons). Most iodide molecules would be ionized by absorption of one-pump photon and two-probe photons (total 12.61 eV), and the absorption of one more probe photon will result in reaching the excited ionic electronic state(s). As mentioned above, the I^+ translational energy distribution at short times is dependent on these excited ionic states. In fact, for many systems the states reached by 3-probe photons may include some bound excited ionic states by ejecting an electron which carries away the excess energy. These ions in bound states proceed either to predissociate to form $R+I^+$(and R^++I), which is a long time-scale process ranging from picosecond to nanosecond, or radiatively decay into the ground-state RI^+. So, the initial $E^+_{avl}(t_0)$ could be equal to, less or larger than the final $E_{avl}(t_f)$ depending on the excited ionic PESs reached at the initial configuration. This can be easily determined from the I^+ speed distribution limits at t_0 and t_f.

In addition, the I^+ KETOF distribution at t_0 gives some information about the ion fragmentation dynamics. At t_f, the KETOF distribution reflects the initial alignment by the pump pulse polarization. If the KETOF distribution at t_0 is similar to that at t_f, the ion fragmentation should be very prompt and preserves the initial alignment, and the excited ionic PES is effectively repulsive. Conversely, if the ion fragmentation is a long time process, the observed KETOF distribution at t_0 should be isotropic and the rotational motion destroys the initial alignment, indicating that the excited ionic state is bound in nature.

In our studies, $E^+_{avl}(t_0)$ was found to be larger than $E_{avl}(t_f)$ for I_2 and HgI_2; for ICN and CH_3I both $E^+_{avl}(t_0)$ and $E_{avl}(t_f)$ are almost equal; and for IBz, $E^+_{avl}(t_0)$ is less than $E_{avl}(t_f)$. However, the I^+ KETOF distribution shapes resulting from transition states and final products are always different. As shown in Sec. 3.4, transition-state probing usually

results in a broader distribution around v_z=0 with less features due to the various ion fragmentations, but for products, the I^+ KETOF distribution has sharp structures relating to the initial alignment and the unique energy release of dissociation. As long as the PESs for the neutral and the ionic species are different, we are able to follow the change of the total available energy to obtain the dissociation dynamics, from the initial to the final configuration of the reaction.

This approach, which we utilized in earlier studies,[8] is analogous to the recently reported anion femtosecond photoelectron spectroscopy from Neumark's group.[12] There, a femtosecond pulse was used to excite a ground-state anion to a repulsive excited state and another fs pulse was employed to detach an electron from the anion. By mapping the wave packet onto accessible neutral surfaces, the evolution of the resulting different kinetic-energy electrons directly reflects the dissociation dynamics of the anion. Here, we follow the evolution of the kinetic-energy resolved cations by accessing ionic surfaces to study the dissociation dynamics of neutral molecules. Both methods use only one probe laser to detect the transition states and final products.

3.4. Results and Discussion

In this section, we discuss the different systems studied here. They range in the level of complexity from diatomics to polyatomics, from direct-mode to complex-mode, from one-center to two-center to four-center reactions.

The diatomic iodine was first examined due to its simplicity. Since all the available energy is released into translational energy of the two I atoms, it represents the case of no coupling to other degrees of freedom, such as vibrational and rotational

motions. This is not the case for polyatomic RI or RI_2. Furthermore, we used this system to calibrate the instrumental response for kinetic-energy resolution in measuring the KETOF distribution. In general, by knowing the excitation energy for a polyatomic molecule, say R-I, the energy disposal after breaking the R-I bond follows the conservation of the total energy:

$$E_{avl} = h\nu + E_I(RI) - D_0^0(R-I) = E_I(R) + E_T, \quad (3.1)$$

where $E_I(RI)$ is the initial internal energy of the parent molecule, $D_0^0(R-I)$ is the dissociation energy from the ground-state parent to the ground-state fragments, and $E_I(R)$ is the internal energy of the fragment R gained during the dissociation. The iodine atom can either be in the ground I or excited I^* spin-orbit state; equation (3.1) is for I release and for I^*, E_T will be reduced by 7605 cm^{-1}.

By measuring the center-of-mass (c.m.) translational energy release, E_T, the internal energy distribution of R can be obtained following equation (3.1). For the I_2 dissociation, $E_I(R)=0$. The c.m. translational energy can then be obtained from the translational energy of I atoms, E_T^I

$$E_T = E_T^I \frac{M}{M-m}, \quad (3.2)$$

where M is the mass of the parent molecule and m is that of the I atom.

3.4.1. One-bond Breakage: Direct-mode Reactions

3.4.1.1. I-I: Pure Translation Motion

The dissociation of I_2 in the A state was studied by using a 690 nm pulse. This system was examined in photofragment translational spectroscopy (PTS) experiments by Wilson and coworkers.[13] At our wavelength, the contribution from the B state is essentially eliminated (see below)[14] and the system dissociates into two iodine atoms in the ground state:

$$I_2 + h\nu \rightarrow [I\cdots I]^{*\ddagger} \rightarrow I + I \ . \qquad (3.3)$$

The time evolution of the I^+ KETOF distributions is shown in Fig. 3.3A ($\chi=90^0$). Notice that the shape changes with the delay time. At the early delay time (-200 fs), the KETOF signal is a broad, symmetric distribution around $v_z=0$ and extends to $v_z=\pm800$ m/s. The predicted v_z value by 3-photon probing of the A state is ±1240 m/s, so part of the photon energy is converted to the electron kinetic energy. The symmetric distribution around $v_z=0$ implies that the probed excited ionic state has a bound character around 12.84 eV (3.56 eV above the ground-state I_2^+) and the predissociation of iodine ions takes a long time. At later times (after 600 fs), the I^+ KETOF distribution remains unchanged and the v_z value changes to ±485 m/s. The time evolution of v_z values from the initial 800 m/s to final 485 m/s reflects the change of the total available energy, as predicted in Sec. 3.3 for the case of $E^+_{avl}(t_0) > E_{avl}(t_f)$.

The χ dependencies of the v_z distributions are given in Fig. 3.3B for a fixed delay time (6 ps). These KETOF distributions clearly show a perpendicular transition for the A-state excitation, as expected.[14] The speed distribution derived from the KETOF distribution at the magic angle is shown in Fig. 3.4, together with the c.m. translational energy distribution. The corresponding speed and translational energy distributions

derived from the pump laser spectrum (dashed line) are also presented for comparison. Since the total available energy is channeled only into the translational energy of two iodine atoms, the instrument resolution at the speed of 440 m/s is obtained to be within ±15 m/s. The higher the speed, the better the expected resolution.

To obtain the temporal behavior, we gated the high-velocity ($340 \le v_z \le 490$ m/s) and low-velocity ($0 \le v_z \le 120$ m/s) portions of the I^+ KETOF distribution at $\chi=90^0$ while varying the delay time. The two transients are shown at the bottom of Fig. 3.5. Each transient is composed of two components with different weights, but has the same dynamics: One is from the iodine ion fragmentation and the other results from the neutral iodine dissociation. By measuring the time zero and the response function *in situ*, the transient was best fitted by a (coherent) delayed, 240 fs, rapid rise and a decay component with a lifetime of 65 fs, as shown in the top of Fig. 3.5. The observed 240 fs shift is the bond-breaking time for separating two I atoms and describes the coherent motion of the wave packet prepared above the dissociation limit on the A-state potential surface. The decay transient actually reflects the evolution of the parent $I_2^{*\ddagger}$ in the transition state. This picture is also consistent with the observed I^+ KETOF evolution. The measured decay time is shorter than the bond-breaking time due to the fact that the wave packet escapes out of the Franck-Condon region before the I atom is totally liberated.

3.4.1.2. I-CN: Translation and Rotation Motions

The dissociation of ICN was the first gas-phase reaction studied by the fs clocking.[11, 15,16] At 306-nm excitation, the bond-breaking time was obtained to be 205 fs by detection of the CN product through LIF. The transition-state lifetime was estimated

to be ~50 fs. Here, we resolve the I^* and I channels with the dissociation times, energy partition and angular distributions.

It is now well established that following electronic excitation via the A continuum ($n\rightarrow\sigma^*$ transition), ICN dissociates through two exit channels, leading to spin-orbit excited and ground-state iodine atoms, I^* and I, respectively:

$$ICN + h\nu \rightarrow [I\cdots CN]^{*\ddagger} \rightarrow I^*/I + CN \quad . \tag{3.4}$$

Time-integrated spectral studies,[17-24] using a variety of methods such as PTS,[17,23] LIF,[18,19] Doppler spectroscopy[20,22] and REMPI-TOF,[24] have provided many detailed features of the dynamics for both channels.

Briefly, the I^*/I branching ratio is dependent on the excitation wavelength and the I^* yield peaks at ~260 nm; it falls off at shorter wavelengths as well as at longer ones. The vibrational excitation of the CN fragment is low (cold), except in the low energy region (350-290 nm) where several percent of CNs are vibrationally excited. However, the rotational excitation of CN is found to be very rich (hot) in the I channel (up to N~60), whereas it is rotationally cooler in the I^* channel, for the medium energy range (248-290 nm). In the low energy region, where the I^* channel is not energetically accessible, the product rotation population shows a single Boltzmann distribution. The average anisotropy parameter β of the I^* channel is larger than that of the I channel. The transition moment is observed to be a mixture of parallel and perpendicular components, especially at shorter and longer wavelengths.

Goldfield *et al.*[25] developed a two-surface empirical model for the ICN dissociation in the A continuum. In their model, the initial excitation is a purely parallel

transition to the potential surface ($^3\Pi_{0+}$), which correlates to the I^*+CN channel, followed by a transition through nonadiabatic interaction to the surface ($^1\Pi_1$), which correlates with the I+CN channel. The $^3\Pi_{0+}$ surface is repulsive in R(I-CN) and has a minimum at $\theta=0^0$ in the θ coordinate (bending angle). This results in the collinear configuration in the dissociation process leading to low rotational excitation in CN fragments. The second surface is also repulsive in R, but has a minimum in θ at $\theta=27^0$. The large torque at small θ favors a bent configuration during the dissociation and leads to high rotational energy for the final fragment. The results from classic trajectory calculations and quantum mechanical studies based on this model agree well with some experiments, but large deviations still exist.[25-31]

Recently, Morokuma and coworkers[32] developed *ab initio* 3D PESs of $^3\Pi_1$, $^3\Pi_{0+}$, $^1\Pi_1$ excited states and found that all PESs involved in dissociation are *bent* near the Frank-Condon region. Classical trajectory and time-dependent quantum mechanical calculations performed on these PESs have produced results which are in good agreement with various experimental findings.[32-36] The absorption is a mixture of parallel and perpendicular transition: $^3\Pi_1$ and $^1\Pi_1$ have perpendicular transitions and $^3\Pi_{0+}$ belongs to a parallel transition. The rotational excitation of the CN fragment is related to the shape of PESs with respect to the bending angle. The higher rotational component in the I channel is attributed to the larger energy gradient of $^1\Pi_1$ with respect to the bending angle. The rotational excitation in the I channel at the long wavelength (290-350 nm) only emerges from the $^3\Pi_1$ surface. The product CN vibrational excitation on $^3\Pi_{0+}$ and $^1\Pi_1$ becomes suppressed while that on $^3\Pi_1$ becomes slightly significant (from the shape

of PES with respect to the C-N distance). On the surface $^3\Pi_{0+}$, a potential well (3855 cm^{-1}) is found along the reaction I-CN coordinate at 2.59 Å.

We performed the fs-clocking and fs-KETOF experiments to obtain the dissociation time, energy partitioning and the anisotropy parameter. The fs-resolved I^+ KETOF distributions at $\chi=0^0$ are shown in Fig. 3.6A and the χ dependencies for a fixed delay time (2 ps) in Fig. 3.6B. All distributions extend to v_z~±600 m/s, but the shape changes dramatically. At the earlier delay time (-290 fs), a symmetric distribution around $v_z=0$ was observed. As in the case of I_2, this reflects that the excited ionic PESs reached by 3-photon probing have a bound character around 15.06 eV (4.15 eV above the ground-state ICN^+) and that the predissociation takes longer time, compared with the rotational period of the ion parent. Some photon energy is converted into the electron kinetic energy because the expected v_z value is ±880 m/s by absorption of 3-probe photons. At later delay times, the distribution shows the clear double splitting for both I^* and I channels, which means that the excitation at 277 nm is a *purely* parallel transition. This is also clear in the distribution at $\chi=90^0$ in Fig. 3.6B. The deduced β values further supports this finding, as discussed below.

The speed distribution for the iodine product derived from the magic angle KETOF distribution and the corresponding c.m. translational energy distribution with assignments of rotational excitation for the CN fragment are shown in Fig. 3.7. The speeds from the I^* and I channels do reach the limits determined by the total available energy for each channel (285 m/s for I^* and 570 m/s for I). The I^* quantum yield is about 60%, consistent with the value reported by Leone.[21] The translational energy release, $\langle E_T \rangle / E_{avl}$, is 70% for the I^* channel and 63% for the I channel, which corresponds to

30% and 37% of the available energy (764 cm^{-1} for I^* and 3756 cm^{-1} for I) channeling into rotational excitation in the I^* and I channels, respectively. The rotational distributions peak at N=20-25 for the I^* channel and N=45-55 for the I channel. These assignments are in agreement with the results from the time-integrated experiments.[20,22]

By simulating the KETOF distribution at $\chi=0^0$ using the derived speed distribution, we deduced the β distribution, which is also shown in Fig. 3.7. All β values are positive, thus indicating that *only* the parallel transition state, $^3\Pi_{0+}$, was excited at 277-nm. (Recent work[22b] has concluded a pure parallel transition for 308-nm excitation; contrary to the expectation of a mix of parallel and perpendicular transitions at long wavelengths.) Therefore, the I product results from the nonadiabatic interaction from $^3\Pi_{0+}$ to $^1\Pi_1$. Most products have very high β values ($\geq$1.6) even with high rotational excitation. During the rapid dissociation, since the rotation of ICN plays a minimal role, the rotational excitation should result from the bent configuration of the excited surface, as suggested by the *ab initio* calculations.[32,34] For both I^* and I channels, the CN fragments in the distribution at higher rotational excitation have decreased β values, which indicates that some large-amplitude bending motion is involved during the dissociation.

The χ dependencies of the transition-state I^+ KETOF distributions and the deduced speed function are given in Fig. 3.8. The speed distribution is very broad and the deduced β values are small, also shown in Fig. 3.8. The average β value is about 0.5, much smaller than that ($\geq$1.6) for the final product. As predicted in Sec. 3.3, this small value reflects the dynamics of the ion fragmentation, and implies that the excited ionic

states reached by 3-photon probing have a bound character and the predissociation takes relatively long time in order to reduce the initial alignment.

The dissociation dynamics was selectively resolved by performing the gating experiments. The parent mass transient is shown in Fig. 3.9a. Using the known time zero and response function, the transient was deconvoluted by a decay signal with a 70 fs lifetime, which reflects the transition-state dynamics of $ICN^{*\ddagger}$. This lifetime can only be obtained by sampling all transition-state configurations through this probing scheme. By gating the high velocities of I^+ KETOF distribution, $150 \leq v_z \leq 300$ m/s and $380 \leq v_z \leq 580$ m/s, respectively, the dissociation times for forming the I^* and I products were obtained, as shown in Fig. 3.9b and 3.9c. Both transients include a contribution from fragmentation around t=0. Therefore, these two transients were fitted by a (coherent) delayed rapid rise, which are shown in Fig. 3.9d and 3.9e for I^* and I, and a decay component (70 fs lifetime) from the transition state. The I^* atoms were born after 220 fs from the time zero and the I atoms take 185 fs to be liberated. Although the rotational dependence of the dissociation times was found, both from the experiments[11] and theoretical calculations,[37] the observed 220 fs here for I^* and 185 fs for I represent the average dissociation times for rotationally populated CN fragments. The longer dissociation time for I^* is consistent with the smaller terminal speed.

We also gated the total I^+ KETOF distribution, *i.e.,* collected all signals. The transients are shown in Fig. 3.10A and 3.10B with the corresponding pump polarization parallel ($\chi=90^0$) and perpendicular ($\chi=0^0$) to the probe one, respectively. By subtracting the contribution of the final iodine products (the contribution should be the same for these two cases as observed in the experiment, and is independent of the pump or probe

polarization), the residual transients were obtained (Fig. 3.10C). These are purely from the probing of the transition state $ICN^{*\ddagger}$ for different polarization combinations. With the pump polarization being parallel to the probe one, the transition-state transient is three times larger than that when the pump polarization is perpendicular. This observation is completely consistent with the theoretical prediction.[38]

3.4.1.3. CH_3-I: Translation and Vibration Motions

The dissociation dynamics from the A-band absorption ($n\rightarrow\sigma^*$ transition) has been extensively studied[39-49] and new insights have been gained. The dissociation steps are:

$$CH_3I + h\nu \rightarrow [CH_3\cdots I]^{*\ddagger} \rightarrow CH_3 + I^*/I \quad . \tag{3.5}$$

Various experimental techniques such as PTS,[40,42] IR emission[41] and absorption,[46] REMPI-TOF,[43,48] Raman,[39] photofragment imaging[44] and ZEKE,[47] have been used to resolve the product-state distributions (rotational and vibrational) and branching ratio of I^*/I, and address the nonadiabatic interaction during the dissociation. For the wavelength we used (277 nm), only one electronic state, $^3Q_{0+}$, is mainly excited through a parallel transition, as observed in ICN, which dissociates to CH_3+I^*. The observed I atoms suggest significant nonadiabatic interactions between $^3Q_{0+}$ and $^1Q_1$ states during the course of dissociation, because the latter, $^1Q_1$ state, correlates to CH_3+I asymptote by a perpendicular excitation.

Although some small excitation in the C-H symmetric stretch (ν_1) of the CH_3 fragment has been reported, only the umbrella mode (ν_2) of CH_3 was found to be strongly

excited in either I^* or I dissociation channel. This is consistent with the structural change, from being with nearly tetrahedral angles in CH_3I to being planar in CH_3. The rotational distribution for motion about the axis perpendicular to the C_3 axis of the CH_3 fragment is relatively hot in the I channel but very cold in the I^* channel. Kinsey and coworkers[39] have concluded from their resonance Raman spectroscopy experiments that during the dissociation the C-I bond extension initially takes place to some extent before the subsequent umbrella motion starts. The dissociation time estimated by photofragment anisotropy measurements,[50] picosecond real-time studies[51] and Raman scattering[39] of dissociating CH_3I is less than 500 fs.

Theoretically, Shapiro and Bersohn[52] suggested a model which considers a linear, pseudotriatomic molecule; the umbrella motion of the CH_3 moiety was approximated by a stretch motion between C and H_3. Both quantal and classical dynamical studies based on this model have produced promising results.[52-54] Very recently, an *ab initio* 6D (all coordinates except the three C-H stretches)[55] and full 9D PESs[56] have been reported by Morokuma and coworkers. These potentials were used to perform classical trajectories,[55,56] 3D wave packet dynamics,[57] including rigid bending of H_3-C-I, and 5D multiconfiguration time-dependent Hartree method calculations.[58] The results are in good agreement with various experimental observations.

The rotational excitation in the I channel is closely related to the shape of the PES with respect to the bending angle outside the conical intersection of $^3Q_{0+}$ and $^1Q_1$, *i.e.*, there might exist a small well for the $^1Q_1$ surface near the linear geometry. The vibrational excitation is determined by the shape of the PESs with respect to the umbrella angle and its coupling with the C-I coordinate. The $^3Q_{0+}$ surface has a shallow well (1710

cm^{-1}) along the reaction C-I coordinate at 3.3 Å. The observed hotter vibrational excitation in the I channel is due to the sudden change of the reaction coordinate from $^3Q_{0+}$ to $^1Q_1$ at the conical interaction. The quantum wave-packet calculations gave a 75 fs dissociation time for a C-I separation of ~5 Å.[57] Here, we are able to clock the fs dissociation dynamics.

The fs-resolved I^+ KETOF distributions are shown in Fig. 3.11A ($\chi=0^0$) and the angular (polarization) dependence (χ) at the 6 ps delay time is in Fig. 3.11B. All fs-KETOF distributions extend to v_z~±600 m/s and have double peaks. Unlike I_2 and ICN, the excited ionic potential surface reached by 3-photon probing is similar to the neutral one and is repulsive around 15 eV (5.46 eV above the ground state CH_3I^+), *i.e.,* the ion fragmentation is very prompt, although the distributions from the transition state have broader peaks and lie closer to $v_z=0$. The predicted v_z value by absorption of 3-probe photons at t=0 is ±791 m/s, larger than the observed value. Therefore, some portion of photon energy is converted to the electron kinetic energy. The fs-KETOF distributions show no change after 600 fs, which means the termination of the bond breaking.

The product speed distribution is derived from the measured I^+ KETOF distribution at the magic angle and taken at times after the bond breaking. The result is shown in Fig. 3.12, also with the c.m. translational energy distribution. The first peak is measured to be at ~410 m/s and this speed corresponds to the spin-orbit excited state I^* dissociation channel. The second peak located at ~530 m/s corresponds to the ground-state I dissociation channel. If all available energy is channeled into translational motion, the expected speeds do reach the limit values indicated by the arrows in Fig. 3.12 (440 m/s for I^* and 587 m/s for I). The average translational energy release, $\langle E_T \rangle / E_{avl}$, is

found to be 87% for I^* and 81.7% for I. The I^* quantum yield is measured to be ~65%, which agrees with the values reported by others.[40,41] By knowing the translational energy release, the internal energy distribution of CH_3 can be obtained. The corresponding umbrella excitation is marked in Fig. 3.12: For the I^* channel, the vibrational peak distributions are v=1,2 and for the I channel, the peaks shift to v=4-5. These observations are consistent with those reported by Lee's group,[40] but 1-2 quanta higher (for the I channel) than the results reported in ref. 43.

From the speed distribution and the I^+ KETOF distribution, obtained at the parallel polarization, we deduced the anisotropy parameter, β~1.85, at 277 nm excitation, which is in good agreement with the values reported by Bersohn (1.81),[50] Houston (1.8),[43] Crim (1.9)[43] and others.[42] This also confirms that the observed I atoms are not from the direct excitation of the $^1Q_1$ state (perpendicular transition and β~-1), instead from the initial $^3Q_{0+}$ state (parallel transition) following a transition through nonadiabatic interactions to the $^1Q_1$ state. From β, Bersohn[65] deduced a lifetime of 70 fs. As shown below, fs clocking gives a 125 fs dissociation time.

The temporal transient is shown in Fig. 3.13B by gating the high v_z values ($500 \leq v_z \leq 380$ m/s). This transient includes a small component from the excited CH_3I^+ fragmentation ($I^+ + CH_3$), as in the cases of I_2 and ICN. The total parent mass signal is also gated and the resulting transient is shown in Fig. 3.13A, which reflects the transition-state dynamics. By measuring the time zero and the response function *in situ*, a 40 fs lifetime was deduced from Fig. 3.13A. The result of Fig. 3.13B was then uniquely fitted to a rapid-rise component with a 125 fs coherent shift, as shown in Fig. 3.13C, and a small portion of the 40 fs lifetime transition-state signal. No attempt was made to separate the I^*

and I channels. The 125 fs dissociation time is longer than the values deduced from the β measurement[50] and the quantum wave-packet calculations.[57] Measurements of the anisotropy (β) are sensitive only to the initial force (short distances) while real-time measurements probe the nuclear separation when fragments become free from the force field of each other (dissociation time).

3.4.2. One-bond Breakage: Complex-mode Reactions

The three systems (I_2, ICN and CH_3I) presented in the above sections all involve direct-mode reactions in that the initial preparation is to a repulsive surface (or weakly bound surface). In other words, the energy is directly deposited into the bond which breaks and the system has no time to involve the multimodes of the complex in coordinates other than the reaction coordinate (see Fig. 3.14). In this section, we study another case, complex-mode reactions, using iodobenzene as an example.

$$C_6H_5I + h\nu \rightarrow [C_6H_5\cdots I]^{*\ddagger} \rightarrow C_6H_5 + I\,(I^*) \qquad (3.6a)$$

$$\rightarrow [C_6H_5\text{-}I]^{*\ddagger} \rightarrow C_6H_5 + I \quad . \qquad (3.6b)$$

At the wavelength we used (277 nm), two states[59] are excited simultaneously: One is a repulsive (n, σ^*) excitation in the C-I bond and the other is a bound (π, π^*) benzene ring excitation. Through time-velocity correlation during the dissociation, we are able to separate the two dynamical channels: A direct-mode dissociation (3.6a) due to the C-I repulsion and a complex-mode, electronic predissociation (3.6b) arising from IVR in the benzene ring which drives energy to the C-I coordinate.

Previous studies of the dissociation dynamics of IBz have been obtained from the PTS and resonance Raman scattering experiments. Bersohn's group[50,60] has measured β and found it to be lower than those observed for alkyl iodides, suggesting the presence of a predissociation channel. El-Sayed's group[61] introduced a state-selective method to determine the spatial and velocity distributions of the nascent ground-state iodine atoms using nanosecond lasers. Two distinct iodine velocity distributions were observed. One is a high velocity, narrow distribution that exhibits a high anisotropy. The other is a low velocity, broader distribution accompanied by a lower averaged anisotropy. Kinsey's group,[59] for excitation to the B-continuum, related the Raman profile and its change to the initial dynamics and the activity of modes.

Measurements of the anisotropy give a limit for τ_{reac}, being less or comparable to τ_{rot}, the average rotational time of the parent molecule. If $\tau_{reac} \geq \tau_{rot}$, the intermediate or long time dynamics is difficult to obtain.[59] Moreover, as pointed out by El-Sayed *et.al.*,[61] if IVR precedes C-I bond breakage, then inference can only be made provided that β can be related to the IVR process. Bersohn's study[60] gave an upper limit of τ_{reac} based on τ_{rot} of IBz as a clock. El-Sayed's group[61] assigned the high velocity distribution to the rapid dissociation on the (n, σ^*) surfaces and the low velocity component to the predissociation of the $^3(\pi, \pi^*)$ state. Using the molecular rotation as a clock, they were able to deduce a time scale for the IBz dissociation: the (n, σ^*) states dissociate much faster than the molecular rotation, whereas the predissociation in the $^3(\pi, \pi^*)$ states takes place on a time scale comparable to the molecular rotation. Here, we are able to directly clock these two dissociation channels and focus on the studies of resolving the translational energy on the

fs time scale to separate the two reaction pathways and to characterize the dissociation dynamics.

Fig. 3.15 shows the I^+ KETOF distributions ($\chi=0^0$) taken at different delay times. In these experiments, a small discrimination aperture (5 mm) was used in front of the MCP detector to eliminate the ions with $v_{xy}\geq 110$ m/s and enhance the kinetic-energy resolution. At earlier delay times ($\leq$30 fs), the KETOF distribution extends to $v_z=\pm 800$ m/s and is symmetric around $v_z=0$. As observed in I_2 and ICN, the excited ionic states probing by 3-photon absorption have a bound character around 14.43 eV (5.7 eV above the ground-state IBz^+). The expected value is $v_z=\pm 1387$ m/s from the 3-photon probing, therefore, some portion of photon energy is converted into the electron kinetic energy. At later times (~2 ps), the KETOF distribution stays unchanged, showing a double splitting and reaching $v_z=\pm 960$ m/s, the limit determined by the total available energy for the I channel.

Clearly, the transition is a parallel type and the I channel is dominant. If the PESs are similar to the alkyl-iodide ones, the I channel results from the nonadiabatic interaction and this coupling is very strong. The high-velocity iodine atoms peak at 820 m/s, which corresponds to 73% of the available energy channeling into the translational energy and 27% into internal excitation of the phenyl radical. The KETOF profiles at long delay times are very similar to those observed by El-Sayed's group[61] using nanosecond lasers. With fs lasers, we can see the KETOF evolution during the dissociation. The lower-velocity ($\leq$550 m/s) iodine atoms appear later than the high-velocity (~800 m/s) ones. By monitoring the intensity of a certain portion of the I^+ KETOF distribution while scanning

the delay time, the dynamics of iodine atom formation with different kinetic energies can be separately observed in this fs-KETOF experiments.

When only the high-velocity ($700 \leq v_z \leq 960$ m/s) iodine signal is collected, the transient exhibits a very rapid rise with a coherent 400 fs shift (not growing) from the zero-of-time, as shown in Fig. 3.16A. The contribution from the ion fragmentation at the earlier delay time was found to be negligible. The observation of the coherent delay is a manifestation of the wave packet motion on the repulsive PES, as observed in I_2, ICN and CH_3I, and establishes the assignment of the high-velocity component to the direct dissociation of the C-I bond through the (n, σ^*) excitation. The delay time therefore reflects the dynamics of the phenyl-iodine bond breakage on the (n, σ^*) potential surface.

By monitoring the medium ($290 \leq v_z \leq 560$ m/s) and low ($0 \leq v_z \leq 270$ m/s) velocities of iodine atoms in the I^+ KETOF distribution, the transients, after subtracting the contributions from the ion fragmentation, are shown in Fig. 3.16B and 3.16C. The build up of these transients are slow (not coherent), reaching their plateau values at about 1.3 and 2.2 ps, respectively. These features can also be seen in Fig. 3.15 under careful examination. The medium-velocity iodine atoms appear earlier than the low-velocity ones. The transient (not shown) obtained by monitoring both the low- and medium-velocity components together exhibits a near-single-exponential build up with a rise time of 550 fs and a ~400 fs delay time. These observations indicate that the low-velocity ($0 \leq v_z \leq 560$ m/s) iodine atoms come from an indirect dissociation channel. The 550 fs rise time reflects the overall rate of the reaction starting from the phenyl-type modes and ending in final C-I fragmentation.

At our pump wavelength, excitation of the phenyl system is to the $^3(\pi, \pi^*)$ state which has a significant oscillator strength because of the presence of the heavy iodine atoms. The optical excitation to the $^3(\pi, \pi^*)$ state at t_0 is not expected to deposit appreciable vibrational energy into the reaction coordinate, as the C-I bond is, in zeroth-order, nearly unaltered upon excitation. Fig. 3.17 schematically illustrates this dynamical process. With this high vibronic energy in the $^3(\pi, \pi^*)$ phenyl ring modes, the wave packet spreads rapidly among vibrational modes and the C-I mode can quickly become activated at $t_1^\ddagger$ through IVR. This is then followed by a coupling to the repulsive (n, σ^*) surfaces, leading to the cleavage of the C-I bond. For a given total energy, the coupling strength between $V(\pi, \pi^*)$ and $V(n, \sigma^*)$ determines the probability of this nonadiabatic transition. Theoretically, this can be treated as a Landau-Zener avoided crossing. If the initial IVR is complete, *i.e.,* the total energy distributes among all vibrational modes we can, in principle, calculate the dissociation rate by RRKM theory, combined with the nonadiabatic transition probability, and the observed transient describes two sequential processes determined by IVR and RRKM rates.

However, in our case, the observed 550 fs rise time is so fast that the initial IVR is expected to be incomplete, *i.e.,* a restricted process (the system has 30 vibrational modes and RRKM rates would be relatively smaller). If the dissociation rate is comparable to the IVR rate, the activated C-I mode can also redistribute its energy to the surrounding bath modes of the phenyl system ($t_2^\ddagger$ in Fig. 3.17). After a certain time, the energy flows back into the C-I coordinate ($t_3^\ddagger$) with less available energy for dissociation. Our experimental results are consistent with this dynamical picture. By detecting the final product of I atoms, we observed a time-velocity correlation for this indirect dissociation:

the low-kinetic-energy iodine atoms build up slower than the medium-kinetic energy ones, as shown in Fig. 3.16B and 3.16C. The 550 fs rise time reflects the overall rate from the restricted IVR and bond-breaking process. The ~400 fs delay time is the minimum time for the C-I bond breakage even though enough energy has already been accumulated in the reaction coordinate of C-I, as observed in the direct dissociation of C-I bond by $\sigma^* \leftarrow$n excitation.

Besides the vibrational coherent motion depicted above, we have also considered the rotational motion of the parent molecules in relation to τ_{reac}, as the initial anisotropy created by the pump laser pulse can, in principle, be rapidly destroyed by rotational dephasing. Specifically, we performed experiments at two rotational temperatures, 10 and 300 K, and found that the transients do not show significant differences. Since the rotational coherence times (τ_c) differ by a factor of 5.5 for these two extreme temperatures,[38] these experimental observations suggest that rotational dephasing does not play a significant role. This is consistent with the fact that the dynamics involved here are faster than τ_c (τ_c(300K)=1.1 ps and τ_c(10K)=6.0 ps). However, it should be noted that, if $\tau_{reac} \geq \tau_c$, then the rotational dephasing has to be considered, especially for the initial dynamics.[38]

3.4.3. Two-bonds Breakage: Sequential Processes

Here, we studied a reaction involving multiple-bond breakage by depositing enough energy into a system with two C-I bonds. The questions then are the following: What are the time scales and what is the mechanism, concerted or sequential? A typical

system is that of a general class of halogen-atom elimination in many organic reactions.[62] The reaction we studied involves the following steps:

$$IF_2C\text{-}CF_2I + h\nu \rightarrow [I\cdots CF_2\text{-}CF_2I]^{*\ddagger} \rightarrow I^*/I + C_2F_4I^{\dagger} \quad (3.7a)$$

$$C_2F_4I^{\dagger} \rightarrow F_2C{=}CF_2 + I \ . \quad (3.7b)$$

Previous studies of this reaction with ps resolution[51,63] revealed that this two-center elimination is a two-step, nonconcerted process, involving the intermediate $C_2F_4I^{\dagger}$.

The time scales for the two bond fissions are two orders of magnitude different: the primary bond breakage, reaction (3.7a), takes several-hundred femtoseconds (<500 fs), but the secondary elimination takes 30-70 ps depending on the excitation energy. The former is due to the direct repulsive (n, σ^*) excitation in the C-I bond, while the latter elimination, reaction (3.7b), is directly governed by the energy redistribution and the rate of bond breakage of $C_2F_4I^{\dagger}$. The PTS experiments[64] at 308 nm from Lee's group gave a ~7.1±2.5 kcal/mol barrier for the dissociation of the intermediate $C_2F_4I^{\dagger}$. Here, with fs resolution and from measurements of the time evolution of products, the product-velocity distributions and the recoil anisotropy, the reaction dynamics and mechanism are microscopically elucidated.

The I^+ KETOF distributions for the parallel ($\chi=0^0$) and magic angle ($\chi=54.7^0$) excitation are displayed in Fig. 3.18 for 1 ps and 600 ps delay times. For the magic angle KETOF shape at 1 ps, the velocity distribution is essentially flat, as predicted by theory for direct fs dissociation, similar to those observed in I_2 and CH_3I. Indeed, this distribution reflects the primary C-I bond breakage. The earlier I^+ KETOF evolution of the first bond breakage around t=0 is the same as that observed in I_2, ICN and CH_3I, but

here we focus on the difference between the first and second bond fission. At longer times, the distribution displays a buildup of intensity around v_z ~0, shown at 600 ps, reflecting the process of the secondary C-I elimination. The intensity difference for the two reaction times is also shown in Fig. 3.18. A similar conclusion is reached for the $\chi=0^0$ results. To obtain the complete temporal behavior, we gated the slow velocity portion of the distribution ($-250 \le v_z \le 250$ m/s) at the magic angle while varying the delay time. The biexponential rise of the fs transient, shown in Fig. 3.19, gives the two distinct reaction times for the two steps of C-I elimination: τ_1~200 fs and τ_2=25 ps, consistent with the behavior of the KETOF distributions.

From the magic angle I^+ KETOF distribution, we obtained the laboratory recoil speed distribution of iodine atoms at 1 ps reaction time (Fig. 3.20a). Two distributions, which peak at 850 m/s and 1200 m/s, were obtained for the primary elimination, corresponding to the formation of the product in both spin-orbit states, I^* and I. This is a characteristic of alkyl halide bond breakage with fs dissociation times. The large translational energy release in such a short time excludes the possibility of breaking two C-I bonds concertedly. The excitation energy is 103 kcal/mol and if two bonds (ΔH~59 kcal/mol for the I channel)[64] are involved, no such translational energy can be produced. This conclusion is entirely consistent with the biexponential transient behavior in Fig. 3.19; the first "rise" (~200 fs) is due to the primary elimination. From measurements of the polarization dependence of the I^+ KETOF distribution (parallel vs. magic angle), we also deduced the anisotropy parameter: $2.0 \le \beta \le 1.9$. The value is close to an ideal parallel transition (β=2.0), *i.e.,* the transition moment is parallel to the C-I bond direction, and

again is consistent with the observed prompt elimination process being caused by the repulsive force.

In the primary C-I breakage, we observe that the I^* and I branching is 0.7 and 0.3, respectively. This branching is similar to that observed in the CH_3I.[40-42] The speed distributions do reach the limiting values determined by the total available energy for both I^* and I channels (1100 m/s for I^* and 1460 m/s for I). The average translational energy release, $<E_T>/E_{avl}$, for each channel is found to be 59% for I^* and 67% for I. Both translational energy distributions are broad and the full-width at half-maximum is 8.5 kcal/mol for I^* and 19.5 kcal/mol for I. Theoretically, we predict that 86% of the available energy should appear as translation for a rigid radical (no vibrational excitation) following an impulsive bond breakage; for a "soft" radical, we obtained 13%.[65] Our experimental values are more toward the rigid radical limit.

The secondary elimination dynamics have different reaction time, velocity characteristic, but surprisingly similar recoil anisotropy. After the fs primary elimination, the observed 25 ps rise of the I atom (Fig. 3.19) represents the time scale for energy redistribution to deposit enough energy in the reaction coordinate of the intermediate $[CF_2I\text{-}CF_2]^\dagger$ to break the second C-I bond. This is consistent with the previous ps studies and is further supported by the observation of the broad speed distribution of I atoms from the secondary elimination (Fig. 3.20a).

The velocity distribution for I atoms from the secondary bond breakage ($\chi=0^0$ of Fig. 3.18) shows a very high angular anisotropy and the deduced anisotropy parameter (β) is ~1.9, nearly the same as that for the primary bond breakage. Since the rotational time of the C_2F_4I intermediate is estimated to be between 2-8 ps, shorter than the

observed 25 ps reaction time, the secondary elimination produces an isotropic, small speed distribution of I atoms. The addition of this small velocity to the large velocity of the c.m. of the C_2F_4I radical does not destroy the initial (t=0) alignment, *i.e.*, the anisotropy of the secondary process "remembers" the primary elimination anisotropy and is determined mainly by the larger c.m. velocity of C_2F_4I (see Fig. 3.20b). Thus, even though the measured anisotropy is very high it does not reflect the long-lived state of the intermediate and it would have erroneously predicted a short-lived intermediate.

The c.m. translational energy release for the first bond breakage and the resulting internal energy distribution of the C_2F_4I intermediate obtained from conservation of energy are shown in Fig. 3.20c. The $P(E_I)$ distributions are broad with peaks at 12 kcal/mol and 17 kcal/mol for the primary, I^* and I channels. Comparing the I atom yield (Fig. 3.18, χ=54.7^0) from the secondary elimination with the total primary iodine product, only ~35% of the intermediate dissociates into C_2F_4 and I. From $P(E_I)$ vs. E_I in Fig. 3.20c, we therefore deduce an activation energy of ~15 kcal/mol; the area under the distribution function of E greater than 15 kcal/mol is about 35% of the total one. This indicates that a small portion of $C_2F_4I^\dagger$ dissociates when it is created from the I^* channel, while a large fraction decomposes if the I channel is involved; the secondary elimination only produces ground-state I atoms because of the energetics.

The deduced dissociation barrier (15 kcal/mol) is greater than the value, 7.1±2.5 kcal/mol, reported from the PTS experiments.[64] The difference may be due to the difficulty in separating the I^* and I channels, and the very broad I distribution at 308 nm excitation.[64] Moreover, the stimulated dissociation of the intermediate, which was observed in the PTS experiments, is negligible in our case because we did not observe the

475 or 670 m/s peaks in the speed distribution at 1 ps; these two values are, respectively, the laboratory peak speeds of $C_2F_4I^{\dagger}$ from the I^* and I channels after the first bond breakage. The weakness of the second C-I bond is due to a concerted electronic path that breaks the C-I bond while forming a new C=C π bond, in contrast with the primary elimination which only involves C-I cleavage. This weak C-I bond energy in the C_2F_4I radical can be estimated from D_0(C-I)-D_0(C=C)=~8 kcal/mol.[66] With this ΔH value and the fact that I addition to C=C is endothermic, our value of the *effective* barrier (potential+centrifugal) is consistent with being larger than ~8 kcal/mol.

Considering the decomposition threshold of ~15 kcal/mol (see Fig. 3.20c), the dissociating C_2F_4I radicals resulting from the primary I^* and I channels have two peak speeds at 435 m/s and 670 m/s (arrows in Fig. 3.20a, bottom), respectively. The recoil speed distribution of the secondary I atoms shows two peaks at ~435 m/s and ~800 m/s. These peak values of the C_2F_4I radical and the secondary I atom, resulting from the primary I^* channel, are the same. This equality supports the previous description of the secondary elimination process. However, the values for the I channel differ by 130 m/s (800 m/s vs. 670 m/s). Besides the expected ~670 m/s peak distribution for the secondary I atoms, it appears that a higher speed component (~800 m/s) is part of the distribution which reflects a faster dissociation of the intermediate with higher internal energies, possibly in a nonthermal distribution.

After detachment of the I atom from $C_2F_4I_2$ in ~200 fs, the C_2F_4I is born with high activation energy. Fig. 3.21 illustrates the dynamical process along the reaction coordinate for this system. At t_0, a wave packet is initially excited on a repulsive surface V(n, σ^*). In about 200 fs, one of C-I bonds is impulsively broken and the $C_2F_4I^{\dagger}$ is created

in special distribution on a time scale shorter than that of vibrational motion(s), prior to IVR and reactivity. The fs-activated, vibrationally-hot $C_2F_4I^{\dagger}$ radical has a broad internal energy distribution ($t^{\dagger}$). Two points should be emphasized here: (1) after the first impulsive C-I bond breaking, the internal energy is initially localized in the CF_2 side, not distributing among all vibrational (rotational) modes in CF_2-CF_2I; (2) the IVR process may not follow the statistical behavior due to the initial special configuration of $C_2F_4I^{\dagger}$. This dynamical entry of the transition state is very critical to any nonstatistical behavior, as also observed in recent experiments involving dissociation of cyclic ketones.[67]

At the saddle point ($t^{\ddagger}$), the C-I bond stretches and the C-C bond shrinks. The dissociation barrier is determined by the concerted breakage of the σ(C-I) bond and the making of a π(C=C) bond. Given the ~15 kcal/mol dissociation barrier and assuming the rotational excitation is inactive during dissociation, RRKM calculations of the radical dissociation rate do give the picosecond time scale, but deviations still exist. So, the initial IVR in $CF_2CF_2I^{\dagger}$ is not akin to complete thermal behavior on this ultrafast time scale and this is consistent with the observation of the 800 m/s peak speed from the secondary iodine atoms (Fig. 3.20a).

By employing fs pulse to activate a reactive species through the breaking of one chemical bond or detachment of one atom in such a short time, the resulting internal energy may localize in some vibrational states or bonds. The species is then made selectively at a special configuration. This suggests some opportunities for investigating non-statistical dynamics, including selective reactions even in the presence of IVR.[68]

3.4.4. Two-bonds Breakage: Saddle-point Transition States

In this section, we extend our studies to the case of ABA (IHgI) reactions which define a saddle-point transition state. The dynamics involve two nuclear coordinates, symmetric and asymmetric stretch, besides the bend motion. The reaction is:

$$IHgI + h\nu \rightarrow [I\cdots Hg\cdots I]^{*\ddagger} \rightarrow I^*/I + HgI(X) \quad (3.8a)$$

$$\rightarrow I^*/I + Hg + I \ . \quad (3.8b)$$

At 277 nm excitation, the complex involves the three types of motion, on both the I^* and I PESs: the asymmetric stretch which leads to I^*/I+HgI(X:v) formation and the symmetric stretch which gives I^*/I+Hg+I products. The bending motion of I-Hg-I is important for the rotational excitation of HgI(X:J) and for changing the molecular initial alignment (β).

The wave packet is prepared well above the saddle point and the three-body dissociation (I^*+Hg+I) energy. Following the preparation, it spreads on the three-dimensional PES toward final products. The final outcome includes the reaction path (3.8a) and (3.8b), for both I^* and I channels (see Fig. 3.22). The energy distribution of I^*/I is very broad and the HgI(X:υ,J) could be formed in all rovibrational levels extending to the dissociation limit.

From this laboratory, two fs-resolved studies of HgI_2 dissociation in the gas phase have been reported before. One[69] focused on reaction (3.8a) by monitoring the HgI formation using the LIF method. Coherent product formation and high rotational excitation of HgI(X:v,J) were observed and studied. In the same system, the solvation dynamics in solutions were also studied,[70] showing manifestations of vibrational relaxation and dephasing. The other study[71] involved the probing of the transition state by

MPI, and two-photon excitation dynamics. The reaction (3.8b) has not been directly observed and studied.

Theoretically, classical and quantum calculations have been carried out by Gruebele *et al.*,[72] using an empirical damped Morse potentials, to simulate the experimental findings. Recently, Burghardt and Gaspard[73] used the semiclassical methods of periodic-orbit quantization and equilibrium-point quantization to study the transition-state dynamics at the lower energy regime. A series of resonances is characterized with regular classical dynamics. Near the saddle point, a chaotic behavior was observed. Tannor and coworkers[74] proposed to control the branching of the two-body and three-body dissociation using sequences of optical pulses.

Here, we report fs studies of the dynamics of both the transition state and all iodine products. The results presented are all for one-photon excitation. This is done by carefully examining the power dependence of the initiating pulse. Fig. 3.23 shows the time evolution of the I^+ KETOF distributions at $\chi=0^0$. The magic angle data and the corresponding speed distributions are shown in Fig. 3.24. For near zero delay time, a very broad distribution is detected; it extends to about 2900 m/s. However, at 6 ps delay time, the distribution terminates at 1450 m/s with a clear double peaks ($\chi=0^0$). No further change was found after 6 ps. At longer delay times, the signal from fragmentation of $IHgI^+$ decreases and the speed distribution narrows. This exactly reflects the time evolution of the transition state, as predicted in Sec. 3.3, for the case $E^+_{avl}(t_0) > E_{avl}(t_f)$. The probed ionic PESs may include both bound and repulsive states as evidenced by the earlier I^+ KETOF distribution at $\chi=0^0$. At long times, the wave packet spreads out on the global PES, and this results in decrease of the signal. Also, at these times, the drop of

both the neutral and ionic potential energy causes the narrowing of the speed distribution of I^+ cations.

The I^+ speed of 2900 m/s at t=0 corresponds to 62314 cm^{-1} of total available energy, relative to I^++HgI. By energy conservation, this value matches a four-photon probing. The three-photon probing gives a 1970 m/s speed limit for I^+ cations. The broad speed distribution can be understood because both three- and four-probe-photon ionization of $IHgI^{*\ddagger}$ can access many ion states and produce I^+ cations with different amount of available energy. From zero to 841 fs delay time, the speed limit drops from 2900 m/s to 2300 m/s while from 841 fs to 6 ps, the limit value only decreases by 800 m/s; see the arrows in Fig. 3.24. This means that the transition-state species exhibits, at least, two different decay behaviors.

To obtain the complete temporal behavior, we gated the high velocity portion of the I^+ distribution ($-2900 \le v_z \le -980$ m/s) at $\chi=0^0$ while varying the delay time. The result, shown in Fig. 3.25A, does not show a single-exponential decay behavior. The fs transient can be fitted to a biexponential decay with two distinct time constants: $\tau_1^{\ddagger}$~230 fs and $\tau_2^{\ddagger}$~1.32 ps, consistent with the observation of the KETOF evolution. We also measured the temporal behavior of Hg^+, which also results from fragmentation of excited $IHgI^+$ (Hg^++I+I). A similar transient was found with two time constants, $\tau_1^{\ddagger}$~200 fs and $\tau_2^{\ddagger}$~1.44 ps, as shown in Fig. 3.25B.

The observed, first ~200 fs decay represents the time for the movement of the wave packet out of the initial Franck-Condon region. This rapid motion occurs because the packet experiences a strong repulsive force. Then, it must pass the transition-state region near the saddle point and enters the valley of the products. Since both Hg and I are

very heavy, the ~200 fs is a reasonable time when compared to those of other systems; $I_2^{*\ddagger}$ (65 fs), $ICN^{*\ddagger}$ (70 fs) and $CH_3I^{*\ddagger}$ (40 fs). After 200 fs, some portion of the wave packet evolves along the valley of the products I^*/I+HgI(X) and the other makes an excursion to form I^*/I+Hg+I. During this process, our probe pulses still can ionize these "loose" transition-state species, and overall they live longer with a decay time constant of ~1.35 ps. This striking longer time of ~1.35 ps represents an average lifetime for all trajectories traveling through the transition-state region until the completion of the reaction (3.8a) and (3.8b). This picture is further supported by the product detection experiments, which are discussed in what follows.

The I^+ KETOF distribution after 6 ps is unchanged and is sensitive to the probe wavelength. This indicates that the observed I^+ signal results from the neutral I-atom ionization. This also excludes the contribution from the HgI^{+*} fragmentation even though HgI is one of the products. The deduced speed distribution from the magic angle data is shown in Fig. 3.26. The speed distribution mainly consists of two components. One is from the reaction (3.8a) and (3.8b) for the I^* channel, *i.e.,* forming I^*+HgI(X) and I^*+Hg+I. The ratio of the reaction (3.8a) to (3.8b) is close to 45%. The other involves the I channel giving I+Hg(X) and I+Hg+I as products. The ratio for these two reaction branches is less than 40%. The ratio for the two channels (I^* and I) is about 4:1, which is less than the early reported value from the quantum yield measurement (~13:1).[75]

If all the available energy (15101 cm^{-1} above I+HgI(X)) is converted to translational motion, the observed speed distribution does indeed reach these limiting values (1000 m/s for I^*+HgI(X) and 1430 m/s for I+HgI(X)). Fig. 3.26 gives the starting speeds for the three-body dissociation: 796 m/s for I^*+Hg+I and 1289 m/s for I+Hg+I,

where the vibrational excitation of HgI(X:v) reaches the dissociation limit, ~2800 cm^{-1}. Considering the rotational excitation of HgI(X) (assuming J=150 for the I^* channel, E_R=634 cm^{-1} and J=200 for the I channel, E_R=1125 cm^{-1}),[38] the speed values for I^* and I shift to 740 m/s and 1228 m/s, respectively. For the three-body dissociation, the translation energy release to I^*/I and I highly depends on the structure of the transition state. For example, assuming that the geometry of $IHgI^{*\ddagger}$ is linear and that both Hg-I stretches receive the same translational energy deposition, the I^* and I would have the same final speed of 663 m/s from the I^*+Hg+I channel. On the other hand, the speed would be 1075 m/s for the I and I coming from the I+Hg+I channel. If the $IHgI^{*\ddagger}$ is bent by 80^0, the speed is 502 m/s for the I^* and I, and 812 m/s for the 2I. In fact, by examining the speed distribution, one concludes that the two iodine atoms have different speeds and that the two symmetric stretches do obtain different energy during dissociation. This implies that the two Hg-I bonds take different time to break.

By performing the gating experiment of the I^+ velocity distribution ($0 \le v_z \le 980$ m/s) at $\chi=0^0$, we do observe the multiple-rise time transient shown in Fig. 3.27A. The transient exhibits a decay signal around t=0. After 1 ps, the signal rapidly increases and then gradually grows up to 6 ps. The transient was independently repeated many times and the results are reproducible. The initial signal decay reflects the contribution from the transition-state population, and the later rise clearly results from neutral I atoms, consistent with the observed KETOF evolution. This rise signal, after subtracting the transition-state contribution, is shown in Fig. 3.27B. The transient is coherently shifted by 1 ps from t=0 and increases rapidly at the beginning. Up to 2 ps, the signal reaches 70% of the asymptotic value. The 1 ps coherent shift is the shortest bond-breaking time for the

reaction (3.8a) and (3.8b). After 2 ps, the transient gradually rises to 6 ps, which indicates that the bond-breaking time for the two Hg-I bonds ranges from 1 ps to 6 ps for reaction (3.8b). This rise signal at long times is *not* a kinetic behavior, instead it represents superpositions of many coherent shifts of Hg-I bond breakage. The time scales will be further discussed after we present studies of the anisotropy in what follows. The anisotropy is directly relevant to the bending motion of I-Hg-I.

From simulation of the parallel I^+ KETOF distribution using the speed distribution deduced from the magic angle KETOF data, we obtained an averaged anisotropy parameter β~0.5 for the final iodine atoms. If we neglect the bending motion of IHgI in the ground state, the initial molecular geometry of IHgI is linear before the pump excitation. The relativistic *ab initio* calculations on $HgCl_2$ by Wadt[76] predict that the first excited state is bent by ~80^0-120^0. An analogous nonlinear geometry for the first excited state is also expected for HgI_2. Using magnetic circular dichroism, Mason[77] concluded that the initial absorption has Σ_u^+ and Π_u characters due to the strong spin-orbital coupling, with a linear geometry description. This means that the initial excitation includes both parallel and perpendicular transitions. According to our study of χ dependencies, the excitation at 277 nm is a parallel transition. From the measured β~0.5, we obtain a ~45^0 average angle of the final recoil velocity relative to the initial transition dipole. So, after initial linear absorption of IHgI, and because of the anisotropic PES of the excited state, the molecule proceeds to a bending motion, together with the repulsive stretch motion. The bending motion results in the observations of the small value of the anisotropy of iodine atoms and the rotational excitation of HgI(X). Also, it enhances the interaction between I^*/I and HgI(X) during dissociation.

The striking long bond breaking time, ranging from 1 ps to 6 ps, can now be rationalized. First, the observed product formation time is consistent with the measured time scale of transition-state decay, and both are in the several-picosecond range. Second, since the terminal speed is small due to the heavy Hg and I atoms, the bond breakage takes longer time, as expected. Assuming that the I^* atom is further moved by 6Å from the equilibrium separation with Hg, for the reaction (3.8a), and that all available energy is converted to the translational motion, the terminal velocity is deduced to be 1330 m/s for I^*+HgI(X: v=0) and the minimum bond-breaking time is calculated to be ~450 fs. This time increases to 590 fs for the highest vibrational excitation of HgI(X:v), *i.e.,* when the vibrational energy reaches the dissociation limit. Finally and importantly, the bending motion, together with the Hg-I stretching increases the bond-breaking time due to the enhancement of the interaction between I^*/I and HgI(X).

Because the terminal speeds of I^*/I+HgI(X), for low and high vibrational excitation of HgI(X:v), are slightly different, the bond breaking time for reaction (14a) has an average dissociation time of ~1 ps. However, reaction (3.8b) is different, and the relative velocity between each other highly depends on the geometry of the transition state. The total available energy (less than that for reaction (3.8a)) needs to be divided into three atoms, and this division generally leads to small velocities. From the speed distribution (Fig. 3.26), the speeds of the two iodine atoms from the three-body dissociation are different and this means that the deposition of the available energy into two Hg-I bonds is different. When less available energy is channeled into the second Hg-I bond, the relative velocity between Hg and I would be very small, although the lab

velocity of the second I atom could be larger because of the addition of the c.m. velocity of Hg-I from the I-Hg bond breakage.

For example, assuming that the three-body dissociation of the I^* channel proceeds with a linear geometry and that the total available energy (4696 cm^{-1}) channels 4175 cm^{-1} into the first I-Hg bond and 512 cm^{-1} into the second Hg-I bond, the observed lab velocities for the final products of I^*, Hg and I are 750 m/s, -136 m/s and -535 m/s, respectively. The relative velocity between Hg and I is only 399 m/s. Therefore, it takes about 1.5 ps to break the second I-Hg bond for I to move 6 Å away from Hg, even without considering the bending motion. The bending motion (for v=1, the period is ~1 ps) is on the time scale of the bond breakage and should also be included in the complete analysis of the HgI_2 dissociation on the three-dimensional PES. Molecular dynamics calculations completely support the dynamic picture.[78]

3.5. Conclusion

By resolving the femtosecond dynamics, together with the angular, state and velocity distributions of reactions, we report studies of elementary steps in complex unimolecular reactions. The level of complexity varies from diatomics to polyatomics, from direct-mode to complex-mode, from one-center to two-center to four-center reactions. The systems examined here are of the following classes: (1) one-bond breakage: direct-mode reactions for iodine, cyanogen iodide, methyl iodide and complex-mode reactions for iodobenzene; (2) two-bonds breakage: sequential processes for 1,2-diiodotetrafluoroethane and saddle-point transition states for mercury iodide.

When a complex unimolecular reaction involves multiple pathways, from the transition state to final products, each pathway results in different energy partitioning among final products. For a given velocity range of a product, we can monitor the temporal evolution and then separately study each reaction path. Specifically, we have obtained: (1) the temporal evolution of the transition state and the final products; (2) the time-resolved KETOF distributions; (3) the recoil anisotropy (β) in each channel; (4) the state-resolved (I^* and I) dynamics. A variety of dynamical behaviors has been revealed, and these include product rotational and vibrational excitation, electronic and vibrational predissociation, saddle-point transition state dynamics. Theoretical studies were also presented as part of the effort to compare with the experimental findings.

3.6. References

1. *Femtosecond Chemistry*, eds. J. Manz and L. Wöste (VCH, Weinheim, 1995).
2. *Femtochemistry: Ultrafast Chemical and Physical Processes in Molecular Systems*, ed. M. Chergui (World Scientific, Singapore, 1996).
3. *Femtochemistry and Femtobiology*, ed. V. Sundström (World Scientific, Singapore, 1998).
4. *Chemical Reactions and Their Control on the Femtosecond Time Scale, XXth Solvay Conference on Chemistry*, Adv. Chem. Phys. **101**, eds. P. Gaspard, I. Burghard, I. Prigogine and S.A. Rice (John Wiley & Sons, New York, 1997).
5. A.H. Zewail, *Femtochemistry: Ultrafast Dynamics of the Chemical Bond* (World Scientific, Singapore, 1994).
6. A.W. Castleman Jr. and K.H. Bowen Jr., J. Phys. Chem. **100** (1996) 12911.
7. G. Gerber, in Ref. (4), and references therein.
8. P.Y. Cheng, D. Zhong and A.H. Zewail, Chem. Phys. Lett. **237** (1995) 399; P.Y. Cheng, D. Zhong and A.H. Zewail, J. Chem. Phys. **105** (1996) 6216.
9. A.H. Zewail, in Ref. (3), and references therein.
10. H. Kühlewind, A. Kiermeier and H.J. Neusser, J. Chem. Phys. **85** (1986) 4427.
11. M. Dantus, M.J. Rosker and A.H. Zewail, J. Chem. Phys. **87** (1987) 2395; M.J. Rosker, M. Dantus and A.H. Zewail, *ibid.* **89** (1988) 6113; M. Dantus, M.J. Rosker and A.H. Zewail, J. Chem. Phys. **89** (1988) 6128.
12. B.J. Greenblatt, M.T. Zanni and D.M. Neumark, Chem. Phys. Lett. **258** (1996) 523; Science, **276** (1997) 1675.
13. G.E. Busch, R.T. Mahoney and K.R. Wilson, J. Chem. Phys. **51** (1969) 837.

14. R.J. Mulliken, J. Chem. Phys. **55** (1971) 288; J. Tellinghuisen, *ibid.* **58** (1973) 2821.

15. S.O. Williams and D. Imre, J. Phys. Chem. **92** (1988) 6648.

16. G. Roberts and A.H. Zewail, J. Phys. Chem. **95** (1991) 7973; **99** (1995) 2520.

17. J.H. Ling and K.R. Wilson, J. Chem. Phys. **63** (1975) 101.

18. M.J. Sabety-Dzvonik and R.J. Cody, J. Chem. Phys. **66** (1977) 125; A.P. Baronavski and J.R. McDonald, Chem. Phys. Lett. **45** (1977) 172.

19. W.J. Marinelli, N. Sivakumar and P.L. Houston, J. Phys. Chem. **88** (1984) 6685; G.E. Hall, N. Sivakumar and P.L. Houston, J. Chem. Phys. **84** (1986) 2120.

20. I. Nadler, M. Mahgerefteh, H. Reisler and C. Wittig, J. Chem. Phys. **82** (1985) 3885.

21. W.P. Hess and S.R. Leone, J. Chem. Phys. **86** (1987) 3773.

22. (a) M.A. O'Halloran, H. Joswig and R.N. Zare, J. Chem. Phys. **87** (1987) 303; J.F. Black, J.R. Waldeck and R.N. Zare, *ibid.* **92** (1990) 3519; J.F. Black, *ibid.* **98** (1993) 6853. (b) S.W. North, J. Mueller and G.E. Hall, Chem. Phys. Lett. **276** (1997) 103.

23. P.W. Kash and L.J. Butler, J. Chem. Phys. **96** (1992) 8923.

24. J. Griffiths and M.A. El-Sayed, J. Chem. Phys. **100** (1994) 4910.

25. E.M. Goldfield, P.L. Houston and G.S. Ezra, J. Chem. Phys. **84** (1986) 3120.

26. H. Guo and G.C. Schatz, J. Chem. Phys. **92** (1990) 1634; L. Liu, J. Fang and H. Guo, *ibid.* **102** (1995) 2404.

27. R.D. Coalson and M. Karplus, J. Chem. Phys. **93** (1990) 3919.

28. C.J. Williams, J. Qian and D.J. Tannor, Chem. Phys. **95** (1991) 1721; J. Qian, C.J. Williams and D.J. Tannor, *ibid.* **97** (1992) 6300.

29. S.Y. Lee, J. Chem. Phys. **97** (1992) 227.

30. J.A. Beswick, M. Glass-Maujean and O. Roncero, J. Chem. Phys. **96** (1992) 7514.

31. M. Baer and R. Kosloff, Chem. Phys. Lett. **200** (1992) 183.

32. S. Yabushita and K. Morokuma, Chem. Phys. Lett. **175** (1990) 518; Y. Amatatsu, S. Yabushita and K. Morokuma, J. Chem. Phys. **100** (1994) 4894.

33. Y. Wang and C.X.W. Qian, J. Chem. Phys. **100** (1994) 2707.

34. J. Qian, D.J. Tannor, Y. Amatatsu and K. Morokuma, J. Chem. Phys. **101** (1994) 9597.

35. J.M. Bowman, R.C. Mayrhofer and Y. Amatatsu, J. Chem. Phys. **101** (1994) 9469.

36 H. Wei and T. Carrington Jr., J. Chem. Phys. **105** (1996) 141.

37. Y. Wang and C.X.W. Qian, Chem. Phys. Lett. **219** (1994) 389.

38. A.H. Zewail, J. Chem. Soc. Faraday Trans. 2 **85** (1989) 1221; Faraday Discuss. Chem. Soc. **91** (1991) 207; J.S. Baskin and A.H. Zewail, J. Phys. Chem. **98** (1994) 3337.

39. D. Imre, J.L. Kinsey, R.W. Field and D.H. Katayama, J. Phys. Chem. **86** (1982) 2564; D. Imre, J.L. Kinsey, A. Sinha and J. Krenos, *ibid.* **88** (1984) 3956; B.R. Johnson, C. Kittrell, P.B. Kelly and J.L. Kinsey, *ibid.* **100** (1996) 7743.

40. R.K. Sparks, K. Shobatake, L.R. Carlson and Y.T. Lee, J. Chem. Phys. **75** (1980) 3838.

41. S.L. Baughcum and S.R. Leone, J. Chem. Phys. **72** (1980) 6531; H.W. Hermann, and S.R. Leone, *ibid.* **76** (1982) 4766.

42. M.D. Barry and P.A. Gorry, Mol. Phys. **52** (1984) 461; G.N.A. van Veen, T. Baller, and N.J.A. van Veen, Chem. Phys. **87** (1984) 405.

43. R.O. Loo, G.H. Hall, H.P. Haerri and P.L. Houston, J. Phys. Chem. **92** (1988) 5; S.M. Penn, C.C. Hayden, K.J.C. Muyskens and F.F. Crim, J. Chem. Phys. **89** (1988) 2909.

44. D.W. Chandler, M.H.M. Janssen, S. Stolte, R.N. Strickland, J.W. Thoman Jr. and D.H. Parker, J. Phys. Chem. **94** (1990) 4839; M.H.M. Janssen, D.H. Parker, G.O. Sitz, S. Stolte and D.W. Chandler, *ibid.* **95** (1991) 8007.

45. K.Q. Lao, M.D. Person, P. Xayariboun and J.L. Butler, J. Chem. Phys. **92** (1990) 823.

46. G.E. Hall, T.J. Sears and J.M. Frye, J. Chem. Phys. **90** (1989) 6234; T. Suzuki, H. Kanamori and E.J. Hirota, *ibid.* **94** (1991) 6607.

47. Y.F. Zhu and E.R. Grant, J. Phys. Chem. **97** (1993) 9582; A. Strobel, I. Fischer, A. Lochschmidt, K. Müller-Dethlefs and V.E. Bondybey, *ibid.* **98** (1994) 2024.

48. J.A. Syage, Chem. Phys. **207** (1996) 411.

49. H. Ohoyama, T. Ogawa, H. Makita, T. Kasai and K. Kuwata, J. Phys. Chem. **100** (1996) 4729.

50. M.K. Dzvonik, S. Yang and R. Bersohn, J. Chem. Phys. **61** (1974) 4408.

51. J.L. Knee, L.R. Khundkar and A.H. Zewail, J. Chem. Phys. **83** (1985) 1996.

52. M. Shapiro and R. Bersohn, J. Chem. Phys. **73** (1980) 3810; S. Kanfer and M. Shapiro, J. Phys. Chem. **88** (1984) 3644; M. Shapiro, *ibid.* **90** (1986) 3644.

53. R.L. Sundberg, D. Imre, M.O. Hale, J.L. Kinsey and R.D. Coalson, J. Phys. Chem. **90** (1986) 5001.

54. H. Guo and G.C. Schatz, J. Chem. Phys. **93** (1990) 393; H. Guo, K.Q. Lao, G.C. Schatz and A.D. Hammerich, *ibid.* **94** (1991) 6562.

55. Y. Amatatsu, K. Morokuma and S. Yabushita, J. Chem. Phys. **94** (1991) 4858.

56. Y. Amatatsu, S. Yabushita and K. Morokuma, J. Chem. Phys. **104** (1996) 9783.

57. H. Guo and G.C. Schatz, J. Phys. Chem. **95** (1991) 3091; H. Guo, *ibid.* **96** (1992) 6629.

58. A.D. Hammerich, U. Manthe, K. Kosloff, H. Meyer and L.S. Cederbaum, J. Chem. Phys. **101** (1994) 5623.

59. S.C. O´Brien, C. Kittrell, J.L. Kinsey and B.R. Johnson, J. Chem. Phys. **96** (1992) 67.

60. A. Freedman, S.C. Yang, M. Kawasaki and R. Bersohn, J. Chem. Phys. **72** (1980) 1028.

61. H.J. Hwang and M.A. El-Sayed, J. Chem. Phys. **96** (1992) 856; J.E. Freitas, H.J. Hwang and M.A. El-Sayed, J. Phys. Chem. **98** (1994) 3322, 12481.

62. T.H. Lowry and K.S. Richardson, *Mechanism and Theory in Organic Chemistry*, 3rd (ed.) (Harper & Row, New York, 1987).

63. L.R. Khundkar and A.H. Zewail, J. Chem. Phys. **92** (1990) 231.

64. G.M. Nathanson, T.K. Minton, S.F. Shane and Y.T. Lee, J. Chem. Phys. **90** (1989) 6157.

65. G.E. Busch and K.R. Wilson, J. Chem. Phys. **56** (1972) 3626, 3638.

66. E.A. Carter and W.A. Goddard, J. Am. Chem. Soc. **110** (1988) 4077.

67. E.W.G. Diau, J.L. Herek, Z.H. Kim and A.H. Zewail, Science **279** (1998) 847.

68. A.H. Zewail, Phys. Today **33** (1980) 27, and references therein.

69. M. Dantus, R.M. Bowman, M. Gruebele and A.H. Zewail, J. Chem. Phys. **91** (1989) 7437.

70. N. Pugliano, A.Z. Szarka and R.M. Hochstrasser, J. Chem. Phys. **104** (1996) 5062; M. Volk, S. Gnanakaran, E. Gooding, Y. Kholodenko, N. Pugliano and R.M. Hochstrasser, J. Phys. Chem. **101** (1997) 638.

71. T. Baumert, S. Pedersen and A.H. Zewail, J. Phys. Chem. **97** (1993) 12447; S. Pedersen, T. Baumert and A.H. Zewail, *ibid.* **97** (1993) 12460.

72. M. Gruebele, G. Roberts and A.H. Zewail, Phil Trans R. Soc. Lond. A **332** (1990) 223.

73. I. Burghardt and P. Gaspard, J. Chem. Phys. **100** (1994) 6395; J. Phys. Chem. **99** (1995) 2732; Also in Ref. (4).

74. J. Somlói and D.J. Tannor, J. Phys. Chem. **99** (1995) 2552.

75. H. Hofmann and S.R. Leone, J. Chem. Phys. **69** (1978) 3819.

76. W.R. Wadt, J. Chem. Phys. **72** (1980) 2469.

77. M.M. Savas and W.R. Mason, Inorg. Chem. **27** (1988) 658.

78. K.B. Møller and A.H. Zewail, Chem. Phys. Lett. **295** (1998) 1.

3.7. Figure Captions and Figures

Figure 3.1a. TOF mass spectra obtained from the expansion of a mixture of 700 Torr He with I_2 (1 Torr), ICN (~1 Torr) and CH_3I (~7 Torr) under the *monomer* condition. Both pump and probe pulses were used and the delay time was 6 ps. Notice that parent peaks are dominant, in contrast to nanosecond experiments; see text.

Figure 3.1b. TOF mass spectra obtained from the expansion of a mixture of 700 Torr He with C_6H_5I (~20 Torr), $C_2F_4I_2$ (~10 Torr) and HgI_2 (1 Torr) under the *monomer* condition. Both pump and probe pulses were employed and the delay time was fixed at 100 ps. The broad peaks of Hg, HgI and HgI_2 are due to the isotope distribution of Hg (196-204), which is shown in the insert.

Figure 3.2a. A general REMPI/MPI scheme for probing simultaneously transition-state species and final products using only one probe fs pulse. V_0 and V_1 are the neutral ground- and excited-state PESs of the molecule AB, respectively. At time t=0, a pump photon of wavelength λ_1 is absorbed. The probe wavelength λ_2 is tuned to ionize A and this wavelength can also ionize the molecule AB (V_2^+). The observed change of the A^+ translational energy distribution with the delay time reflects the time evolution of the total available energy from E^+_{avl} at t=0 to E_{avl} at $t=t_f$, *i.e.,* mapping out the evolution of the nuclear separations from the initial reactants to final products.

Figure 3.2b. A typical femtosecond pump-probe scheme for studying transition states and products using the LIF method. At t=0, a pump photon of λ_1 is absorbed by the vertical transition from the ground-state V_0 to the excited-state V_1. In order to detect the final product or the transition-state species, the probe wavelength need to be tuned to resonate with A^* or AB^{**} (V_2).

Figure 3.3. (A) Fs-resolved I^+ KETOF distributions arising from the dissociation of I_2 at $\chi=90^0$. Note the significant change in shape with the pump-probe delay time. (B) I^+ KETOF distributions for the different χ's at a fixed delay time of 6 ps, which shows a perpendicular transition for the A-state excitation of I_2 at 690 nm.

Figure 3.4. Upper panel: The speed distributions of iodine atoms (from I_2) deduced from the I^+ KETOF signal for $\chi=54.7^0$ at 6 ps (solid line) and from the pump-pulse bandwidth (dashed line). The instrument resolution is obtained to be within ±15 m/s at the speed of 440 m/s from comparison. Lower panel: The corresponding c.m. translational energy distributions from the dissociation of I_2, which equals to the total available energy.

Figure 3.5. (A) I^+ transient obtained by gating the high-velocity portion in the I^+ KETOF distribution (bottom) of iodine dissociation. By measuring the time zero and pump-probe correlation *in situ* (dashed line), the transient is best fitted by a small decay component ($\tau^{\ddagger}$=65 fs) and a large 240 fs delayed one. The decay I^+ signal is due to excited I_2^+ fragmentation and reflects the transition-state $I_2^{*\ddagger}$ dynamics and the delayed one,

which is shown at the top, after subtraction of the small decay signal, results from the neutral I_2 dissociation. (B) I^+ transient obtained from collecting the low-velocity portion in the I^+ KETOF distribution (bottom). The signal is fitted as in (A) by two components: a 65 fs lifetime decay and a 240 fs delayed rise. The decay signal is separately shown at the top after subtraction of the contribution from the neutral I_2 dissociation.

Figure 3.6. (A) Fs-resolved I^+ KETOF distributions from the dissociation of ICN at $\chi=0^0$. At the early delay time, the I^+ signal is from excited ICN^+ fragmentation and at the later time, it results from the neutral iodine atoms. The distribution remains the same after 600 fs. Note the dramatic change in shape with the delay time. (B) I^+ KETOF distributions for the different χ's at a fixed delay time of 2 ps, which shows a pure parallel transition for excitation of ICN at 277 nm.

Figure 3.7. The speed distribution deduced from the I^+ KETOF signal at the 2 ps delay time for $\chi=54.7^0$ (top left); ICN reaction. Both I and I^* channels are clearly identified and reach their speed limits (see arrows). The corresponding anisotropy distribution is shown at the top, which is obtained by nonlinear-least-squares fit of the parallel polarization KETOF signal (top right) using the derived speed distribution. All β's are positive and the average is larger than 1.6. The c.m. translational energy distribution with the corresponding rotational excitation of CN is shown at the bottom.

Figure 3.8. I^+ KETOF distributions (ICN reaction) for the different χ's at the early delay time (-210 fs) shown at the left topside. Note the difference when comparing with

Fig. 3.6B. The speed distribution derived from the magic angle KETOF distribution at -210 fs delay time is shown in the right bottom side, which is very broad as expected for ion fragmentation. The anisotropy distribution is shown at the right top, which is obtained by nonlinear-least-squares fit of the parallel polarization KETOF signal (left bottom) using the deduced speed distribution. The average anisotropy is about 0.5, much smaller than that from the neutral ICN dissociation (1.6).

Figure 3.9. (a) Transient obtained by monitoring the signal of the ICN^+ mass channel. By measuring the response function *in situ* (dashed line in d or e), the transient was best fitted by a single exponential decay with a 70 fs lifetime. (b) and (c) Transients obtained by gating the I^* ($150 \leq v_z \leq 300$ m/s) and I ($380 \leq v_z \leq 580$ m/s) channels. Both transients were fitted by two components: one as a decay signal from ion fragmentation around t=0 with a lifetime of 70 fs and the other as a shift, rapid rise. (d) and (e) Transients with 220 fs and 185 fs coherent shifts for the I^* and I channels, respectively, were obtained by subtracting the contributions from the transition-state species. Note that measuring the time zero and the cross correlation *in situ* is a key for accurate fitting of these transients.

Figure 3.10. (A) and (B) Transients obtained by collecting all I^+ signal corresponding to the pump polarization parallel ($\chi=90^0$) and perpendicular ($\chi=0^0$) to the probe, respectively (ICN reaction). Both transients are fitted by one component from the transition-state contribution (70 fs lifetime) and a shift, rapid rise from the neutral ICN dissociation, as in Fig. 3.9. (C) Transients obtained by subtraction of the shift rise component from (A) and (B). Both transients represent the decay dynamics of the

transition state with the different pump-probe polarization combinations. As predicted from the theory, the signal from the parallel is three times larger than from the perpendicular one.

Figure 3.11. (A) Fs-resolved I^+ KETOF distributions from CH_3I dissociation at $\chi=0^0$. The signal at early times results from excited CH_3I^+ fragmentation. After 600 fs, the distribution is unchanged. Unlike I_2 and ICN, all distributions are similar in shape. (B) I^+ KETOF distributions from the different χ's at 6 ps delay time, which shows a pure parallel transition for excitation of CH_3I at 277 nm.

Figure 3.12. The speed distribution derived from the magic angle I^+ KETOF distribution at 6 ps delay time (CH_3I reaction). Both I^* and I channels are identified and reach their speed limits (see arrows on the upper panel). The c.m. translational energy distribution with the corresponding vibrational excitation of CH_3 umbrella mode is shown on the lower panel.

Figure 3.13. (A) Transient obtained by monitoring the signal of the CH_3I^+ mass channel. By measuring the response function *in situ* (dashed line in C), the signal is best fitted by a single exponential decay with a lifetime of 40 fs. (B) Transient obtained by gating the high v_z values ($500 \leq v_z \leq 380$ m/s) and it is fitted by a small decay component with a 40 fs lifetime and a shift, rapid rise. (C) Transient with a 125 fs coherent shift obtained by subtraction of the small decay signal from (B).

Figure 3.14. A schematic representation for the mechanism of direct-mode and complex-mode reactions.

Figure 3.15. Fs-resolved I^+ KETOF distributions for the dissociation of iodobenzene at $\chi=0^0$. The shading intensity is roughly proportional to the ion signal, for clarification purposes. The distribution only extends to ±800 m/s at the early delay times and reaches ±960 m/s at the later times. After ~2 ps, the distribution remains unchanged. Note that the signal around $v_z=0$ grows slower than that of the high v_z range.

Figure 3.16. (A) Transient obtained by gating only the high-velocity ($680 \le v_z \le 960$ m/s) component of the I^+ KETOF distribution (iodobenzene dissociation). A 400 fs coherent shift from the time zero is observed. The system response function (dashed line) is shown. Note that no ion fragmentation signal produced at this high velocity. (B) and (C) Transients obtained by collecting the medium ($290 \le v_z \le 960$ m/s) and low ($0 \le v_z \le 270$ m/s) velocity ion signal in the KETOF distribution. A small contribution from ion fragmentation around t=0 has been subtracted from both transients. Note that the transient B with the higher velocities appears earlier than the transient C with the lower ones. The transient B has a ~400 fs coherent shift from the time zero and the transient C has a 550 fs rise; see the text for detail.

Figure 3.17. A schematic drawing of the excited bound- and repulsive-state, $V(\pi,\pi^*)$ and $V(n,\sigma^*)$ PESs, respectively, illustrating the time-velocity correlation during dissociation in iodobenzene. At t=0, a wave packet is created on the $V(\pi,\pi^*)$ surface by

absorption of one-pump photon. At $t_1^{\ddagger}$, enough energy flows into the C-I coordinate through IVR and the C-I bond is broken with high total available energy. The observed I^+ KETOF signal has a large-velocity distribution and high anisotropy. The C-I stretching motion can also couple with other bath modes ($t_2^{\ddagger}$). After a certain time, the energy flows back to the C-I coordinate and the C-I bond breaks with low total available energy ($t_3^{\ddagger}$). The resulting I^+ KETOF shows a small-velocity distribution and low anisotropy.

Figure 3.18. I^+ KETOF distributions (1,2-diiodotetrafluoroethane elimination reaction) for two typical delay times of 1 and 600 ps at $\chi=54.7^0$ (top) and $\chi=0^0$ (bottom). The difference of each two KETOF distributions (solid line) represents the contribution of the secondary iodine bond cleavage. The clear double peaks of the I^+ KETOF distributions at $\chi=0^0$ shows a pure parallel transition with a very high anisotropy.

Figure 3.19. Transient obtained by gating the slow-velocity ($-250 \le v_z \le 250$ m/s) portion of the I^+ KETOF distribution at the magic angle as a function of the delay time ($C_2F_4I_2$ reaction). The slow rise signal results from the secondary iodine bond breakage with a 25 ps lifetime and the initial rapid rise is due to the primary iodine bond cleavage with a ~200 fs. Three structures are shown on the top to indicate the reaction: prior to the femtosecond excitation (t_i), after the primary bond breaking ($t^{\dagger}$), and when the final elimination (t_f) is reached.

Figure 3.20a. The recoil speed distributions of iodine from the primary and secondary C-I bond breakage deduced (and smoothed) from the magic angle I^+ KETOF signal for

the 1 ps and 600 ps delay times, respectively ($C_2F_4I_2$ reaction). Both I and I^* channels are present from the primary bond breakage and reach their speed limits. The second iodine C-I cleavage only produces the ground-state I atoms because of energetics. The two arrows in the secondary speed distribution (bottom) indicate the peak speeds of the dissociating C_2F_4I radicals produced from the I^* and I channels.

Figure 3.20b. A schematic representation of the velocity distribution evolution during dissociation, illustrating the observed high anisotropy for the secondary iodine atom. At $t^\dagger$, the c.m. velocity (**v**) of the C_2F_4I radical is obtained from the impulsive primary C-I bond breakage. At $t^\ddagger$, the high-activated radical dissociates into C_2F_4 and I, producing a small, isotropic velocity distribution (**w**) for the secondary I atom in the c.m. frame. Finally (t_f), the observed laboratory velocity distribution for the secondary I atom is addition of the two velocities, **v** and **w**. Because **w** is very small compared with **v**, the final velocity observed is dominated by **v**.

Figure 3.20c. Upper panel: the c.m. translational energy distribution from the primary iodine bond breakage at 1 ps delay time. This is composed of two components from the I^* and I channel. Lower panel: the internal energy distributions of the C_2F_4I radicals resulting from the I^* an I channels, obtained by subtraction of the c.m. translational energy from the total available energy. The deduced decomposition threshold is also indicated and the C_2F_4I radicals with the internal energy larger than E_{th} dissociate into C_2F_4 and I; see the text for detail.

Figure 3.21. Schematic diagram of the reaction path for the two-iodine elimination from $C_2F_4I_2$. After the impulsive dissociation for the first C-I bond (t_0), the $C_2F_4I^\dagger$ is born at a special configuration with a broad vibrational excitation ($t^\dagger$). Some C_2F_4I radicals (~35%) pass the decomposition barrier (~15 kcal/mol) through a process of C-I stretching and C-C shrinking ($t^\ddagger$) to break the second C-I bond and make the C=C bond (t_f). The final products are two iodine atoms with difluoroethylene. The other 70% radicals stays in the ground state. The corresponding structures at different stages are illustrated at the top.

Figure 3.22. A schematic contour PES map at a linear configuration with two typical trajectories for the two-body and three-body dissociation. The wave packet is prepared on a deep repulsive wall right above the saddle point. The final products are shown in the two inserted panels.

Figure 3.23. Fs-resolved I^+ KETOF distributions from dissociation of IHgI at $\chi=0^0$. The signal at the early delay time is from excited $IHgI^+$ fragmentation and the distribution stays unchanged after 6 ps. Note the dramatic change of the KETOF shape and the velocity limit change with time.

Figure 3.24. Fs-resolved I^+ KETOF distributions at $\chi=54.7^0$ (IHgI reaction) shown on the right. The deduced speed distributions are on the left. Note the large change of the speed limits (shown by the arrows), which reflects the time evolution of the total available energy during dissociation, as discussed in Sec. 3.3.

Figure 3.25. (A) Femtosecond transient obtained by gating the high-velocity component of the I^+ KETOF distribution at $\chi=0^0$ (IHgI reaction). The transient does not show a single exponential decay behavior and can be fitted by a biexponential decay with two distinct time constants: $\tau_1^{\ddagger}$= 230 fs and $\tau_2^{\ddagger}$= 230 fs. (B) Femtosecond transient obtained from detecting the Hg^+ signal with a similar time behavior ($\tau_1^{\ddagger}$=200 fs and $\tau_2^{\ddagger}$= 1.44 ps). Both (A) and (B) signals are from fragmentation of excited $IHgI^+$ and reflect the transition-state dynamics of $IHgI^{*\ddagger}$.

Figure 3.26. The speed distribution for the final neutral iodine atoms deduced from the I^+ KETOF distribution at $\chi=54.7^0$ for the 10 ps delay time (IHgI reaction). The recoil iodine speed distributions from the corresponding two-body and three-body dissociation for both I and I^* channels are indicated. When the vibrational excitation energy of HgI (v) is equal to the dissociation limit, ~2800 cm^{-1}, the three-body dissociation begins.

Figure 3.27. (A) Femtosecond transient taken by gating the slow-velocity component of the I^+ KETOF distribution at $\chi=0^0$ (IHgI reaction). The signal around t=0 results from excited $IHgI^+$ fragmentation, which reflects the transition-state dynamics of $IHgI^{*\ddagger}$, as observed in Fig. 3.25. The delayed signal is from neutral iodine atoms. This transient was repeated many times and is reproducible. (B) Femtosecond transient obtained by subtracting the transition-state contribution from (A). This transient gives a coherent shift of 1 ps from the time zero and increases rapidly at the beginning. Up to 2 ps, the signal reaches 70% of the asymptotic value and then gradually rises to 6 ps (see text).

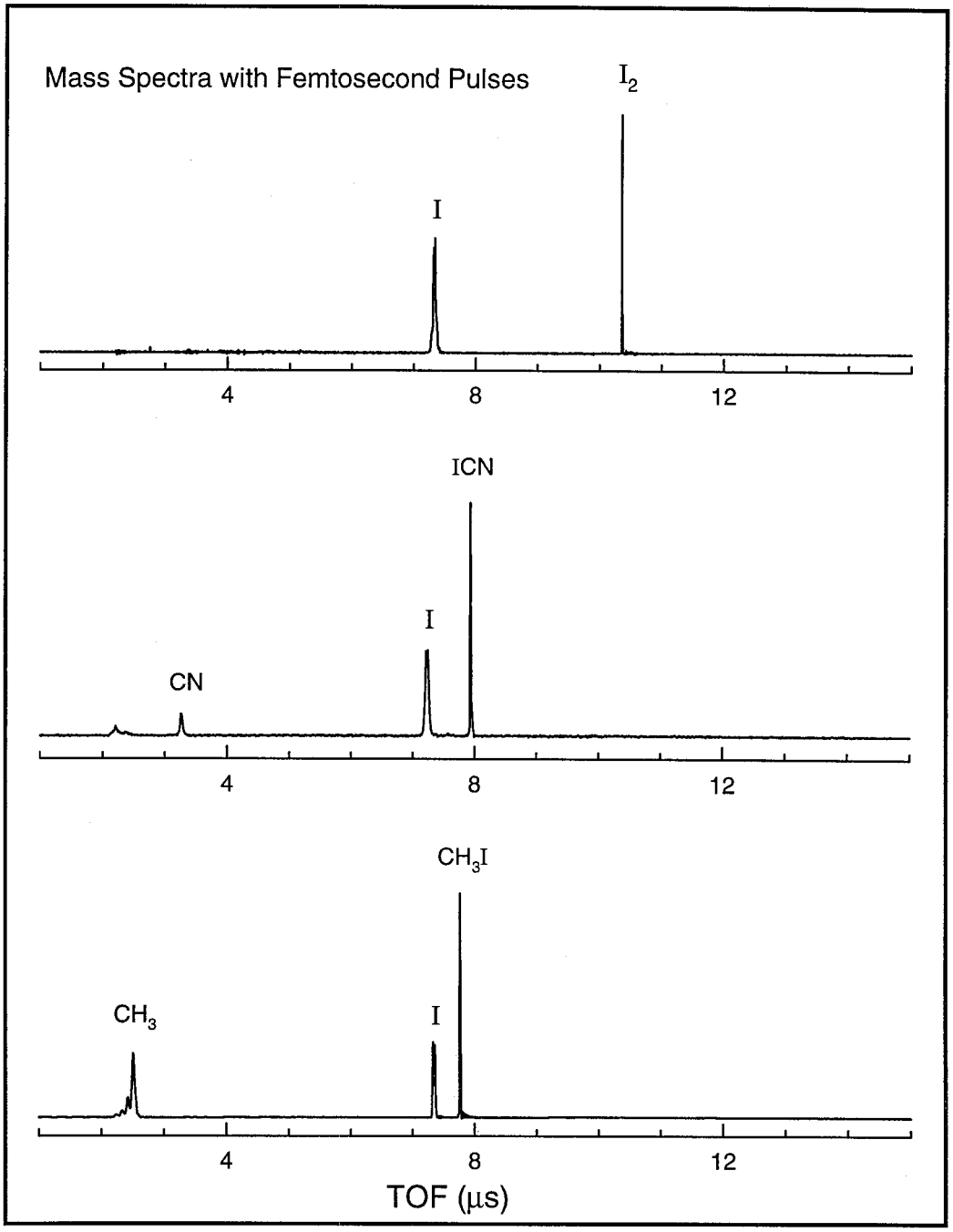
Mass Spectra with Femtosecond Pulses
I_2
I
4
8
12
ICN
I
CN
4
8
12
CH_3I
CH_3
I
4
8
12
TOF (μs)

Figure 3.1a

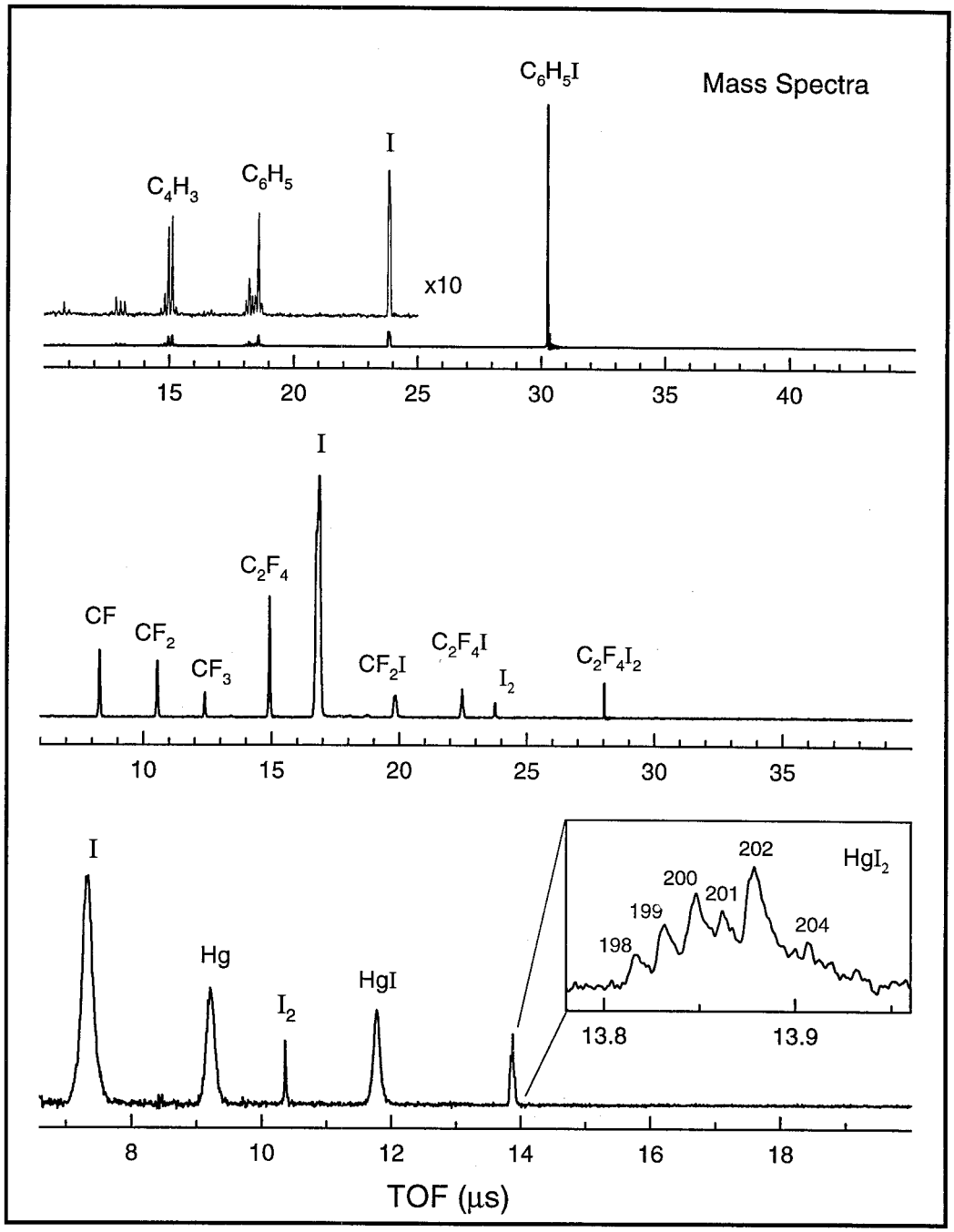
Mass Spectra
C_6H_5I
I
C_4H_3
C_6H_5
x10
15
20
25
30
35
40
I
C_2F_4
CF
CF_2
CF_3
CF_2I
C_2F_4I
I_2
$C_2F_4I_2$
10
15
20
25
30
35
I
Hg
I_2
HgI
202
200
201
199
198
204
HgI_2
13.8
13.9
8
10
12
14
16
18
TOF (μs)

Figure 3.1b

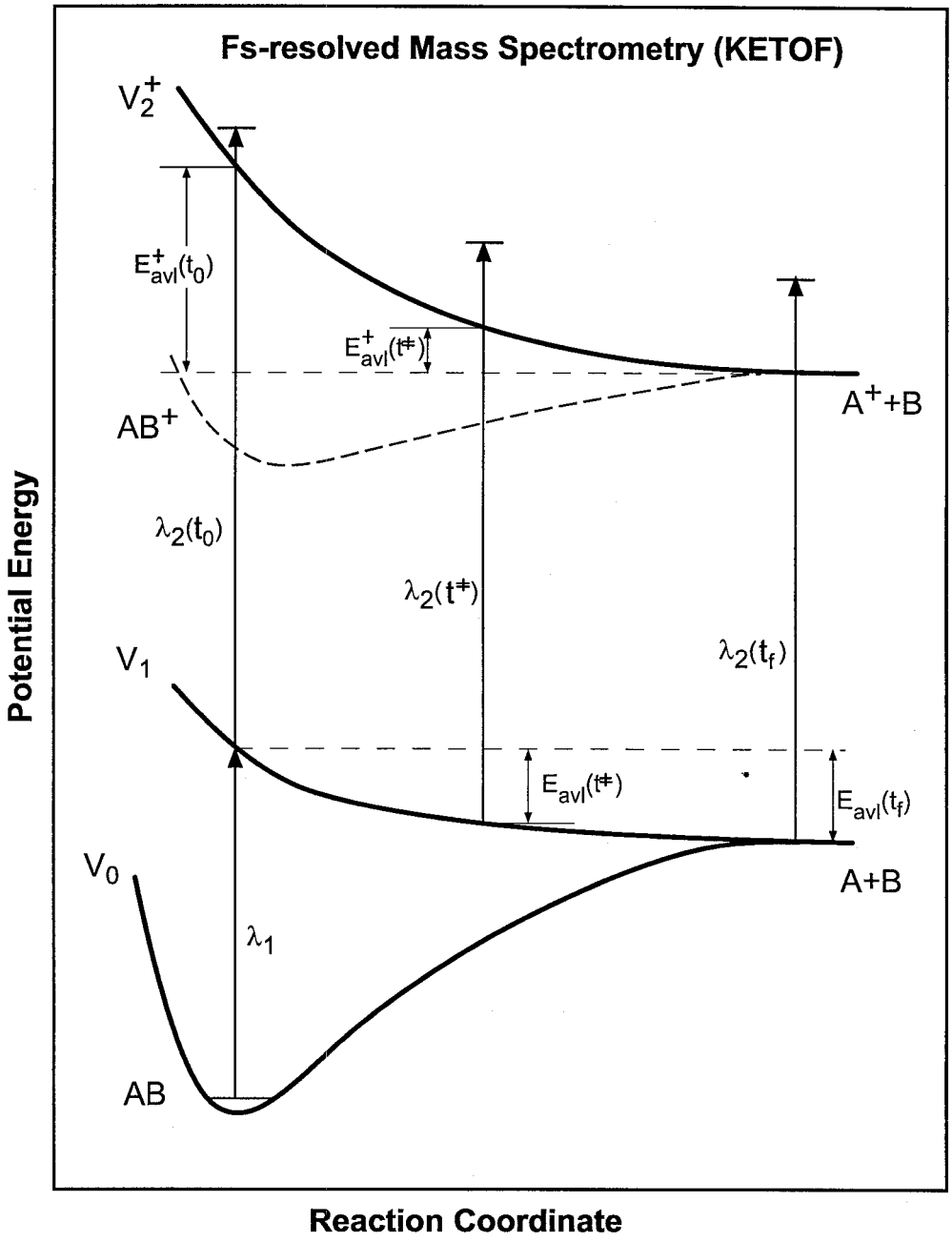
Fs-resolved Mass Spectrometry (KETOF)
V_2^+
$E^+_{avl}(t_0)$
$E^+_{avl}(t^\ddagger)$
A^++B
AB^+
$\lambda_2(t_0)$
$\lambda_2(t^\ddagger)$
$\lambda_2(t_f)$
V_1
$E_{avl}(t^\ddagger)$
$E_{avl}(t_f)$
A+B
V_0
λ_1
AB
Potential Energy
Reaction Coordinate

Figure 3.2a

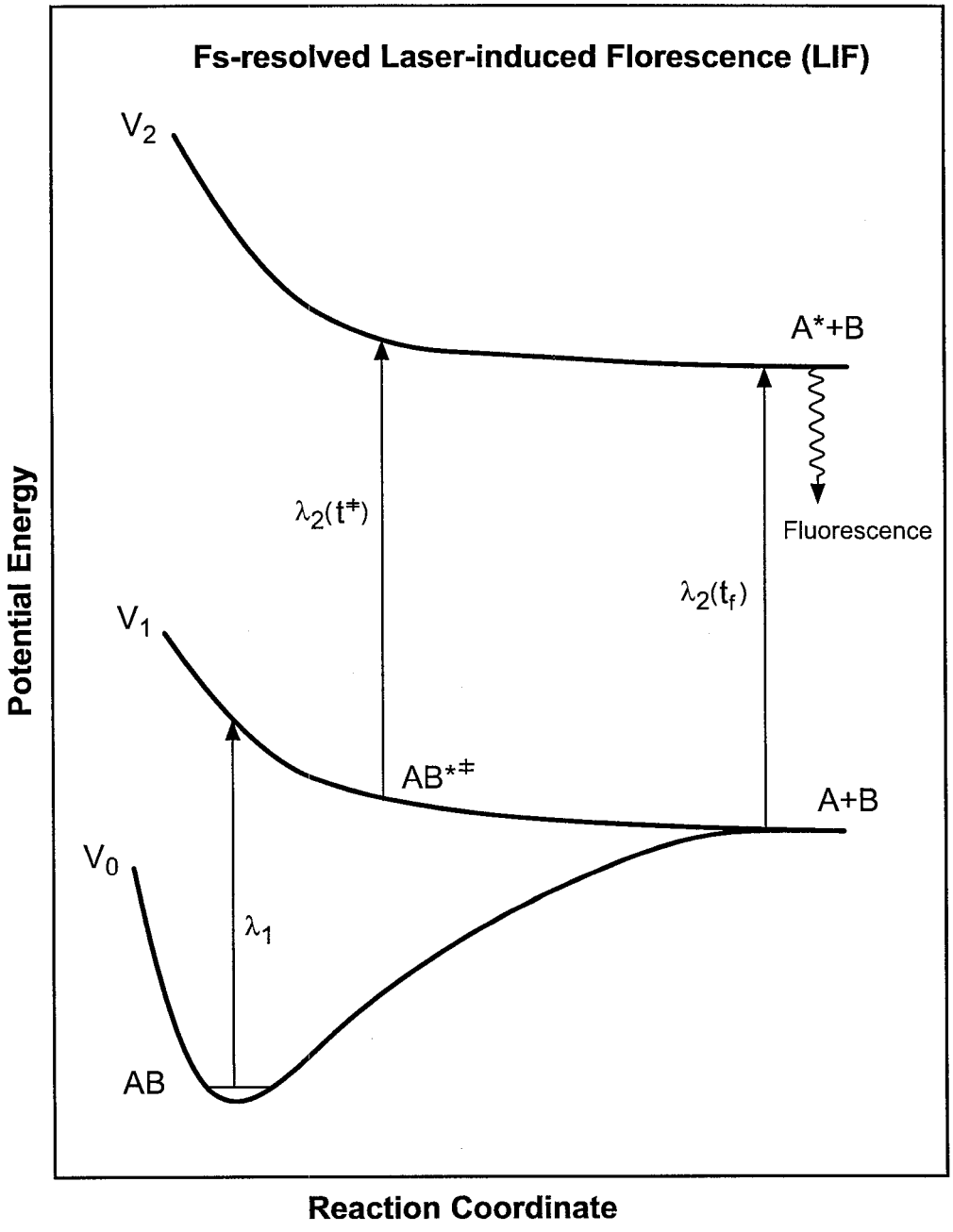
Fs-resolved Laser-induced Florescence (LIF)
V2
A*+B
λ2(t*)
Fluorescence
λ2(tf)
V1
AB*±
A+B
V0
λ1
AB
Potential Energy
Reaction Coordinate

Figure 3.2b

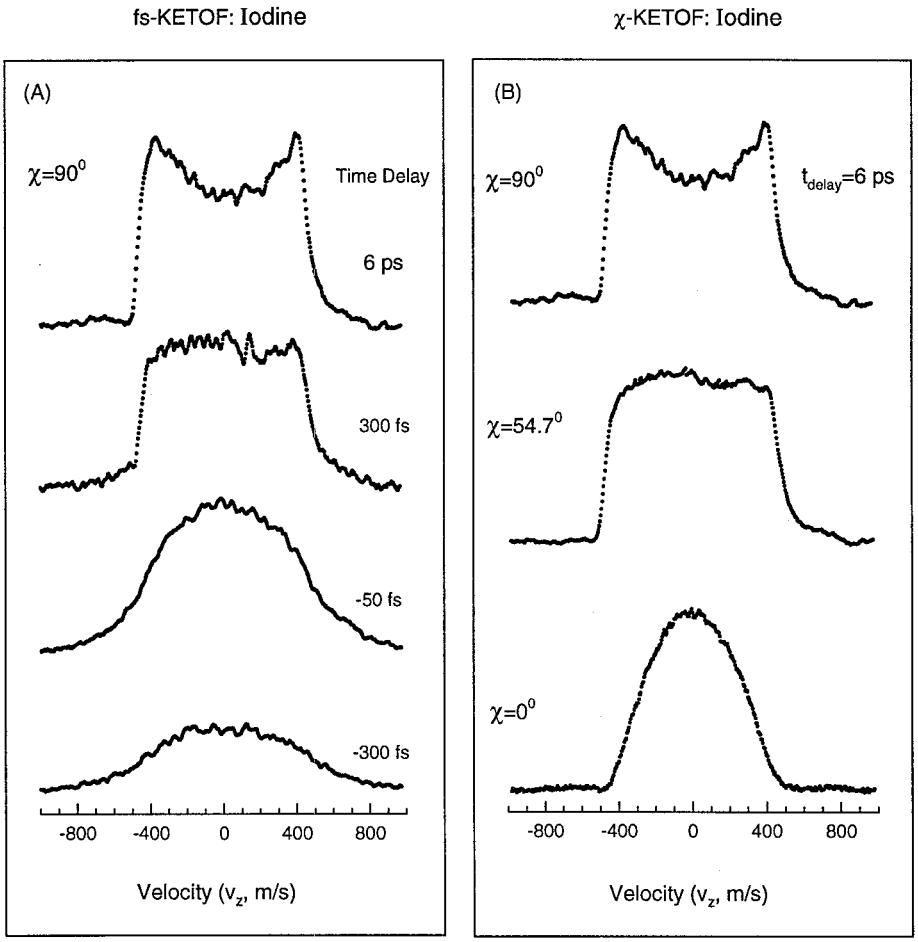
fs-KETOF: Iodine
χ-KETOF: Iodine
(A)
χ=90⁰
Time Delay
6 ps
300 fs
-50 fs
-300 fs
-800
-400
0
400
800
Velocity (v_z, m/s)
(B)
χ=90⁰
t_delay=6 ps
χ=54.7⁰
χ=0⁰
-800
-400
0
400
800
Velocity (v_z, m/s)

Figure 3.3

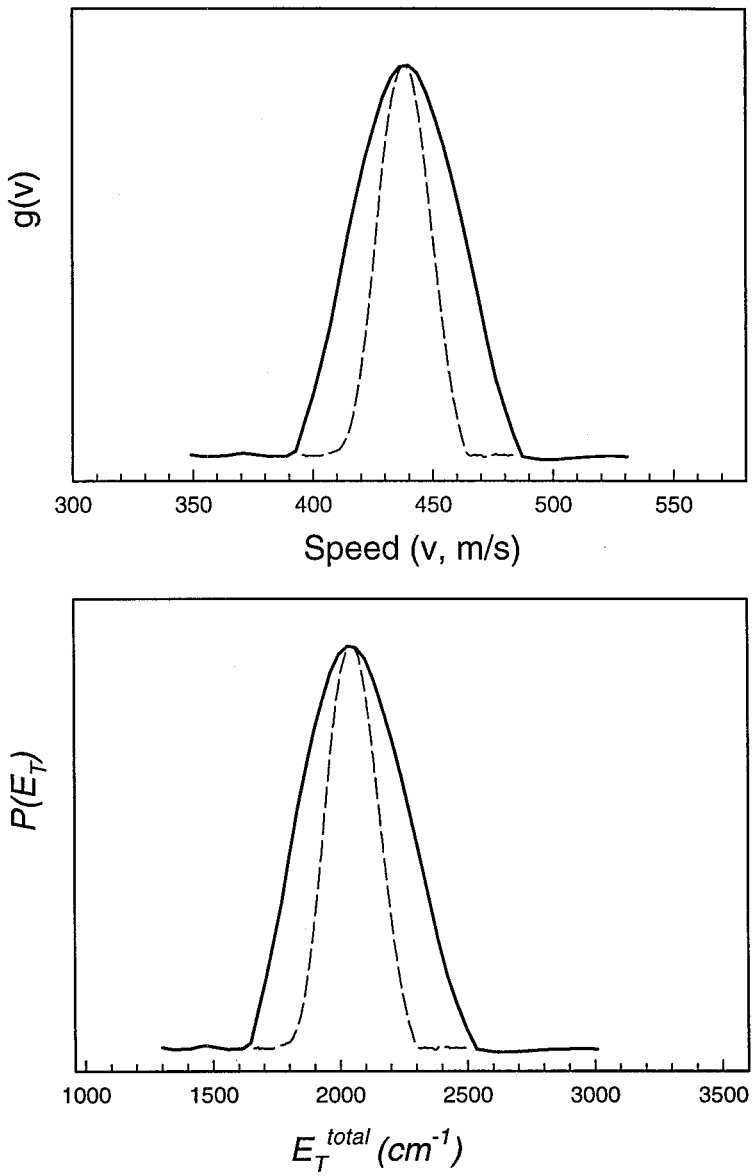
g(v)
300
350
400
450
500
550
Speed (v, m/s)
P(E_T)
1000
1500
2000
2500
3000
3500
E_T^total (cm^-1)

Figure 3.4

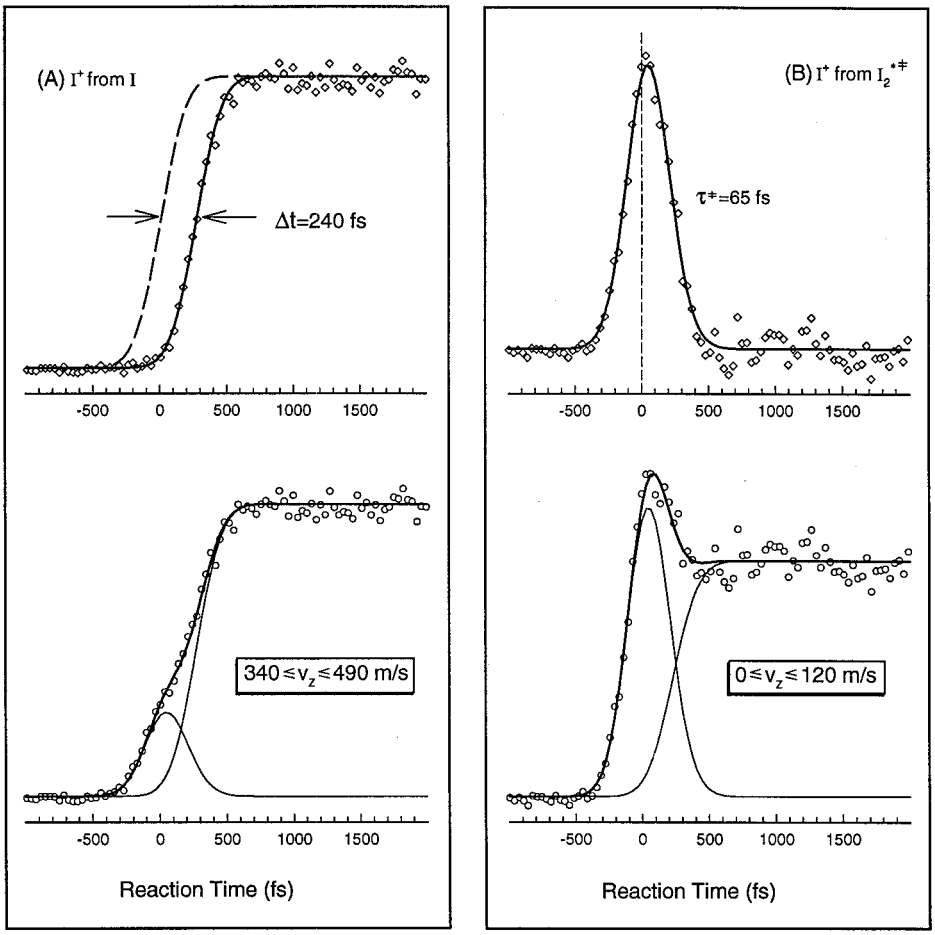
(A) I⁺ from I
Δt=240 fs
-500
0
500
1000
1500
340≤v_z≤490 m/s
Reaction Time (fs)
(B) I⁺ from I₂*‡
τ‡=65 fs
0≤v_z≤120 m/s
Reaction Time (fs)

Figure 3.5

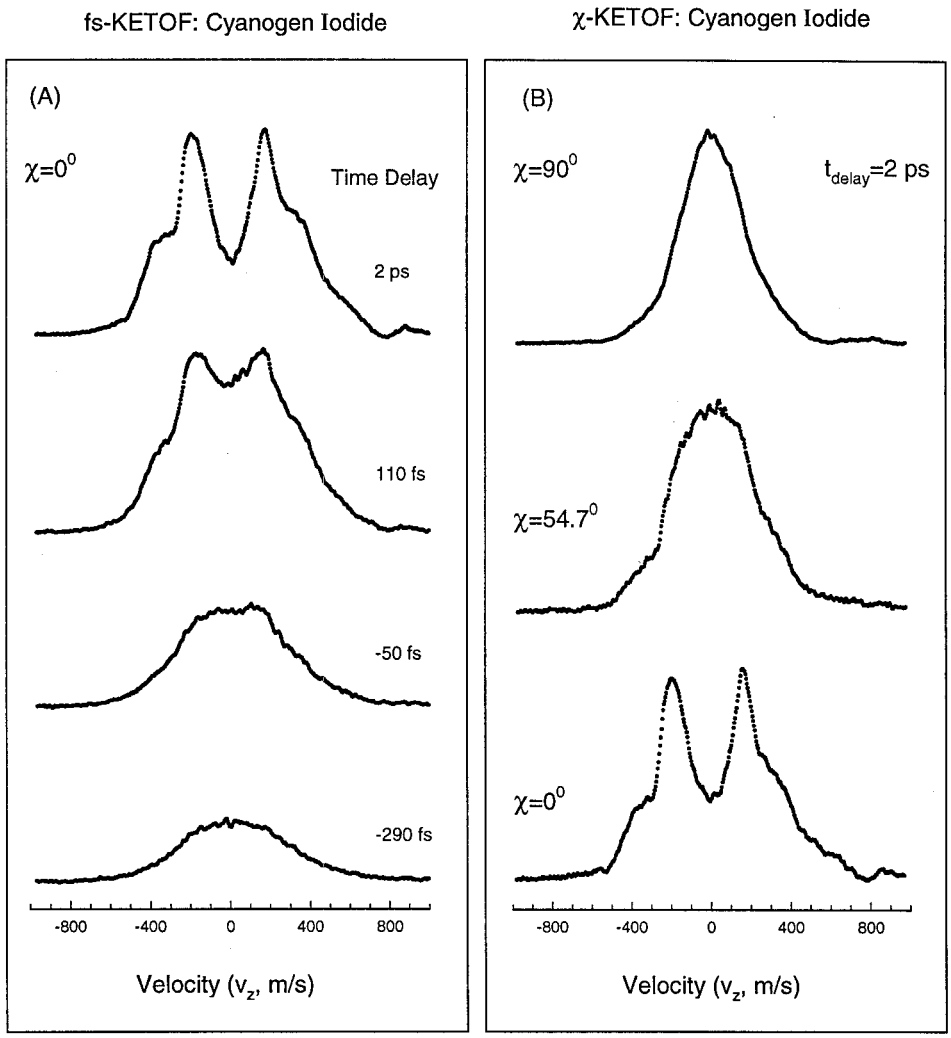
fs-KETOF: Cyanogen Iodide
χ-KETOF: Cyanogen Iodide
(A)
χ=0°
Time Delay
2 ps
110 fs
-50 fs
-290 fs
-800
-400
0
400
800
Velocity (v_z, m/s)
(B)
χ=90°
t_delay=2 ps
χ=54.7°
χ=0°
-800
-400
0
400
800
Velocity (v_z, m/s)

Figure 3.6

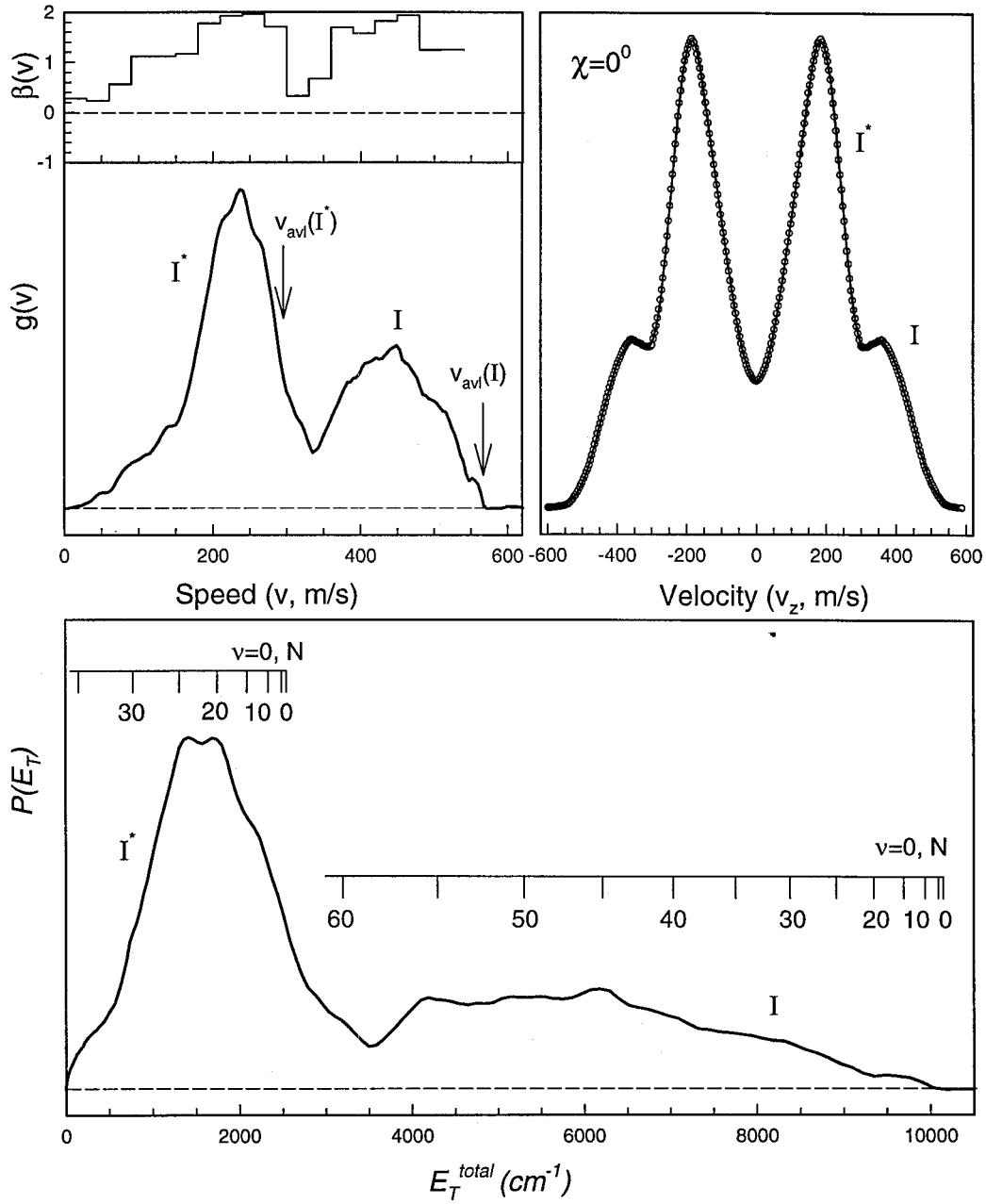
β(v)
g(v)
I*
I
v_avl(I*)
v_avl(I)
Speed (v, m/s)
χ=0°
Velocity (v_z, m/s)
P(E_T)
v=0, N
E_T^total (cm^-1)

Figure 3.7

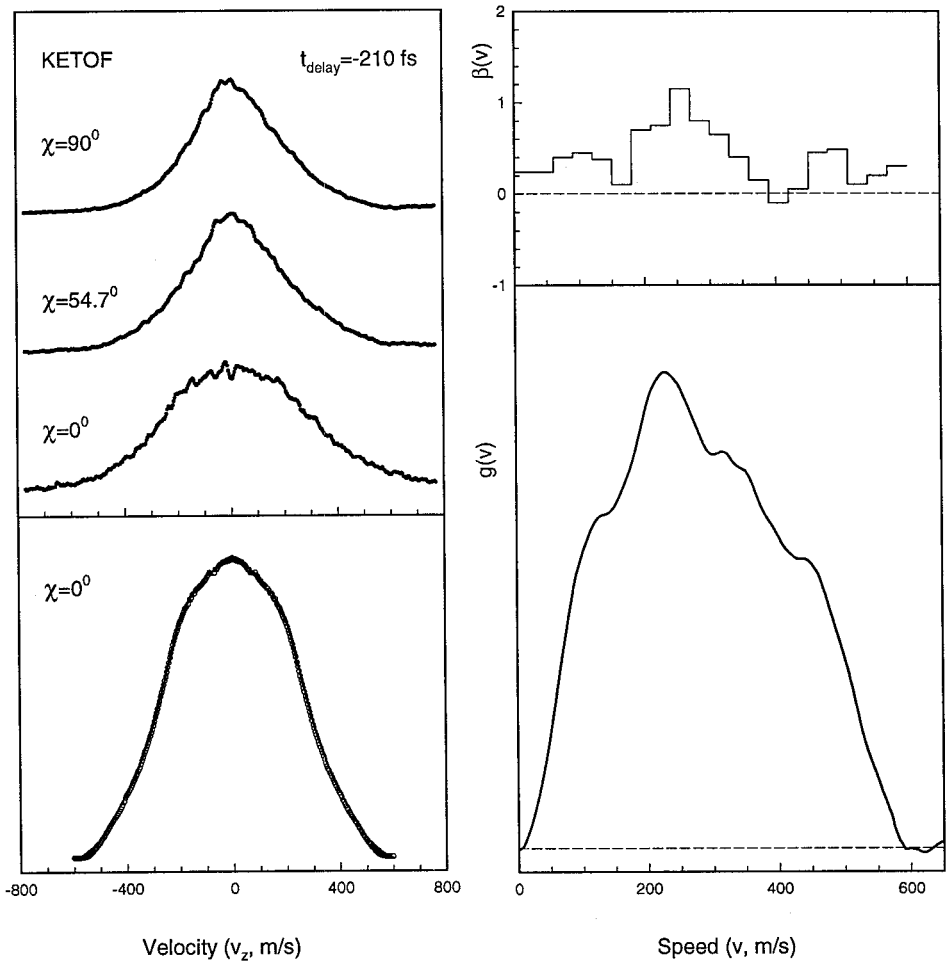
KETOF
t_{delay}=-210 fs
χ=90°
χ=54.7°
χ=0°
χ=0°
-800
-400
0
400
800
Velocity (v_z, m/s)
β(v)
2
1
0
-1
g(v)
0
200
400
600
Speed (v, m/s)

Figure 3.8

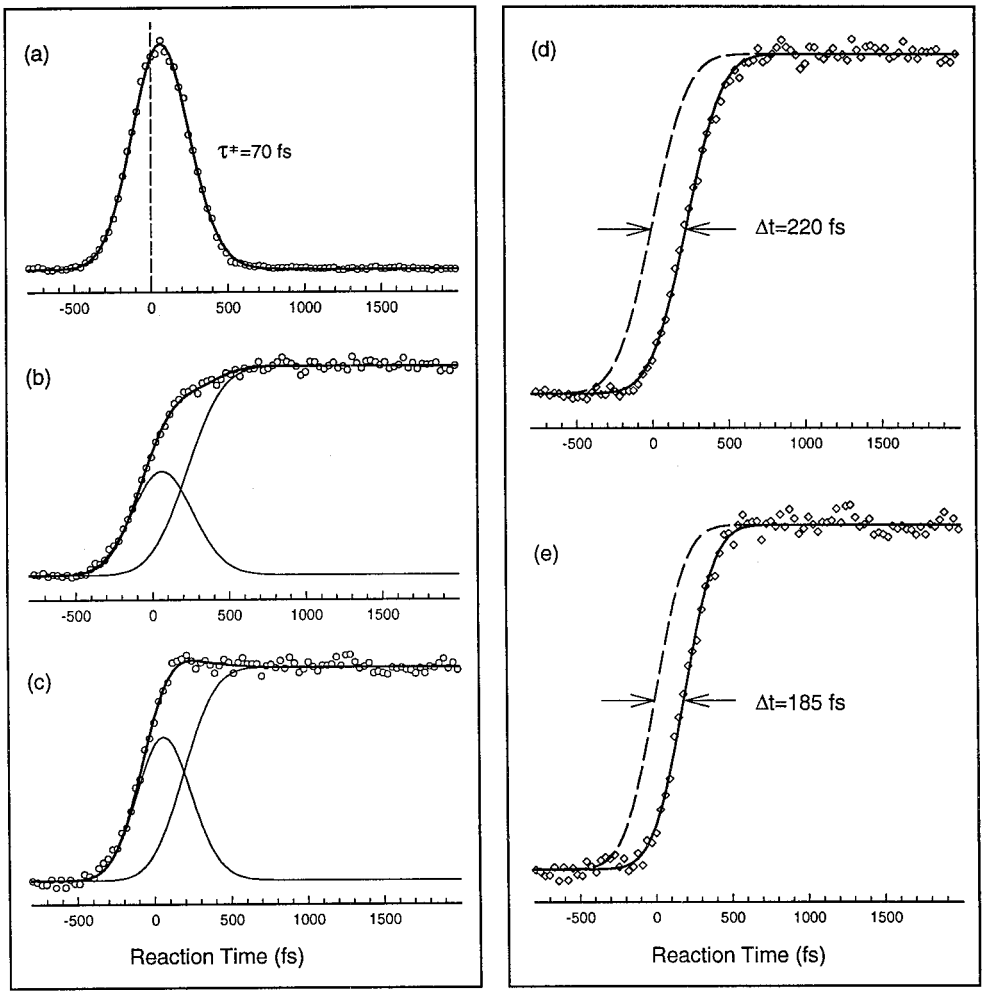
(a)
τ*=70 fs
-500
0
500
1000
1500
(b)
(c)
Reaction Time (fs)
(d)
Δt=220 fs
(e)
Δt=185 fs
Reaction Time (fs)

Figure 3.9

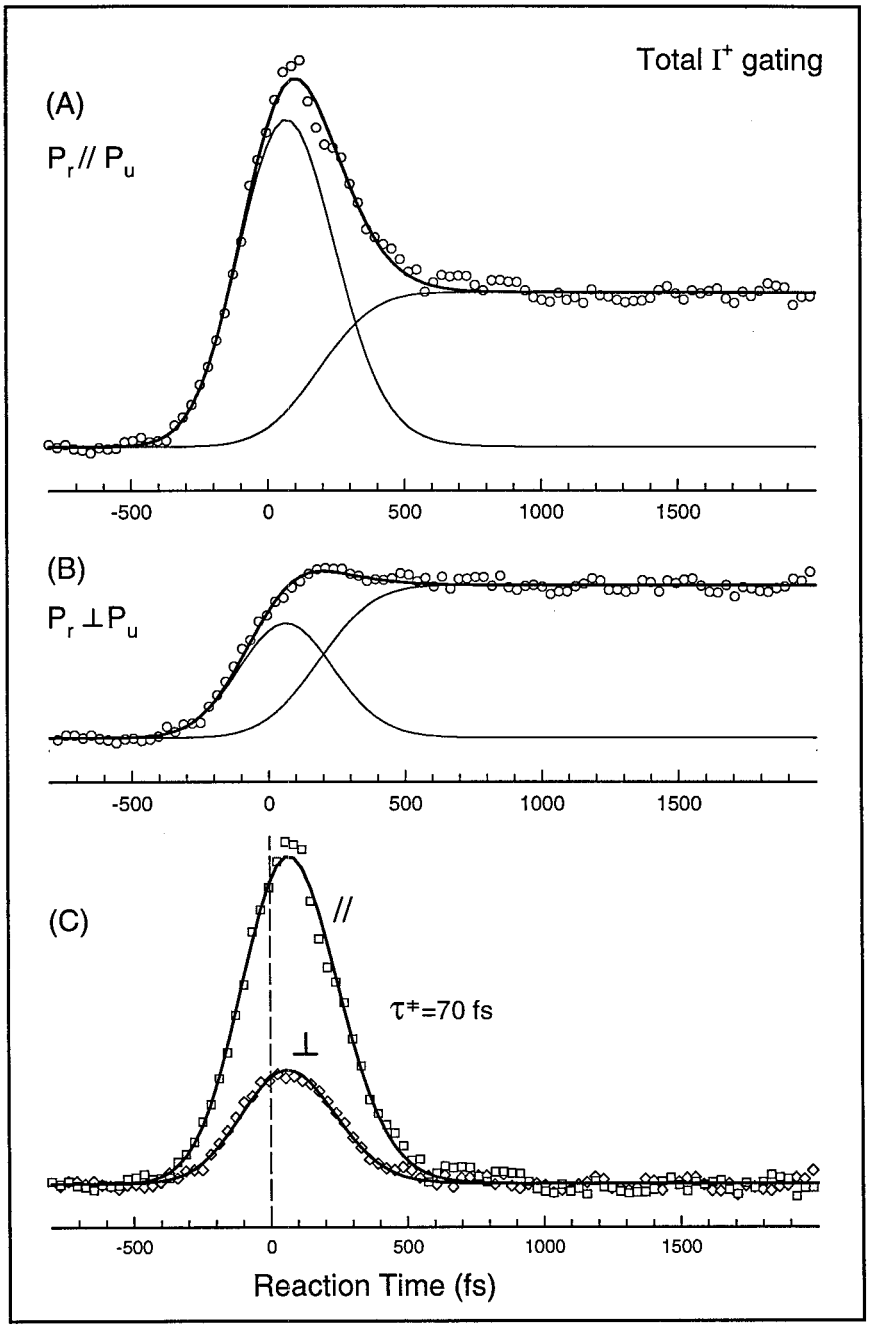
Total I+ gating
(A)
Pr// Pu
-500
0
500
1000
1500
(B)
Pr ⊥Pu
-500
0
500
1000
1500
(C)
//
τ*=70 fs
⊥
-500
0
500
1000
1500
Reaction Time (fs)

Figure 3.10

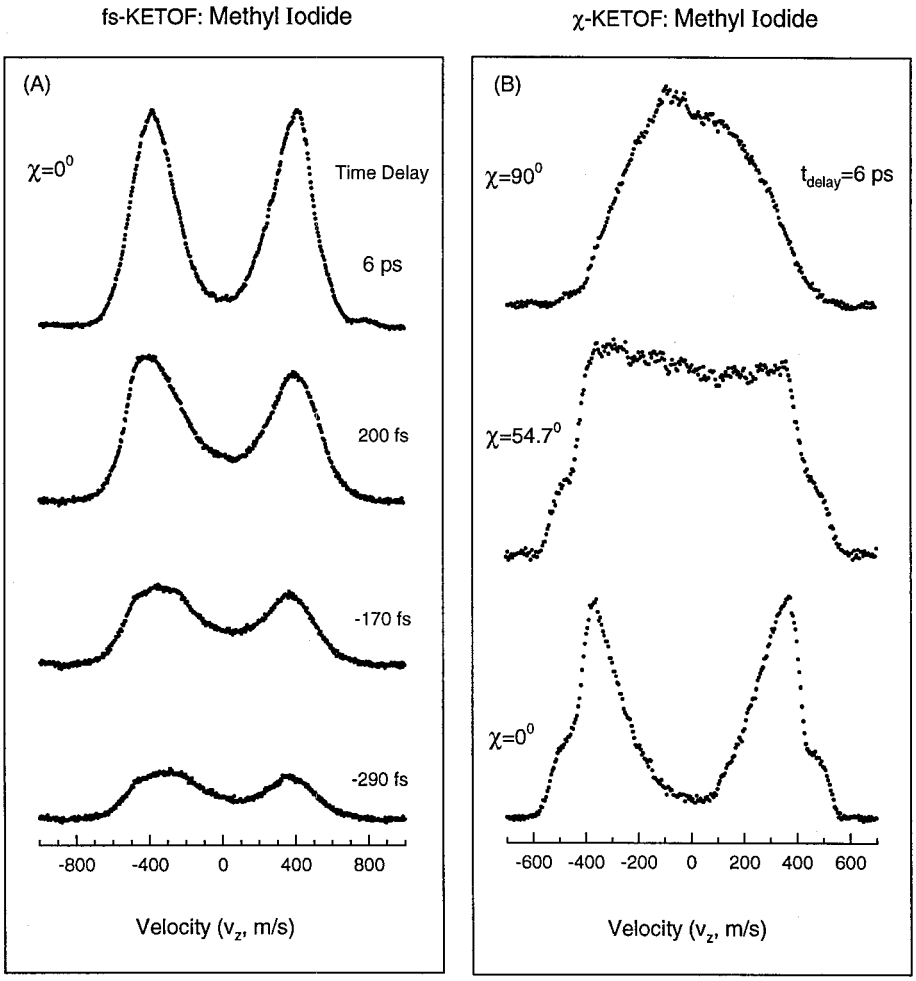
fs-KETOF: Methyl Iodide
χ-KETOF: Methyl Iodide
(A)
χ=0⁰
Time Delay
6 ps
200 fs
-170 fs
-290 fs
-800 -400 0 400 800
Velocity (v_z, m/s)
(B)
χ=90⁰
t_delay=6 ps
χ=54.7⁰
χ=0⁰
-600 -400 -200 0 200 400 600
Velocity (v_z, m/s)

Figure 3.11

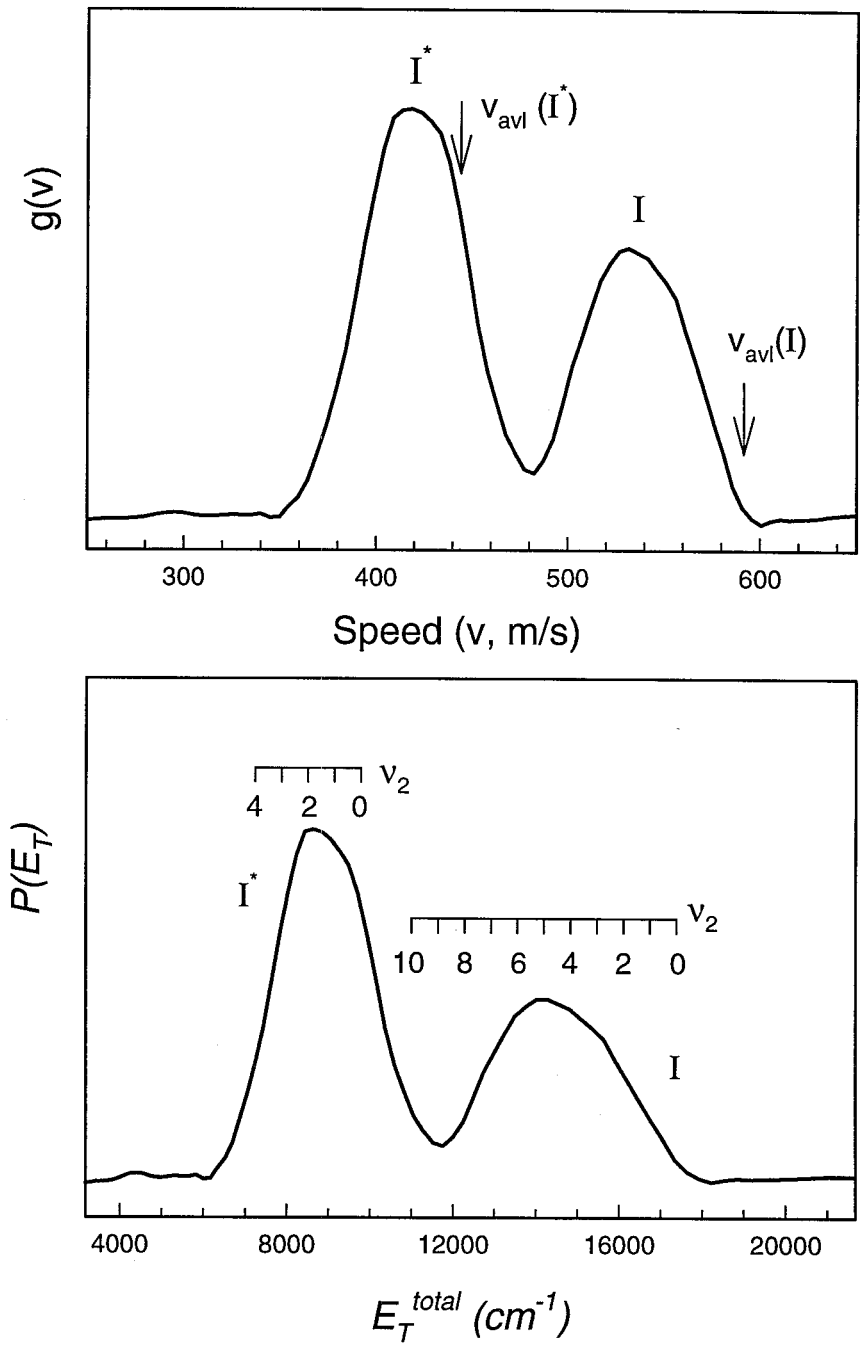
I*
v_{avl} (I*)
I
v_{avl}(I)
g(v)
300
400
500
600
Speed (v, m/s)
ν_2
4 2 0
I*
ν_2
10 8 6 4 2 0
I
$P(E_T)$
4000
8000
12000
16000
20000
E_T^{total} (cm^{-1})

Figure 3.12

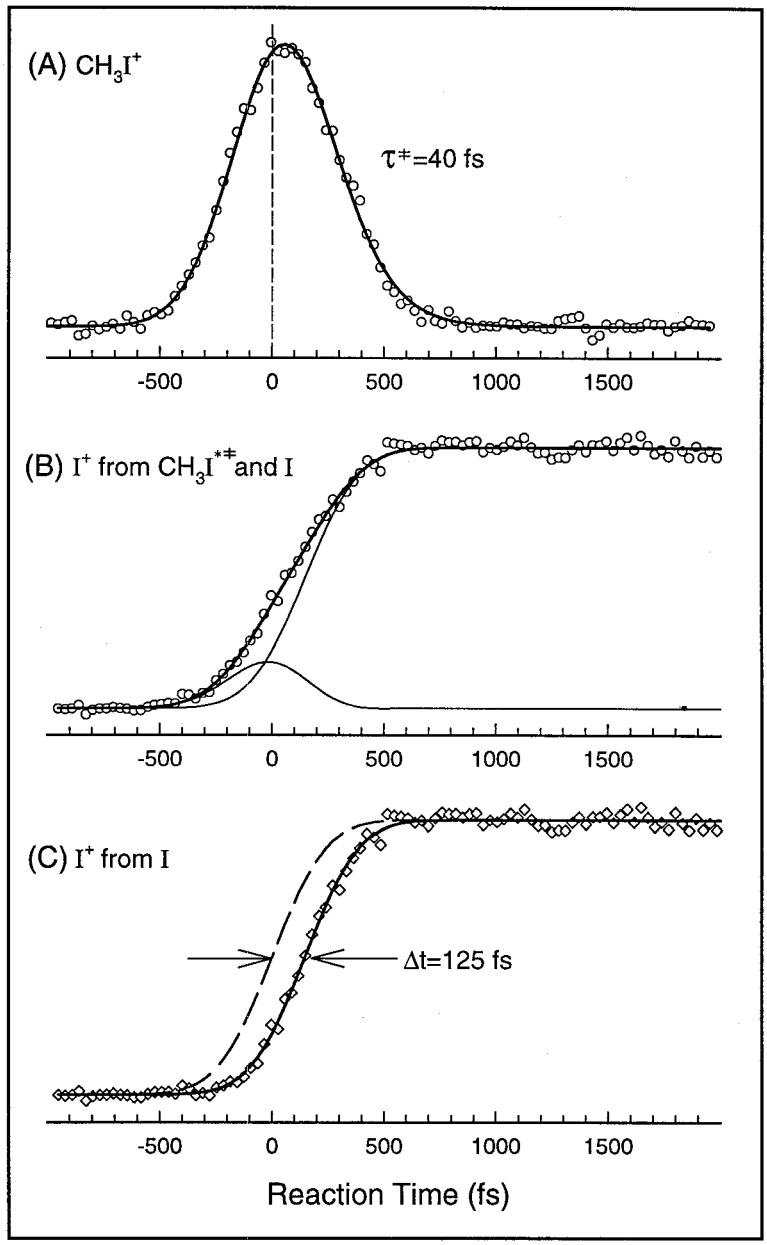
(A) CH_3I^+
$\tau^{\ddagger}$=40 fs
-500
0
500
1000
1500
(B) I^+ from $CH_3I^{*\ddagger}$ and I
-500
0
500
1000
1500
(C) I^+ from I
Δt=125 fs
-500
0
500
1000
1500
Reaction Time (fs)

Figure 3.13

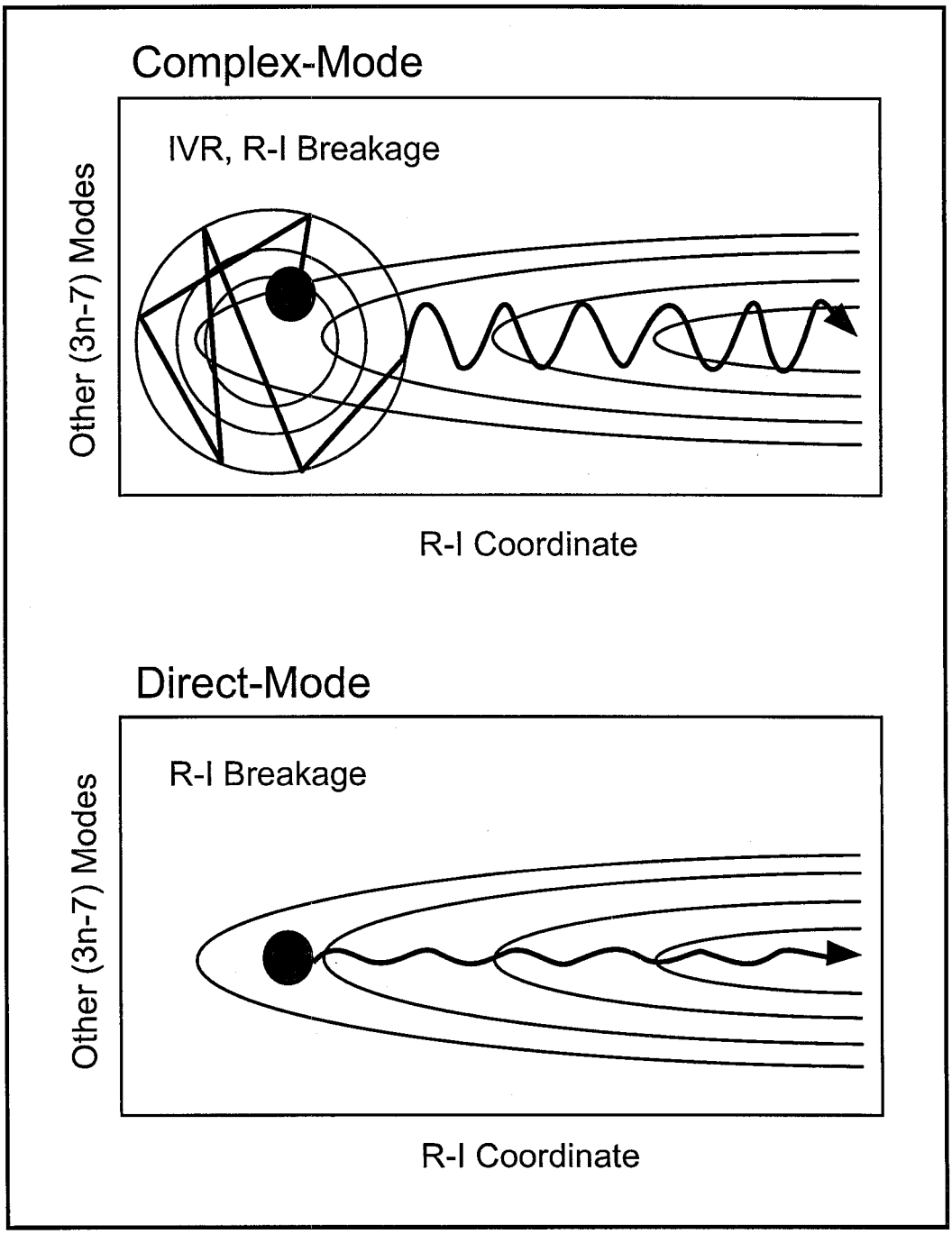
Complex-Mode
IVR, R-I Breakage
Other (3n-7) Modes
R-I Coordinate
Direct-Mode
R-I Breakage
Other (3n-7) Modes
R-I Coordinate

Figure 3.14

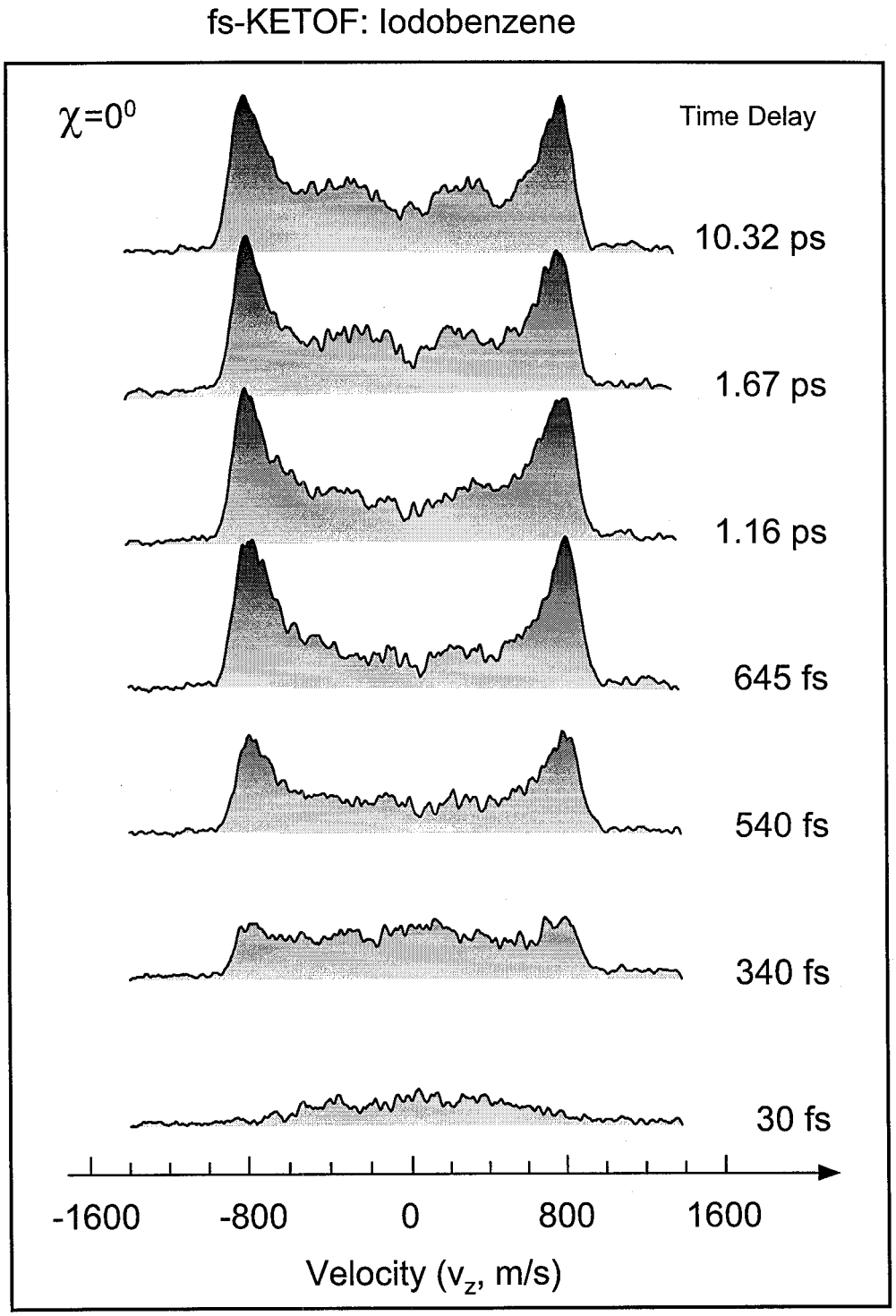
fs-KETOF: Iodobenzene
χ=0⁰
Time Delay
10.32 ps
1.67 ps
1.16 ps
645 fs
540 fs
340 fs
30 fs
-1600
-800
0
800
1600
Velocity (v_z, m/s)

Figure 3.15

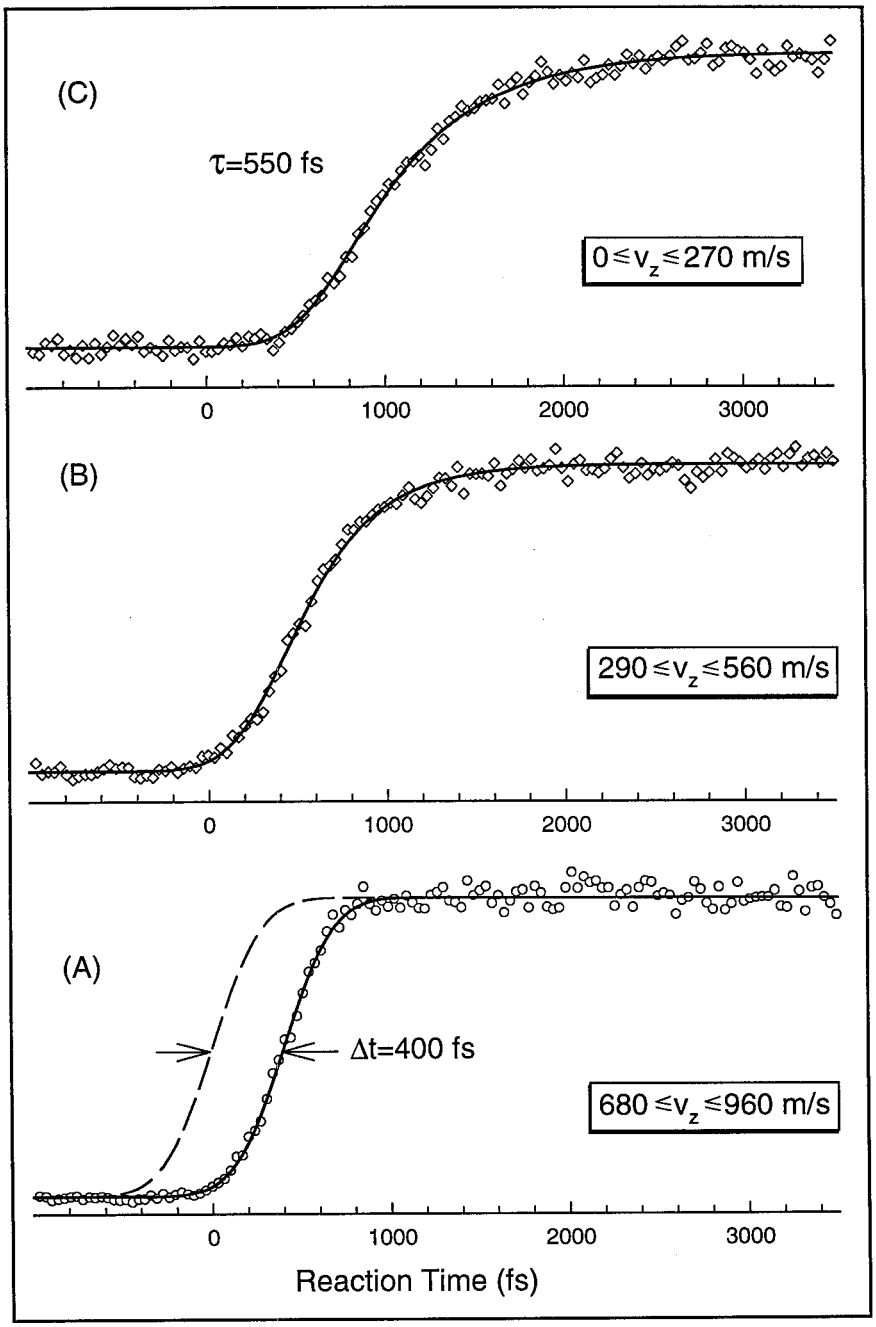
(C)
τ=550 fs
0≤v_z≤270 m/s
0
1000
2000
3000
(B)
290≤v_z≤560 m/s
0
1000
2000
3000
(A)
Δt=400 fs
680≤v_z≤960 m/s
0
1000
2000
3000
Reaction Time (fs)

Figure 3.16

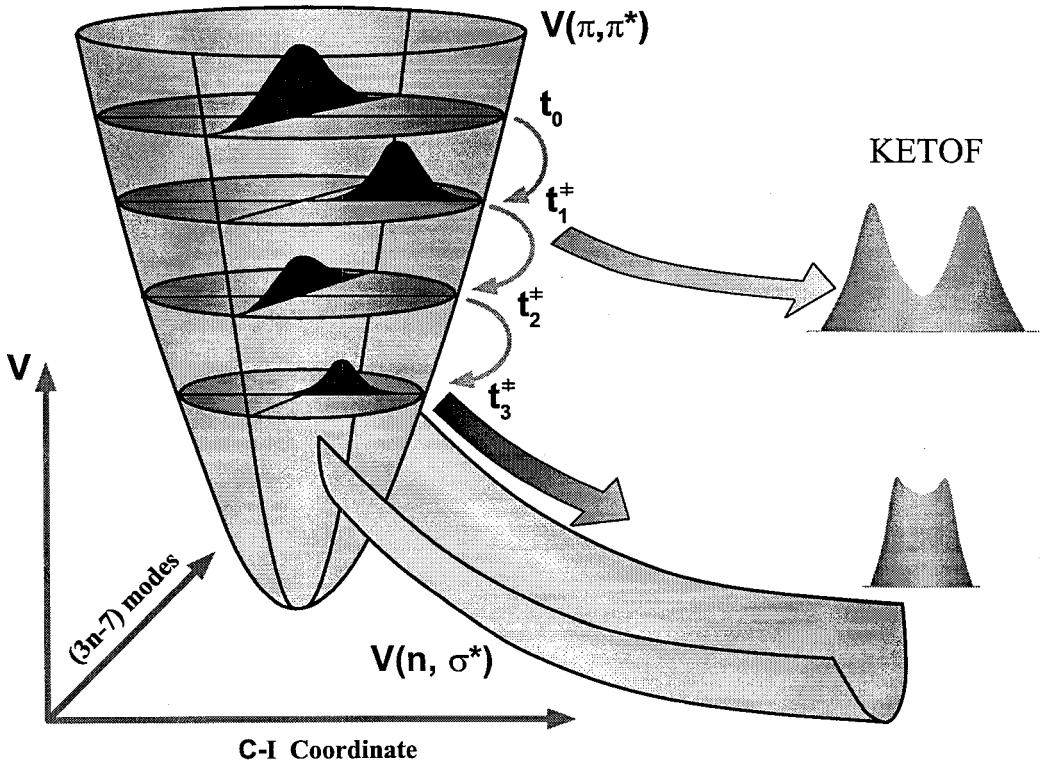

Figure 3.17

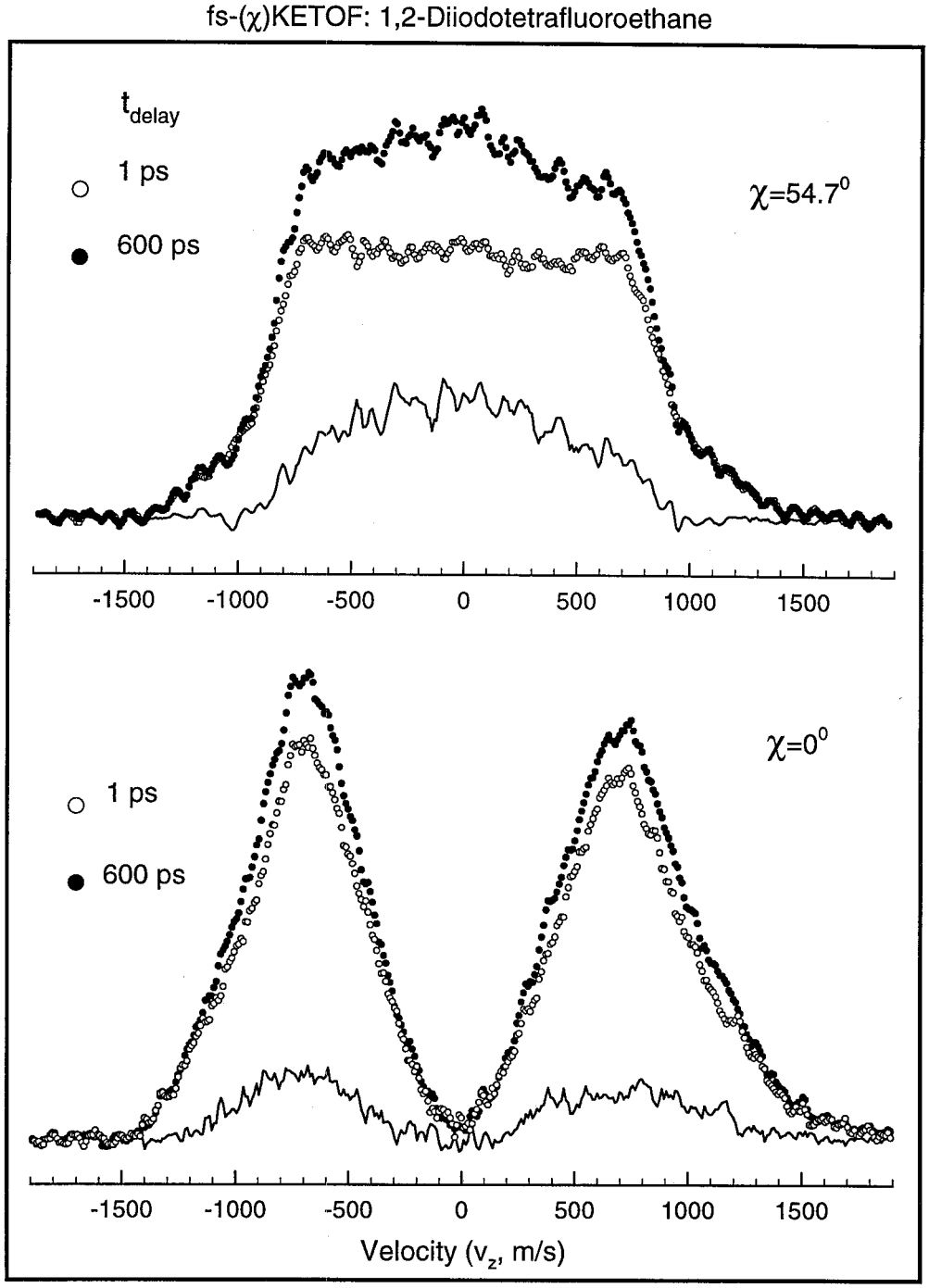
fs-(χ)KETOF: 1,2-Diiodotetrafluoroethane
t_{delay}
1 ps
600 ps
χ=54.7°
-1500
-1000
-500
0
500
1000
1500
χ=0°
1 ps
600 ps
-1500
-1000
-500
0
500
1000
1500
Velocity (v_z, m/s)

Figure 3.18

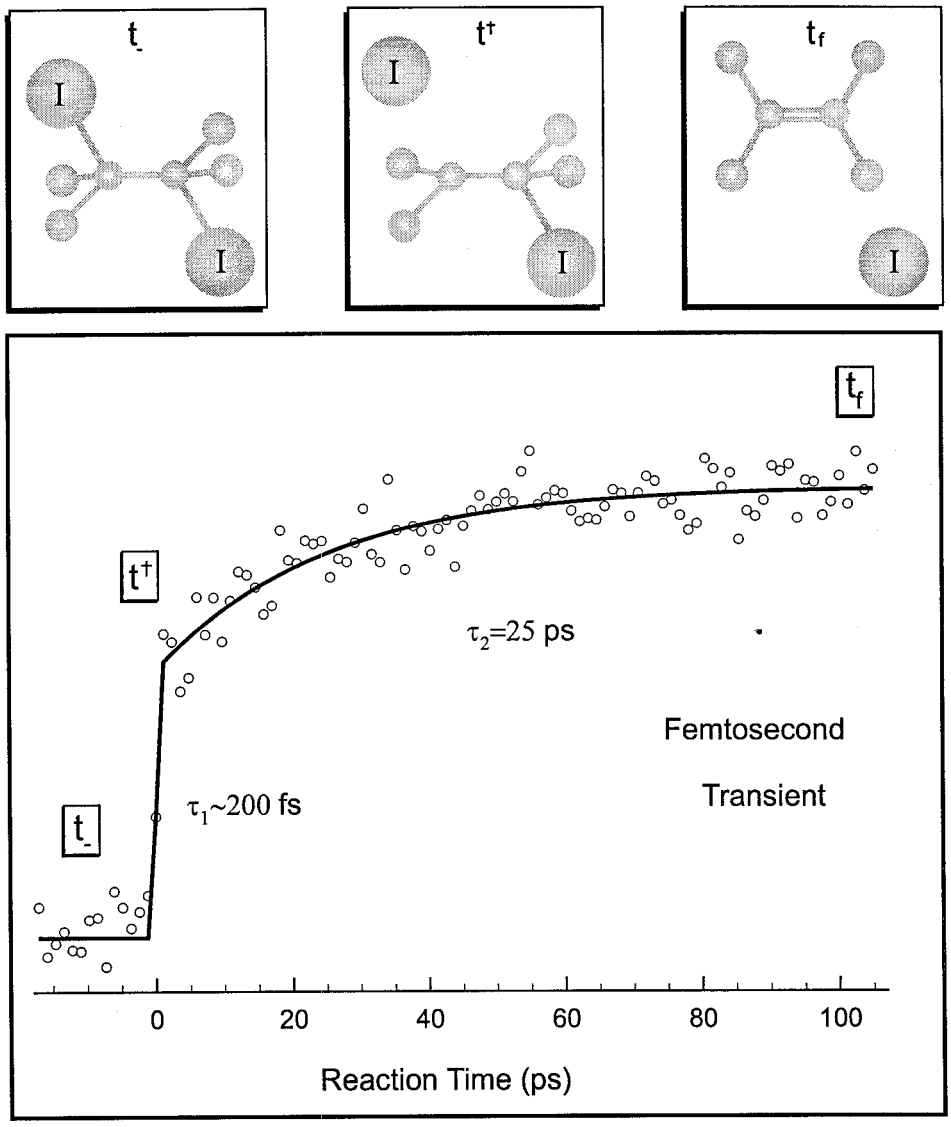
t-
I
I
t†
I
I
tf
I
tf
t†
t-
τ2=25 ps
τ1~200 fs
Femtosecond
Transient
0
20
40
60
80
100
Reaction Time (ps)

Figure 3.19

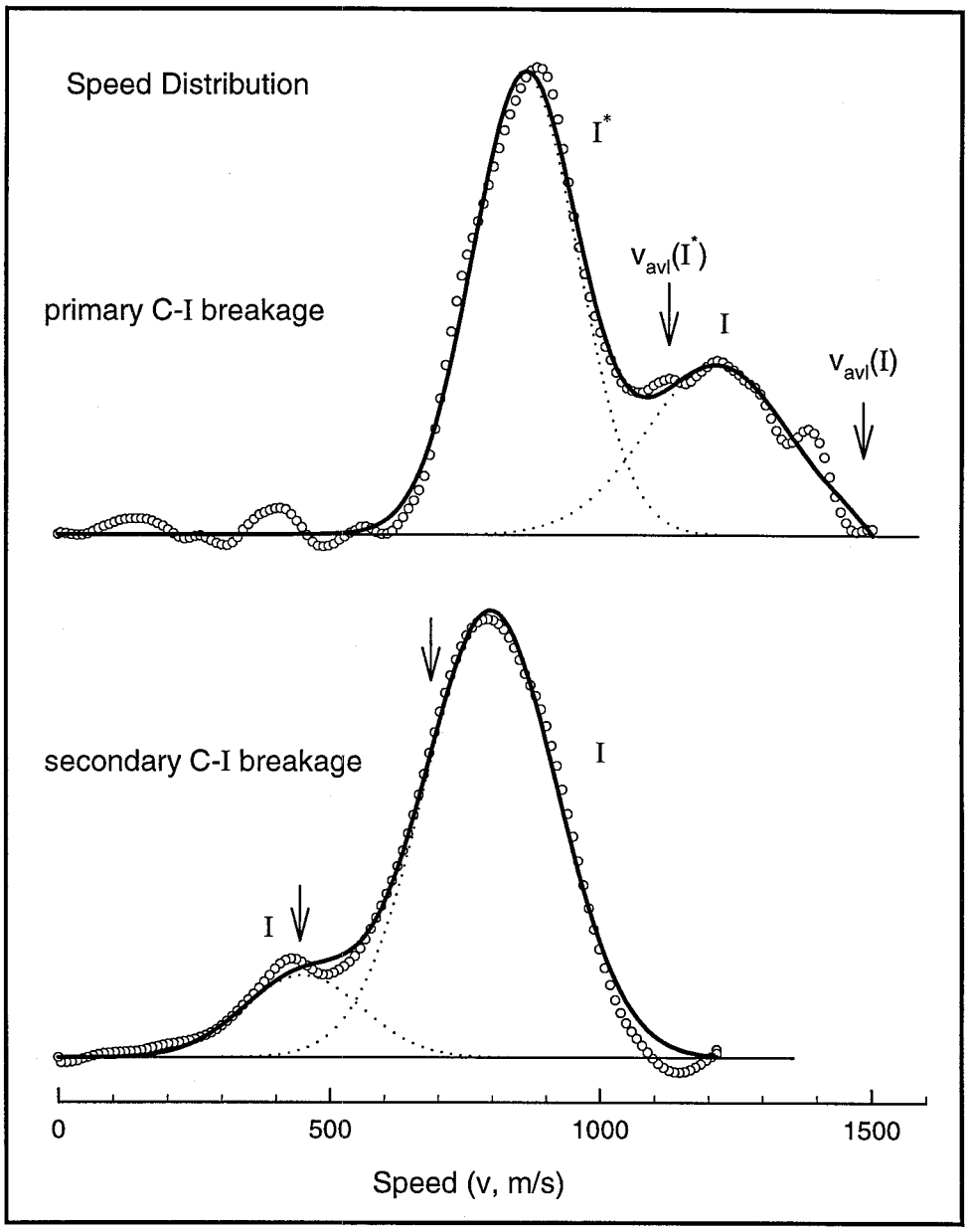
Speed Distribution
primary C-I breakage
I*
v_avl(I*)
I
v_avl(I)
secondary C-I breakage
I
I
0
500
1000
1500
Speed (v, m/s)

Figure 3.20a

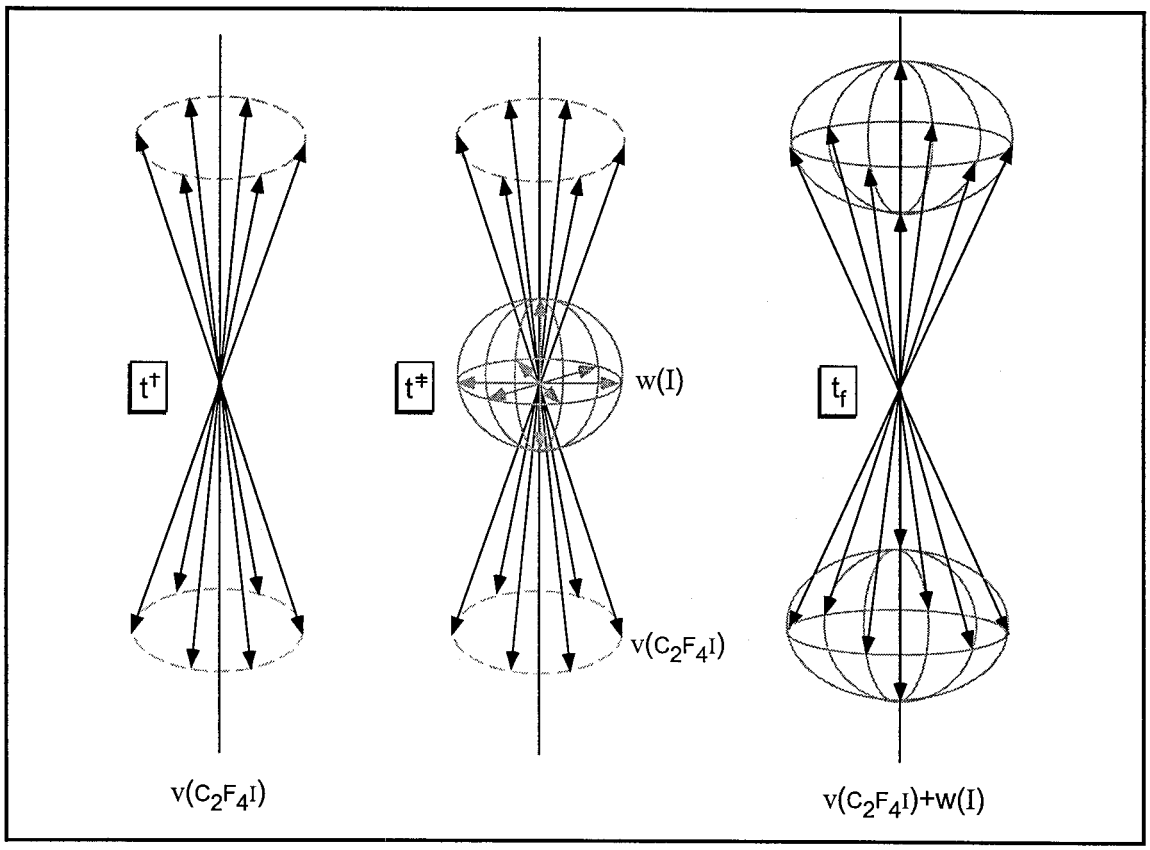

Figure 3.20b

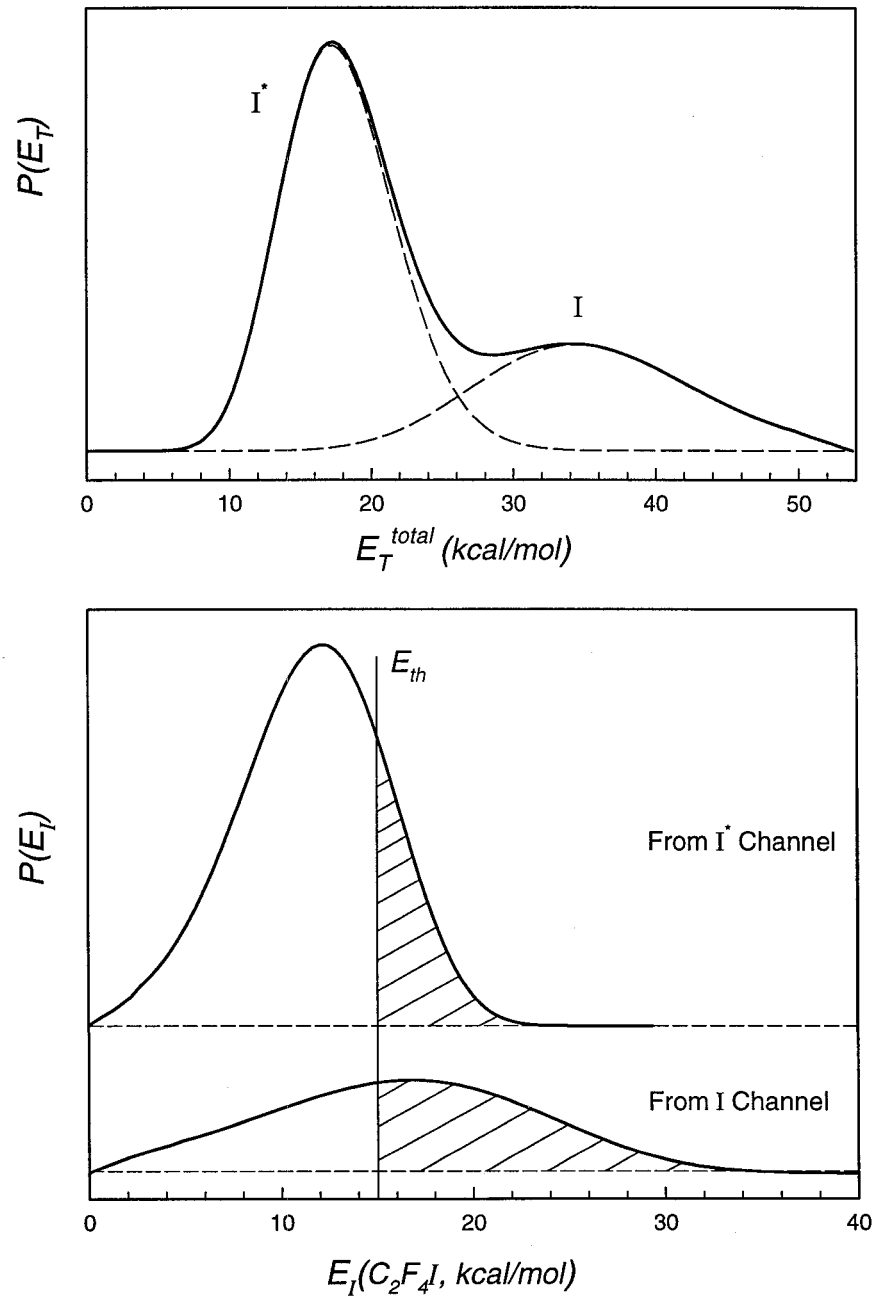
P(E_T)
I*
I
0
10
20
30
40
50
E_T^total (kcal/mol)
P(E_I)
E_th
From I* Channel
From I Channel
0
10
20
30
40
E_I(C_2F_4I, kcal/mol)

Figure 3.20c

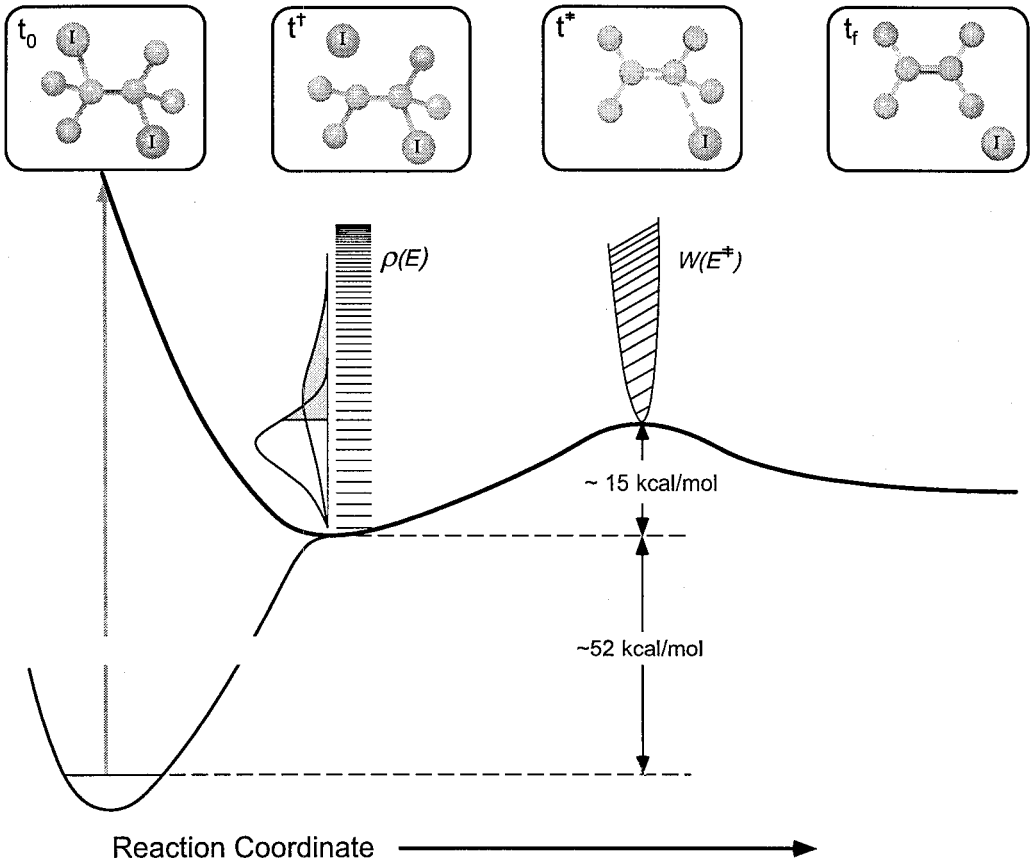
t_0
$t^\dagger$
t^*
t_f
I
$\rho(E)$
$W(E^*)$
~ 15 kcal/mol
~52 kcal/mol
Reaction Coordinate

Figure 3.21

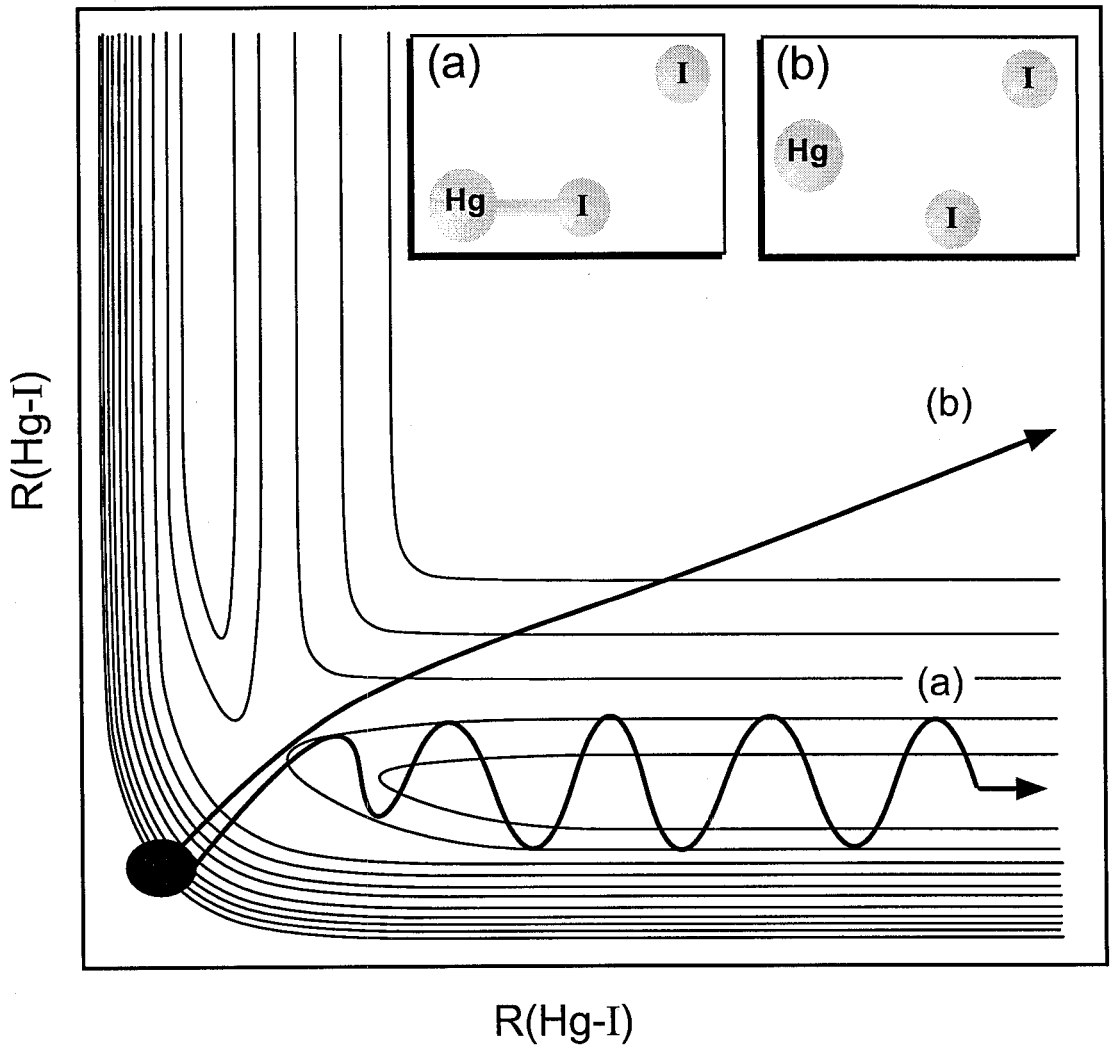

Figure 3.22

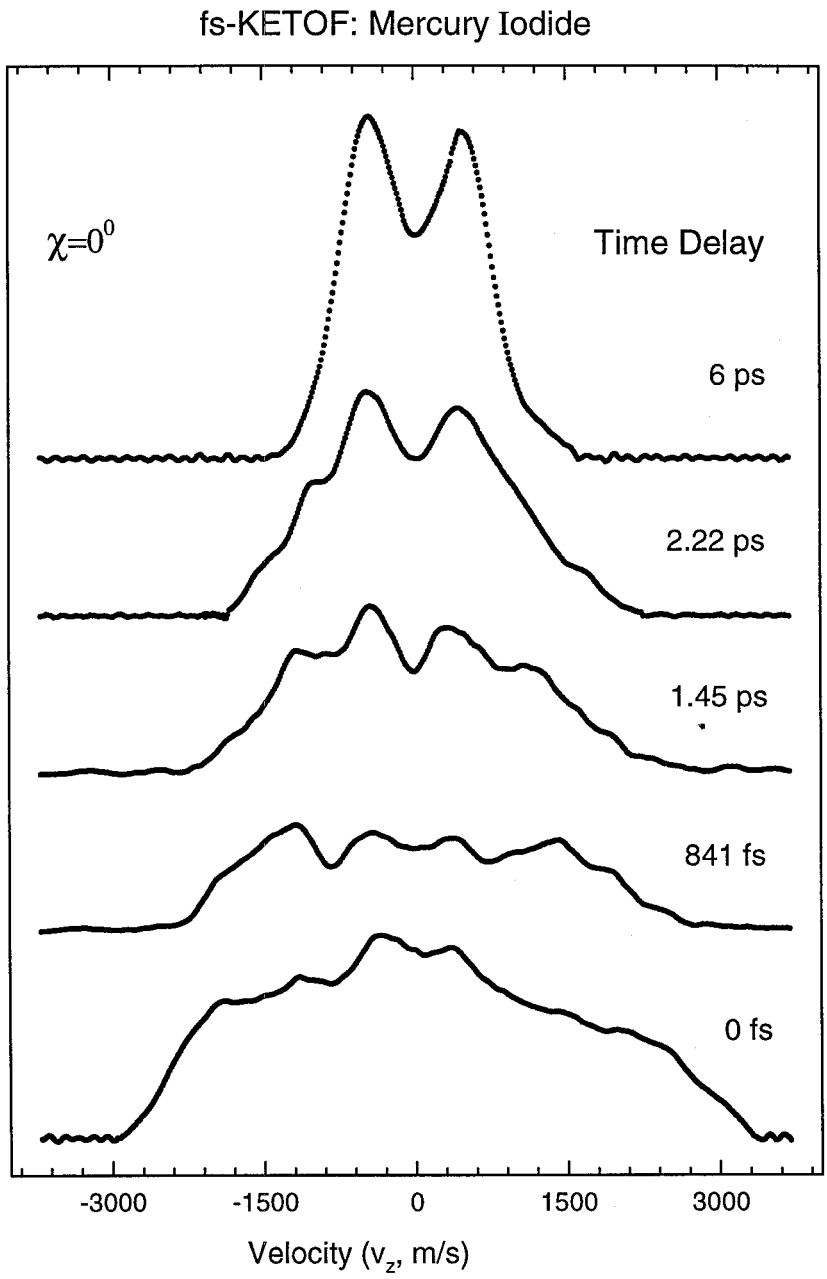
fs-KETOF: Mercury Iodide
χ=0⁰
Time Delay
6 ps
2.22 ps
1.45 ps
841 fs
0 fs
-3000
-1500
0
1500
3000
Velocity (v_z, m/s)

Figure 3.23

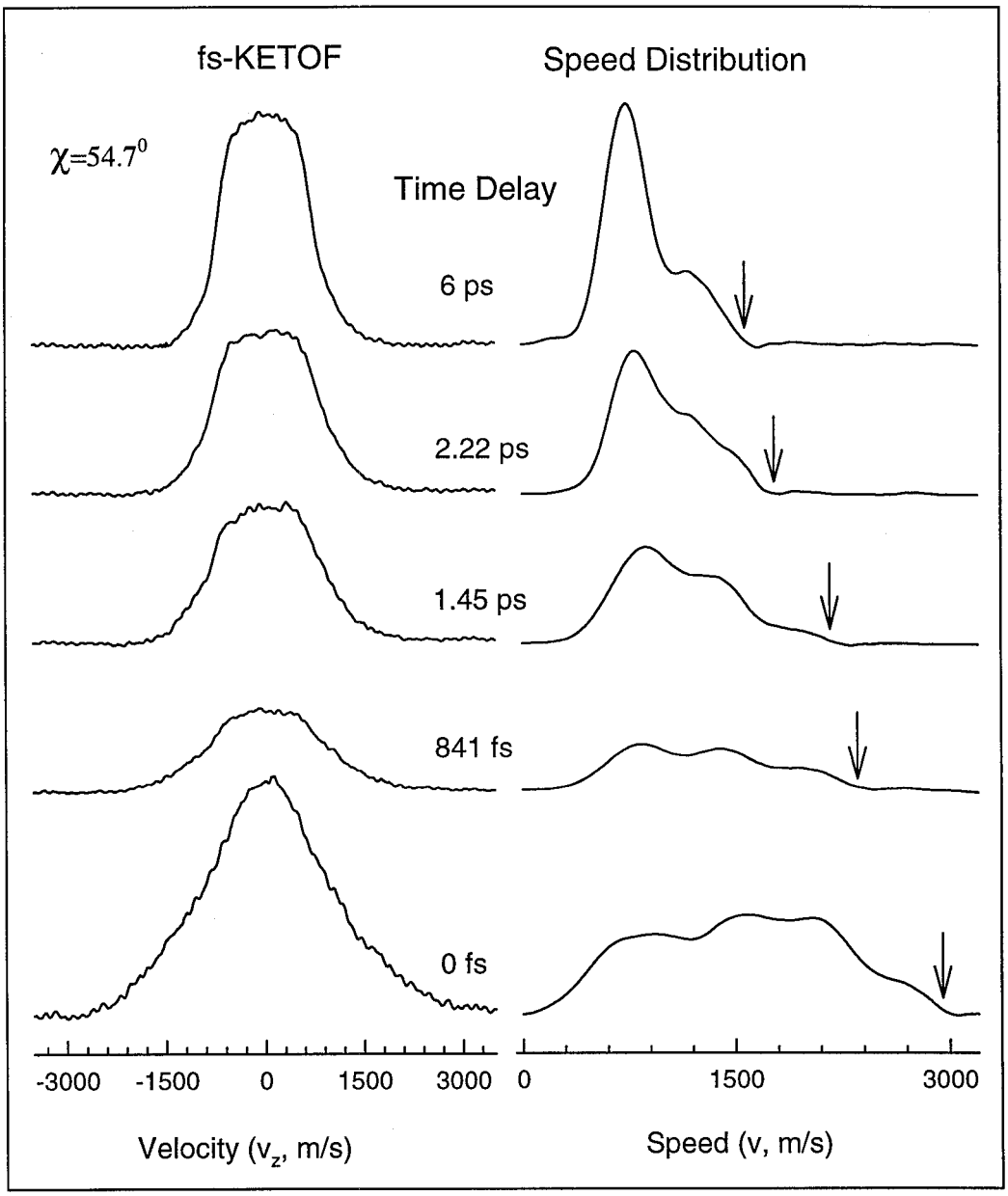
fs-KETOF
Speed Distribution
χ=54.7⁰
Time Delay
6 ps
2.22 ps
1.45 ps
841 fs
0 fs
-3000
-1500
0
1500
3000
0
1500
3000
Velocity (v_z, m/s)
Speed (v, m/s)

Figure 3.24

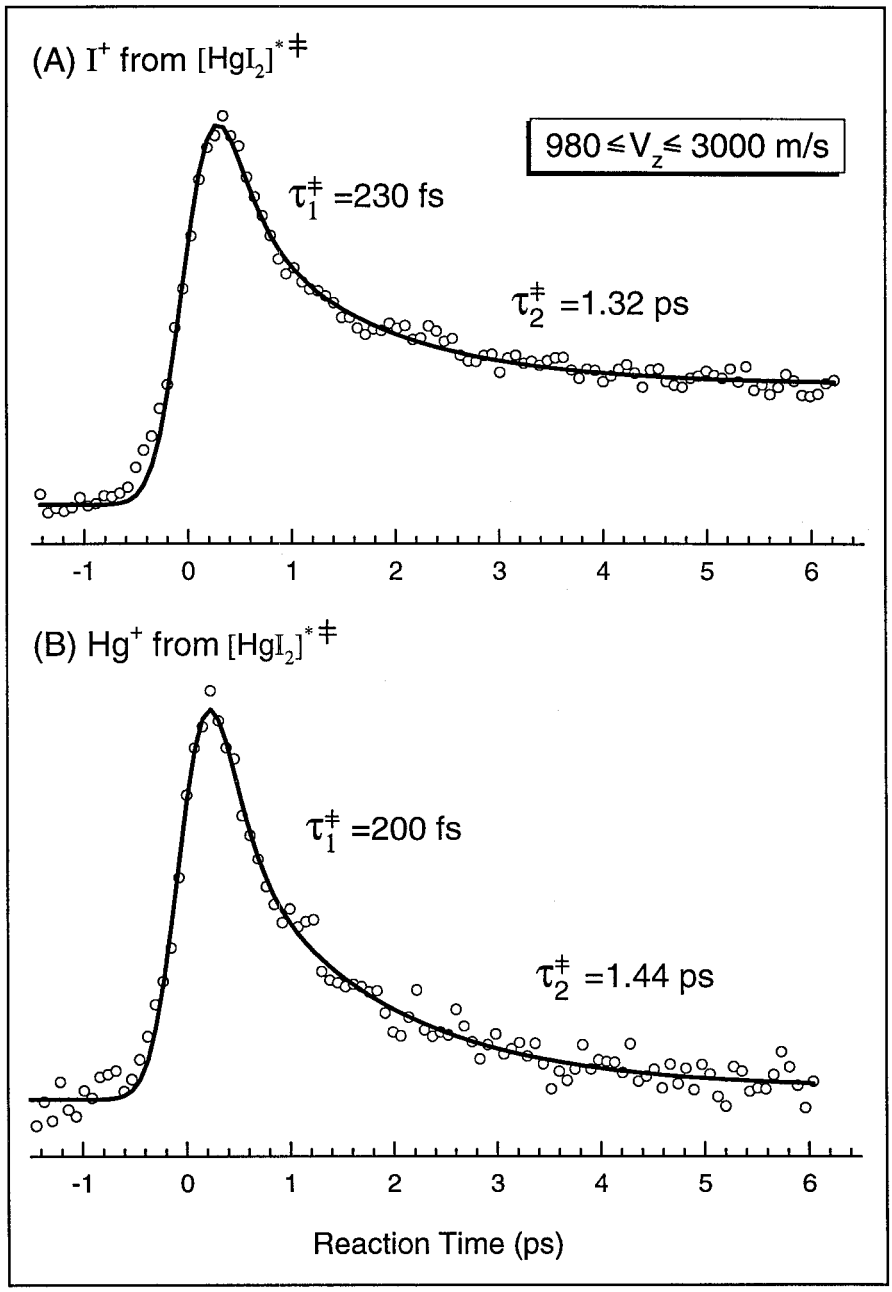
(A) I^+ from $[HgI_2]^{*\ddagger}$
980 ≤ V_z ≤ 3000 m/s
$\tau_1^{\ddagger}$ =230 fs
$\tau_2^{\ddagger}$ =1.32 ps
-1
0
1
2
3
4
5
6
(B) Hg^+ from $[HgI_2]^{*\ddagger}$
$\tau_1^{\ddagger}$ =200 fs
$\tau_2^{\ddagger}$ =1.44 ps
-1
0
1
2
3
4
5
6
Reaction Time (ps)

Figure 3.25

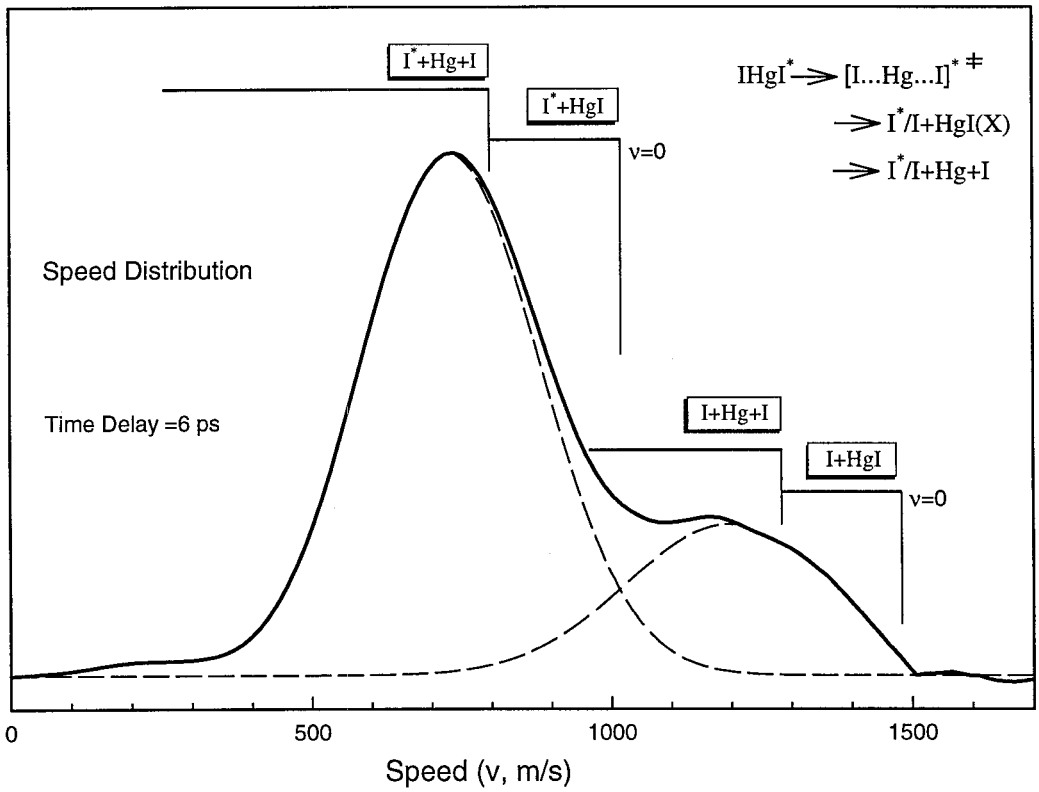
I*+Hg+I
I*+HgI
v=0
IHgI* → [I...Hg...I]* ≠
→ I*/I+HgI(X)
→ I*/I+Hg+I
Speed Distribution
Time Delay =6 ps
I+Hg+I
I+HgI
v=0
0
500
1000
1500
Speed (v, m/s)

Figure 3.26

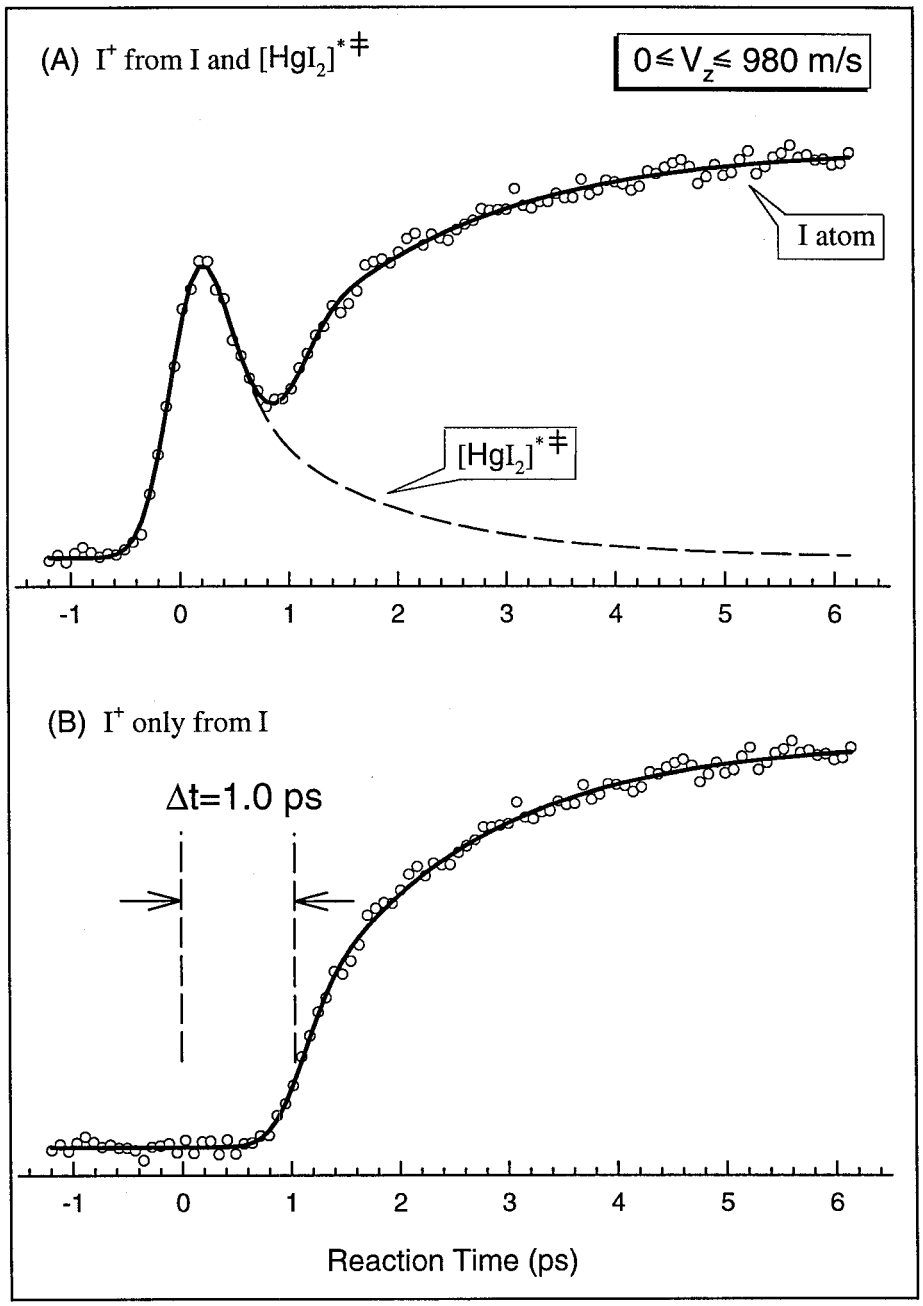
(A) I+ from I and [HgI2]*‡
0≤Vz≤ 980 m/s
I atom
[HgI2]*‡
-1
0
1
2
3
4
5
6
(B) I+ only from I
Δt=1.0 ps
-1
0
1
2
3
4
5
6
Reaction Time (ps)

Figure 3.27

Chapter 4

Femtosecond Real-Time Probing of Bimolecular Reactions: Direct Observation of Transition-State Dynamics and Structure in Charge-Transfer Reactions[‡]

[‡] Adapted from: P.Y. Cheng, D. Zhong and A.H. Zewail, J. Chem. Phys. **103** (1995) 5153-5156; **105** (1996) 6216-6248.

4.1. Introduction

Charge-transfer (CT) reactions play a central role in many areas of chemistry and biology. Common to all CT reactions is the coupling between ionic and covalent (neutral) configurations which establishes a unique transition state. The transition state is a hybrid of these ionic and covalent structures with an ultrafast interconversion (usually less than a picosecond), accompanied by bond breakage and bond formation. A generic description of bimolecular charge-transfer reactions of $A+BC$ (A^*+BC) is illustrated schematically in Fig. 4.1.

In the entrance channel the system converts from being covalent to being ionic in nature by utilizing the harpooning mechanism at long internuclear separations. The near degeneracy of the covalent and ionic energies facilitates such transformation, even at the long distances of 5-10 Å (entrance channel). In the transition state, the CT establishes the structure $[A^{+}\cdots{}^{-}BC]$ over a range of distances. Ultimately, in the exit channel, the transition state (TS) either continues on the adiabatic harpoon potential, utilizing the coulomb attraction to form $A^{+}B^{-}+C$, or searches for the covalent channel of $AB+C$. The elementary steps involved are:

$$A + BC \rightarrow [A^{+}\cdots{}^{-}B\cdots C]^{\ddagger} \rightarrow A^{+}B^{-} + C \qquad \text{(ionic channel)} \qquad (4.1)$$

$$\rightarrow AB + C \qquad \text{(neutral channel)}\,. \qquad (4.2)$$

The TS can be reached thermally from the entrance channel or directly by a photon excitation.

In a Communication,[1] we have reported on our approach to this problem, to reach the TS directly through a CT excitation of a bimolecular van der Waals (vdW) complex

of *A* and *BC* using femtosecond (fs) laser pulses. The fs pulse (denoted by solid arrow in Fig. 4.1) prepares the TS, $[A^{+}\cdot\cdot^{-}BC]^{*\ddagger}$, from a well-defined ground-state TS, $[A\cdot\cdot BC]^{\ddagger}$, at known intermolecular separations and geometry. The dynamics is then followed by monitoring the TS or the reaction products by using probe fs pulses, with a mass spectrometry arrangement in the molecular beam apparatus. The advantage of using a vdW complex as the reaction precursor in the fs real-time studies is twofold:[2,3] (1) the zero-of-time of the reaction is precisely defined and (2) the impact geometry is defined by the structure of the vdW complex. These bimolecular CT reactions are unique among the different classes of CT reactions studied on the fs and ps time scales, which include unimolecular harpooning reactions,[4] intramolecular CT reactions,[5] proton transfer in acid-base reactions,[6] harpooning reactions of $Xe+I_2$[7] and, more recently, $Xe+Cl_2$[8]. The specific system of interest here is the bimolecular reaction of polyatomic molecules (electron donor, D) benzene (Bz) or methyl substituted benzenes (MBz) with a diatomic molecule (electron acceptor, A) of molecular iodine (I_2); see Fig. 4.2. The system is rich in many aspects of structure and dynamics and has been extensively studied for nearly 50 years since the seminal works by Hildebrand[9] and Mulliken.[10,11]

The concept of the experiment is illustrated in Fig. 4.3 by considering the two nuclear coordinates, the Bz-I and I-I distances. If the t=0 pulse is at the vdW distance ($\lambda^{\ddagger}$), then the TS is reached by direct CT, for a given geometry, followed by bond breakage along the I-I coordinate. On the other hand, if the t=0 pulse (λ^{∞}) is tuned to longer distances, then the situation is equivalent to a bimolecular collision with full impact parameter sampling; in this case the crossing of the covalent to the ionic curve is crucial to the outcome. Vertical excitation from the vdW geometry to the CT state

induces a fs electron jump from benzene to iodine and suddenly turns on the Coulomb field between the two. The iodine molecular anion is then rapidly pulled in by the strong electrostatic force to a closer distance from the benzene cation and then the reaction occurs. The products are a free iodine atom and a $Bz^{+}\cdot I^{-}$ complex. While in the TS, an electron may return back to benzene and the covalent exit channel (BzI+I) opens up. By monitoring the decay of the TS, the appearance of the free I atoms, and their kinetic energies, we are able to directly observe the evolution of the TS from a well-defined structure. By measuring the vectorial correlation between the direction of recoil and the initial alignment we obtain the (impact) geometry at t=0 for the TS.

Comparisons with other (time-integrated) approaches are relevant. In Polanyi's TS spectroscopy of the $Na+XCH_3$ system,[12] they reach the covalent branch and then by crossing, through harpooning, the final products are made. The scheme in Fig. 4.1 is similar to that of the $M+X_2$ harpoon reactions, where M= alkali-metal atom and X= halogen atom, except that the present system requires a photon to induce the electron jump and enters the transition-state region directly. The preparation is from "beneath" the potentials of interest and in this regard analogous to Neumark's[13] photodetachment experiments. The preparation is off-resonant with the absorption of either reactants, similar in design to Brooks and Curl experiments.[14] The mechanism also bears a close similarity to that in reactions of $Xe\cdot X_2$ (X= Cl, Br)[15] and $Hg\cdot Cl_2$ complexes reported by Jouvet and Soep,[16] and the laser-assisted reactions of Xe/X_2 collision pairs reported by Setser's group.[17] In these cases, the vdW complexes (or collision pairs) were excited to their CT states by one or two photons and the product's (XeX^{*} and $HgCl^{*}$) emission was detected. Finally, unlike the hot-atom reactions,[2,18] the $Bz\cdot I_2$ system is entirely prepared

on a reactive potential at t=0 and has a well-defined impact geometry, as discussed below, and in this sense is a prototype for both Polanyi's surface-aligned reactions[19,20] and dissociative reactions at electrodes as described by Savéant,[21] Eberson[22] and others.

In this Chapter, we give a full account of our work reported in the earlier Communication.[1] Although donor-acceptor complexes of benzene with I_2 have been extensively studied for nearly half century, very little is known about the nature of the TS state and its dynamics. The present study is aimed at elucidating the dynamics of the 1:1 complex following the CT excitation in a collisionless environment free of solvent perturbations. Elsewhere, we described the effect of further solvation with benzene.[23] Because the complexes were prepared in a supersonic molecular beam, the internal temperatures of the complexes are very low (~ 10 K). The conditions were carefully adjusted to ensure the dominance of 1:1 complexes in the molecular beam. The energetics of the TS were varied by changing the initial pulse wavelength. Geometry (impact parameter) and symmetry considerations were examined by studying the following donor aromatics: D= benzene, deutrobenzene, toluene, and also xylenes and trimethylbenzenes of different symmetries. We employed the fs time-resolved kinetic energy time-of-flight and anisotropy measurements to reveal the product translational energy distributions and the nature of the two distinct channels involving the neutral and ionic potentials. Theoretical studies involving *ab initio* calculations and molecular dynamics are also reported.

4.2. The CT System

It has been recognized for more than a century that different colors develop when iodine is dissolved in a variety of solvents.[24] Organic solvents were in those days distinguished based on the colors of their iodine solutions since, in general, saturated solvents gave a violet color and unsaturated ones gave a brown color. In 1949, in an attempt to reveal the origin of this phenomena, Benesi and Hildebrand[9] discovered a strong UV absorption band that is characteristic of neither the aromatic solvents nor the iodine molecules alone. They attributed these new absorption bands to the formation of aromatic-I_2 ($D{\cdot}I_2$) complexes and proposed that they be stabilized by "acid-base" interactions in solutions. Soon after this discovery, Mulliken[10,11] developed a theory to account for the stability and the strong UV absorption of $D{\cdot}I_2$ complexes. He proposed that the complex be stabilized by resonance interactions between a "no-bond" ($D\text{-}I_2$) and a "dative-bond" ($D^+\text{-}I_2^-$) CT structures, in which the aromatic molecule acts as an electron donor and I_2 the electron acceptor. The new absorption band is then simply due to the excitation of the ground state complex to the CT state.

Based on Mulliken's theory, the CT absorption band energy can be approximated by the following equality:

$$h\nu_{CT} = I_D - E_A^V - W, \tag{4.3}$$

where I_D is the ionization potential of the electron donor, E_A^V is the vertical electron affinity of the electron acceptor, and W is the Coulomb interaction energy (e^2/R). Many experiments were followed to test Mulliken's theory. However, it was soon clear, based on experimental evidences as well as theoretical arguments,[25] that the contribution of the CT state to the ground state stability is small. Nevertheless, spectroscopic studies of a

variety of electron donor/acceptor systems have in many cases confirmed the correlation of the CT band energy with the I_D and E_A^V.[11,26,27] It is now generally accepted that the strong characteristic UV absorption bands of D•I_2 and other related complexes are due to the CT excitation. However, the ground state complexes are bound simply by the dispersion force and electrostatic multipole interactions.

Benzene•I_2 (Bz•I_2) and other similar complexes are probably the most well studied CT complexes.[26,27] Various conventional spectroscopic methods have been employed to investigate these complexes in the liquid, gas and solid phases. In Fig. 4.4(A) representative absorption spectra reproduced from the literature show the original ultraviolet-visible absorption reported by Benesi and Hildebrand[9] for several I_2/D solutions. The CT absorption band maximum of the I_2/Bz solution is at 297 nm. Note the much smaller extinction coefficient in the UV region when I_2 is dissolved in an "inert solvent" such as CCl_4. Fig. 4.4(B) shows clear absorption spectra of Bz•I_2 isolated in Ar and Xe solid matrices at 20 K.[28] The center of the absorption band in the Ar matrix is at 281 nm. Fig. 4.4(C) shows gas-phase absorption spectra of a Bz/I_2 vapor mixture at 340 K.[29] The CT absorption maximum shifts to 268 nm in the gas phase. Similar CT absorption bands of many I_2/D systems have been observed and widely studied. In general, the positions of the CT absorption maxima exhibit a strong correlation with the I_D's of the electron donors and qualitatively agree with the prediction made by Eq. (4.3).[11,26,27]

The D•I_2 complexes are known to be stable even in room temperature solutions. The heat of complex formation of Bz•I_2 in the gas phase has been determined by spectrometric methods to be on the order of -2 to -3 kcal/mol.[29,30] A more recent

molecular beam experiment[31] has reported the binding energy of $Bz{\cdot}I_2$ to be 745±70 cm^{-1}. An early "*ab initio*" study[32] has predicted a binding energy of about 700 cm^{-1} for $Bz{\cdot}I_2$. As discussed below, our *ab initio* calculations[33] of the 1:1 complex give a similar binding energy.

Mulliken[10] initially suggested that $Bz{\cdot}I_2$ has a "resting" structure, with the I-I bond lying above and parallel to the benzene molecular plane. However, IR spectroscopic studies[34] of Bz/halogen solutions suggest an axial structure similar to the one shown in Fig. 4.2. In this structure, the I-I axis is along the benzene C_6 axis and the complex has a C_{6v} symmetry. X-ray studies of two very similar systems, namely $Bz{\cdot}Br_2$ and $Bz{\cdot}Cl_2$,[35] in their 1:1 crystal forms have also shown results that are consistent with the axial structure. UV and IR spectroscopic studies of $Bz{\cdot}I_2$ in solid matrices have also concluded that the complex has an axial structure.[36] Several theoretical studies,[32,33,37] including *ab-initio* calculations,[32,33] have predicted that the axial structure is indeed the most stable form of the $Bz{\cdot}I_2$ complex. The experimental results mentioned above, although favoring the axial structure, are far from conclusive for the structure of the isolated 1:1 $Bz{\cdot}I_2$ complex. In this paper, we provide clear evidence of the structure of the 1:1 $Bz{\cdot}I_2$ complex derived from experimental studies of the isolated species.

Photochemistry of $D{\cdot}I_2$ complexes was also a subject of interest for many years. Microsecond flash photolysis studies of I_2/D solutions[38] and vapor mixtures[39] have reported transient visible absorption bands that can be assigned to D-iodine atom (D·I) complexes. The first ultrafast picosecond (ps) laser studies[40] found that D·I complexes are formed very rapidly in I_2/D solutions upon I_2 and CT excitation. The time resolution was not sufficient to resolve the initial dynamics. With the advent of fs laser spectroscopy, the

photochemistry of D•I_2 complexes has attracted new interest. Fs laser studies[41-44] have been reported recently and shown that the formation of D•I complexes is indeed extremely fast (25-500 fs) upon CT excitation of I_2/D solutions. We will review and compare results of the liquid-phase fs studies with our gas-phase and cluster results in Sec. 4.5.

4.3. Experimental

Two fs laser systems were used here, the colliding pulse mode-locked ring dye laser (CPM) and the synchronously-pumped dye laser, both with amplifiers. The CPM system has been given elsewhere[45] and the synch-pumped laser system has been described in Chapter 2. The CPM system was used for its high time resolution (~60 fs) while the synch-pumped system provided versatility in tunability and in the resonance detection of the iodine atom. The CPM system with the molecular beam[46] was specifically used to measure the ultrafast decay of the TS and the synch-pump systems was used for all other experiments.

Briefly, a supersonic molecular beam containing the species of interest was produced in the first chamber, skimmed and intersected by the fs laser beams in the extraction region of a two-stage linear TOF-MS housed in the second chamber. The ions were detected by a 25 mm diameter microchannel plate assembly (MCP). The molecular beam, TOF-MS axis, and the fs laser beams were orthogonal to each other. A pair of deflection plates was used in the field free region to correct for the drift of ion trajectories due to the molecular beam velocity component perpendicular to the TOF axis. The TOF-MS was also used as a kinetic energy spectrometer, as described in Chapter 2, to resolve the translational energy distribution of reaction products.

The $D \cdot I_2$ complexes were produced by expanding gas mixtures containing donor aromatics, iodine, and He through a pulsed valve (General Valve Series 9) with an orifice of 0.5 mm in diameter. The gas mixtures were prepared by allowing pure He gas (800-1000 Torr) to flow, first through a reservoir containing electron donors, and then over iodine crystals loosely packed in a Teflon tube. This ensured complete mixing of gases before expansion. The iodine crystals were kept at room temperature (~ 22°C). The donor reservoir was immersed in a large cold bath. The concentration of the donor vapor in the gas mixture was adjusted by varying the cold bath temperature which was carefully monitored and controlled during the experiments. All electron donors studied in this work were used as purchased (Aldrich, >98%).

As expected, because of the relatively large polarizabilities of the D's and I_2, they cluster very easily in the jet. Since only the iodine atom products were monitored, it is very important to control and diagnose the cluster size distribution in the beam. This was achieved by controlling the donor vapor concentration in the gas mixtures. We used the pump laser (277 nm) alone as the ionization laser to monitor the cluster size distribution. Fig. 4.5(A) shows a series of mass spectra taken at different benzene concentrations with all other conditions fixed. We believe that these spectra reflect the true beam composition because the complexes were ionized at a total energy not much higher than their I_D's. Under our beam conditions, the benzene concentrations needed to be as low as 0.5 Torr to avoid any appreciable amount of $n \geq 2$ clusters. At higher benzene concentrations, larger clusters were clearly present in the beam. Similar behaviors were observed for all D/I_2 systems studied here. The results presented in this work, except those in Fig. 4.5(B), are all obtained under the 1:1 complex condition.

4.4. Results and Analyses

4.4.1. The Bz·I_2 Complex: Characterization and Preparation

Free iodine atoms were readily detected by the probe laser when Bz·I_2 complexes were excited to their CT absorption band region in the molecular beam. The iodine atom transient, *i.e.*, the trace representing the iodine atom signal as a function of pump-probe delay time, depends strongly on the benzene vapor concentration in the expanding gas mixture, as shown in Fig. 4.5B. At high benzene concentrations, the transients are characterized by bi-exponential rises, with the slower component being 20-75 ps, depending on the benzene concentration.[23] As the benzene concentration is reduced, the ratio of the slow to fast component decreases. At the lowest benzene concentration (0.5 Torr, (A) in Fig. 4.5), the long-time component essentially vanishes, and the iodine atom signal stays at a constant level for more than 200 ps. However, at this low benzene concentration, the density of the complexes also becomes so low that the background I^+ signal arising from the much more populated uncomplexed molecular iodine in the beam becomes significant. Fig. 4.6(b) shows an early-time transient taken under this very low benzene concentration condition. A background iodine atom transient shown in Fig. 4.6(a) was recorded right after[47] the Fig. 4.6(b) transient was taken but with He gas bypassing the benzene reservoir, *i.e.,* no benzene in the gas mixture. Fig. 4.6(c) is a corrected transient obtained by subtracting (a) from (b). As also shown in the same figure, the rise of the corrected transient is clearly slower than the response function and can be described by an apparent single-exponential rise of 750±50 fs (see below).

The build up of free iodine atoms produced by the 1:1 Bz•I_2 CT state reaction was established based on the following. Firstly, this transient iodine atom signal can be observed *only* when benzene and iodine vapors are both present in the expanding gas mixture. As manifested in Fig. 4.6, when pure iodine vapor is expanded with He gas alone, only a much weaker iodine atom background can be observed (see Fig. 4.4A for solution phase work). These observations indicate that the transient iodine atom signal must arise from complexes associated with both Bz and I_2. The weak iodine background transient may involve a very weak absorption of I_2 as well as I_4 in the pump laser wavelength region, as discussed by Mulliken.[48] Contributions due to multiphoton absorption of I_2 is also possible. Secondly, as shown in Fig. 4.5, the change of the iodine atom transients is unequivocally associated with a dramatic evolution in the mass spectra as the benzene vapor concentrations were varied. At high benzene concentrations, large-sized clusters dominate the beam composition, whereas the Bz•I_2 1:1 complex is the only one detectable at the lowest (0.5 Torr) benzene concentration. Further lowering of the benzene concentration decreases the transient iodine atom signal, but does not change the shape (rise time constant) of the transients. Based on these observations, we conclude that the transients observed at the lowest (0.5 Torr) benzene concentration are due to the *1:1 Bz•I_2 complex.* The transients observed at higher benzene concentrations have been discussed elsewhere on the basis of the caging dynamics in larger clusters.[23]

Further support comes from the initial preparation. The pump laser wavelength (260-285 nm) used here is near the reported CT absorption maxima of the complex (see Fig. 4.4).[9,28,29] The CT band of Bz•I_2 complex is well known for its strong absorption due to the inherent CT nature of the transition described by Mulliken's theory.[10,11] The

uncomplexed I_2, on the other hand, absorbs very weakly in this spectral region.[48] Gas phase studies[29] have shown that the extinction coefficient of the Bz·I_2 complex is at least 150 time larger than that of the free I_2 in the pump laser wavelength region. This strong CT absorption is consistent with our observation that many more I atoms are produced from the Bz·I_2 complexes, even though their concentration is expected to be only a few percent of the uncomplexed I_2 in the molecular beam. Moreover, the lowest pump laser photon energy employed here is about 3,000 cm^{-1} lower than the free benzene $S_1 \leftarrow S_0$ band origin. For many mixed bimolecular complexes containing benzene, the spectral shifts of the benzene $S_1 \leftarrow S_0$ transition are usually smaller than ± 200 cm^{-1}.[49] Therefore, excitation through the local benzene $S_1 \leftarrow S_0$ transition is not possible, but instead, the *initial excitation must reach the Bz·I_2 CT state.*

At higher benzene concentrations the $(Bz)_n$·I_2 complexes can be ionized by the pump laser alone through 1+1 REMPI, as shown in Fig. 4.5(A). If reactions occur in the complex's cation, which may also produce neutral iodine atoms, transient rises of iodine atom signal could be observed. To clarify this possibility, we have performed diagnostic experiments to measure the pump laser intensity dependence of the transient iodine atom signal. The results are shown in Fig. 4.7. A pump laser intensity dependence of ~ 0.9 was measured, indicating the transient iodine atom signal observed was produced at a one-photon excitation level. This is further supported by observations that the iodine atom transients were eventually unchanged when the pump laser intensity was reduced by nearly a factor of 10.

The iodine transients were also measured at several different pump laser wavelengths between 260 - 285 nm in order to elucidate the initial energy dependence.

The results are shown in Fig. 4.8, in which the measured rise time constants are plotted against the pump laser wavelength. Clearly, the apparent rise becomes faster as the excitation energy increases.

4.4.2. Other D·I_2 Complexes: Tuning the CT and Changing the Structure

To understand the dependence of the reaction dynamics on the nature of the electron donor, we have studied similar I_2 complexes with six methyl-substituted benzenes (MBz) and deutrobenzene (d_6) at λ_{pu}=277 nm. Fig. 4.9 shows representative iodine atom transients resulting from the reactions of C_6D_6·I_2, toluene·I_2, m-xylene·I_2 and 1,2,4-trimethylbenzene·I_2. The apparent rise time constants are all in the range of 0.6-1.0 ps. Note that in the C_6D_6·I_2 case, the time constant is essentially identical to that of Bz·I_2. The other two xylene isomers also give similar rise time constants as the o-xylene, and mesitylene·I_2 gives about 1.0 ps. Except for toluene·I_2, these results seem to suggest that the rise time increases as the number of methyl groups on the benzene ring increases.

The CT absorption bands of these MBz·I_2 are expected to be lower in energy than that of Bz·I_2 because of the lowering in I_D's of the donors. For example, the gas phase CT band maximum of mesitylene·I_2 is at ~ 301 nm,[50] about 0.5 eV lower than the Bz·I_2 maximum. Hence, our excitation energy (277 nm) falls at the blue side of the MBz·I_2 CT absorption bands.

The S_1 states of MBz are also lower in energy than Bz(S_1).[59] Some MBz have S_1 zero-point energies close to or even below our excitation energy. Excitation to the MBz locally excited states is therefore possible. However, the CT transition is much stronger than the aromatic $S_1 \leftarrow S_0$ local excitations, making the contribution of the locally excited

S_1 state small. This is consistent with the following: (1) in the xylene•I_2 and mesitylene•I_2 cases, we have tuned the photon energy down to ~ 290 nm and observed no significant changes in the rise times; (2) no drastic dynamical change was observed in going from Bz•I_2 to trimethylbenzene•I_2; and (3) the $S_1 \leftarrow S_0$ transition dipoles in MBz are polarized in the molecular plane which is inconsistent with the conclusion we will reach later regarding the recoil anisotropy. As mentioned before, for Bz•I_2, we only reach the CT state as the $S_1 \leftarrow S_0$ of benzene is at higher energy.

4.4.3. KETOF: Translational Energy Distributions

The translational energy distributions of iodine atoms produced from the CT reactions bear detailed signatures of the underlying reaction mechanisms. Fig. 4.10(A) shows the iodine atom KETOF distributions observed from the o-xylene•I_2 CT reaction at three pump laser polarizations with respect to the TOF-MS axis. Strictly speaking, they are the v_z distribution since the TOF has been transformed into the v_z domain. These distributions clearly suggest that two distinct components with very different translational energies are present. Using the data analysis procedures described in Chapter 2, the two components are unambiguously revealed in the speed distributions derived from the magic angle data, as shown in Fig. 4.11a (upper panel). The higher-speed component peaks at ~ 1000 m/sec and the lower-speed one at ~ 400 m/sec. The distribution derived is the speed distribution of iodine atoms with respect to the center of mass (c.m.) of the complex. In order to estimate the relative weights of the two components, the speed distributions were fit to a linear combination of two gaussian functions (solid line), which were then integrated separately. In this case, the total signal is composed of 45±5 % of

low speed component and 55±5% of high-speed component. The choice of the two-gaussian model is rather arbitrary and is only meant to guide the eyes and to estimate the relative weights.

The speed distribution $g(\mathrm{v})$ is then transformed into the translational energy distribution $P(E_t)$, shown in Fig. 4.11a (lower panel), by the following relations:

$$P(E_t) = \frac{g(\mathrm{v})}{m_I \mathrm{v}} \qquad \text{and} \qquad E_t = \frac{1}{2} m_I \mathrm{v}^2 \ , \tag{4.4}$$

where m_I is the mass of the iodine atom. Note that E_t is the iodine atom translational energy with respect to the c.m., *not* the total c.m. translational energy released. We prefer presenting the translational energy in this manner because the exact kinematics associated with the reaction is not clear (two- vs. three-body dissociation) and may not be uniform throughout the entire distribution. In the energy domain, the high-energy distribution is centered at ~5,000 cm^{-1} and the low-energy one at ~900 cm^{-1}. Note that *the two components do not correspond to two reaction channels separated by the iodine atom spin-orbit energy* (~7,600 cm^{-1}). Strong supporting evidence is that, as will be shown below, the two components exhibit markedly different temporal behaviors. Moreover, it will become clear in the discussion section that the iodine atoms resulted from exit channels separated by the spin-orbit energy do not have translational energies consistent with the two components.

The iodine atom transient signal arising from the background I_2 in the molecular beam is not corrected for in the KETOF distributions presented here. However, as shown in the previous section, the total transient iodine atom signal contains only 10 - 15% of background signal. Furthermore, the background iodine atom KETOF distribution

measured without aromatic donors in the gas mixtures is rather isotropic with no sign of any high-energy wings. Subtraction of this background KETOF distribution with a 10% weight from the D•I_2 ones eventually results in identical speed distributions as the uncorrected ones.

The KETOF distributions observed for the Bz•I_2 reaction, shown in Fig. 4.10(B), are somewhat different from the o-xylene•I_2 ones in their appearances. The Bz•I_2 parallel polarization data also exhibit a high-energy shoulder but is not as obvious as in the o-xylene•I_2 case. Nevertheless, as shown in Fig. 4.11b, the speed and translational energy distributions obtained from analyzing the magic angle KETOF data again clearly reveal the presence of two distinct components. The high-energy component is similar to the one observed in the o-xylene•I_2 case in terms of the peak energy and width. However, the low-energy component is clearly broader and shifted to slightly higher energy, which effectively blurs the appearance of the high-energy component in the KETOF distribution. This is evident when the results of the two-gaussian fit in both cases are compared. The low-speed component in the o-xylene•I_2 case can be well simulated by a gaussian function with a center speed of 390 m/sec and a width (fwhm) of 330 m/sec, respectively. However, in the Bz•I_2 case, the center speed shifts to 490 m/sec and the width becomes 450 m/sec. The contribution of the high-energy component in the Bz•I_2 reaction was underestimated in our preliminary report[1] partly due to the fact that the low-energy component is broader and higher in energy and partly due to the much longer TOF of I^+ (~23 μsec) which discriminates against the higher speed fragments as a result of the longer flight tube and lower acceleration voltages previously used.

The recoil anisotropy distribution $\beta(v)$ is then obtained by fitting the parallel polarization KETOF distributions using the speed distribution derived from the magic angle polarization data. Fig. 4.12 shows the $\beta(v)$ of four representative systems along with their iodine atom speed distributions, while Fig. 4.13 shows two typical results of the fits. Two important features are readily seen in Fig. 4.12. First, $\beta(v)$'s are definitely positive for all systems at all speeds, indicating a parallel-type transition is dominant. Second, β is always nearly zero at low speed ($\leq$ 400 m/sec). These results are crucial in understanding the CT state dynamics as well as their structures, as discussed below. We shall not focus on the variation of β as a function of speed, instead a weighted, averaged β_{av} is estimated for the low- and high-energy components. The low-energy components have β_{av}'s ~ 0.2-0.3 and the high-energy components have β_{av}'s ~ 0.7-1.0.

Similar KETOF distributions were observed for all other D•I_2 complexes that we have studied. The translational energy distributions for these systems are displayed in Fig. 4.14 for comparison. Note that the high-energy components are located at almost exactly the same energy and have similar widths for all systems, whereas the low-energy ones exhibit some dependence on the electron donor. The low-energy components in the Bz•I_2 and C_6D_6•I_2 reactions are clearly broader and higher in energy than other systems.

4.4.4. Time-Resolved KETOF: Dynamics of Different Channels

We chose the o-xylene•I_2 reaction as a prototype for the fs time-resolved KETOF studies because it produces clearly separated low- and high-energy components. Fig. 4.15(A) and (B) show the temporal evolution of KETOF distributions measured at the magic angle and parallel polarizations, respectively, as the pump-probe delay time

increases. The time-resolved translational energy distributions obtained from the magic angle data are displayed in Fig. 4.16. These data clearly show that there is strong time dependence in the KETOF distributions. At very early times (0.5 ps) the low-energy component weighs only about 20% but increases to about 45% at later times (> 6 ps), indicating a slower rise than the high-energy component. These results undoubtedly show that the iodine atom transients described in the previous sections are composed of at least two temporal components and that the time constants derived from the single-exponential fit are merely the apparent time scales for the reactions.

To better describe the differences in their time scales, we estimated the contributions of the low- and high-energy components at different times by the procedure described in the last section using the two-gaussian model. Shown in Fig. 4.17 are the integrated intensities of the low- and high-energy components plotted against the delay times. The data points of the high-energy component can be simulated by a single exponential rise of 450 fs convoluting with the system response of 500 fs. The low-energy component data, on the other hand, give a single-exponential time constant of 1.4 ps. As discussed in the next section, we used the CPM laser system to gain better resolution and observe the ~ 250 fs mesitylene component at early times.

4.4.5. Transient Decay: Initial Transition-State Evolution

To reveal the motion of the initially prepared CT state of $Bz{\cdot}I_2$, we have monitored the $Bz{\cdot}I_2^+$ ion signal as a function of the pump-probe delay time. The idea was to ionize the CT state of $Bz{\cdot}I_2$ with the 304-nm photons while it is moving through the transition state toward the exit region. However, the transient signal of $Bz{\cdot}I_2^+$ was

extremely weak under the 1:1 complex condition. In fact, even the time-independent signal of $Bz{\cdot}I_2^+$ was quite weak. This is primarily due to the energetic to ionization as well as unfavorable Franck-Condon factors which cause fragmentation in the parent ions upon two-photon absorption of the CT state at 304 nm.

As a result, we observed intense transient signal from the Bz^+ mass channel, as shown in Fig. 4.18(A) with two different pump-probe polarization orientations. These transients observed in the Bz^+ mass channel resemble the initial dynamics of the $Bz{\cdot}I_2$ CT state for the following reasons: (1) the transient signal is observed only when Bz and I_2 are simultaneously present in the gas mixture. When benzene vapor was expanded alone with pure He, no transient signal was observed; (2) benzene does not absorb in the pump laser wavelength region (277 nm). Even if it did, the S_1 state of benzene is known to have a lifetime of ~100 nsec, whereas the decay we observed here is shorter than 1 ps. The triplet states of benzene are out of the question for the same reason. Hence, these Bz^+ transient signals can only come from the fragmentation of the $Bz{\cdot}I_2^+$ parent ions, which are produced by the ionization of the $Bz{\cdot}I_2$ CT state. The observed Bz^+ transient therefore represents the dynamics of the initial CT state. Further support comes from the transient signal observed directly from the $Bz{\cdot}I_2^+$ mass channel under the larger cluster conditions; the decay is still on a similar time scale. The successful detection of the $Bz{\cdot}I_2^+$ transient signal under larger cluster conditions is due to the lower I_D's and ionic fragmentation of larger $(Bz)_n{\cdot}I_2$ clusters.

The transients shown in Fig. 4.18(A) exhibit a bi-exponential decay behavior dominated by an extremely fast initial decay component. With our cross-correlation of ~500 fs, for the synch-pumped laser system, we could only conclude that $\tau_1 < 200$ fs. The

second component is much weaker (≤ 20%) and has a decay time constant of ~ 800 fs. The rapid initial decay of the Bz^+ transients suggests that the $Bz{\cdot}I_2$ CT state is indeed very short lived (< 200 fs). The bi-exponential decay behavior of the initial CT state provides some insight into the nature of the TS as discussed in the next section.

With the CPM amplified laser pulse (~ 60 fs) we observed similar decays by monitoring the mesitylene ion signal with λ_{pump}=310 nm and λ_{probe}=620 nm. As shown in Fig. 4.18(B) for the mesitylene$\cdot I_2$ system, the decay is 250 fs, again consistent with the results obtained from time-resolved KETOF and from the detection of Bz^+. The slower decay observed in this case could be a result of the much lower excitation energy (310 nm vs. 277 nm). The long decay component is less than few percent compared to $Bz{\cdot}I_2$, and this is consistent with the change in the contribution of the two channels discussed next. From these experiments we established $\tau^{\ddagger}$ of the TS to be ~ 250 fs.

4.5. Discussion

The experimental results presented above can be briefly summarized as follows: (1) upon the CT preparation of $D{\cdot}I_2$ complexes, iodine atoms are produced very rapidly on a time scale of less than 1 ps; (2) the iodine atom translational energy distributions exhibit two very different components, one which peaks at a low energy (less than 1,000 cm^{-1}) and the other at a high energy of about 5,000 cm^{-1}; (3) the recoil anisotropy of the iodine atoms is 0.2-0.3 for the low-energy component and is ~0.7-1.0 for the high-energy one; (4) the two components of the translational energy also show different temporal behaviors, the high-energy one rises very rapidly (450 fs), whereas the low-energy component builds up much slower (1.4 ps for D=o-xylene); (5) the reaction time

decreases with increasing energy and is robust in all MBzs; and (6) following the evolution of the transition states gives a decay time $\tau^{\ddagger}$ of 250 fs. In this section, we will begin by describing the energetics of the system. Then, we will give a description of the dynamics and mechanism, together with elucidation of the initial structure of the TS.

4.5.1. The Energetics

4.5.1.1. The Geometry and TS Entrance Channel

The nuclear configuration of the initial state is determined by the structure of the Bz·I_2 complex ground state since the reaction is initiated by a vertical excitation. As mentioned earlier, several experimental and theoretical studies have provided evidences that the axial structure is the most stable configuration for Bz·I_2. Recently, our group has also performed *ab-initio* calculations at the MP2 (Møller-Plesset perturbation theory) level of theory, and found that the axial structure is more stable than the resting structure by about 2 kcal/mol. The Bz·I_2 molecular structure shown in Fig. 4.2 is based on these *ab-initio* calculations. A detailed account of the *ab-initio* results is published elsewhere.[33] For complexes having MBz's as the donors, small deviations from the perfect axial form are expected. In this Chapter, we will first restrict our discussion to the axial structure for the Bz·I_2 complex and we will show that our experimental results are in fact consistent with the axial rather than the resting structure.

For Bz·I_2, the axial structure belongs to the C_{6v} point group. In the simplest picture, based on the Mulliken's theory,[10,11] the first CT excitation promotes an electron from the HOMO (π) of benzene to the LUMO (σ^*) of the molecular iodine, as illustrated conceptually in Fig. 4.19, forming a benzene cation and a molecular iodine anion. The

HOMO of benzene is of the e_1 symmetry and the LUMO of I_2 is of the a_1 symmetry in the C_{6v} complex frame. The electronic symmetry of the first CT state is therefore E_1 in C_{6v}. The degeneracy can be removed by methyl substitutions of benzene and by distortion from the axial structure. The bond energy of I_2^- (1.10 eV) is lower than that of I_2 (1.58 eV) due to an additional electron in the anti-bonding orbital (σ^*).

At the infinite separation between Bz^+ and I_2^-, the asymptotic energy is simply $I_D^{ad}(Bz) - E_A^{ad}(I_2)$ =6.67 eV, where I_D^{ad} and E_A^{ad} are the adiabatic ionization potential and electron affinity, respectively. As Bz^+ and I_2^- approach closer, the potential energy is lowered, mainly due to the Coulomb energy $-e^2/R$, until the repulsion between the two moieties becomes significant. In Fig. 4.20, a schematic potential energy curve (thick solid line) for the $Bz{\cdot}I_2$ CT state is depicted along the Bz-I coordinate based on this oversimplified picture. The curve is obtained by fitting available spectroscopic information and reasonable estimates for the equilibrium Bz--I_2 separation.

Note that the curve is adiabatic in all internal coordinates of Bz and I_2. Upon CT excitation, internal levels of Bz^+ and I_2^- can also be populated according to their Franck-Condon overlaps with the neutral ground states. To visualize this multi-dimensional problem, we can think of it as a series of CT potential energy curves which correspond to different internal levels of Bz^+ and I_2^-, along the Bz-I coordinate. One of these curves (dashed line) which corresponds to the vertical electron attachment of I_2 neutral, is also shown in Fig. 4.20. The asymptotic energy of this curve is $I_D^{ad}(Bz) - E_A^{v}(I_2)$=7.57 eV, where E_A^{v} is the vertical electron affinity.

The Franck-Condon overlaps in the I_2 and Bz internal and Bz-I_2 intermolecular coordinates govern the initial nuclear configuration reached by the pump pulse.

Photoelectron spectroscopic studies[52] have shown that a large fraction of the benzene cation is produced in its vibrationless level upon photoionization of benzene. Although several fundamentals are also excited with small probabilities, these low excitations of the benzene cation modes are rather unimportant in the reactions discussed here, and we shall neglect the benzene cation internal excitation hereafter.

On the other hand, because of the very different equilibrium bond lengths between the neutral and anionic molecular iodine as a result of the additional electron in the antibonding orbital, electron attachment of I_2 is expected to produce I_2^- with a broad distribution of vibrational excitation. Based on the potential energy curves derived by Chen and Wentworth,[53] vertical electron attachment of I_2 should produce I_2^- at some high vibrational levels close to the dissociation limit. In the Bz-I coordinate, the equilibrium separations between Bz and the nearest I atom in the ground (r_e'') and CT states (r_e') of the Bz•I_2 complexes are expected to be quite different as a result of the very different intermolecular interactions. Vertical excitation therefore also prepares the initial state with a moderate vibrational excitation in the Bz-I coordinate. The CT absorption bandwidth is simply the result of the broad Franck-Condon envelopes in these two coordinates. The net effect in going toward the blue side of the CT absorption band is to increase the vibrational excitations in both I-I and Bz-I coordinates.

The picture is now clear, at least qualitatively, for the TS entrance channel. At t=0, the system is brought to the CT state and the Coulomb potential along the Bz-I coordinate is suddenly turned on - harpooning at these particular separations (see Fig. 4.1). While the two moieties start executing a large amplitude vibrational motion in the coulomb potential, I_2 also immediately begins to vibrate upon acceptance of the electron.

A potential energy curve corresponding to a locally excited state which dissociates to $Bz(S_1)$ and neutral I_2 ground state is also shown in Fig. 4.20. Although the energetics of this state is near our excitation energy, especially for the MBzs, its contribution to the initial state can be ruled out, as mentioned in the previous section. However, it is worthwhile to point out that when $Bz(S_1)$ collides with neutral I_2, there is a finite probability that the system can cross and enter the CT state. This is possible because the I_D of $Bz(S_1)$ is only 4.48 eV, making it behave like an alkali metal atom capable of ejecting an electron to a flyby I_2 at a large distance and then pull the halogen molecule in to a closer distance by the long-range Coulomb force allowing the reaction to occur. This represents another possible entrance channel that is similar to the harpoon mechanism of alkali/halogen reactions. Note that in our approach the harpooning is directly achieved by fs laser excitation.

4.5.1.2. The Product Exit Channels

We are mainly concerned with the exit channels in the I-I coordinate because the reactions we have probed must involve I-I bond breakage. Schematic potential energy curves of several energetically possible exit channels along the I-I coordinate are depicted in Fig. 4.20.

4.5.1.2.1. The Ionic Exit Channel: Harpooning

Once the system enters the CT transition state through the entrance channels, the I_2^- can break apart to give rise to an ionic $Bz^+ \cdot I^-$ complex and a neutral iodine atom, provided that it is energetically feasible. Although charge redistributions must take place,

the electronic configuration is not changed along this reaction coordinate, *i.e.*, the CT entrance and ionic exit channels are on a single potential energy surface (PES). We will call this PES "ionic surface" hereafter. An empirical ionic PES will be presented in Sec. 4.5.6.

A potential energy curve is shown in Fig. 4.20 to qualitatively describe the ionic channel along the I-I coordinate. The curve is simply a I_2^- potential that is offset to match the asymptotic energy of $Bz^+ \cdot I^- + I$. This is, of course, a crude approximation since the presence of the benzene cation in the near vicinity must introduce some perturbation to the bonding of I_2^-. The ionic product $Bz^+ \cdot I^-$ is simply the CT excited state of the Bz·I complex. The CT absorption band maximum of Bz·I has been reported to be at 430 nm in the gas phase.[39] Based on the available spectroscopic data[39,54] and reasonable estimates for the equilibrium separations, we predicted that the zero-point level of $Bz^+ \cdot I^-$ lies at about 2.5 eV above its ground state (see molecular dynamics section 4.5.6. for details). This gives ~0.4 eV of available energy for the $Bz \cdot I_2$ reaction at 277 nm excitation.

For systems with MBz's as the electron donors, gas phase spectroscopic data are not always available. However, liquid-phase studies[55] have shown that there is an excellent correlation between the CT absorption maxima of D·I complexes and the I_D's of D. We can therefore estimate the zero-point energy of $MBz^+ \cdot I^-$ using $Bz^+ \cdot I^-$ as a reference, *i.e.*, $E(MBz^+ \cdot I^-) = E(Bz^+ \cdot I^-) - \Delta I_D$, where $\Delta I_D = I_D(Bz) - I_D(MBz)$.

When the two iodine atoms are separated far enough, the neutral iodine atom product can be readily detected by our probe laser as a free iodine atom using mass spectrometry. The ionic product $D^+ \cdot I^-$ complex is very strongly bound (~ 4eV). Even though a fraction of the available energy is expected to flow into the $D^+ \cdot I^-$ vibration, it is

certainly not enough to break it apart. The ionic complex can relax to the ground state either radiatively or non-radiatively and then dissociate. These processes are expected to proceed with much longer time scales and are not observable in our experiments. This expectation is supported by the fact that the lifetimes of CT excited states (B state) of many rare-gas halide complexes, such as XeI, are on the order of 10 nsec.[56] Therefore we expect the ionic channel produces only one detectable iodine atom from a $D{\cdot}I_2$ complex in our experiments.

The ionic exit channel has been observed in many similar systems of bimolecular encounters both in bulk collisions and in weakly bound complexes. For example, in Rg^*+X_2 reactions[57,58] (Rg: rare-gas atoms, X_2: molecular halogens), the Rg atom is first electronically excited by a photon and then the system enters the $Rg^+{\cdot}I_2^-$ CT state at the ionic-covalent intersection region. The reaction then proceeds through the ionic channel and produces $Rg^+{\cdot}X^-$ which then decays by slow CT emission. The ionic product CT emission has been widely observed in many cases, including reactions in $Rg{\cdot}X_2$ vdW complexes.[15] Another example is the famous harpoon reactions $M+X_2$ (M: alkali metal atom).[59] In these reactions, the zero-point of the CT state is lower than the neutral reactant asymptote. Therefore, the system can enter the CT state at the crossing of the ionic-covalent surfaces through thermal bimolecular collisions.

4.5.1.2.2. The Neutral Exit Channel: Electron Transfer

Dissociation of I-I bond can also take place in the $Bz{\cdot}I_2$ CT state by coupling to some low-lying I_2 locally excited states that are not bound with respect to the excitation energy. Near our excitation energy, there are many I_2 repulsive states which dissociate

into I+I, I+I* and I*+I*.[48] Three of these states are schematically shown in Fig. 4.20. Most of these repulsive states are due to ($\sigma \rightarrow \sigma^*$), ($\pi \rightarrow \sigma^*$) and two-electron ($\pi^* \rightarrow \sigma^*$) excitations. The vertical energies of these repulsive states at the equilibrium bond distance of the I_2 ground state (2.66 Å) have been estimated by Mulliken.[48] Some improved vertical energies[60] obtained by calculations including the relativistic effect have been reported recently. The repulsive potential energy curves shown in Fig. 4.20 were obtained by fitting the curves "drawn" by Mulliken.[48] It is clear, based on these approximated curves, that the $Bz^+ \cdot I_2^-$ ionic potential must intersect some of these repulsive states in the transition-state region.

If the neutral I_2 locally excited states have the same symmetry as the CT state in the complex molecular frame, surface crossing is avoided and the initial state prepared in the ionic region of the adiabatic surface can exit through regions of neutral characteristics. The branching between the ionic and neutral exit channels depends on the extent of the avoiding (*i.e.,* the ionic-neutral coupling). In the limit of very weak avoiding, the reaction mostly proceeds through the ionic exit channel, whereas in the limit of very strong avoiding the reaction mostly goes through the neutral exit channel.

The result of these mixings is to switch the system, or the transition state, to purely repulsive surfaces that undergo a direct dissociation. A large translational energy disposal is expected from such processes. Hence, the dynamics of the $Bz \cdot I_2$ CT state is expected to be strongly influenced by the nature of the ionic-neutral surface interaction. Although the shape of these repulsive states have not been well determined, the asymptotic energies corresponding to free I or I* are very accurately known. Therefore, the available energies for these neutral exit channels are very certain because the

presence of neutral benzene is not expected to alter the I-I bond energy. *Note that when the transition state hops from the ionic surface to the neutral ones, one electron must flow from I_2^- back to the benzene cation. This is equivalent to a spontaneous back electron transfer process.* We will discuss this important point in more details below in Sec.4.5.4.

After the ionic-neutral surface jump, the potential along the I-I coordinate is changed from covalently bound to purely repulsive. On the other hand, the potential along the Bz-I coordinate is switched from a strong Coulomb to a weak van der Waals (vdW) interaction. The fragmentation kinematics is determined by the coupling of the two dissociation coordinates. The nearly direct dissociation of I_2 can release a significant amount of translational energy impulsively. The iodine atom that does not directly face Bz is expect to depart freely without interacting with the rest of the system. However, the one that directly faces Bz may not be able to dissociate promptly without interacting with Bz first. The latter behavior becomes essentially a *one-molecule caging* mechanism similar to the one-atom caging observed in Rg•HX[61,62] (X=halogen atom) complexes by other groups. Hereafter, when we discuss the neutral exit channels we will call the iodine atom that directly faces Bz the "caged iodine atom", and the other one the "uncaged iodine atom". The binding energy between Bz and an iodine atom is about 0.2 eV at the most.[63,64] Unless the uncaged iodine atom takes away most of the available energy, the caged iodine atom is likely to escape the one-molecule cage, leading to a three-body dissociation.

If Bz and I have a substantial relative velocity when the ionic-neutral switching occurs, Bz-I dissociation can also occur right away because the Coulomb potential that holds the two suddenly disappears. Hence, depending on the crossing points, a fraction of

the available energy can be partitioned into the Bz-I coordinate. A neutral vdW potential energy curves are shown in Fig. 4.20 along the Bz-I coordinate to illustrate this point. The curve correlates to $Bz+I_2^*$, where I_2^* denotes the I_2 repulsive excited states. In this case, the ionic-neutral switching also leads to a three-body dissociation.

4.5.2. Dynamics and the Mechanisms

Based on the above considerations of the TS entrance and product exit channels, the reaction mechanism can be described by the following elementary steps:

$$[D{\cdot}I_2]^{\ddagger} \rightarrow [D^+{\cdot}I_2^-]^{*\ddagger} \rightarrow D^+{\cdot}I^- + I \qquad \text{(ionic channel)} \qquad (4.5)$$

$$\rightarrow D{\cdot}I_2^* \rightarrow D+I+I \text{ or } D{\cdot}I + I, \quad \text{(neutral channels)} \qquad (4.6)$$

where I_2^* denotes the repulsive excited states of I_2. Note that the I atom products in the neutral channel can either be in the ground or in the spin-orbit excited state.

The available energies for the ionic channels are determined by the zero-point energy of the ionic product $D^+{\cdot}I^-$, which in turn, depend on the I_D's of the electron donors. As discussed earlier, at 277 nm excitation, the available energy is about 0.4 eV (3,200 cm^{-1}) for $Bz{\cdot}I_2$. Assuming no internal excitation in the products, one finds that the translational energy of the iodine atom is ~2,000 cm^{-1} based on the dissociation kinematics. This value is an upper limit, since a large fraction of the available energy is expected to be partitioned into the vibrational excitation of the $Bz^+{\cdot}I^-$ product because of the early attractive nature of the PES. The translational energy distribution is therefore expected to peak at a much lower energy and to tail at this threshold energy of ~2,000 cm^{-1}. This expectation is consistent with the low-energy components observed in the $Bz{\cdot}I_2$ and $C_6D_6{\cdot}I_2$ translational energy distributions.

For MBz•I_2 reactions, the available energies are higher due to the lowering of the I_D's in the electron donors. For example, the available energy for mesitylene•I_2 at 277 nm excitation is expected to increase to about 1.24 eV (10,000 cm^{-1}). The upper limit for the iodine atom translational energy is ~6,600 cm^{-1}, in this case based on the dissociation kinematics. For systems with toluene and xylenes as electron donors, the upper limits are between those of the Bz•I_2 and mesitylene•I_2 cases. Therefore, the low energy components observed for the MBz•I_2 reactions should tail to higher energies, which is not consistent with the experimental observations. Thus, the contribution of the ionic channel to the low-energy component must be relatively smaller.

As for the high-energy component, the above energetics considerations clearly suggest that it can not be a direct result of the ionic channel since its energy is too high for all cases. Moreover, as discussed above, the independence of this component on the electron donors is also inconsistent with our expectation for the ionic channel.

In contrast to the ionic channel, the available energies for the neutral exit channels do not depend on the electron donors; they are solely determined by the dissociation limits along the I-I coordinate. At 277 nm excitation, the available energies for the three possible dissociation limits are 1.01 eV (I^*+I^*), 1.96 eV ($I+I^*$), and 2.9 eV (I+I). In the case of three-body dissociation leading to D+I+I (I^*), the available energies would decrease by about 0.1-0.2 eV, which is roughly the binding energy of the D•I ground state. Hence, both the peak energy and the invariance of the high-energy components seem to favor the neutral channels. To support this assignment, we estimate the translational energies of the iodine atoms produced by the neutral channels under two

simple, extreme models. In both models, we assume all the available energy goes into the I-I coordinate and consider two extreme kinematics conditions.

In the first extreme model, we assume that no interaction between D and I is encountered during the I-I dissociation, *i.e.,* D is simply a spectator. In this case, all the available energy is partitioned equally into the two iodine atoms' translational energy. For the uncaged iodine atoms, the c.m. translational energies for each iodine atom are 4,100 cm^{-1} (I^*+I^*), 7,900 cm^{-1} ($I+I^*$), and 11,700 cm^{-1} (I+I) for the three possible dissociation asymptotes. In Fig. 4.11, these threshold energies are indicated by thick long arrows except for the (I+I) channel which is not within the energy range displayed. Note that this does not imply the (I+I) channel is ruled out because these thresholds are the upper limits. Following the I-I dissociation, the caged iodine atom collides with D with the same amount of translational energy (relative to the c.m. of the $D{\cdot}I_2$ complex), forming a collision complex well above its binding energy. If we further assume a head-on, elastic collision, we can obtain translational energies of the postcollision iodine atoms, which are 230 cm^{-1}(I^*+I^*), 450 cm^{-1} ($I+I^*$), and 670 cm^{-1} (I+I) for $Bz{\cdot}I_2$. These threshold energies are indicated in Fig. 4.11b by thin long arrows. For heavier electron donors which are still lighter than the iodine atom, the post-collision iodine atoms have even lower threshold energies, as indicated in Fig. 4.11a for D=o-xylene. In fact, based on this simple model, the iodine atom would come to a complete stop if the donor were as heavy as the iodine atom. For example, in the trimethylbenzene$\cdot I_2$ systems where the electron donor is only 7 amu lighter than an iodine atom, the model predicts the postcollision iodine atom threshold energies to be only 3.3 cm^{-1} (I^*+I^*), 6.3 cm^{-1} ($I+I^*$), and 9.4 cm^{-1} (I+I).

In the second extreme model, we assume that there is a stiff repulsion between D and I at the moment when I_2 begins to dissociate such that the dissociation first produces an iodine atom and a D•I complex which then subsequently falls apart. For the Bz•I_2 reaction, the c.m. translational energies of the uncaged iodine atoms are 5,100 cm^{-1} (I^*+I^*), 9,800 cm^{-1} (I+I^*), and 14,500 cm^{-1} (I+I). The thresholds are slightly higher for heavier electron donors. For example, for trimethylbenzene•I_2, the threshold energies are 5,400 cm^{-1} (I^*+I^*), 10,400 cm^{-1} (I+I^*), and 15,400 cm^{-1} (I+I). Note the relatively small variations in going from Bz to trimethylbenzene. These threshold energies are also indicated in Fig. 4.11 by the thick short arrows. For the caged iodine atom that flies away with D, we assume it somehow separates from D due to the repulsion but does not release significant translational energy. The c.m. translational energy of the iodine atoms thus produced are 1,900 cm^{-1} (I^*+I^*), 3,700 cm^{-1} (I+I^*), 5,500 cm^{-1} (I+I) for Bz•I_2. These thresholds are indicated in Fig. 4.11 by thin short arrows.

These model calculations, of course, oversimplify the dynamics and are only meant to estimate the translational energies to support the proposed mechanism. Note that in the two extreme models, we assume all the available energy is channeled into the I-I dissociation coordinate. This is not strictly valid since a fraction of the available energy may be partitioned into the D-I coordinate, as mentioned earlier. Hence, the threshold energies for the uncaged iodine atoms must be considered as the upper limits for both models. The energies derived for the postcollision iodine atoms in the first model are likely to be the lower limits for the following two reasons. First, the caged iodine atom may acquire more energy if a fraction of energy is channeled into the D-I coordinate. Second, for collisions with finite impact parameters, *i.e.,* not head-on collision, the

translational energy loss of the caged iodine atom can be much less. In fact, we will show in a later section that the recoil anisotropy results suggest an oblique structure which is consistent with the latter point.

As can be seen in Fig. 4.11, all the threshold energies estimated for the uncaged iodine atoms fall in an energy range greater than 4,000 cm^{-1} (thick arrows). In particular, the threshold energies for the I^*+I^* and $I+I^*$ dissociation limits are consistent with the high-energy component observed in the translational energy distribution. The broad distribution of the high-energy component is probably due to a distribution of the ionic-neutral crossing points as well as the three possible dissociation asymptotes. On the other hand, the predicted threshold energies for the postcollision iodine atoms fall in an energy range smaller than 4,000 cm^{-1} (thin arrows), which is in accordance with the low-energy component. The peak energy of the low-energy component and its dependence on the mass of D agree well with the threshold energies predicted by the first extreme model, *i.e.,* decrease as the mass of D gets closer to that of the iodine atom. Overall, the results of these simple model calculations indicate that both the low- and high-energy components are consistent with the neutral exit channel based on the translational energy considerations.

The observed recoil anisotropy (β) distributions of the iodine atoms also strongly support the neutral, caging mechanism. The averaged anisotropy of the low-energy iodine atoms is clearly lower than that of the high-energy ones for all systems studied. This is consistent with the assignment of the one-molecule caging mechanism, since a large and/or broad distribution of deflection angles is expected for the caged iodine atoms. On the other hand, a higher recoil anisotropy can be expected for the uncaged iodine atom

because of its free and nearly direct dissociation. Although the above discussion is based on an axial $D \cdot I_2$ structure, the neutral/caging mechanism is essentially consistent with any structure that effectively intercepts the dissociation of one iodine atom but allows the free departure of the other. On the other hand, if $D \cdot I_2$ assumes the perfectly "resting" structure, no obvious interpretation can be made (based on either ionic or neutral exits) regarding the two distinct components in the translational energy distributions and their different temporal behaviors. Hence, our results suggest that the structure of $D \cdot I_2$ is more axial-type. A direct evidence of the structure will be discussed in Sec. 4.5.3.

The neutral, caging mechanism is also consistent with the time dependence results. The time-resolved KETOF studies show that, at least for the o-xylene$\cdot I_2$ reaction, the high-energy component rises within 450 fs. This extremely rapid rise is the characteristic of a direct dissociation, consistent with the high translational energy associated with this component. The time we observed (450 fs) includes the time needed, after electron transfer, for I-I to separate far enough for the free iodine atom detection. Therefore, the electron transfer could be actually much faster than 450 fs. This conclusion is in accordance with the extremely rapid (<200 fs) initial state decay observed in the transients shown in Fig. 4.18, which must be assigned to the time scale for the ionic-neutral surface switching based on this mechanism. The initial state decay exhibits a shorter time scale than the product rise because the wave packet can disperse and move out of the probing region much faster than the formation of the free products.

The low-energy component rises much slower with a time constant of ~ 1.4 ps. This slowing down is not surprising on the basis of the one-molecule caging mechanism and the 1.4 ps rise simply reflects the lifetime of the collision complex at the given

energy. The implication of this time scale to the caging dynamics will be discussed in more details below.

Although only the o-xylene•I_2 reaction was studied by the time-resolved KETOF, we believe that all other systems are similar in nature. As shown in Fig. 4.9, the apparent rise of the iodine atoms becomes slower as the number of methyl groups attached on the benzene ring increases, although toluene•I_2 is an exception. The apparent rises are simply mixtures of the two components with roughly equal weights. Therefore, if we assume the rates of the ionic-neutral switching are independent of D, then it is the low-energy component that gets slower. Since the available energy for the neutral channel does not depend on the electron donors, the slower rises of the low-energy components indicate that the iodine atom takes longer time to escape from the one-molecule cage as the number of methyl group increases. This could be simply due to the increase of the D•I binding energy as well as the physical size of D.

Similar arguments can also be applied to the excitation energy dependence of the Bz•I_2 reactions shown in Fig. 4.8, in which the apparent rise times of the iodine atoms are shown to decrease with the excitation energy. Since the available energy for the neutral channel increases with the excitation photon energy, the energy partitioned into the caged iodine atom also increases accordingly. Hence, the excitation energy dependence results suggest that higher energy iodine atoms escape from the one-molecule cage faster.

Overall, the discussions presented in this section suggest that the high-energy component arises solely from the prompt dissociation of the uncaged iodine atoms through the neutral exit channel, whereas the low-energy component is a hybrid of the ionic exit and the neutral, caging mechanisms. The contribution of the ionic channel can

be estimated. Since the ionic and neutral channels are parallel exit routes and the ionic-neutral surface jump takes ~ 200 fs, on the basis of a simple kinetics model, the ionic channel can have a branching percentage of 10% if the time scale for the pure ionic channel is 2 ps, which is a very reasonable estimate based on our trajectory calculations (see Sec. 4.5.6). The temporal behavior of these 10% iodine atom products coming from the ionic channel would be difficult to isolate as it should be as fast as the high-energy iodine atoms. The overlap in KETOF distribution makes such isolation difficult to achieve. The low-energy components in the $Bz{\cdot}I_2$ and $C_6D_6{\cdot}I_2$ translational energy distributions have the largest relative weights (~ 60%) and are also the broadest among all systems studied. A plausible interpretation is that, in $Bz{\cdot}I_2$ and $C_6D_6{\cdot}I_2$ reactions, the ionic-neutral surface switching is relatively slower so that the branching ratio for the ionic channels is higher. This could be due to the symmetry constraint imposed by the highly symmetric benzene (and also C_6D_6) moiety which makes the ionic-neutral coupling weaker. These symmetry constraints are probably more relaxed in MBz's, and the very efficient ionic-neutral surface coupling in $MBz{\cdot}I_2$ captures the trajectories toward the covalent exit.

More direct evidence to the existence of the ionic channel is the bi-exponential behavior observed in the initial state decay of $Bz{\cdot}I_2$ shown in Fig. 4.18. The small component (< 20%) of ~800 fs can be assigned to an intermediate state leading to the ionic channel. Further discussion of this point will be made in more details in Sec. 4.5.4.

4.5.3. The Structure

An important result obtained in this work is the recoil anisotropy parameter β of the iodine atom products. The values of β obtained experimentally are for both channels of the reaction and are all larger than zero, not negative. The lower averaged β's of 0.2-0.3 for the low-energy component reflect cage exit dynamics which takes ~ 1ps. For all systems studied, the averaged β's of the high-energy components are ~ 0.7-1.0. From the time-resolved experiments, we know that the high-energy iodine atoms are produced in less than 450 fs. In such a prompt dissociation, the effects of rotational and vibrational motions are negligible, especially under our cold beam condition. The averaged β's therefore suggest that the recoil direction is tilted away from the transition dipole moment by an angle of ~ 35°–40°. In order to fully understand the correlation between the recoil velocity **v** and the transition dipole moment μ we consider the direction of μ in relation to the structure.

First, we briefly review Mulliken's resonance-structure theory for the CT transition in an electron donor-acceptor (D-A) complex.[10,11] The main idea of Mulliken's theory is that the complex is an admixture of the "no-bond" and the "dative bond" structures. The ground-state wave function of the D-A complex can be written as:

$$\Psi_N = a\phi_0(\mathrm{D,A}) + b\phi_1(\mathrm{D^+ - A^-}), \tag{4.7}$$

where $\phi_0(\mathrm{D,A})$ is the "no-bond" configuration wave function and $\phi_1(\mathrm{D^+ - A^-})$ is the "dative" CT configuration wave function. An important requirement for the mixing is that ϕ_0 and ϕ_1 need to be of the same symmetry in the entire D-A complex frame. The first CT state wave function is primarily dative and has the form:

$$\Psi_E = a^*\phi_1(\mathrm{D}^+ - \mathrm{A}^-) - b^*\phi_0(\mathrm{D,A}). \tag{4.8}$$

Note that in the generalized version of this theory,[11] higher energy CT as well as the locally excited configurations have been included.

The electric dipole transition moment corresponding to the CT excitation can be given by:

$$\begin{aligned}\mu_{CT} &= \langle \Psi_E | \hat{\mu} | \Psi_N \rangle \\ &= a^* b\mu_{11} - ab^*\mu_{00} + (aa^* - bb^*)\mu_{01}\end{aligned} \tag{4.9}$$

μ_{00} and μ_{11} are simply the static dipole moments of the neutral "no-bond" and ionic "dative" configurations, and μ_{10} is the transition dipole moment between them. If D and A are both centro-symmetric, such as Bz and I_2, then $\mu_{11} \propto e\mathbf{R}$, where $\mathbf{R}$ is the vector pointing from the "center of charge" of D^+ to that of A^-. Hence, for typical vdW separations the magnitude of μ_{11} is on the order of 20 Debye. On the other hand, μ_{00} should be nearly zero or much smaller than μ_{11}, and Eq. (4.9) reduces to

$$\mu_{CT} \approx a^* b\mu_{11} + aa^*\mu_{10} \tag{4.10}$$

Therefore, the CT transition is dominated by the two major components. μ_{10} has been shown by Mulliken[10,11] to be roughly proportional to the spatial overlap of the donating and accepting orbitals. Since D and A are in a vdW contact, this component is expected to be small, although Mulliken[11] later pointed out that this term may be important due to the larger size of the accepting orbital. On the other hand, μ_{11} can be very large as mentioned above. The orientation of μ_{11} is rather invariant in the complex, pointing

roughly from the center of mass of D to that of A. However, the contribution of this component is largely reduced because the mixing coefficient b is usually small. In particular, if the mixing is forbidden by symmetry, then the first term in Eq. (4.10) vanishes.

It is difficult to judge the relative importance of the two components based on the above discussion and it might differ from case to case. However, the μ_{10} component alone is certainly not enough to explain the observed strong CT transition in D/I_2 systems. The μ_{11} term should dominate the CT transition whenever the ionic-neutral mixing is enhanced. The manifestation of this effect can be found in the strongly enhanced D•I_2 CT absorption intensity in solutions where the mixing can largely be enhanced by lowering of the symmetry as well as by solvation.

Having discussed the CT transition dipole moment, we now use Bz•I_2 as a prototype and explore three possible structures considered by Mulliken,[10] namely the "axial", "resting", and "oblique" structures, as schematically shown in Fig. 4.21. In the cases of the resting and oblique structures, the azimuth angle is arranged such that a plane of symmetry (xz) perpendicular to the benzene molecular plane is retained.

In the case of the *axial structure*, the complex belongs to the C_{6v} point group. The ground state is of A_1 symmetry, and the CT state is of E_1 symmetry. Based on group theory, the CT transition dipole is polarized in the benzene molecular plane. Since the CT state and the ground neutral state are of different symmetry, mixing between them is not allowed. Thus, no transition dipole component perpendicular to the benzene plane is present in the perfectly axial structure. *In this case, the transition dipole is perpendicular*

to the recoil direction of the high-energy iodine atom and the limiting value for β is -1. Obviously, this is in direct contradiction to the experimental results of β being positive.

If the complex assumes the *resting structure*, the point group of the complex is C_{2v}. The ground state is still A_1, but the CT state is split into two states with A_1 and A_2 symmetries due to the removal of the degeneracy. The transition from the ground state to the A_1 CT state is allowed and is perpendicular to the benzene plane. In this case, the CT transition can arise from both μ_{11} and μ_{10} terms as the A_1 ionic configuration can mix with the A_1 neutral configuration. The transition to the A_2 CT is forbidden. *Therefore, the transition dipole is also perpendicular to the recoil direction and the limiting value for β is -1, which is again in contradiction to the experimental findings.* Furthermore, the resting structure is not consistent with the observed two translational energy components from which a caging mechanism must be included.

In the case of *oblique structure*, the complex has a C_s symmetry. The ground state is of the A' symmetry and the CT state is again split into two states with A' and A" symmetries. Transitions from the ground state to both CT states are allowed. The transition to the A" state is polarized in the benzene plane and perpendicular to the symmetry plane. This transition can not be the dominant one since the transition dipole is perpendicular to the recoil direction and thus β=-1. For the transition to the A' state, by group theory the transition dipole is polarized in the plane of symmetry. However, Mulliken's theory shows that this transition can have a component perpendicular to the benzene plane. This is because the A' ionic configuration can mix with the A' neutral configuration to give rise to a nonzero μ_{11} term. On the other hand, the orientation of μ_{10} corresponding to the transition from the pure "no-bond" ground state (A') to the pure

"dative-bond" ionic states (A') is only known to be polarized in the plane of symmetry. However, its exact orientation should follow a smooth evolution when the complex is transformed from axial to resting structures. Hence, for small tilting angles, the complex is more like an axial structure and μ_{10} should be more parallel to the benzene plane. Likewise, for large tilting angles, μ_{10} should be more parallel to the norm of the benzene plane. Combining both μ_{11} and μ_{10}, it is possible to obtain an I_2 tilting angle θ such that the angle between the CT transition dipole and the recoil direction is about 35° which gives a theoretical β value of ~ +1.0, consistent with the experimental results.

Based on the above considerations, our results suggest that the Bz•I_2 structure is neither axial nor resting, since we clearly observed positive values for β's. The only possible structure that can account for the observed β is the oblique structure. This conclusion does not conflict with the many experimental and theoretical predictions that the axial structure is the most stable form. For a stable axial structure of Bz•I_2, our results simply suggest that I_2 is undergoing a large amplitude torsional motion at the moment when the complex is excited. This is to be expected even for the zero-point level because of the relative flatness of the potential energy along the I_2 internal rotational coordinate. Thus, when the Bz•I_2 CT state is prepared by fs laser pulses, the wave packet is launched at a nuclear configuration resembling an oblique structure, as schematically shown in Fig. 4.22. This picture brings to focus the importance of the angular part of the potential between Bz and I_2, similar to the case of Rg•HX.[65] Furthermore, in this quasi axial structure of lower symmetry, the wave packet samples transitions greatly enhanced by the μ_{11} component which might therefore dominate the CT excitation. At the exact axial geometry μ_{11} is zero and the system utilizes the much weaker μ_{01} contribution.

This conclusion is in a good agreement with the results of recent semi-empirical calculations concerning the transition dipole of Bz·I_2 reported by the Wiersma group.[42] The main conclusion of their calculations is that the transition dipole component parallel to the benzene plane is always much smaller than the perpendicular component. With the exception of the perfectly axial conformation, the direction of the transition dipole moment was found to be pointing (within ~10°) from the center of the benzene ring to the I_2 c.m. for all investigated structures including the three forms we have considered above. For the perfectly axial structure, they found that although the transition dipole is polarized in the benzene, its oscillator strength is ~ 200 times smaller then the maximum value found at a tilting angle of ~30°. Thus, their calculations suggest that the μ_{11} component is much more important than the μ_{10} component, making the transition dipole always perpendicular to the benzene plane. Since the experimental studies by Lenderink *et al.*[42] were conducted in solutions, the excitation of tilted configurations is done by photoselections through the $\mu \cdot \varepsilon$ interaction.

4.5.4. The Electron Transfer: Ionic/Neutral Branching

The ionic-neutral surface switching is eventually an intermolecular back electron-transfer process as a result of the mixing between the CT and neutral locally excited I_2 repulsive states. This process of ionic-covalent coupling is widely present in many chemical and biological D-A systems[66] where both ionic and covalent states are bound, as generically shown in Fig. 4.23(A). A schematic representation of the potential energy curves along the reaction coordinate for the present system is also shown for comparison in Fig. 4.23(B). The final state in the present system is repulsive and leads to an

irreversible dissociative electron transfer. The observed initial CT state decay (~ 250 fs) and the high-energy iodine build up (~ 450 fs) thus provide the important time scales for the intermolecular electron transfer between D^+ and I_2^-. Upon CT excitation, an electron is promoted from the HOMO (π) of benzene to the LUMO (σ^*) of I_2, creating an "electron-hole" pair in the complex (see Fig. 4.19). One of the electrons in the inner orbitals (σ, π, and π^*) of I_2 then rapidly jumps back to benzene in ~250 fs, producing an excited state of I_2 at the same energy as the initial CT state. On the other hand, the return of the σ^* electron originally promoted is greatly hindered by the large energy gap and may have to be accompanied by a radiative decay which is a much slower process.

In the limit of crossing or very weak avoiding, the reaction will dominantly proceed on the ionic potential. We have shown that this is not the case for the present systems since we clearly identify a large fraction of the iodine atom product arising from the neutral exit channel. In the limit of very strong avoiding, the reaction will mostly proceed through the lower adiabatic surfaces shown in Fig. 4.23(B), but the system switches its character from being ionic to being covalent at the avoiding region. This picture is consistent with our conclusion that the neutral channel is an important exit route, suggesting a strong surface avoiding exists along the seam near the region where the two surfaces intersect. Depending on the exact shape of the two surfaces, a barrier to dissociation may exist as a result of the avoided crossing and can influence the dissociation. The probability for crossing can be calculated using the Landau-Zener formalism, as applied for the harpoon reaction of NaI.[67]

Based on Mulliken's predictions,[48] there are at least 15 neutral repulsive states that can intersect the ionic surface of $Bz{\cdot}I_2$, including singlet and triplet states. Not all of these

states have the right symmetry to mix with the ionic state. In the perfectly axial structure, the electronic symmetry of the Bz•I_2 CT state is E_1. However, there are only three out of the 15 states that are of the π symmetry which transforms into E_1 under C_{6v} point group. On the other hand, if Bz•I_2 assumes an oblique structure, the symmetry constraint is greatly reduced. The electronic symmetry of the split CT states are A' and A". Since transition from the ground state to both CT states are allowed, all 15 I_2 repulsive states are allowed to mixed with the ionic states by symmetry. Since all neutral and ionic channels are parallel exit routes of the initial state, the ionic channel is suppressed simply by the outnumbered neutral exit channels. The symmetry constraint can also be relaxed in MBz•I_2 reactions even for the axial structure. Therefore, the extremely fast and similar time scales observed for the back electron transfer process in the Bz•I_2 and MBz•I_2 reactions give further support to the conclusion that the initial CT state is oblique. In solutions, as discussed in Sec. 4.5.7, the effective coupling is enhanced due to the instantaneous symmetry breakage by the solvent molecules.

There is no doubt that if all neutral channels could be turned off, the ionic channel can proceed as expected. In cases where the avoiding of the two surfaces is not so strong, the wave packet encountering the avoided region can have a small but finite probability to transmit across to the upper adiabatic surface. The wave packet entering the upper surface can either decay back to the lower surface through the same small transmission probability or proceed through the ionic part of the surface if energetically possible. Thus, depending on the rates of the two decay paths, the wave packet can be trapped in the upper surface for a long period of time. This gives the system a finite probability to

proceed through the ionic channel and the transient build up of its products will exhibit a different temporal behavior from the neutral channel.

Two evidences support the above points. First, the initial CT state decay for Bz•I_2 exhibits a bi-exponential behavior, as shown in Fig. 4.18(A). The smaller component of ~800 fs can be assigned to the decay of the wave packet that is trapped in the upper adiabatic surface and the rate (1/0.8 ps^{-1}) is the sum of both the ionic channel and the crossing back to the lower surface. For the mesitylene•I_2 system, Fig. 4.18(B), the smaller component is not as prominent. This is consistent with the smaller ionic branching ratio due to the lowered symmetry. Second, in Bz•I_2 and C_6D_6•I_2 reactions, the low-energy components observed in the iodine atom translational energy distributions weigh more than those in other reactions. This could be a result of larger ionic branching ratio in these two reactions due to the reduced ionic-covalent mixing caused by the highly symmetric donors involved.

4.5.5. One-molecule Caging

To describe the encounter of the caged iodine atom with the donor molecule, one has to consider the binding energy of the D•I complex and the relative collision energy between D and I. The D•I complexes have been shown in general to be more strongly bound than their corresponding molecular iodine complexes.[63] In particular, the heat of complex formation of o-xylene-I in solution has been reported to be -4.4 kcal/mole,[64] whereas that of Bz•I_2 complex is only about -2 kcal/mole. Therefore, the binding energy of o-xylene-I complex could be as high as 1,500 cm^{-1}. In the first extreme model discussed in Sec.4.5.2, the relative collision energies in the c.m. frame of D and I are ~

1,800 cm^{-1} (I^*+I^*), 3,600 cm^{-1} ($I+I^*$), and 5,400 cm^{-1} (I+I) for the three dissociation asymptotes. In the limit of the second extreme model, the collision energy is assumed to be zero and the available energy is partitioned between the uncaged iodine atom and the newly formed D•I complex. Therefore, the relative collision energy is expected to be lower than the values predicted by the first extreme model if the actual kinematics is somewhere between the two extreme cases. On the other hand, if a fraction of the available energy is initially in the D-I coordinate upon I_2 dissociation, the D-I collision energy can be higher. Overall, it is plausible that the observed 1.4 ps rise time is a result of the low collision energy and strong D-I binding. We will show below in Sec. 4.5.6. that this feature of relatively long dissociation times can be reproduced in molecular dynamics (MD) simulations. In addition, if the D•I_2 complex has an oblique structure, a finite impact parameter exists for the D-I collision and the associated centrifugal barrier may play a role in slowing down the dissociation.

Another consideration is that, during the collision, some available energy is channeled into the internal modes of D's, reducing the energy available for dissociation, and lengthening the complex lifetime. This T-V process is expected to be rather inefficient within the observed dissociation time scales owing to the weak coupling between the D internal modes and the D-I intermolecular vdW mode. The "inverse process" of V-T by predissociation typically takes 10 - 100 ps.[68] However, if D-I collision results in a collision complex of new chemical identity as an intermediate toward chemical reactions, the energy can be transferred to the internal modes of D in a short period of time thorough a much stronger chemical interaction. The 1.4 ps is then the lifetime of this "chemical" collision complex. This channel is supported by the results of

a cross-beam experiment on a similar system of "Br + chlorotoluene" reactions,[69] for which the collision complex was found to have a lifetime not much shorter than a rotational period (~ 5 ps) at collision energies of 20-35 kcal/mol. The translational energy disposal was also found to be very low, indicating that a significant amount of the available energy ends up in the internal vibrational modes of the aromatic ring. Although the collision energies in our case are below the threshold for the ring substitution (ΔH° ~ +1.84 eV for Bz) and hydrogen atom abstraction (ΔH° ~ +1.65 eV for ring H) reactions, they may be above the barrier to some "transition state" such as "iodocyclohexadienyl", which can have a finite lifetime long enough for the available energy to be distributed into the internal modes of the ring through a much stronger interaction. In this regard, the caging is fulfilled by chemical forces instead of the physical vdW interactions. What is clear is that the observed dynamics of the complex indicate its 1 ps duration. The complex can engage the vibrational phase space during the ps duration and breaks up by exit channels on a potential determined by the physical/chemical forces (see MD of Sec. 4.5.6).

4.5.6. Molecular Dynamics

Classical trajectory calculations were performed on empirical PES's for both the ionic and neutral exit channels. The purpose of these calculations was to provide a qualitative picture of the reaction dynamics. To simplify the task, we treated, given the time scale involved, the donor as a point mass with no internal degree of freedom. No angular part is included in the PES and the D-I-I system is assumed to be collinear. In the following discussion, r_1 is the I-I separation and r_2 is the D-I separation. Empirical PES's

are constructed by summing the potentials along r_1 and r_2 coordinates, *i.e.*, $V(r_1, r_2) = V_1(r_1) + V_2(r_2)$.

Trajectories were obtained by solving the equation of motion through numerical integration with a fixed time interval of 0.5 fs. The calculations were checked by making sure that the c.m. of the system was immobile and the total energy was conserved over the period of the calculated trajectories with satisfactory accuracy. The production of a free iodine atom is detected whenever the criterion of r_1 and/or $r_2 \geq 8$ Å is reached. The final speeds of the free iodine atoms were calculated with respect to the c.m. of the D-I-I system. We could also simulate the decay of the initial transition state by following the trajectory from t=0 and the motion in the transition state region. Only representative trajectories were calculated by launching the initial configurations at estimated r_1 and r_2. No attempt was made to average a large number of trajectories as the purpose of the current calculation is only to provide guidance and support to the proposed microscopic elementary steps.

4.5.6.1. The Ionic Channel: Harpooning

The PES for the CT state is constructed by combining a $Bz^+ \cdot I^-$ coulomb potential and a I_2^- Morse potential. The $Bz^+ \cdot I^-$ potential has the following form:

$$V_2(r_2) = \frac{C_{12}}{r_2^{12}} - \frac{C_1}{r_2} \tag{4.11}$$

The two parameters (C_{12}=1.159×10^5 eVÅ^{12} and C_1=11.4 eVÅ) are obtained by simultaneously fitting Bz·I_2 and Bz·I absorption maxima, 268 nm and 430 nm,

respectively, and by estimating the $Bz^+ \cdot I^-$ equilibrium separation of 2.9 Å. The ground state Bz-I equilibrium separation is assumed to be 3.6 Å in the fit. The parameter C_1 is smaller than the theoretical value of 14.42 eVÅ, reflecting either an incomplete charge-transfer or localized charge distributions. The I_2^- Morse potential is the one given by Chen and Wentworth:[53]

$$V_1(r_1) = -2k_A D\exp(-k_B\beta(r_1 - r_e)) + k_R D\exp(-2k_B\beta(r_1 - r_e)) \quad (4.12)$$

The parameters are given in Ref. 53.

For the $Bz \cdot I_2$ reaction, our 277-nm excitation is near the $Bz \cdot I_2$ CT absorption maximum and the initial CT configuration should be near the ground state equilibrium separations in both I-I and Bz-I coordinates. We calculated several trajectories with initial configurations within the range of (r_1=2.62-2.66 Å, r_2=3.6 Å), which correspond to available energies of ~0.3-0.5 eV. The reaction times for these trajectories are in the range of 1.0-2.4 ps, and the final speed of the neutral iodine atom is in the range of 100-650 m/sec. Fig. 4.24a shows a typical trajectory on the ionic PES. Vibrational excitation is seen in the $Bz^+ \cdot I^-$ product. It is interesting to note that these values are in accordance with the experimental results.

4.5.6.2. The Neutral Channel: Caging

The PES for the neutral channel is produced by combining a Bz-I vdW and I-I repulsive potentials. The forms of the potentials are:

$$V_1(r_1) = A\exp(-\frac{r_1}{L}), \quad V_2(r_2) = \frac{C_{12}}{r_2^{12}} - \frac{C_6}{r_2^6} \tag{4.13}$$

The parameters for V_1 are A=300 eV and L=0.5 Å, which are typical results from fitting the curves drawn by Mulliken for the I_2 repulsive states in Ref.(48). The parameters for V_2 are C_{12}=5.875×10^5 eVÅ^{12} and C_6= 540 eVÅ^6. These were obtained by assuming a vdW well depth of 1,000 cm^{-1} and an equilibrium D-I separation of 3.6 Å. The available energies are assumed to be localized in the I-I bond and are adjusted by initiating the trajectories at three different I-I separations to match the available energies of three dissociation asymptotes. Trajectories were calculated for several representative Bz-I separations between 3.2-4.0 Å, resembling a distribution of the ionic-neutral crossing points.

The results can be summarized as follows. For the I^*+I^* dissociation asymptote v= 900-1000 m/sec, τ= 380-440 fs (for the uncaged iodine atoms); v=300-475 m/sec, τ=850-1500 fs (for caged iodine atom if initial r_2=3.6-4.0 Å, Bz•I is bound if initial r_2=3.2-3.4 Å). For the I^*+I dissociation asymptote v= 1200-1350 m/sec, τ= 310-335 fs (for the uncaged iodine atom); v=350-780 m/sec, τ=570-1700 fs (for the caged iodine atom). Finally for the I+I dissociation asymptote v= 1480-1600 m/sec, τ= 270-290 fs (for the uncaged iodine atom); and v=400-730 m/sec, τ=470-700 fs (for the caged iodine atom). A typical trajectory is shown in Fig. 4.24b.

These results clearly show two distinct components both in the recoil speed (translational energy) and the dissociation times. In particular, the I^*+I^* and $I+I^*$ channels produce speeds that quantitatively agree with our measurements (note the distinct two components in each channel for velocity and reaction time). An interesting result is that

some trajectories give bound D•I complexes. These trajectories all start from a short Bz-I separation. The probability for Bz•I complexes to survive the dissociation is probably smaller in reality. The reason is that if the I_2 dissociation occurs at short Bz-I separation, a significant fraction of the available energy might stay in the Bz-I coordinate after the ultrafast ionic-neutral switching. Therefore, there is more energy for the Bz-I dissociation. Overall, it is satisfactory to see that MD simulations, with simple potentials, give a consistent picture of the dynamics and mechanism.

4.5.7. Comparison with Liquid Phase and Cluster Studies

4.5.7.1. Liquid Phase Studies

In this section, an attempt is made to bridge the dynamics of the isolated reaction to those in clusters and liquids. In the gas phase and in solutions, the CT spectra are clearly evident as shown in Fig. 4.4. With ps resolution, Langhoff *et al.*[40(a)] and Hilinski *et al.*[40(b)] explored the dynamics of these complexes and showed the ultrafast nature of the reaction, though not resolved. Two fs studies of D•I_2 reactions in the liquid phase have been reported recently by the groups of Wiersma[41] and Sension.[43] Here, we will discuss these results and compare the initial dynamics (<1 ps) reported in solutions with our findings. Long-time dynamics due to recombination and vibrational relaxation in solutions are not considered here.

Using a CPM laser system, Lenderink *et al.*[41] excited the complexes in I_2/mesitylene and I_2/toluene solutions at 310 nm and probed the photoproducts over the wavelengths range from 400 to 700 nm. When probed at 620 nm, they found that the transient absorption of the D•I complex rose within 25 fs. A transient absorption spectrum

characteristic of molecular I_2 in solutions was also observed to appear on the same time scale, suggesting an impulsive fragmentation along the D-I_2 coordinate. Lenderink *et al.*[41] concluded that the excited complex branches into two different channels through parallel exit routes in 25 fs. The major channel (75%) involves breaking up of the D•I_2 into its constitute molecules of D and I_2. In the other channel, the D-I complex and an iodine atom are formed.

The fs study reported by Pullen *et al.*[43] focused on the reactions of CT complexes in I_2/mesitylene solutions. Using a Ti:Sapphire laser system, they excited the complexes at 400 nm and probed the products at wavelengths ranging from 400 to 750 nm. The characteristic transient absorption spectrum of the mesitylene•I complex was found to be fully developed within 500 fs of the pump pulse. The authors also concluded that photodissociation occurs along both the mesitylene•I_2 and the I-I coordinates with a branching ratio of 2:3. The time scale for the bond breaking was estimated to be $\leq$ 250 fs in this study. Both studies indicated that the dissociations occur in both D•I_2 and I-I coordinates on a very short time scale of 25 ~ 250 fs. The difference in the time scales of reactions could be simply due to the different excitation wavelengths. As pointed out by Pullen *et al.*,[43] the 310 nm and 400 nm excitation are, respectively, in the blue and red ends of the I_2/mesitylene solution CT absorption band. Sension's group has also measured transient absorption and anisotropy decay of hexamethylbenzene•I_2 in solutions and concluded that the complex has an oblique, nearly axial, geometry in alkanes. This result is consistent with our conclusion discussed in Sec. 4.5.3.

We have recently used a Ti:Sapphire amplified system and obtained the transient absorption by exciting I_2/mesitylene solution at 400 nm and probing the reaction at 620

nm. We too see a rise within 100 fs and confirm the form of the transient reported by Lenderink *et al.*[41] The extremely rapid birth of the D•I complex in solutions following the CT excitation is consistent with the ultrafast ionic-neutral surface switching mechanism we proposed for the gas-phase $D•I_2$ reactions.

In solutions, the $D•I_2$ reaction centers are surrounded by solvent molecules. Following the ionic to neutral transition, the caged iodine atoms may remain bound to the donors and are detected as D•I complexes because of the presence of other solvent molecules in the immediate vicinity. The transient absorption in solutions could therefore appear faster (25 fs)[41] than the build up of the high-energy iodine atoms observed (450 fs) in our experiments. This is because the I-I separation does not need to be as large in solutions to develop the characteristic absorption of the D•I complexes (in our case, iodine atoms have to be separated far enough to be detected as a free iodine atom by the mass spectrometry). Furthermore, the random solute-solvent orientations in solutions can enhance the ionic-neutral state mixing and therefore increase the dissociation rates. The opening of the neutral channel produces ground state D•I complexes in solution and this is consistent with the fact that transient absorption observed in solution and gas phases has been assigned as due to ground state absorption of D•I, not $D^+•I^-$. Thus, the comparisons discussed above show that the initial dynamics of $D•I_2$ reactions in the isolated gas phase is similar to that in solutions.

Another interesting result obtained by Lenderink *et al.*,[41] and confirmed by us, is that a slower rise (t=400 fs) was also observed following the rapid initial rise of 25 fs. They attributed this to the additional mesitylene-I complexes that are formed by iodine atoms launched into the solvent and which subsequently react with other solvent

molecules. Their interpretation is strongly supported by the observation that the 400 fs component is much less intense in mixed mesitylene/alkane solutions where fewer mesitylene molecules are available to react with. This picture is very similar to the caged iodine atom in our case, since it is the one that directly faces a solvent molecule as the impulsive dissociation of I_2 occurs. Our results show that it takes about 1 ps for the iodine atom to escape from the solvent force field. In solutions, the bouncing iodine atom are surrounded by more solvent molecules which can rapidly cool it down translationally such that it is finally bound to a specific solvent molecule. This process should take a shorter time than the complete cage exit.

An important exit channel considered in solutions is the dissociation along the D-I_2 coordinate. By measuring a transient absorption in the visible, both groups suggested that this process takes place very rapidly, as fast as the formation of D•I product. Although we have no information on the transient I_2 formation, we believe that this channel is relatively minor in the isolated 1:1 complex. However, the neutral channel in the 1:1 complex would lead to some I_2 formation. In the presence of large solvent bath, the dissociating I_2 molecules can be caged rapidly (translational cooling) and a fast geminate recombination may take place on the sub-ps time scale as, *e.g.*, in the case of I_2 in Ar solvent.[70] With the aid of solvent perturbation, non-adiabatic couplings to the ground state can lead to bound, vibrationally-hot I_2 molecules. This kind of non-adiabatic processes can be very fast in solutions, although vibrational relaxation is typically on the ps time scale. For example, the reverse process of I_2 B-state predissociation, a slow process in the gas phase, has been shown to occur in ~ 200 fs in solution[71] and this time

scale is determined by the non-adiabatic coupling between the B state and the repulsive potentials.

4.5.7.2. Cluster Studies

We have previously reported[23] on the iodine atom transients when solvation with benzene is increased. The observed behavior at high benzene concentrations, Fig. 4.5(B), was related to the cage exit dynamics in large $(Bz)_n \cdot I_2$ clusters.[23] It was concluded that two distinct types of cluster solvations are present: one in which iodine atoms are caged by the solvent molecules and the other for which only one iodine atom is caged. These structures were considered with the reactive pathway determined by the harpoon channel. In view of the contribution of the neutral channel we shall consider both channels in our discussion here.

Under high benzene concentration conditions, a broad size distribution of clusters is present in the molecular beam, as clearly manifested by the TOF-MS spectra shown in Fig. 4.5(A). The iodine atoms detected under such conditions thus come from a wide range of clusters of different sizes and structures. Yet, the observed transients exhibit distinct bi-exponential behaviors which is robust under all experimental conditions. The evolution of the transients is clearly accompanied by the change of the size distribution of clusters in the beam. These observations provide some clues to the fundamental architecture of the clusters.

First, the much slower rise components (τ~ 20-75 ps) observed under cluster conditions (Fig. 4.5(b)-(e)) suggest a structure that is very different from the 1:1 complex. We attribute this slow-rise component to those complexes in which the iodine atoms are

caged. Since the one-molecule caging time is on the order of 1.4 ps and the back electron transfer releases at least 1 eV of energy, we believe that the solvent cage which gives rise to the slow component must be sufficiently large. The evolution of the time constants of the slow-rise component from 20 to 75 ps and their relative weights are a manifestation of the increase of the averaged cluster size in the beam, consistent with the corresponding TOF-MS spectra.

As discussed earlier in this Chapter, the initial apparent rise observed in the 1:1 complex is a synthesis of two components: an extremely fast one (450 fs) arising from the prompt dissociation of the uncaged iodine atom and a slower one ($\tau \sim 1.4$ ps) which comes from the caged iodine atom. As the cluster size increases (Fig. 4.5(b)-(e)), the initial apparent rise also becomes slower reaching longer than 2 ps. We attribute the initial rise to those trajectories in which at least one iodine atom is not caged by the solvent molecules. These include cluster structures with an incomplete solvent shell and with I_2 bound to the surface of a pure solvent cluster. In this architecture, the uncaged iodine atoms are still able to dissociate from the complexes freely without direct interactions with the rest of the system, although they may take a longer departing time due to the stronger vdW attraction resulting from the larger solvent clusters. After dissociation, the caged iodine atoms encounter, instead of a single solvent molecule, a cluster of solvent molecules, which should significantly slow down the escape of the caged iodine atoms. For small clusters (n=2,3), the dissociation times of the caged iodine atoms are expected to be slightly longer than those in the 1:1 complex. For larger clusters, they may take significantly longer times to escape the solvent clusters and

therefore can contribute to the slow components. Trapping of the caged iodine atoms in large clusters is also possible.

In addition to monitoring the escaped iodine atoms, we have also followed the initial CT state dynamics in large clusters by monitoring the transient signal directly from parent $(Bz)_n \cdot I_2^+$ mass channels (n=1-4) under large cluster conditions. The successful detection of the transient signal in these parent mass channels is due to the lower I_D's and fragmentation of the larger cluster cations, and therefore each transient is likely to be a hybrid of transients arising from clusters larger than the one monitored. Transients observed from n=1-4 mass channels are almost identical and are dominated by an extremely fast decay with a similar time scale to those observed for the 1:1 complex. This result clearly shows that, although the cage exit takes tens of ps, the initial motion in the transition state is so fast such that the system moves out of the probing window in ~200 fs even in large clusters. The result is completely consistent with the solution results where the reaction is found to be ultrafast (25 - 250 fs) even when I_2 is surrounded by a large number of solvent molecules.

In summary, the two time scales observed in the iodine atom transients can be assigned to the caged and uncaged iodine atoms present in the $(B_Z)_n \cdot I_2$ clusters studied here. This characteristic is remarkably persistent from the 1:1 complex to the large $(Bz)_n \cdot I_2$ clusters, providing important insights into the solvation structure as well as cage exit dynamics. The fs initial state decay observed in large clusters indicates the ultrafast nature of the motion in the transition state. The distinct solvent structures found here have analogy in theoretical studies made recently on, *e.g.*, $HF(Ar)_n$,[72] $I_2(Ar)_n$[73] and $I_2^-(CO_2)_n$.[74] A full account of cluster studies is given in Chapter 7.

4.6. Conclusion

In this contribution, we have studied the transition state of CT reactions of 1:1 donor (D)-acceptor (A) complexes of benzene and its deuterated and methyl substituted species with iodine, isolated in a molecular beam, using fs transition-state spectroscopy and time-resolved kinetic-energy mass spectrometry. The CT transition state was directly reached by fs excitation and the dynamics were followed by monitoring either the product build up or the initial state decay. Upon CT preparation of the complexes, free iodine atoms were found to appear very rapidly, on a time scale of less than 1 ps for all systems studied. The initial transition state decays extremely fast (~ 250 fs) and exhibits a bi-exponential behavior in the $Bz{\cdot}I_2$ case.

The translational energy distributions of the iodine atom products exhibit two distinct components: one peak at a low energy (less than 1,000 cm^{-1}) and the other at a high energy of about 5,000 cm^{-1}. The two components also show different temporal behaviors: the high-energy one rises very rapidly (450 fs), whereas the low-energy component builds up much more slowly (1.4 ps). The recoil anisotropy (β) was measured for the two distributions. From these experiments, we obtained the direction of recoil relative to the direction of the transition moment, 30-35°, indicating that the transition state structure is nearly axial, oblique.

The elementary dynamics involve two exit channels, namely the ionic and covalent pathways, Bz^+I^- + I and BzI + I respectively. After fs initiation of the CT, the prepared wave packet quickly moves on the CT surface and bifurcates near the ionic-neutral interaction region. Some portion of the population continues on the adiabatic,

harpooning potential. The remaining, larger portion of the wave packet population then quickly (250 fs) switches to the neutral repulsive surface through an intermolecular back electron transfer, leading to a direct I+I dissociation. The uncaged iodine atom dissociates freely and gives rise to the rapid (450 fs) high-translational-energy component. The caged iodine atom, on the other hand, encounters the electron donor molecule and slowly escapes from its force field with significant loss in its translational energy. At the interaction region, a small portion of the wave packet population transmits into the trapping well formed by the avoided crossing of the ionic and neutral surfaces. The trapped wave packet then slowly decays (~ 800 fs) by proceeding through the ionic exit or transmitting back to the lower neutral surface. MD simulations and descriptions of the HOMO/LUMO orbital interactions support our picture.

The present study reveals the complexity involved in the reaction dynamics of a seemingly simple system, studied for more than half century, whose initial state spectra or product-state yields do not permit the elucidation of the dynamics in the transition-state region nor would they indicate the nature of the ionic-covalent channels. Through the studies in collisionless environments and with the aid of fs temporal and translational-energy resolutions, the dynamics can be revealed and the structure elucidated. The ability of fs time resolution to initiate the reaction wave packet from a well-defined region of intermolecular separations is critical to such studies. This work promises other applications, including different reactions, solvation dynamics, and CT reactions on or near surfaces.

4.7. References

1. P. Y. Cheng, D. Zhong, and A. H. Zewail, J. Chem. Phys. **103** (1995) 5153.
2. N. F. Scherer, L. R. Khundkar, R. B. Bernstein, and A. H. Zewail, J. Chem. Phys. **87** (1987) 1451; I. R. Sims, M. Gruebele, E. D. Potter, and A. H. Zewail, *ibid.* **97** (1992) 4127.
3. A. H. Zewail, Science **242** (1988) 1645.
4. T. S. Rose, M. J. Rosker, and A. H. Zewail, J. Chem. Phys. **91** (1989) 7415.
5. J. A. Syage, P. M. Felker, and A. H. Zewail, J. Chem. Phys. **81** (1984) 2233.
6. S. K. Kim, J. J. Breen, D. M. Willberg, L. W. Peng, A. Heikal, J. A. Syage, and A. H. Zewail, J. Phys. Chem. **99** (1995) 7421.
7. E. D. Potter, J. L. Herek, S. Pedersen, Q. Liu, and A. H. Zewail, Nature **355** (1992) 66.
8. C. Dedonder-Lardeux, M. Berdah, C. Jouvet, S. Martrenchard-Barra, J. M. Mestdagh, D. Solgadi, and J. P. Visticot, J. Chem. Phys. **104** (1996) 2740.
9. H. A. Benesi and J. H. Hildebrand, J. Am. Chem. Soc. **71** (1949) 2703.
10. R. S. Mulliken, J. Am. Chem. Soc. **72** (1950) 610; **74** (1952) 811.
11. R. S. Mulliken and W. B. Person, *Molecular Complexes: A Lecture and Reprint Volume* (Wiley-Interscience, New York, 1969).
12. K. Liu, J. C. Polanyi, S. Yang, J. Chem. Phys. **96** (1992) 8628; **98** (1993) 5431; J. C. Polanyi and J. X. Wang, J. Phys. Chem. **99** (1995) 13691.
13. R. B. Metz, S. E. Bradforth, and D. M. Neumark, Adv. Chem. Phys. **81** (1992) 1; D. M. Neumark, Annu. Rev. Phys. Chem. **43** (1992) 153.

14. P. Hering, P. R. Brooks, R. F. Curl, R. S. Judson, and R. S. Lowe, Phys. Rev. Lett. **44** (1980) 687; P. R. Brooks, Chem. Rev. **88** (1988) 407.

15. M. Boivineau, J. Le Calvé, M. C. Castex, and C. Jouvet, Chem. Phys. Lett. **128** (1986) 528; Chem. Phys. Lett. **130** (1986) 208; J. Chem. Phys. **84** (1986) 4712.

16. C. Jouvet, M. Boivineau, M. C. Duval, and B. Soep, J. Phys. Chem. **91** (1987) 5416.

17. T. O. Nelson, D. W. Setser, and J. Qin, J. Phys. Chem. **97** (1993) 2585.

18. S. I. Ionov, G. A. Brucker, C. Jaques, L. Valachovic, and C. Wittig, J. Chem. Phys. **99** (1993) 6553; S. A. Wright, M. F. Tuchler, and J. D. McDonald, Chem. Phys. Lett. **226** (1994) 570; R. D. van Zee and J. C. Stephenson, J. Chem. Phys. **102** (1995) 6946.

19. St. J. Dixon-Warren, E. T. Jensen, J. C. Polanyi, G. Q. Xu, S. H. Yang, and H. C. Zeng, Faraday Disscus. Chem. Soc. **91** (1991) 451.

20. J. C. Polanyi and A. H. Zewail, Acc. Chem. Res. **28** (1995) 119.

21. J. M. Saveánt, Adv. Phys. Org. Chem. **26** (1990) 1.

22. L. Eberson, Acta. Chem. Scand. **B36** (1982) 533; L. Eberson, *Electron Transfer Reactions in Organic Chemistry* (Springer-Verlag, Berlin, 1987).

23. P. Y. Cheng, D. Zhong and A. H. Zewail, Chem. Phys. Lett. **242** (1995) 369.

24. E. Beckmann, Z. Physik. Chem. **5** (1889) 76.

25. M. W. Hanna, J. Am. Chem. Soc. **90** (1968) 285; M. W. Hanna and J. Lippert, in *Molecular Complexes*, ed. R. Foster (Elek Science, London, 1973), and references therein.

26. L. J. Andrews, Chem. Rev. **54** (1954) 713; S. McGlynn, Chem. Rev. **58** (1958) 1113.

27. *Spectroscopy and Structure of Molecular Complexes,* ed. J. Yarwood (Plenum Press, New York, 1973); *Molecular Complexes,* ed. R. Foster (Elek Science, London, 1973).

28. E. M. Voigt and B. Meyer, J. Chem. Phys. **49** (1968) 852.

29. F. T. Lang and R. L. Strong, J. Am. Chem. Soc. **87** (1965) 2345.

30. D. Atack and O. K. Rice, J. Phys. Chem. **58** (1954) 1017.

31. T. D. McLean, B. B. Ratcliff, J. Z. Pastalan, and K. K. Innes, J. Quant. Spectrosc. Radiat. Transfer **42** (1989) 445.

32. E. Kochanski and J. Prissette, Nouv. J. Chim. **4** (1980) 509.

33. J. Su and A. H. Zewail, J. Phys. Chem. **102** (1998) 4082. The *ab initio* calculations found a near flat potential for I_2 on benzene, consistent with X-ray structural findings for similar halogen-benzene systems.[35]

34. E. E. Ferguson, J. Chem. Phys. **25** (1956) 577.

35. O. Hassel and K. O. Strømme, Acta. Chem. Scand. **12** (1958) 1146; *ibid.* **13** (1959) 1781.

36. L. Fredin and B. Nelander, J. Am. Chem. Soc. **96** (1974) 1672.

37. J. C. Schug and M. C. Dyson, J. Chem. Phys. **58** (1973) 297; J. C. Schug and K. A. Levinson, Theoret. Chim. Acta. **37** (1975) 269; I. Jano, Theoret. Chim. Acta. **66** (1985) 341.

38. T. A. Gover and G. Porter, Proc. R. Soc. A, **262** (1961) 476; S. J. Rand and R. L. Strong, J. Am. Chem. Soc. **82** (1960) 5; N. Yamamoto, T. Kajikawa, H. Sato, and H. Tsubomura, J. Am. Chem. Soc. **91** (1969) 265.

39. V. A. Brosseau, J. R. Basila, J. F. Smalley, and R. L. Strong, J. Am. Chem. Soc. **94** (1972) 716.

40. (a) C. A. Langhoff, K. Gnädig and K. B. Eisenthal, Chem. Phys. **46** (1980) 117; (b) E. F. Hilinski and P. M. Rentzepis, J. Am. Chem. Soc. **107** (1985) 5907.

41. E. Lenderink, K. Duppen, and D. A. Wiersma, Chem. Phys. Lett. **211** (1993) 503.

42. E. Lenderink, K. Duppen, F. P. X. Everdij, J. Mavri, R. Torre, and D. A. Wiersma, J. Phys. Chem. **100** (1996) 7822.

43. S. Pullen, L. A. Walker II, and R. J. Sension, J. Chem. Phys. **103** (1995) 7877.

44. L. A. Walker II, S. Pullen, B. Donovan, and R. J. Sension, Chem. Phys. Lett. **242** (1995) 177.

45. M. J. Rosker, M. Dantus, and A. H. Zewail, J. Chem. Phys. **89** (1988) 6113.

46. A. H. Zewail, *Femtochemistry: ultrafast dynamics of the chemical bond* (World Scientific, Singapore, 1994), and articles therein.

47. After the benzene vapor was shut off, pure He was allowed to flow over the iodine crystals through the gas lines for a short period of time, typically 10-30 minutes depending on the donors until no benzene parent ion could be seen in the TOF-MS. This procedure removed adsorbed benzene.

48. R. S. Mulliken, J. Chem. Phys. **55** (1971) 288.

49. E. R. Bernstein, in: *Atomic and Molecular Clusters*, ed. E. R. Bernstein (Elsevier, New York, 1990).

50. C. N. Rao, G. C. Chaturvedi, and S. N. Bhat, J. Mol. Spectrosc. **33** (1970) 554.

51. J. Birks, *Photophysic of Aromatic Molecules* (Wiley, New York, 1970) and references therein.

52. L. Asbrink, E. Lindholm, and O. Edqvist. Chem. Phys. Lett. **5** (1970) 609.

53. E. C. M. Chen and W. E. Wentworth, J. Phys. Chem. **89** (1985) 4099.

54. A. Engdahl and B. Nelander, J. Chem. Phys. **78** (1983) 6563.

55. K. D. Raner, J. Lusztyk, and K. U. Ingold, J. Phys. Chem. **93** (1989) 564.

56. Ch. A. Brau, in: *Excimer Lasers*, ed. C. K. Rhodes (Springer-Verlag, Berlin 1979).

57. J. K. Ku and D. W. Setser, in: *Photochemistry and Photophysics above 6 eV*, ed. F. Lahmani (Elsevier, Amsterdam, 1985).

58. R. J. Donovan, P. Greenhill, M. A. MacDonald, A. J. Yencha, W. S. Hartree, K. Johnson, C. Jouvet, A. Kvaran, and J. P. Simons, Faraday Discuss. Chem. Soc. **84** (1987) 221.

59. D. R. Herschbach, Adv. Chem. Phys. **10** (1966) 319; J. L. Kinsey, G. H. Kwei, and D. R. Herschbach, J. Chem. Phys. **64** (1976) 2133.

60. J. Li and K. Balasubramanian, J. Mol. Spectrosc. **138** (1989) 162; C. Teichteil and M. Pelissier, Chem. Phys. **180** (1994) 1.

61. J. Segall, Y. Wen, C. Wittig, A. Garcia-Vela, R. B. Gerber, Chem. Phys. Lett. **207** (1993) 504; C. Jaques, L. Valachovic, S. Ionov, E. Bohmer, Y. Wen, J. Segall, C. Wittig, J. Chem. Soc. Faraday Trans. **89** (1993) 1419.

62. R. B. Gerber, A. B. McCoy, and A. Garcia-Vela, Annu. Rev. Phys. Chem. **45** (1994) 275.

63. G. Porter and J. A. Smith, Proc. Roy. Soc. **A261**, 28 (1961); R. L. Strong, J. Phys. Chem. **66** (1962) 2423.

64. R. L. Strong and J. Perano, J. Am. Chem. Soc. **89** (1967) 2535.

65. R. B. Bernstein, *Chemical Dynamics via Molecular Beam and Laser Techniques* (Oxford University Press, 1982).

66. R. A. Marcus and N. Sutin, Biochim. Biophys. Acta **811** (1985) 265; *Photoinduced Electron Transferm,* eds. M. A. Fox and M. Chanon (Elsevier, Amsterdam, 1988).

67. T. S. Rose, M. Rosker, and A. H. Zewail, J. Chem. Phys. **91** (1989) 7415.

68. D. M. Willberg, M. Gutmann, J. J. Breen, and A. H. Zewail, J. Chem. Phys. **96** (1992) 198.

69. G. N. Robison, R. E. Continetti, and Y. T. Lee, J. Chem. Phys. **89** (1988) 6226.

70. J. K. Wang, Q. Liu, and A. H. Zewail, J. Phys. Chem. **99** (1995) 11309; Q. Liu, J. K. Wang, and A. H. Zewail, J. Phys. Chem. **99** (1995) 11321.

71. N. F. Scherer, D. M. Jonas, and G. R. Fleming, J. Chem. Phys. **99** (1993) 153.

72. T. Schröder, R. Schinke, S. Liu, Z. Bacic, and J. W. Moskowit, J. Chem. Phys. **103** (1995) 9228.

73. C. C. Martens, in: *Femtochemistry, the Lausanne Conference*, ed. M. Chergui (World Scientific, Singapore, 1996)

74. J. M. Papanikolas, P. E. Maslen, and R. Parson, J. Chem. Phys. **102** (1995) 2452.

4.8. Figure Captions and Figures

Figure 4.1. The reaction path relevant to charge-transfer reactions and the concept of the approach presented in this work. The transition state $[A^{+}\cdot\cdot{}^{-}B\cdot\cdot C]^{\ddagger}$, which is a hybrid of the ionic and covalent configurations, can be reached by harpooning at the covalent-ionic intersection in the entrance channel (reactants), or by direct fs excitation at t=0 from the ground state through CT transition. The reaction then proceeds through ionic and/or covalent channels depending on the nature of the transition state.

Figure 4.2. Molecular structure of Bz·I_2 based on the results of *ab-initio* calculations.[33]

Figure 4.3. (A) A schematic diagram showing the cuts on the PES along the Bz-I and I-I coordinates. In the present study, CT transition state is directly reached by the t=0 fs pulse ($\lambda^{\ddagger}$). The reaction proceeds through the exit channels either on the same CT PES shown in (B) or through nonadiabatic transitions which leads to the I-I bond breakage. (B) A PES contour map of the Bz·I_2 CT state and a representative trajectory of the reaction on this PES (see text).

Figure 4.4. (A) Absorption spectra of iodine solutions with various solvents. The absorption in the visible region is due to the uncomplexed I_2 B←X band, whereas that in the UV region is due to the complex CT absorption. Note the different scales in the two regions and the very weak absorption when iodine is dissolved in the "inert solvent" CCl_4. The figure is adapted from Ref. 9. (B) Absorption spectra of Bz·I_2 in Ar and Xe

solid matrices at 20 K. The broad absorption bands centered at 281 nm (Ar) and 285 nm (Xe) are due to the Bz·I_2 CT absorption. The sharp features in the $\lambda \leq 260$ nm region are due to the uncomplexed benzene $S_1 \leftarrow S_0$ absorption. Note that when only I_2 was deposited in the matrix no CT absorption was observed (dashed line). Adapted from Ref. 28. (C) UV absorption spectra of gas phase benzene, iodine, and Bz/I_2 mixtures at a temperature of 340 K. The Bz·I_2 complex absorption spectrum was obtained from the difference. The concentration of the Bz·I_2 complex was estimated to be 2-3 orders of magnitudes smaller than those of uncomplexed I_2 and Bz in the gas mixture. Adapted from Ref. 29.

Figure 4.5. (A) TOF-MS spectra taken under identical conditions except with different benzene vapor pressures in the gas mixtures: (a) 0.5 Torr; (b) 1.3 Torr; (c) 3.3 Torr; (d) 9.5 Torr and (e) 24 Torr. These spectra were obtained by using the 277 nm fs pulses alone as the ionization laser. The laser intensity was reduced to minimize fragmentation of cluster ions. The TOF-MS parameters were optimized for the general mass range of n= 4-6 clusters. (B) Free iodine atom transients obtained under the corresponding conditions in (A). The transients displayed in the right panel show the long-time behavior while those displayed in the left panel show the early-time dynamics. The open circles are the raw data and the solid lines are the results of bi-exponential rise fits. The time constants for the slower components were obtained by fitting the long-time transients. The time constants for the faster component were then obtained by fitting the short-time transients with the slow component time constants fixed. All transients were

normalized to the same maximum for comparison. The absolute transient iodine atom signal actually increases with the benzene concentration.

Figure 4.6. (a) Background iodine atom transient obtained when only I_2 is present in the gas mixture. (b) iodine atom transient recorded when both I_2 and benzene are present in the gas mixture. The benzene vapor pressure is ~0.5 Torr, *i.e.*, the 1:1 condition. (c) result of subtraction of transient (a) from transient (b). The open circles are the raw data and the solid line is a single exponential fit. The dashed line is an aniline 1+1 REMPI transient resembling the system response. Note the similarity between transient (b) and (c).

Figure 4.7. Pump laser (277 nm) intensity dependence of the transient iodine-atom signal measured at a pump-probe delay time of ~1ps. These measurements were carried out under the "cluster condition" as the signal level under the 1:1 condition is too low to be measured accurately with reduced laser intensity. However, at 1 ps the contribution from the larger clusters is minimal. Moreover, the pump laser intensity dependence measured at a very long delay time of ~500 ps gave essentially the same result, indicating that the iodine atoms are produced at a one-photon excitation level for both the 1:1 and larger complexes. The slope is 0.94±0.05.

Figure 4.8. Pump laser wavelength dependence of the apparent rise time constants of the iodine transient observed for the Bz·I_2 reaction. Each data point (•) represents the

result of a single run of experiment. The solid straight line is only for guidance of the trend.

Figure 4.9. Typical iodine atom transients resulting from 277 nm excitation of D•I_2 complexes. The electron donors for the transients shown here are, from top to bottom, deutrobenzene, toluene, m-xylene and 1,2,4 trimethylbenzene. The apparent rise time constants are indicated for each case.

Figure 4.10. KETOF (v_Z) distributions of iodine atoms resulting from (A) o-xylene•I_2 and (B) Bz•I_2 complexes, excited at 277 nm, for three pump laser-polarization angles (χ) with respect to the TOF-MS axis. The pump-probe delay time was fixed at ~6 ps in both cases.

Figure 4.11 (a) *Upper panel:* Recoil speed distribution of free iodine atoms produced from the o-xylene•I_2 reaction at a pump-probe delay time of ~6 ps. The open circles are the raw data derived from the magic angle data shown in Fig. 4.10(A) and the solid line is the result of a two-gaussian fit. Note that the speed is the relative speed of the iodine atom with respect to the c.m. of the precursor complex. *Lower panel:* Translational energy distribution of the free iodine atom resulting from the o-xylene•I_2 reaction. The long arrows indicate the energies calculated by the first extreme model described in the text, whereas the short arrows are for those predicted by the second extreme model. The thick arrows denote the uncaged iodine atom and the thin arrows denote the caged iodine atom. The accompanied * and ** indicate the dissociation asymptotes I+I^* and I^*+I^*,

respectively, along the I-I coordinate in the neutral exit channels. Note that the energy is the relative translational energy of the iodine atom with respect to the c.m. of the precursor complex. (b) Recoil speed and translational energy distributions of the free iodine atoms resulting from the Bz•I_2 reaction at a pump-probe delay time of ~ 6 ps. These are derived from the magic angle data shown in Fig. 4.10(B). All other aspects are the same as those described in (a).

Figure 4.12. Recoil anisotropy parameters and speed distributions of the free iodine atoms produced in four D•I_2 reactions. The electron donors of the complexes are indicated in each figure and the solid curve in the speed distribution is the result of the two-gaussian fit.

Figure 4.13. Typical results of the non-linear least square fit of the parallel polarization KETOF distributions to the speed distributions derived from the magic angle data. The open circles are the raw data and the solid lines are the results of the fit. Since the fitting procedure only uses the first half ($v_Z>0$) of the KETOF distribution, the second half ($v_Z<0$) of the data shown here are the replica of the first half.

Figure 4.14. Translational energy distributions of iodine atoms produced from various D•I_2 complexes excited at 277 nm and measured at a pump-probe delay time of ~6 ps. The electron donors of the complexes are (a) benzene; (b) deutrobenzene; (c) toluene; (d) p-xylene; (e) m-xylene; (f) o-xylene; (g) mesitylene; and (h) 1,2,4-trimethylbenzene. Note the broader low-energy components in the cases of Bz•I_2 and C_6D_6•I_2.

Figure 4.15. Time-resolved, KETOF distributions of iodine atoms resulting from the o-xylene•I_2 reaction measured at a series of pump-probe delay times. Pump laser polarization is (A) at the magic angle and (B) 0° (parallel) with respect to the TOF-MS axis. The pump-probe delay times are indicated for each distribution.

Figure 4.16. Time-resolved, translational energy distributions of iodine atoms resulting from the o-xylene•I_2 reactions measured at a series of pump-probe delay times. These data are derived from the magic angle KETOF distributions shown in Fig. 4.15(A).

Figure 4.17. Plots of the integrated intensities (•) of the low- and high-energy components of the time-resolved, translational energy distributions shown in Fig. 4.16 against the pump-probe delay times. The solid lines are the results of single-exponential fits to these data points with the system response convolution (see text).

Figure 4.18. (A) Transients obtained by monitoring the signal in the Bz^+ mass channel as a function of the pump (277 nm) and probe (304-nm) delay time for the Bz•I_2 reaction using the synch-pumped laser system. As described in the text, these transients reflect the dynamics of the initial CT state of Bz•I_2. The solid lines are results of bi-exponential decay fits. (B) Transient obtained in a similar experiment on the mesitylene•I_2 reaction using the CPM laser system. The pump and probe wavelengths are 310 nm and 620 nm, respectively (see text).

Figure 4.19. (A) Schematic diagram showing the electronic configurations of benzene and molecular iodine. The arrow represents the first CT excitation which promotes an electron from the HOMO of the donor to the LUMO of the acceptor. (B) Schematic diagram showing the back electron transfer process which leaves the molecular iodine electronically excited. (C) Pictorial representation of the HOMO (benzene) and LUMO (I_2).

Figure 4.20. Potential energy curves along the Bz-I and I-I coordinates. The thick solid curves correlate to the zero-point levels of Bz^+ and I_2^- (also Bz and I_2). The dashed curve shown in the Bz-I coordinate correlates to I_2^- with a vibrational excitation due to vertical electron attachment (see text for detail).

Figure 4.21. Pictorial illustration of the three structures considered for the Bz·I_2 complex: (A) axial, (B) oblique, and (C) resting. The two balls represent the iodine atoms and the rectangle the benzene plane. In (B) and (C), a plane of symmetry (xz) is retained. The ground and CT state symmetries and the associated transition dipole orientations are also shown for each case, as described in the text.

Figure 4.22. PES contour map of the Bz·I_2 complex in a polar representation V(R, θ), where R is the distance between the c.m.'s of the two moieties and θ is the I_2 pivoting angle around its c.m. The shaded rectangle represents the benzene molecular plane. The PES has a global minimum at θ=0 (white spot). However, the wave packet in the initial

CT state can be prepared at some finite angle (gray spot) because of the large amplitude torsional motion and the much enhanced transition dipole moment at large θ.

Figure 4.23. (A) Potential energy curves along the reaction coordinate for generic charge-transfer reactions. (B) Potential energy curves along the reaction coordinate for dissociative charge-transfer reactions of D·I_2 discussed in this Chapter.

Figure 4.24 (a) *Upper panel:* Ionic PES contour map along with a typical trajectory from MD calculations. *Lower panel:* time-distance plot of the trajectory shown in the upper panel. **(b)** A typical trajectory on the neutral PES. Note the different time scales for the Bz-I and I-I dissociations.

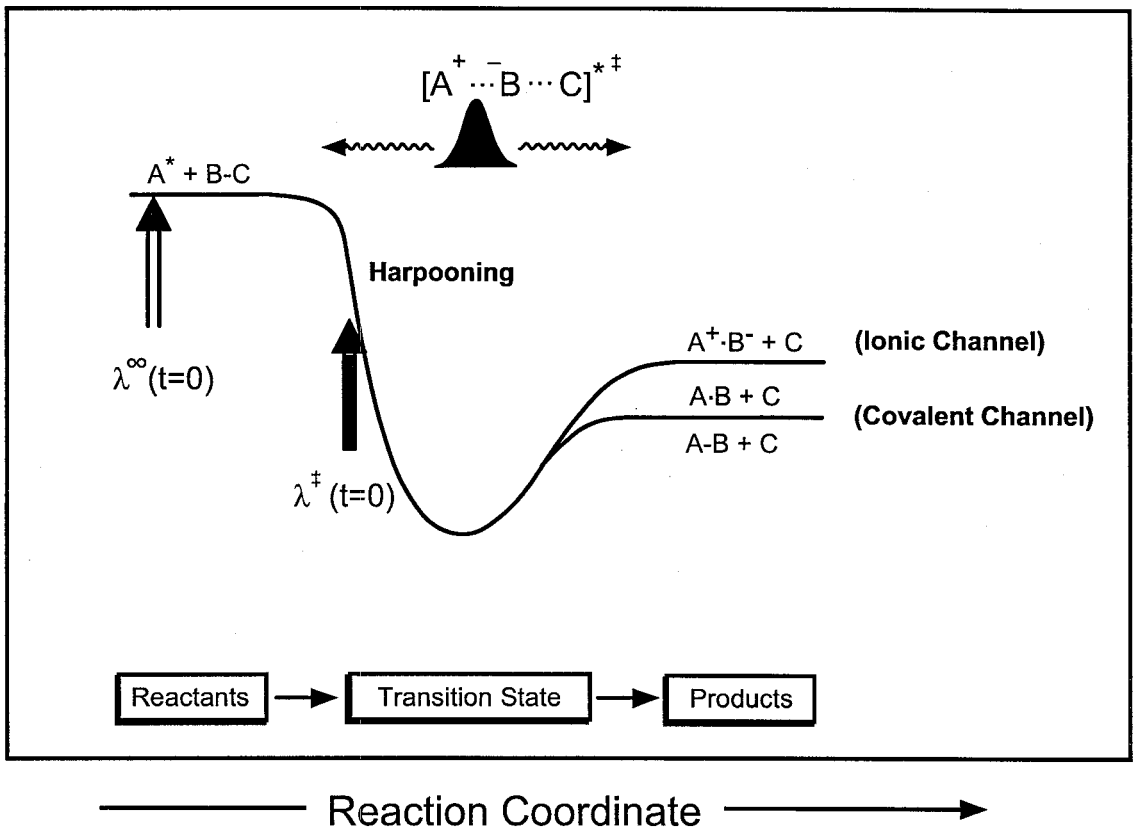
[A+ ··· B− ··· C]*‡
A* + B-C
Harpooning
λ∞(t=0)
λ‡(t=0)
A+·B- + C
(Ionic Channel)
A·B + C
(Covalent Channel)
A-B + C
Reactants
Transition State
Products
Reaction Coordinate

Figure 4.1

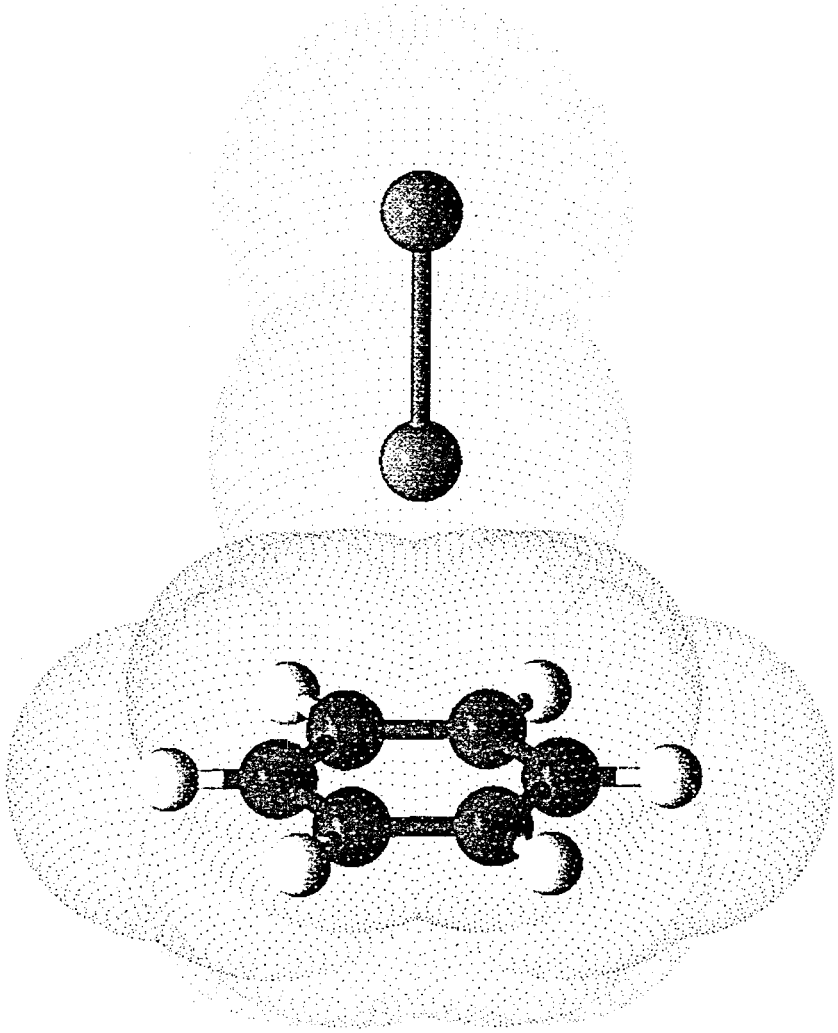

Figure 4.2

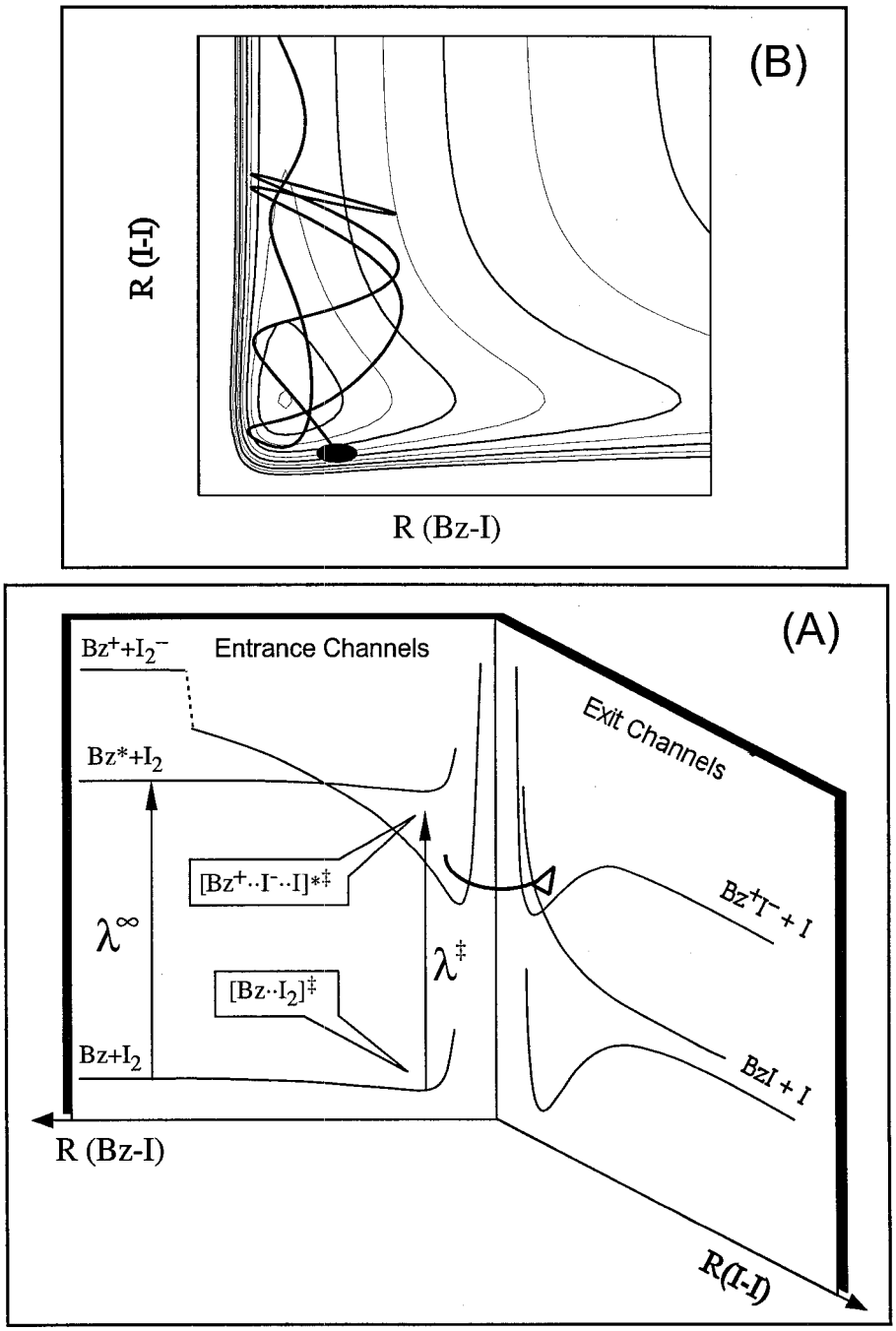
(B)
R (I-I)
R (Bz-I)
(A)
Bz+I2−
Entrance Channels
Exit Channels
Bz*+I2
[Bz+..I−..I]*‡
λ∞
λ‡
[Bz..I2]‡
Bz+I2
Bz+I− + I
BzI + I
R (Bz-I)
R(I-I)

Figure 4.3

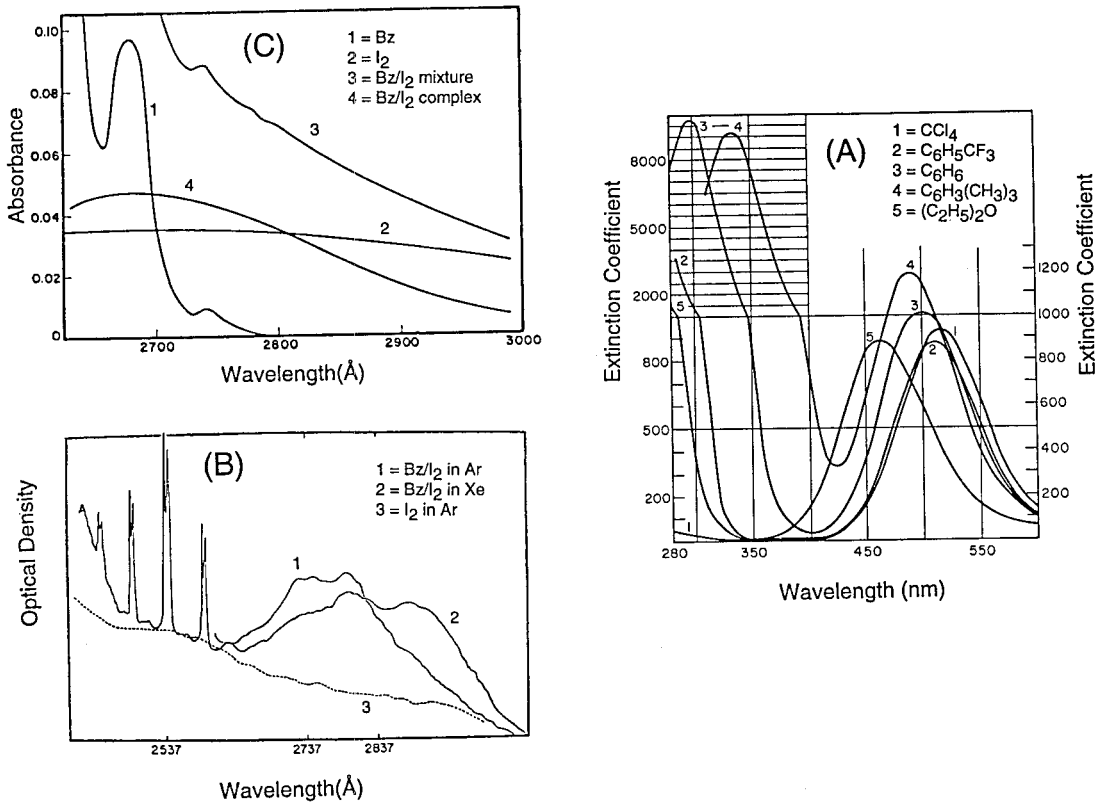
(C)
1 = Bz
2 = I_2
3 = Bz/I_2 mixture
4 = Bz/I_2 complex
Absorbance
0.10
0.08
0.06
0.04
0.02
0
2700
2800
2900
3000
Wavelength(Å)
(B)
1 = Bz/I_2 in Ar
2 = Bz/I_2 in Xe
3 = I_2 in Ar
Optical Density
2537
2737
2837
Wavelength(Å)
(A)
1 = CCl_4
2 = $C_6H_5CF_3$
3 = C_6H_6
4 = $C_6H_3(CH_3)_3$
5 = $(C_2H_5)_2O$
Extinction Coefficient
8000
5000
2000
800
500
200
1200
1000
800
600
400
200
280
350
450
550
Wavelength (nm)

Figure 4.4

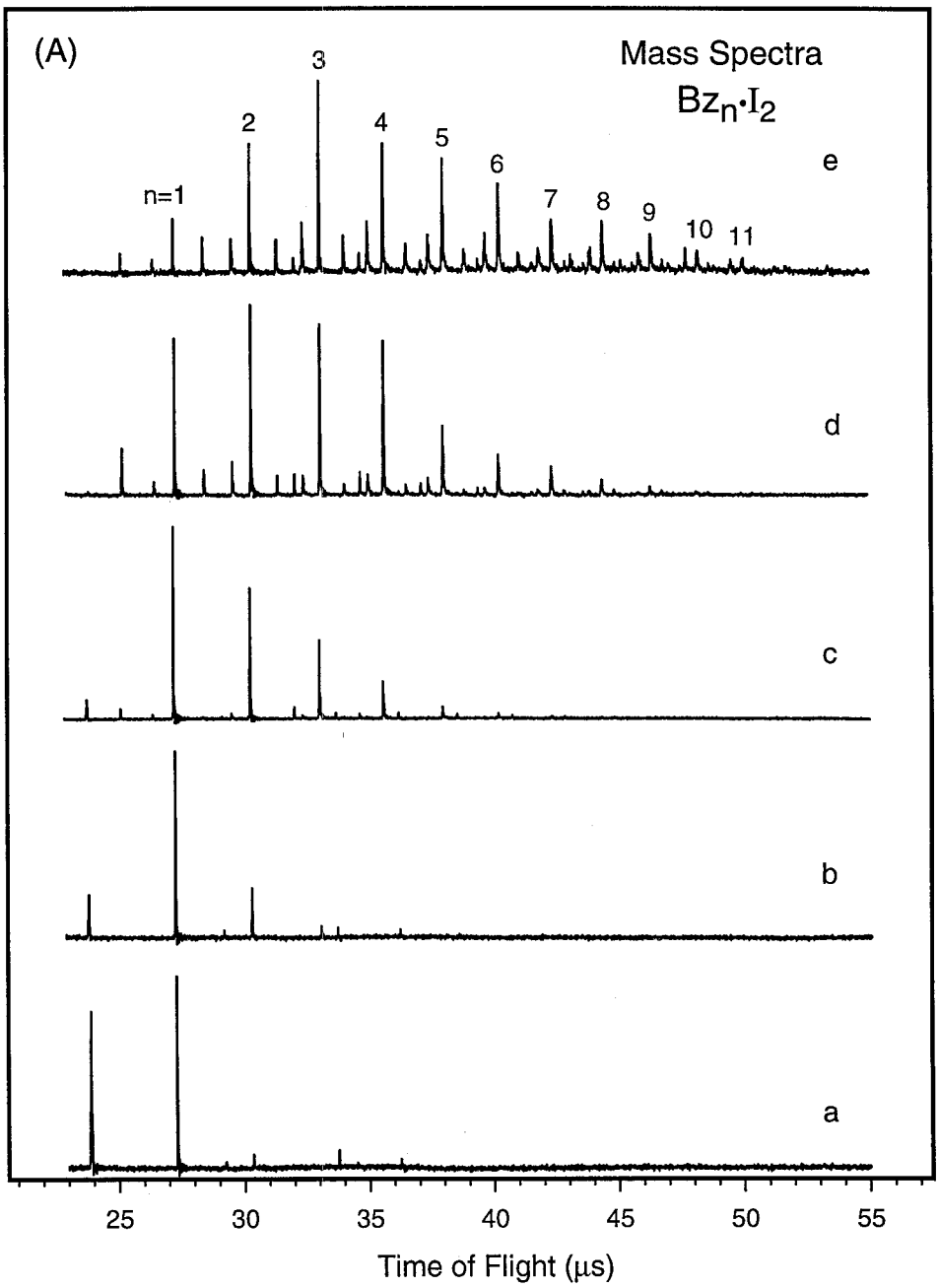
(A)
Mass Spectra
$Bz_n \cdot I_2$
n=1
2
3
4
5
6
7
8
9
10
11
e
d
c
b
a
25
30
35
40
45
50
55
Time of Flight (μs)

Figure 4.5A

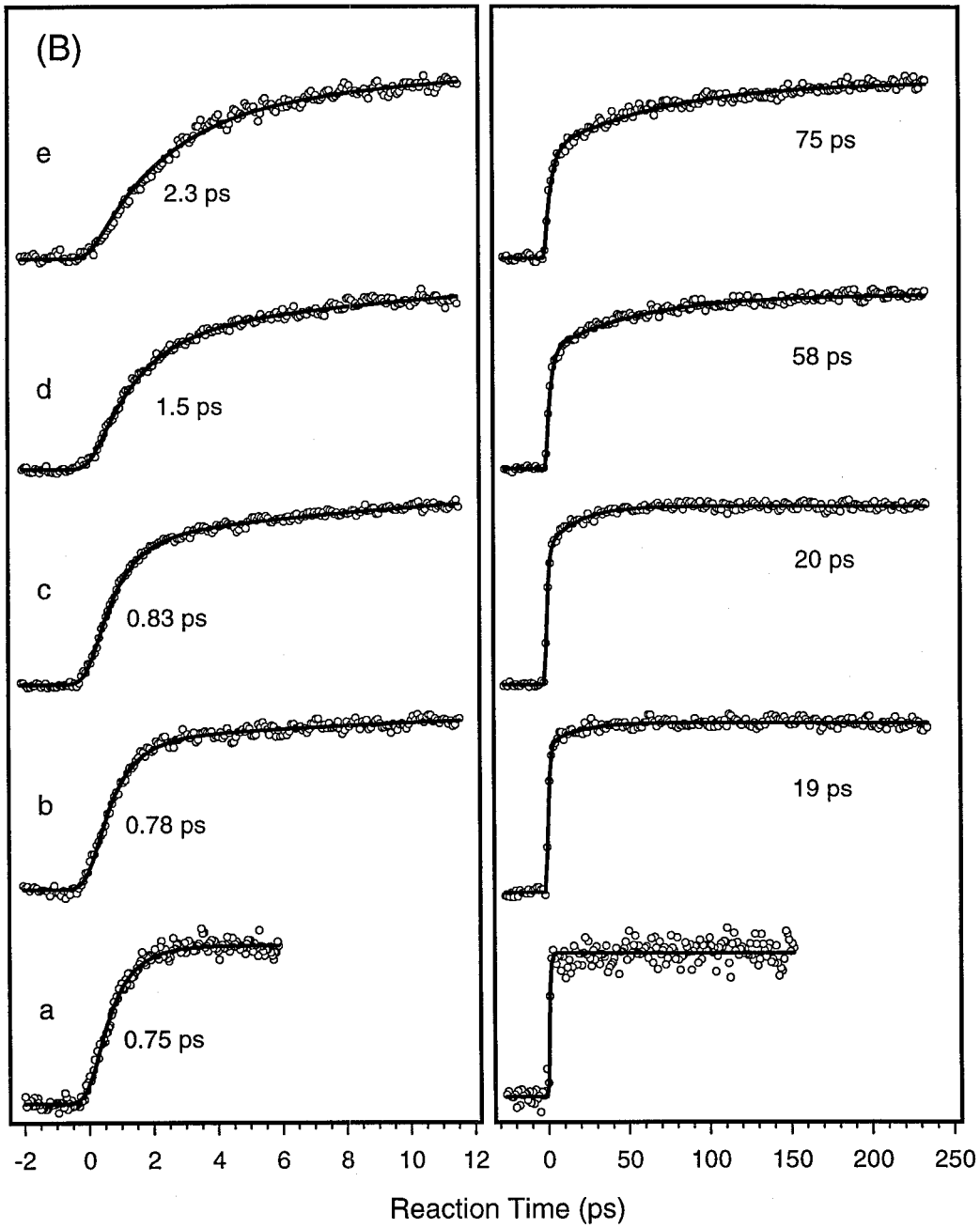
(B)
e
2.3 ps
d
1.5 ps
c
0.83 ps
b
0.78 ps
a
0.75 ps
75 ps
58 ps
20 ps
19 ps
-2
0
2
4
6
8
10
12
0
50
100
150
200
250
Reaction Time (ps)

Figure 4.5B

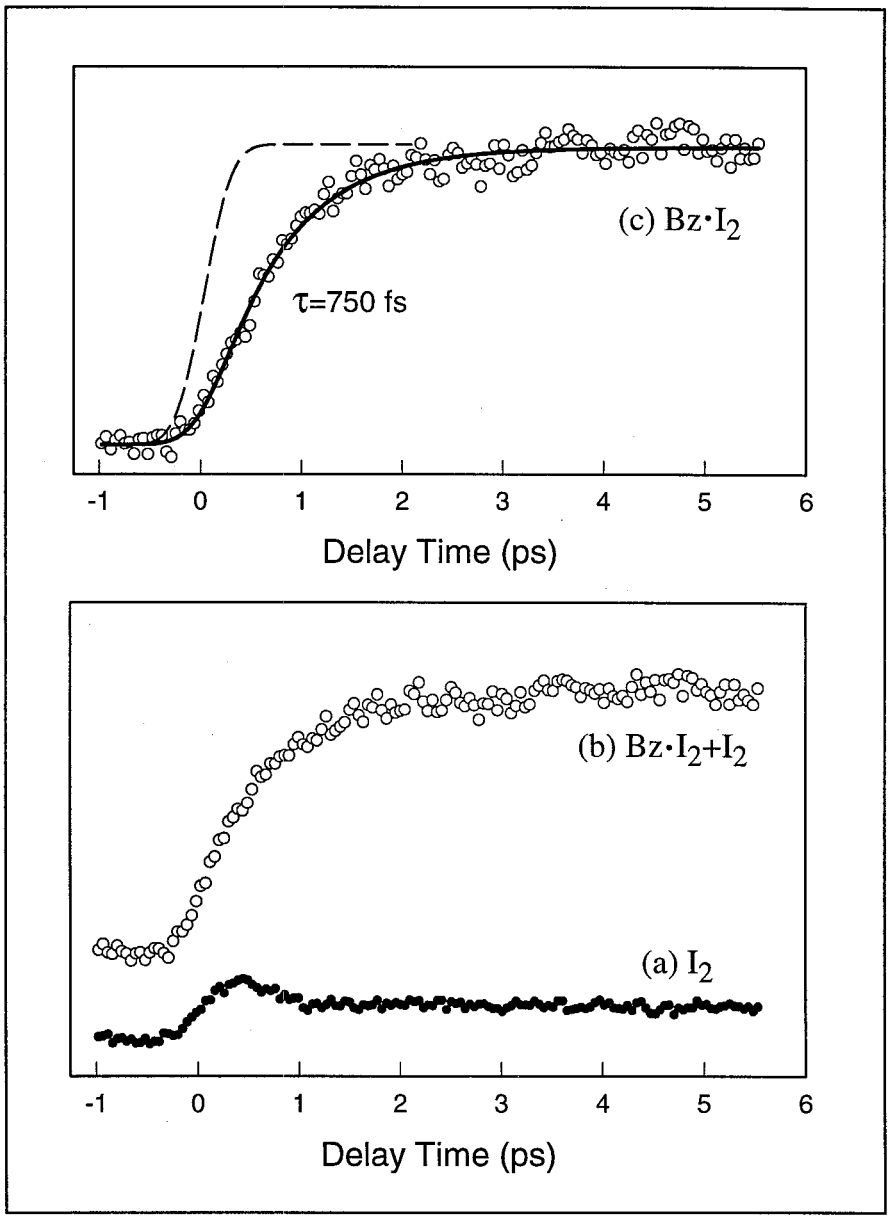
(c) Bz·I2
τ=750 fs
-1
0
1
2
3
4
5
6
Delay Time (ps)
(b) Bz·I2+I2
(a) I2
-1
0
1
2
3
4
5
6
Delay Time (ps)

Figure 4.6

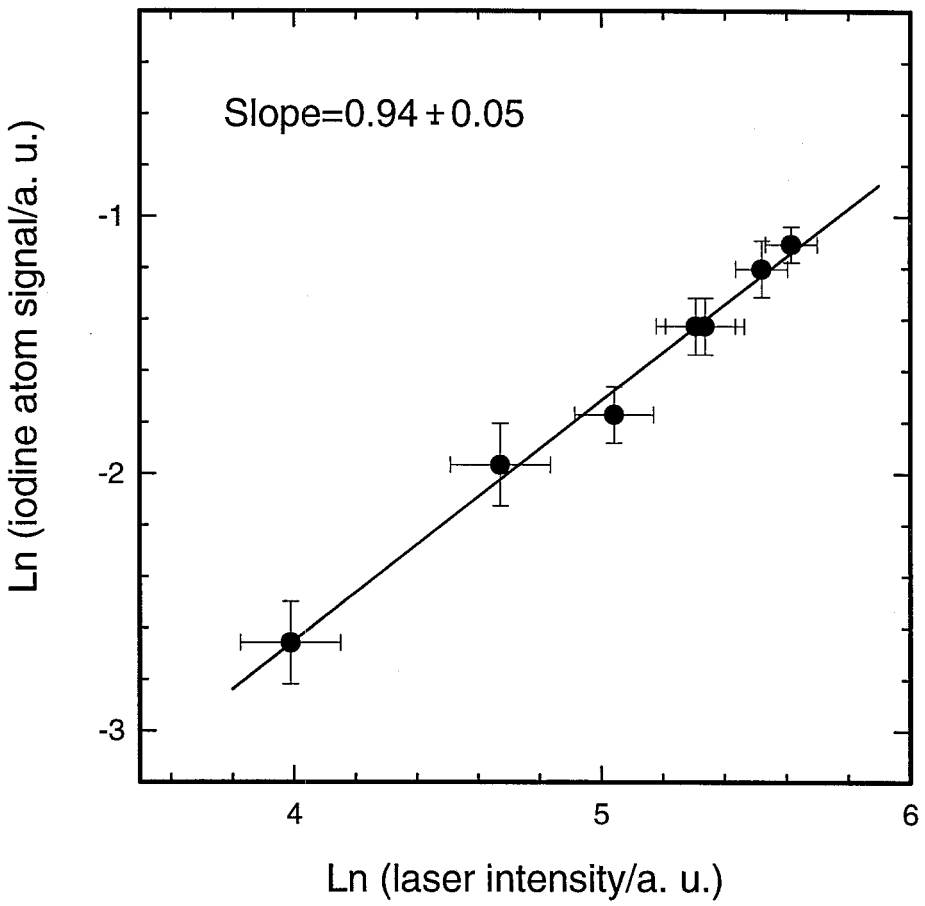
Slope=0.94 ± 0.05
Ln (iodine atom signal/a. u.)
-1
-2
-3
4
5
6
Ln (laser intensity/a. u.)

Figure 4.7

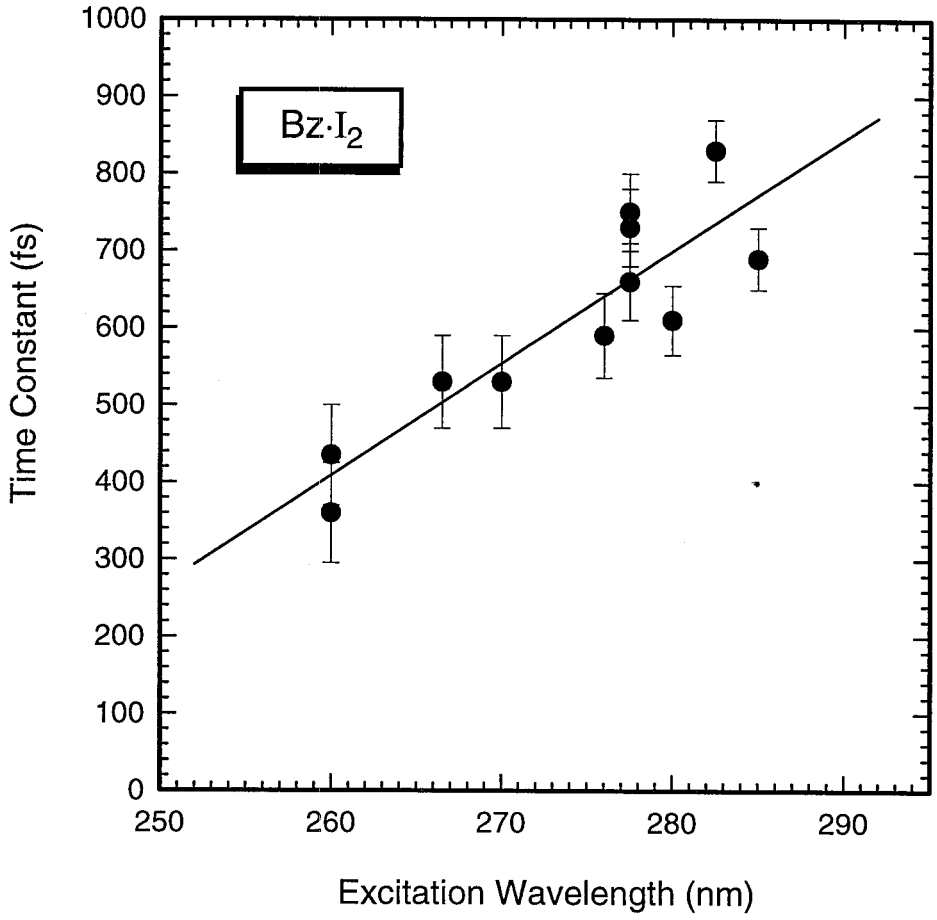
Bz·I2
Time Constant (fs)
Excitation Wavelength (nm)
1000
900
800
700
600
500
400
300
200
100
0
250
260
270
280
290

Figure 4.8

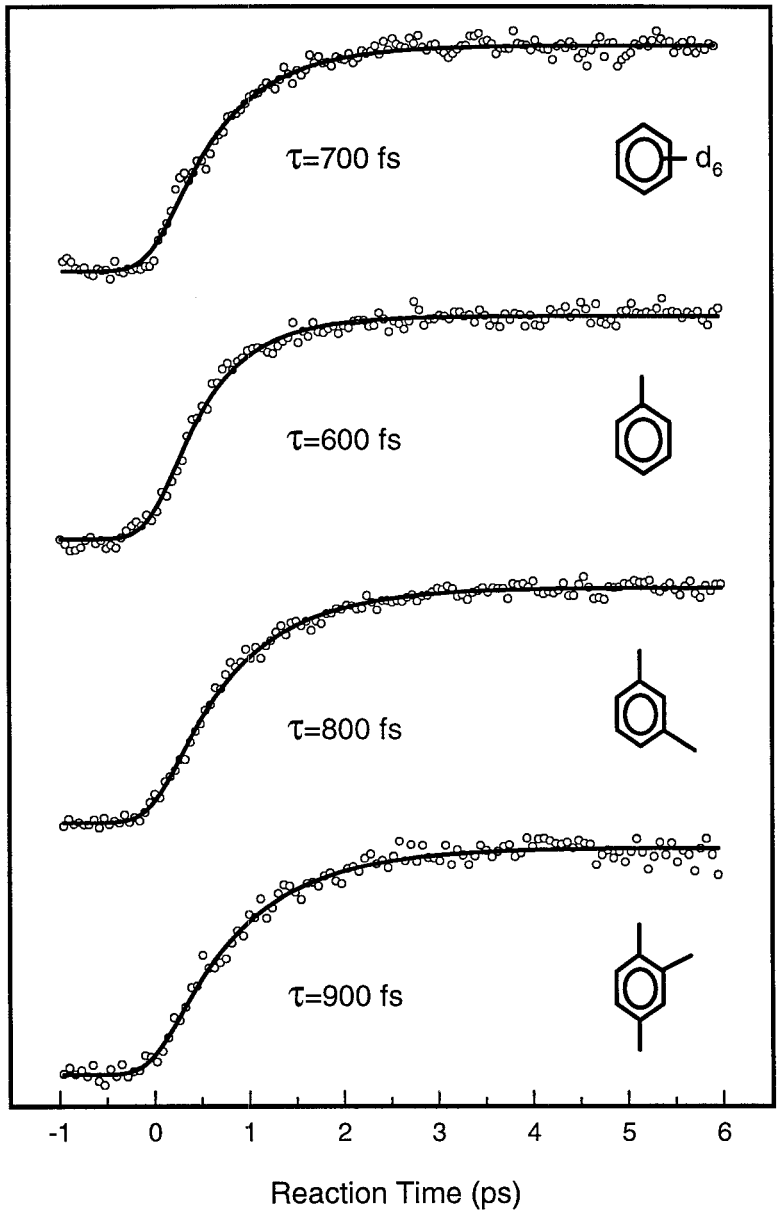

Figure 4.9

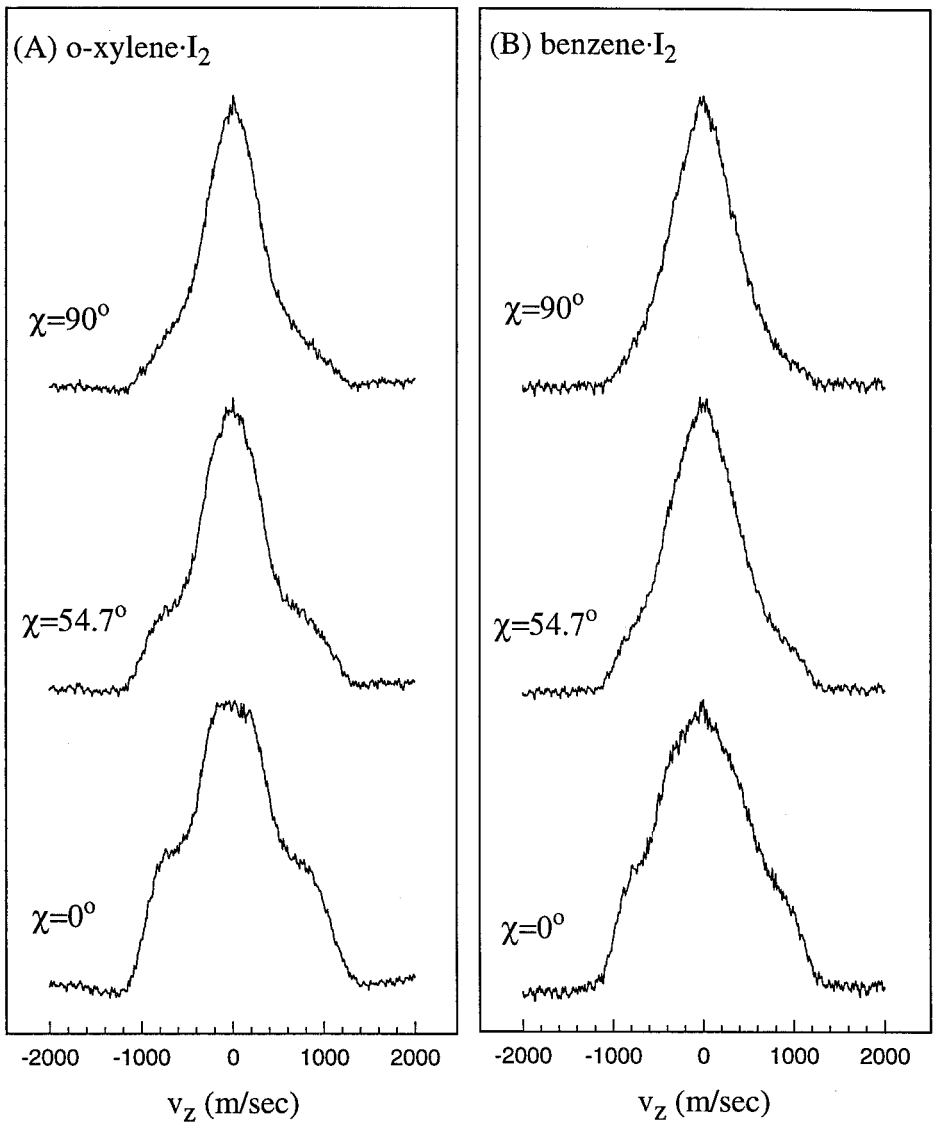
(A) o-xylene·I_2
χ=90°
χ=54.7°
χ=0°
-2000
-1000
0
1000
2000
v_z (m/sec)
(B) benzene·I_2
χ=90°
χ=54.7°
χ=0°
-2000
-1000
0
1000
2000
v_z (m/sec)

Figure 4.10

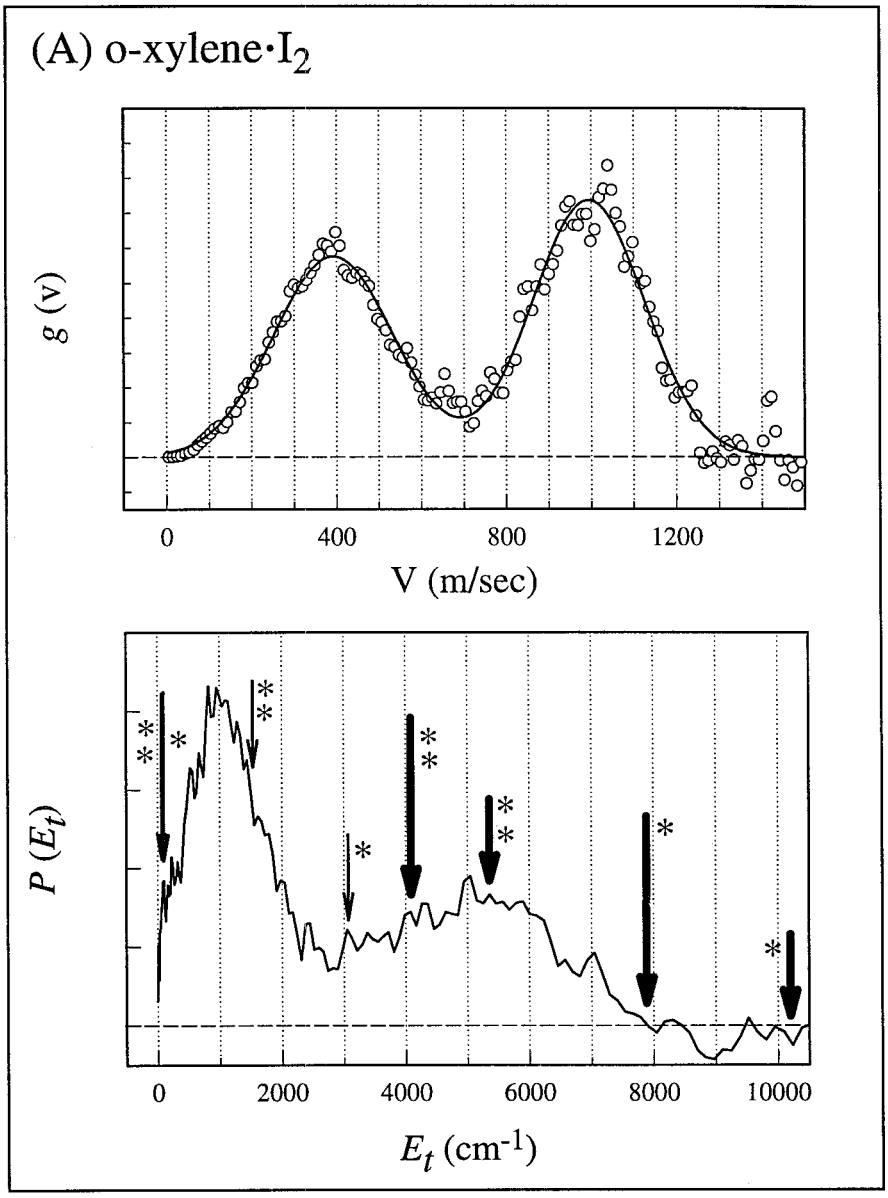
(A) o-xylene·I_2
g (v)
0
400
800
1200
V (m/sec)
P (E_t)
0
2000
4000
6000
8000
10000
E_t (cm^{-1})

Figure 4.11a

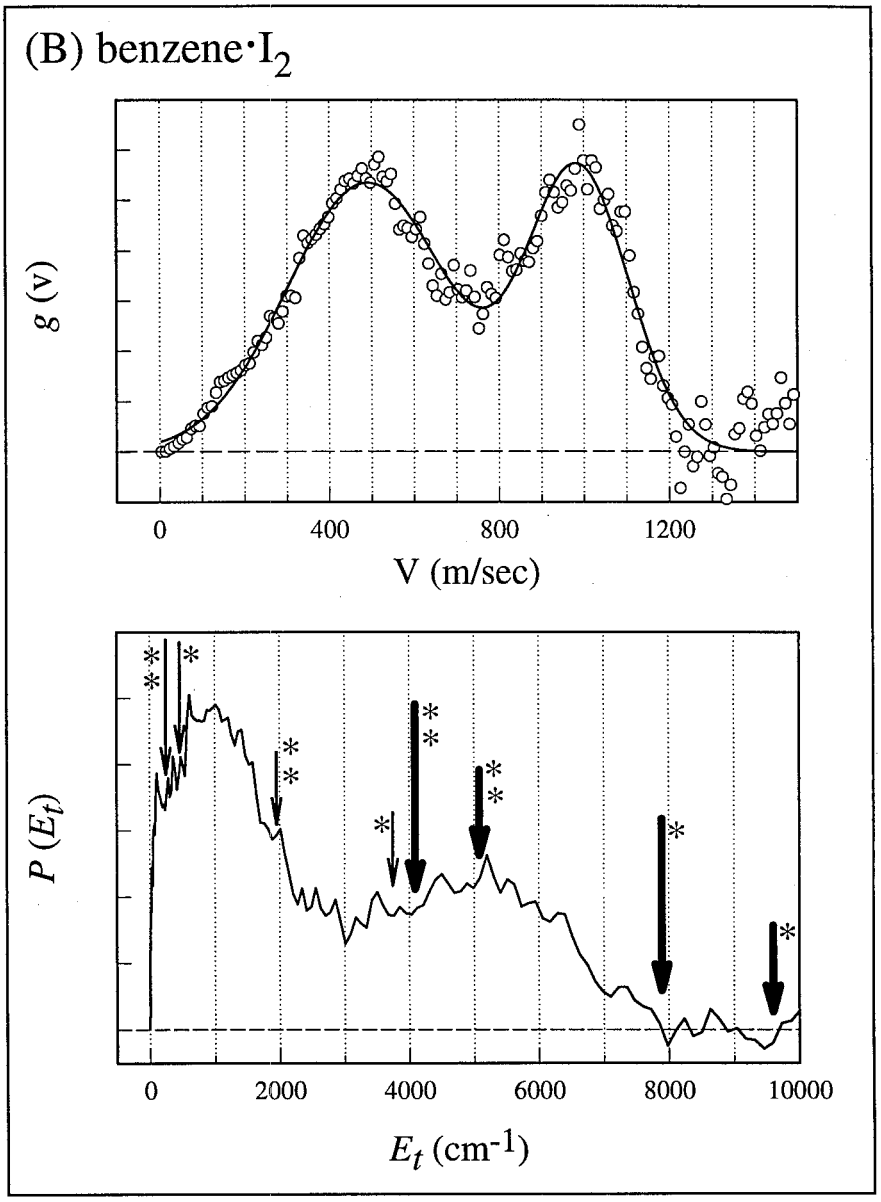
(B) benzene·I2
g (v)
0
400
800
1200
V (m/sec)
P (Et)
0
2000
4000
6000
8000
10000
Et (cm-1)

Figure 4.11b

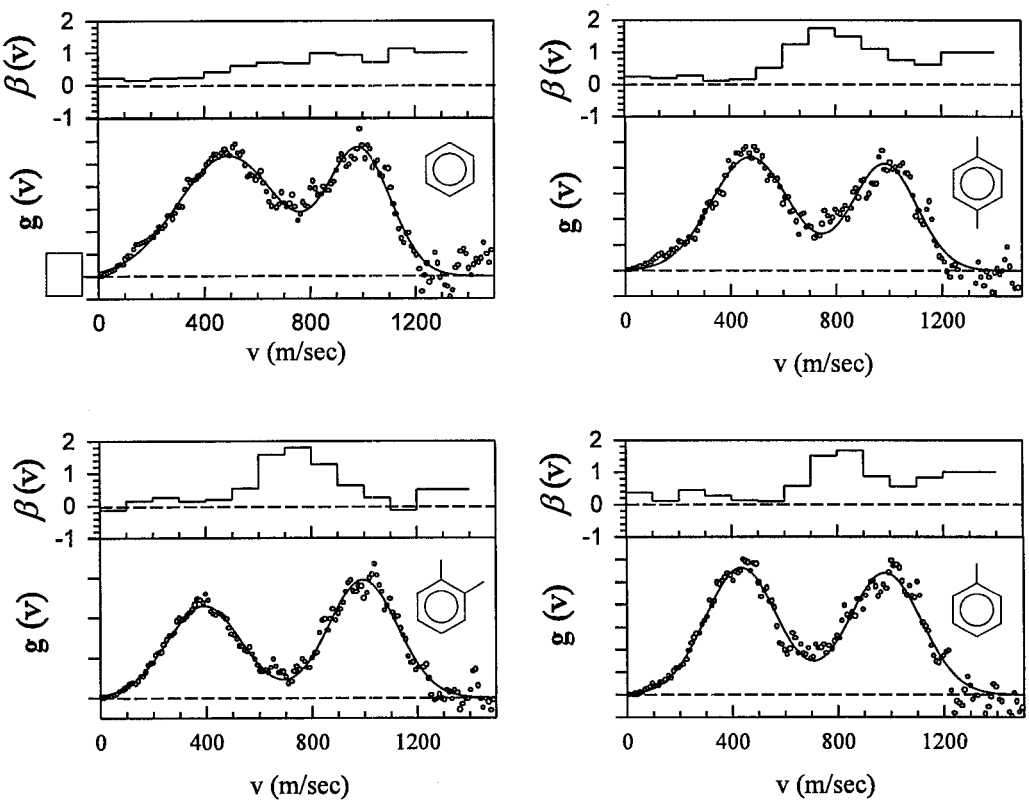

Figure 4.12

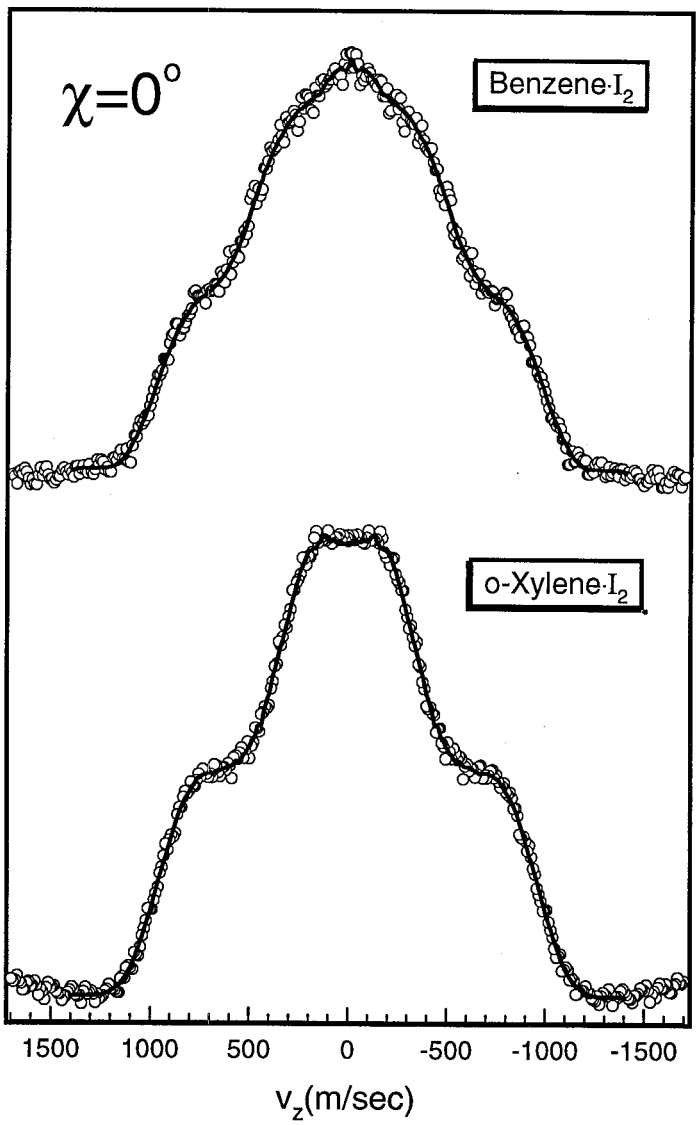

Figure 4.13

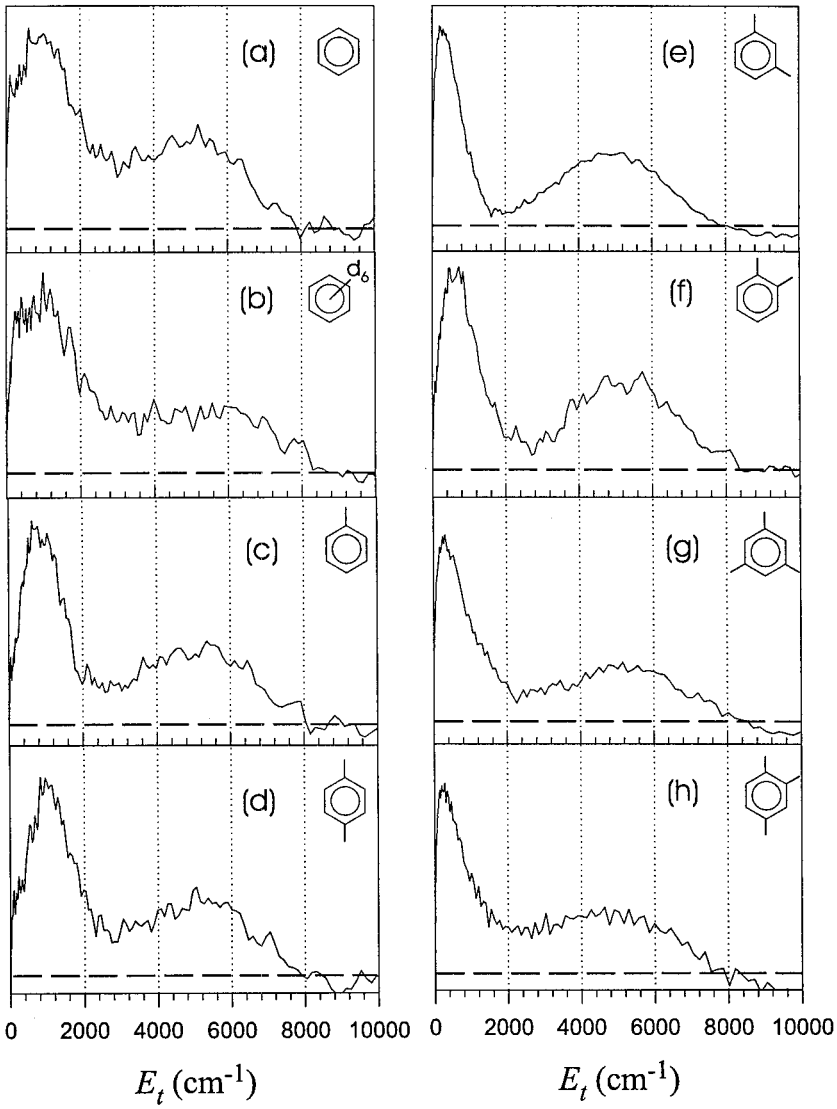
(a)
(b)
d_6
(c)
(d)
(e)
(f)
(g)
(h)
0 2000 4000 6000 8000 10000
0 2000 4000 6000 8000 10000
E_t (cm^{-1})
E_t (cm^{-1})

Figure 4.14

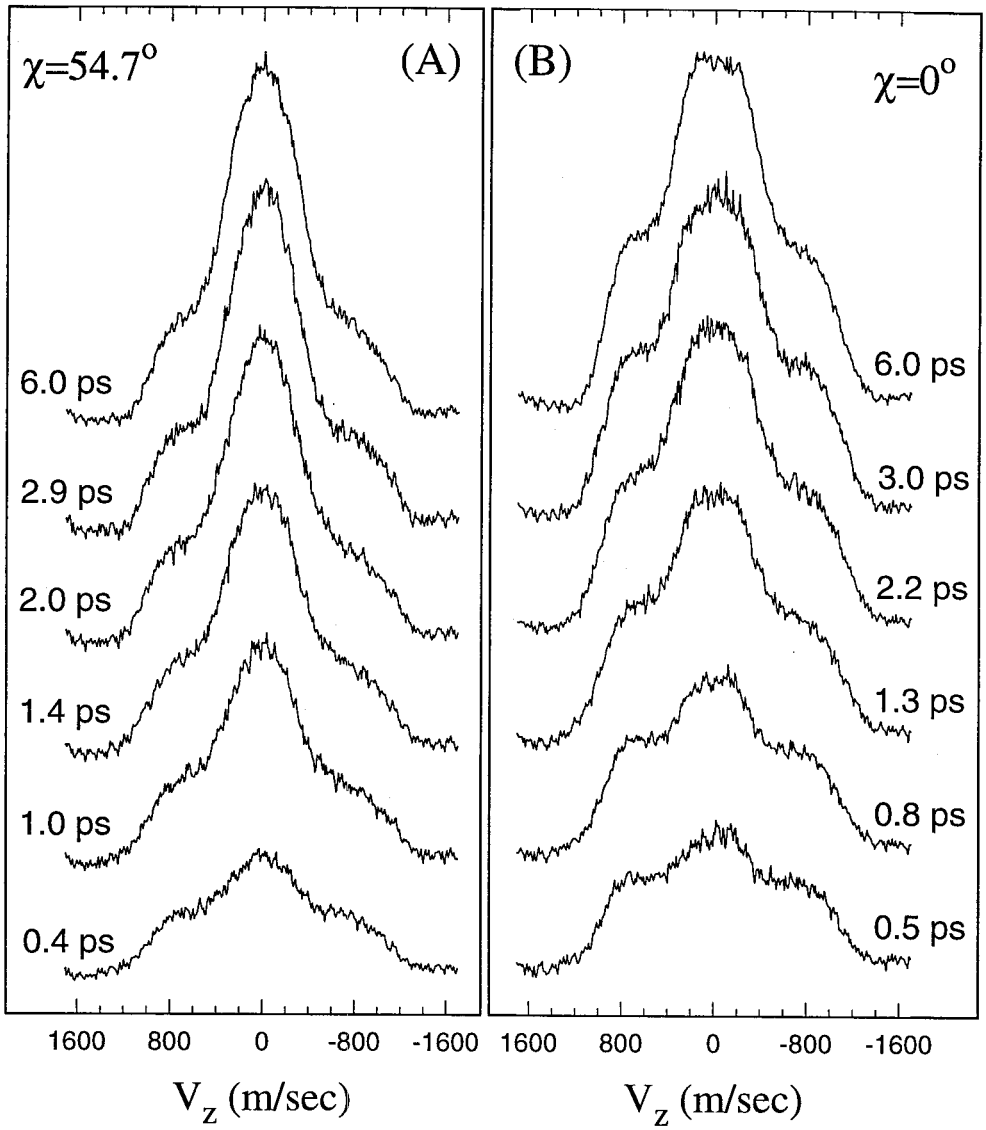
χ=54.7°
(A)
6.0 ps
2.9 ps
2.0 ps
1.4 ps
1.0 ps
0.4 ps
1600
800
0
-800
-1600
V_z (m/sec)
(B)
χ=0°
6.0 ps
3.0 ps
2.2 ps
1.3 ps
0.8 ps
0.5 ps
1600
800
0
-800
-1600
V_z (m/sec)

Figure 4.15

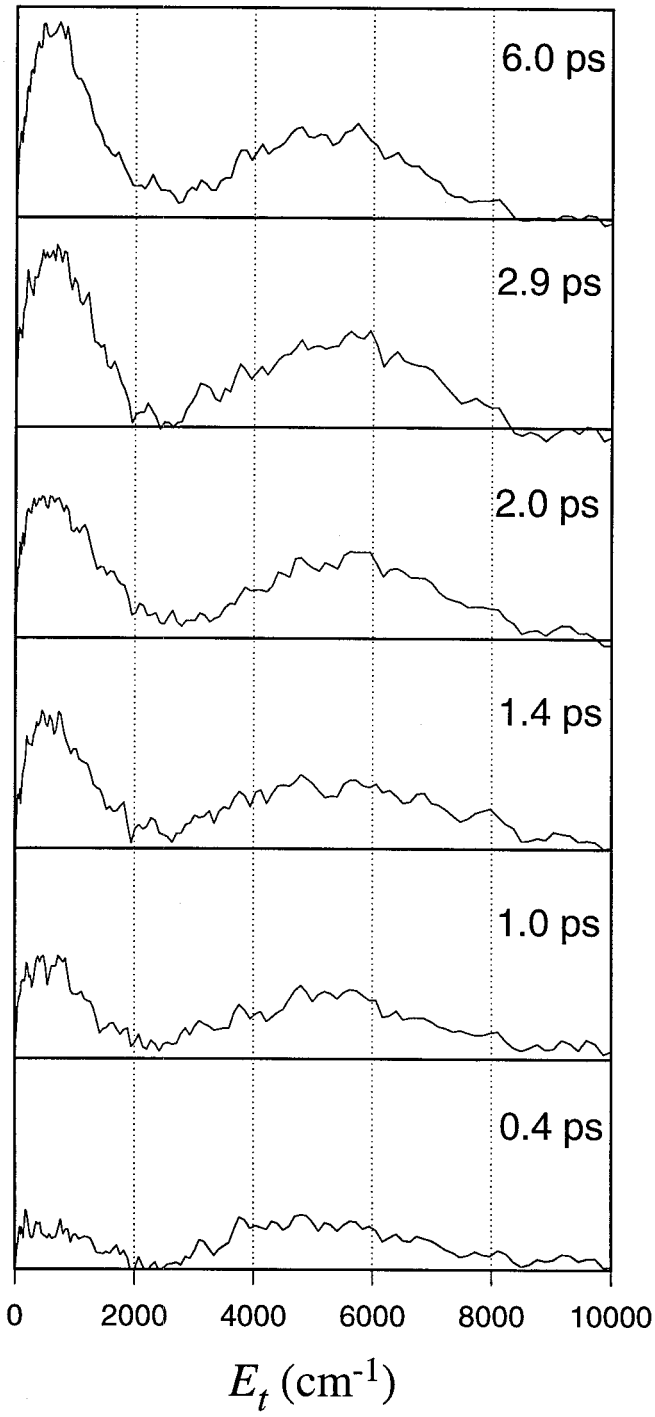
6.0 ps
2.9 ps
2.0 ps
1.4 ps
1.0 ps
0.4 ps
0
2000
4000
6000
8000
10000
E_t (cm^{-1})

Figure 4.16

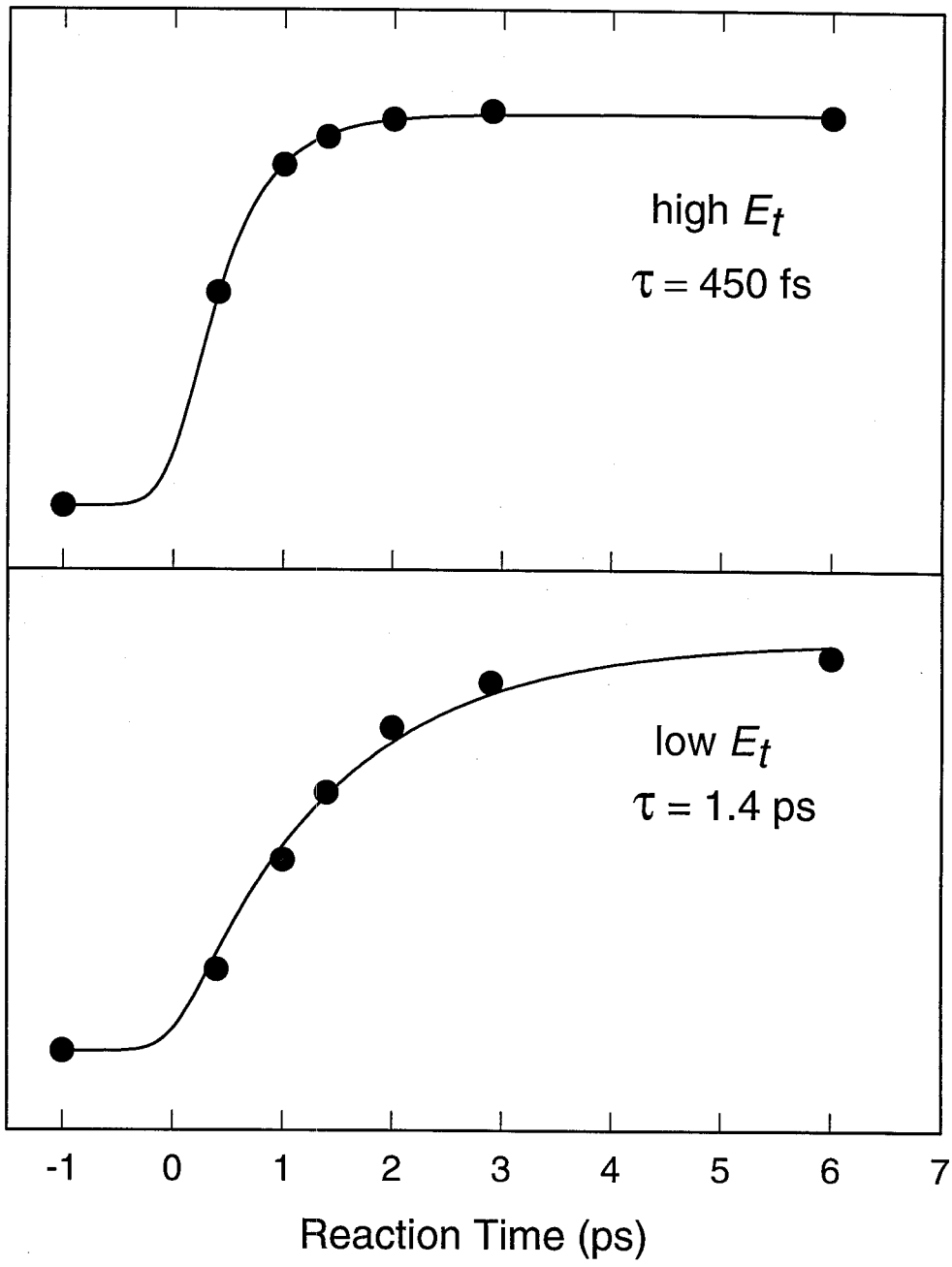

Figure 4.17

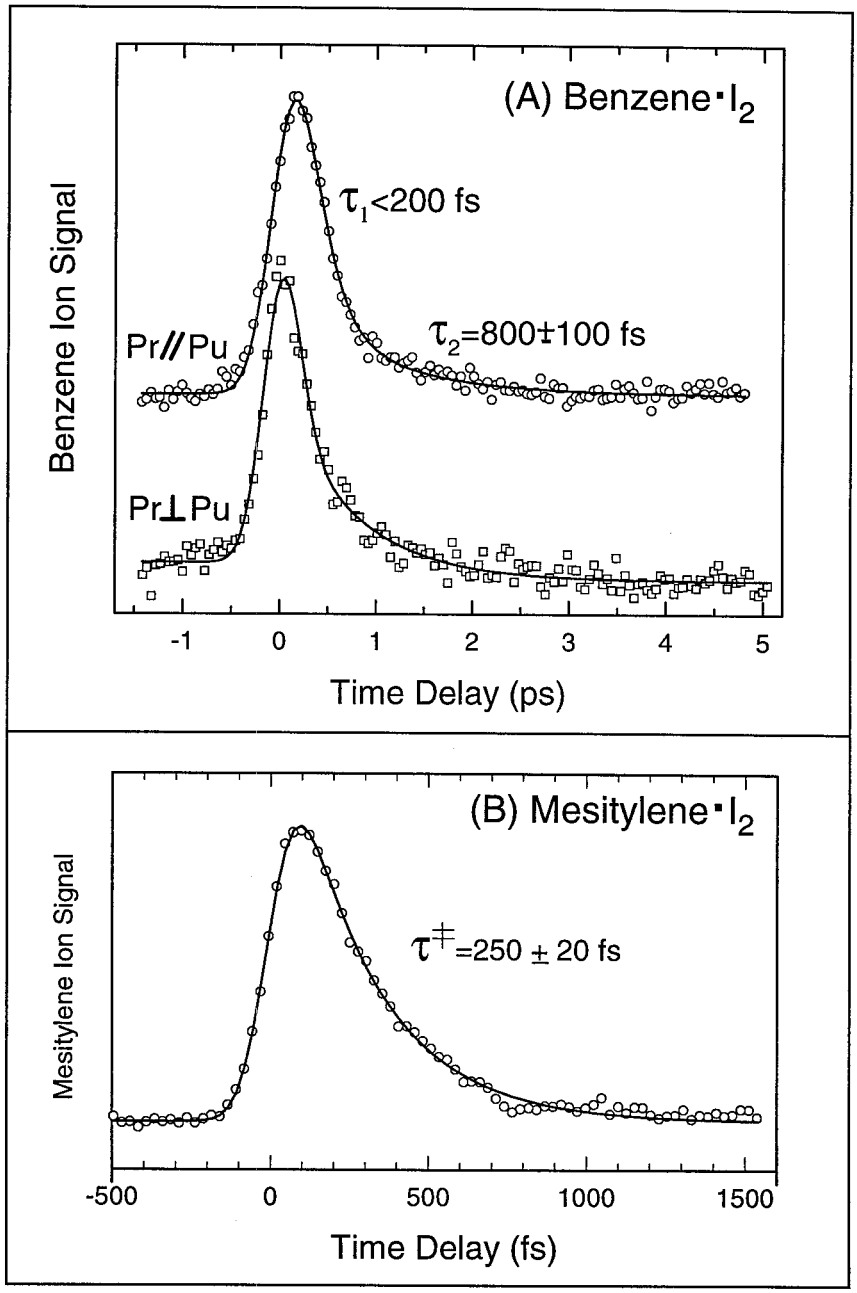
(A) Benzene·I2
τ1<200 fs
τ2=800±100 fs
Pr//Pu
PrPu
Benzene Ion Signal
-1
0
1
2
3
4
5
Time Delay (ps)
(B) Mesitylene·I2
τ⁺=250 ± 20 fs
Mesitylene Ion Signal
-500
0
500
1000
1500
Time Delay (fs)

Figure 4.18

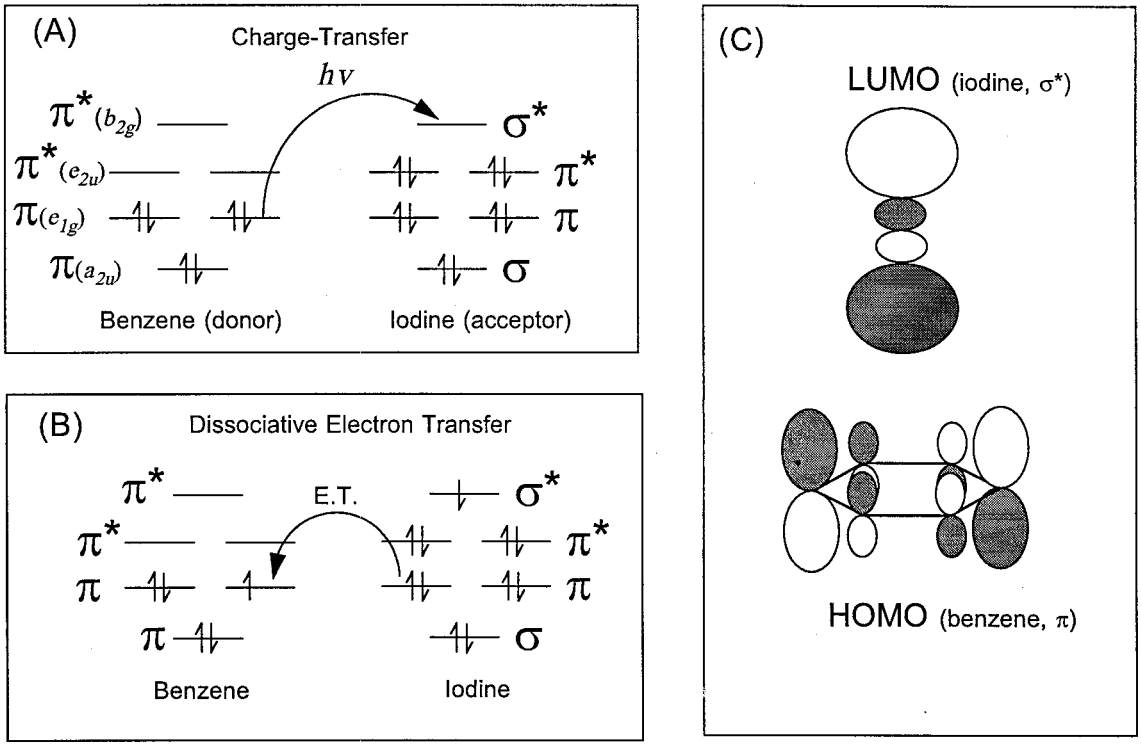
(A)
Charge-Transfer
hν
π*(b2g)
π*(e2u)
π(e1g)
π(a2u)
σ*
π*
π
σ
Benzene (donor)
Iodine (acceptor)
(B)
Dissociative Electron Transfer
E.T.
π*
π*
π
π
σ*
π*
π
σ
Benzene
Iodine
(C)
LUMO (iodine, σ*)
HOMO (benzene, π)

Figure 4.19

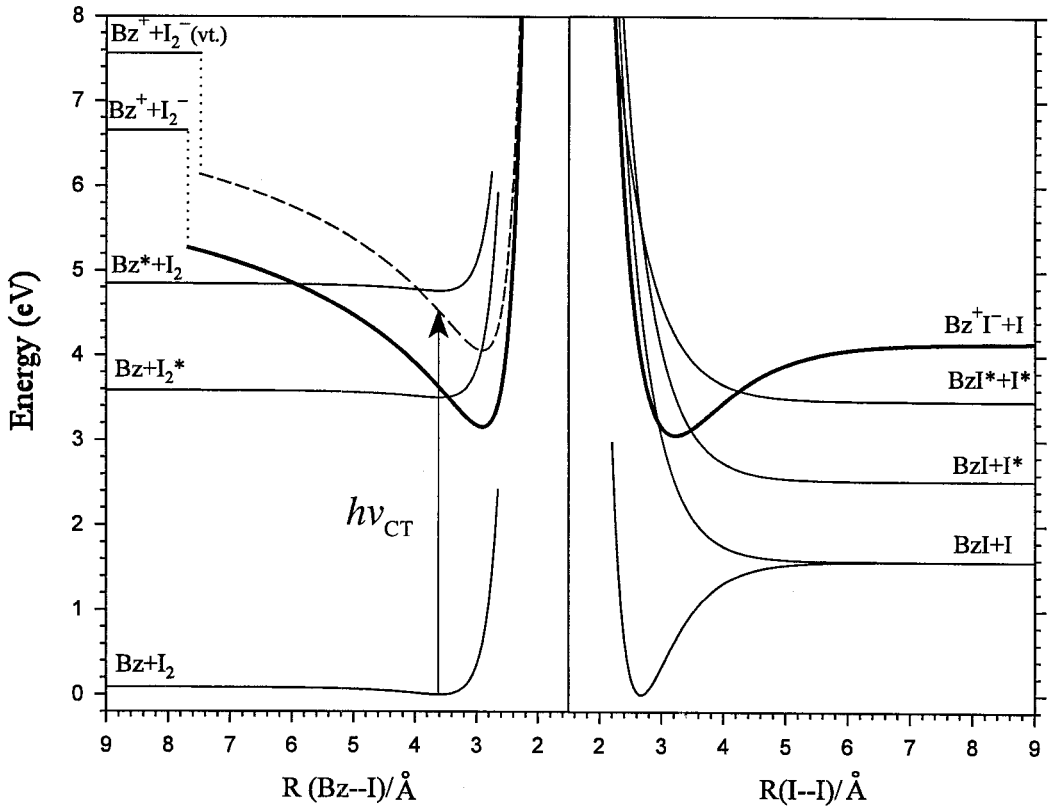
Energy (eV)
Bz+I2-(vt.)
Bz+I2-
Bz*+I2
Bz+I2*
Bz+I2
hνCT
Bz+I-+I
BzI*+I*
BzI+I*
BzI+I
R (Bz--I)/Å
R(I--I)/Å

Figure 4.20

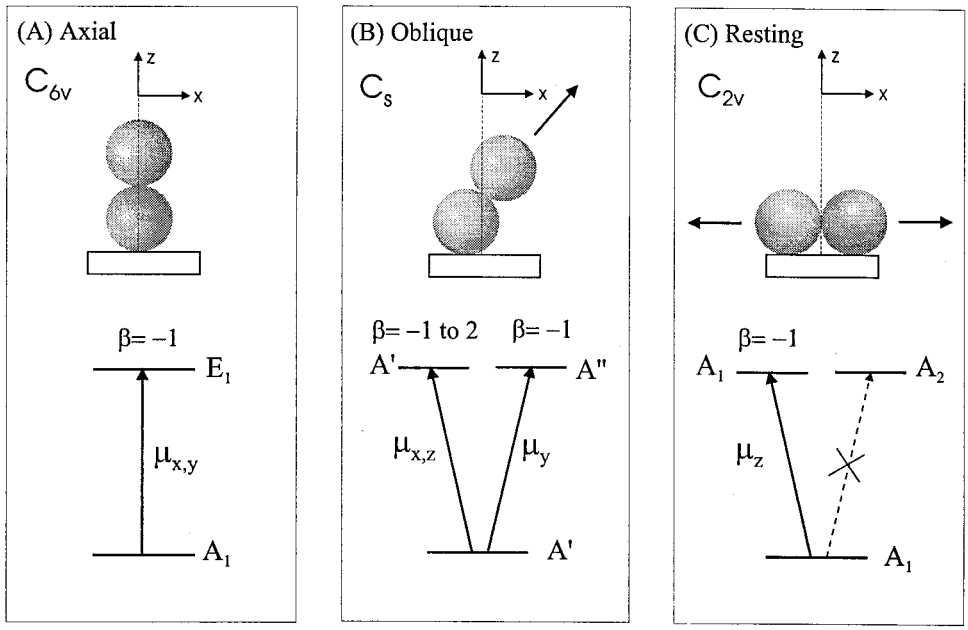
(A) Axial
C_{6v}
z
x
β= −1
E_1
$\mu_{x,y}$
A_1
(B) Oblique
C_s
z
x
β= −1 to 2
β= −1
A'
A"
$\mu_{x,z}$
μ_y
A'
(C) Resting
C_{2v}
z
x
β= −1
A_1
A_2
μ_z
A_1

Figure 4.21

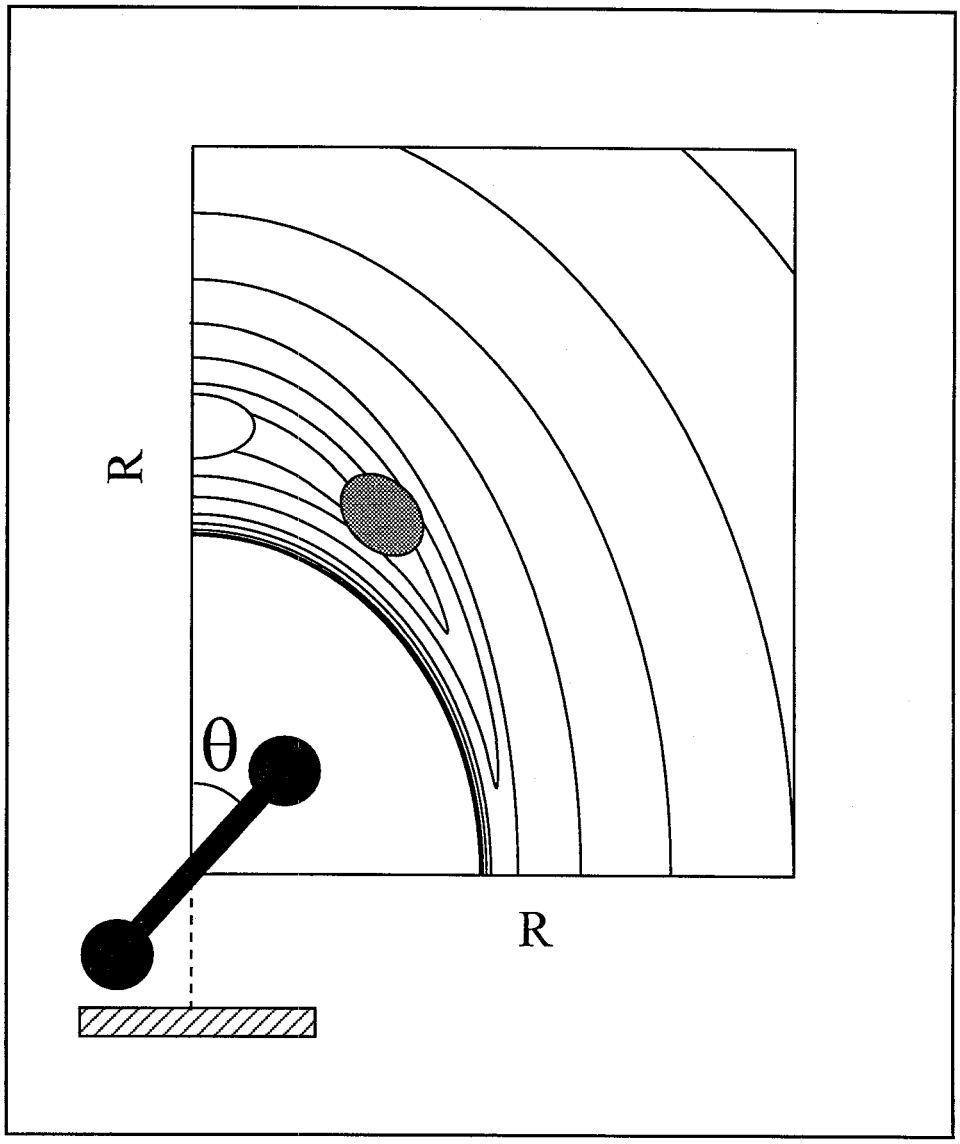

Figure 4.22

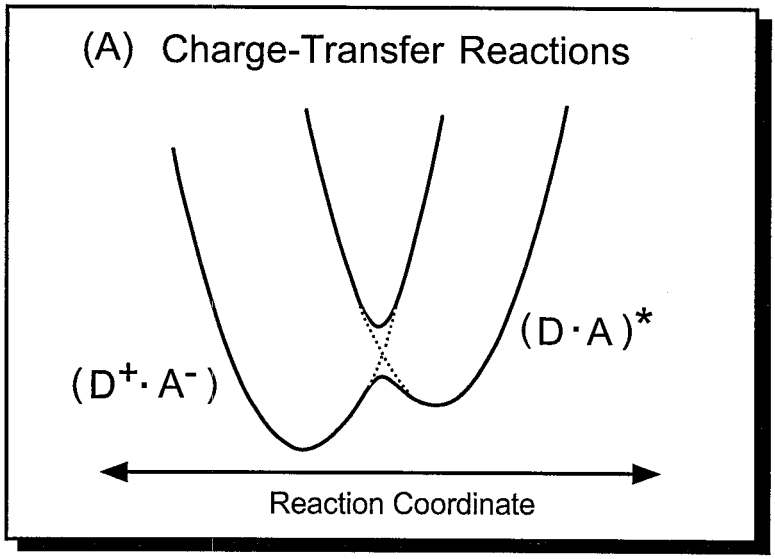
(A) Charge-Transfer Reactions
$(D^+ \cdot A^-)$
$(D \cdot A)^*$
Reaction Coordinate

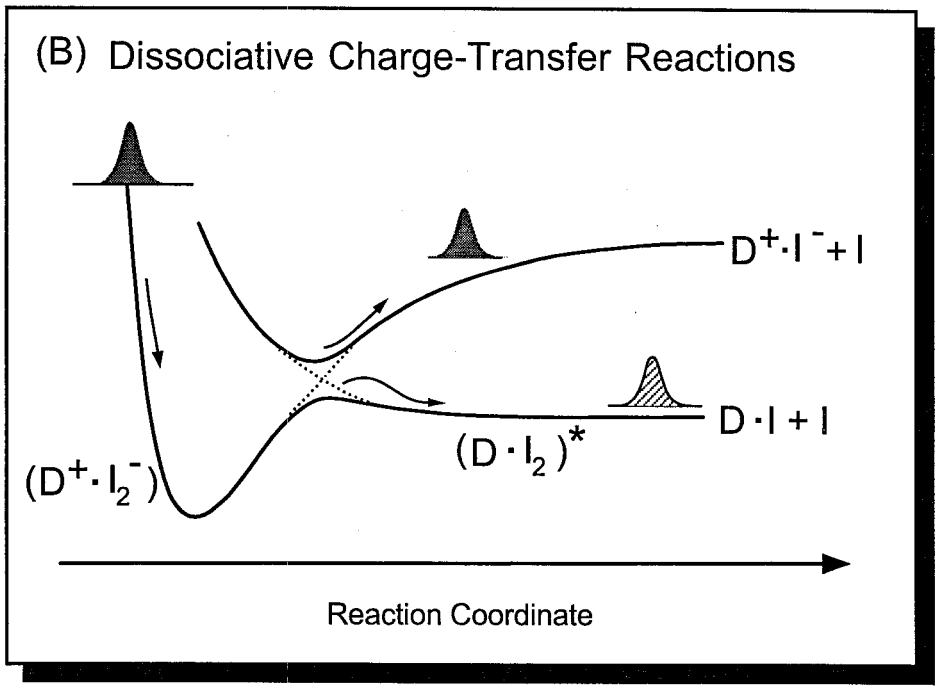
(B) Dissociative Charge-Transfer Reactions
$D^+ \cdot I^- + I$
$D \cdot I + I$
$(D \cdot I_2)^*$
$(D^+ \cdot I_2^-)$
Reaction Coordinate

Figure 4.23

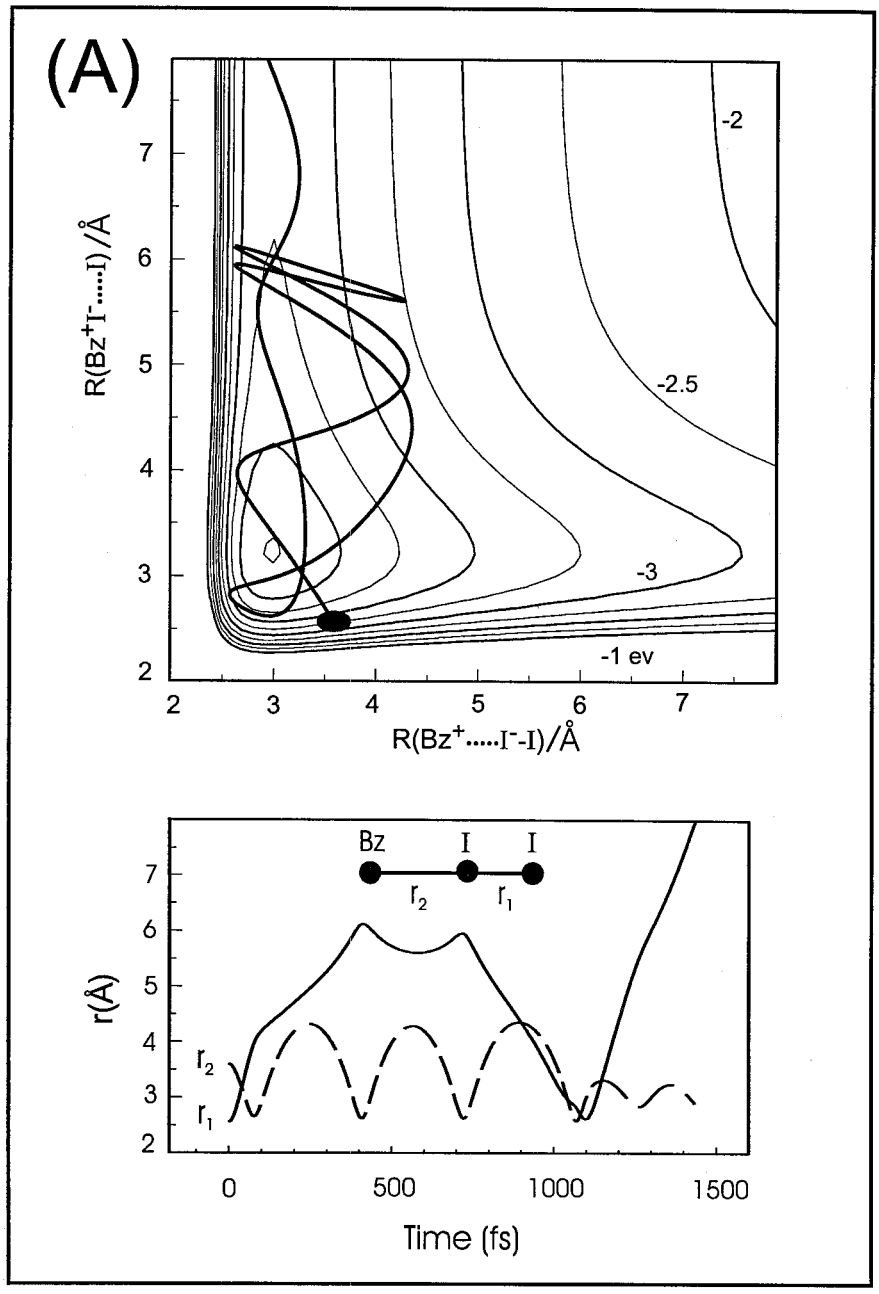

Figure 4.24a

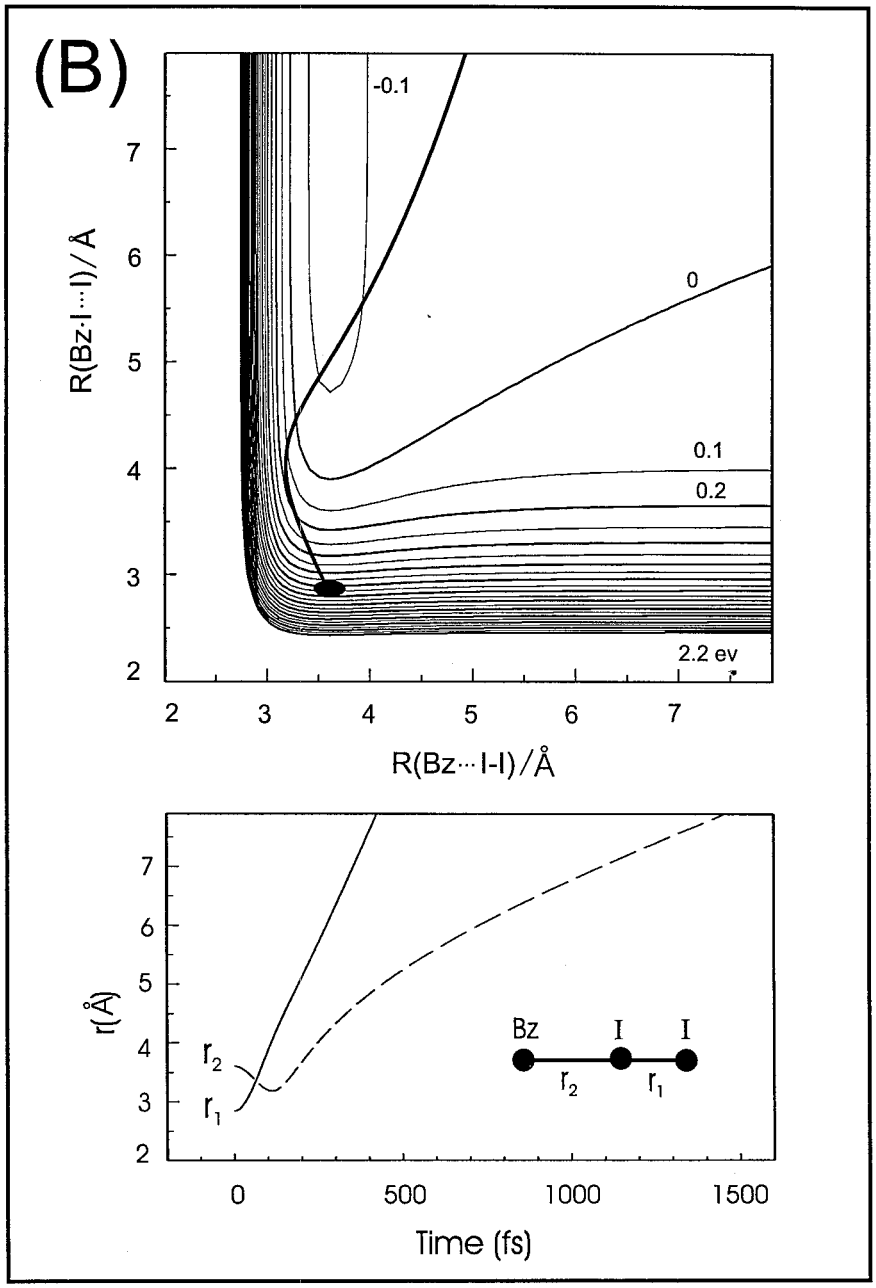

Figure 4.24b

Chapter 5

Femtosecond Real-Time Probing of Bimolecular Reactions: Dynamics of Dative-Bonding Transition State and Concepts of Reversible and Dissociative Charge-Transfer Reactions[‡]

[‡] Adapted from: D. Zhong and A.H. Zewail, Proc. Natl. Acad. Sci. USA **96** (1999) 2602-2607; D. Zhong, T.M. Bernhardt and A.H. Zewail, J. Chem. Phys., *submitted.*

5.1. Introduction

In the description of the chemical bond, the contribution of *covalent* and *ionic* characters is essential to energetics and dynamics and hence to the physical and chemical properties. Such a concept was evident in early theories of chemical bonding by Lewis,[1] Pauling,[2] Mulliken[3] and others. In many classes of reactions, where the covalent and ionic potential energy surfaces become close in energy, the description of the dative bond takes into account the two resonance structures, and the wave function becomes[4]:

$$\Psi_{\text{dative}}(D^+ - A^-) = m\Psi_{\text{covalent}}(D-A) + n\Psi_{\text{ionic}}(D^+, A^-) \quad , \tag{5.1}$$

where the covalent and ionic structures are distinct for the "supramolecular" donor (D)-acceptor (A) complex and the coefficients (m and n) depend on the coupling strength of the two degenerate potential energy surfaces (covalent and ionic).

The nature of these charge-transfer (CT) complexes was described by Mulliken in 1952[3] after Hildebrand in 1949 observed a new absorption band in a solution of benzene and iodine dissolved in n-heptane.[5] Since then there have been numerous studies in the liquid, gas and solid phases.[6-9] Ultrafast studies in solutions have revealed the dissociation and caging dynamics on different time scales.[10-13] Under the isolated, binary condition of D and A there have been few studies. Only recently has the dynamics been studied[14,15] for the famous benzene-iodine system; see Chapter 4. Studies of electron-transfer and related processes have provided a microscopic picture in clusters[16] under controlled solvation,[17-19] in a precursor-determined geometry,[20-22] and in matrices.[23]

For isolated CT reactions between D and A, the dynamics are unique in that the nature of the bond changes with time. With femtosecond (fs) time resolution it is possible

to prepare the system in an dative (0<m<n<1) structure by CT excitation and observe the temporal bond evolution from the dative-bonding region (0<m,n<1) to the final ionic (m=0, n=1) configuration or covalent (m=1, n=0) structure by reversible electron transfer (RET). In the process, chemical bonds may form or break and the dynamics will elucidate such bond changes following the initial ET. Such processes, relevant in many electrochemical and surface studies,[24-27] are important to the mechanism which involves the following central questions: What is the time scale for CT reactions and its possible RET pathway? Are the subsequent chemical events concerted or nonconcerted after the initial ET? What is the geometrical structure in the TS region? And what is the nature of the reaction trajectory, coherent or incoherent?

In a series of CT reactions, we report direct observation of the temporal bond and structure evolution and the resolution of the speed and angular distributions of the reactions at different times, using fs kinetic-energy resolved time-of-flight (KETOF) mass spectrometry.[28,29] The isolated, bimolecular reactions were studied in a molecular beam, varying the donors and acceptors to change the initial complex structures and control the energetics, *i.e.*, the location of the CT state. Specifically, we studied: diethylsulfide, *p*-dioxane, acetone, benzene as donors, and iodine and iodine monochloride as acceptors. In Figure 5.1, we present the concept of the experiment, illustrated for the reaction of diethylsulfide (D) and iodine (A). The fs pulse prepares the complex at t=0 from the "covalent" structure at the van der Waals (vdW) distance in the neutral ground state to the dative structure through absorption of one photon to the first CT state by utilizing the harpooning mechanism at long internuclear separation. The ground-state bonding in nature is mainly the electrostatic interactions between the donor

and the acceptor, and the CT state of the dative-bond configuration is mostly the ionic character bound by the Coulomb attraction. Vertical excitation from the vdW geometry to the CT state induces a fs electron jump from sulfide to iodine and suddenly switches on the ionic bonding between the donor and the acceptor. The iodine molecular anion is then rapidly pulled in by the strong Coulomb attraction force to a closer distance from the diethylsulfide cation and the reaction starts. For the donor and acceptor themselves, the fs ionization to a localized cation geometry and vertical electron attachment to a localized anion configuration initiate nuclear rearrangement to achieve the new stable complex structure.

In the TS region, where is illustrated in Fig. 5.1 by the multi-dimensional adiabatic ionic potential (the elliptic paraboloid) crossing with one of dissociative covalent potentials (the repulsive curve), the dative bond between S and I evolves toward the covalent character, which is facilitated by the degeneracy of the covalent and ionic energies. Meanwhile, the total energy begins to dissipate into different vibrational modes in the supramolecular complex. After the complex is trapped in the TS potential well for certain time and if the reaction pathway still follows the ionic potential and enough energy flows into I-I$^-$ bond, the CT reaction ends up with D^+I^-+I in the ionic exit channel. However, during the energy redistribution in the TS region, an electron from the acceptor can return back to the donor by a nonadiabatic transition. The dative bond completely transforms into the covalent character, along with the electronic excitation of the donor and/or acceptor. Shown in Fig. 5.1 is one of the dissociative covalent pathways of $D{\cdot}I_2^* \rightarrow D{\cdot}I{+}I$ in the exit channel. Thus, the time scales of the RET and CT reactions determine the dynamics of energy dissipation and the corresponding nuclear motions and

complex structure evolution, thus are critical for the effective dimensionality of the nuclear motion and the degree of concertedness.

Experimentally, we follow the dynamics after charge separation by monitoring the product (I) as a function of *time, kinetic energy (speed)* and *orientation.* The kinetic energy resolution of the I-atoms elucidates the reaction mechanism, *i.e.,* which final channel is dominant, ionic or covalent. The temporal behavior gives the time scales of the bond evolution, RET and energy dissipation, and explicates the reaction dynamics. The recoil direction of the exterior I-atom in the complex, relative to the CT transition dipole moment, illustrates the initial complex structure in the neutral ground state. The correlation of the recoil speed and the recoil direction indicates the structural change with the energy release.

The results reported here are striking in demonstrating that, although the initial ET occurs at early times from D to A, an electron from the acceptor reversibly goes back to the donor, leaving the acceptor with enough energy to break the I-I bond. In other words, the initial dative configuration ($0<m<n<1$) totally converts to the covalent bonding ($m=1$, $n=0$). During this transformation, the dative bond, for instance, in the case of diethylsulfide with I_2, lives about 500 fs from the liberation time of the exterior I-atom. We observe further dynamic process from the interior I-atom after RET. This interior I-atom is trapped coherently in the force field of the "substrate" (diethylsulfide) for 800 fs and completely departs in 1.15 ps. The orientation measurement of the exterior I-atom indicates a nearly linear structure of S-I-I ($\sim 165^0$, see Fig. 5.1) in the ground state.

5.2. The CT System

The CT complexes were extensively studied in 1950s, both experimentally[6-9,31-34] and theoretically.[3,4] The experiments mainly focused on the physical and chemical properties of the complex in the ground state, including the binding energy, the equilibrium formation constant, the electronic, vibrational and NMR spectra, and the complex dipole moments and structures. The observed new UV absorption band from the mixture of the donor and acceptor draw special attentions because it is from neither the donor nor the acceptor molecules alone, and is attributed to the donor-acceptor complex. In Figure 5.2, a typical example of UV absorption is shown from the diethylsulfide-I_2 mixture in the gas phase.[35] For an isolated system, the binding energy, structure and electronic spectra are three main properties for characterizing the CT complex.

The nature of the bonding in the complex was systematically described by Mulliken.[3,4] The complex is stabilized by resonance interactions between a "no-bond" (D,A) and a "dative-bond" (D^+-A^-) ET structure. The potential energy levels[4,9,34] for a donor-acceptor complex is shown in Figure 5.3. The ground-state wave function of the complex can, to a first approximation, be written as the sum of two terms

$$\Psi_N = a\phi_0(D,A) + b\phi_1(D^+ - A^-) \quad , \tag{5.2}$$

where ϕ_0(D,A) is the no-bond configuration wave function and ϕ_1(D^+-A^-) is the dative ET configuration wave function. An important requirement for the mixing is that ϕ_0 and ϕ_1 need to be of the same symmetry in the entire D·A complex frame. The no-bond configuration ϕ_0(D,A) mainly results from the dispersion force and classic electrostatic multipole interactions between D and A (vdW interactions). The dative-bond

configuration $\phi_1(D^+\text{-}A^-)$ conceptually is associated with the interaction of molecular orbitals and involves the transfer of an electron from the highest filled donor orbital (HOMO) to the lowest vacant molecular orbital (LUMO) of the acceptor.

The stability and structure of the complexes are very dependent on the particular orbitals that participate in the electron transfer. The donor molecules, according to their HOMOs, can be divided into three types: n, σ, π, *i.e.,* the molecule donates an electron from the n-unshared nonbonding electron pair of the heteroatom (N, O, S), the bonding electron pair of the σ-bond (such as cyclohexane) or the bonding π-electrons (aromatic and unsaturated compounds). The acceptor molecules can also be divided into three types from the character of the accepting orbitals: υ, σ, π, *i.e.,* the lowest molecular orbital (LUMO) is the vacant υ-valence orbital of the metal atom, the antibonding σ-orbital of halogens or the antibonding π-orbitals (such as tetracyanoethylene, TCNE).

Generally, the interaction of the πσ-complex is relatively weak (~1-4 kcal/mol)[6,34] and the complex in the ground state is stabilized mainly due to the vdW forces. Thus, the no-bond configuration becomes dominant for the weak πσ-complex and the contribution of the dative structure is very small. For example, in the benzene·ICl complex, the dative-bond contribution is ≤8.3% (a~0.93 and b~0.28).[36] The heat of formation is determined to be on the order of -2.54 kcal/mol.[37,38] On the other hand, the nσ-complex usually has a strong binding energy (≥3-13 kcal/mol)[6,34] and the dative-bond contribution is not negligible. The dative-bond contribution is 6.5% for *p*-dioxane·I_2, 12% for diethylsulfide·I_2 and ~25% for pyridine·I_2.[9,39] The heat of complex formation is determined in the range of -8.3 to -9.0 kcal/mol for diethylsulfide·I_2 in the gas phase,[35,40,41] -3.3 to -3.8 kcal/mol for *p*-dioxane·I_2[42,43] in CCl_4 and -3.7 to -5.8 kcal/mol

for acetone·I_2 in Freon.[44-46] The dative-bond contributions change in the sequence from the nitrogen (N)-containing donor (largest), to sulfide(S)- and to oxygen(O)-containing donor.

According to Mulliken's theory, the new UV absorption band is simply the excitation of the complex from the ground state to the first CT state and the wave function is primarily dative and has the form

$$\Psi_E = a^* \phi_1(D^+ - A^-) - b^* \phi_0(D,A) \quad . \tag{5.3}$$

For most CT complexes, the dative-bond configuration is dominant (≥90%) and a^* is large and b^* is small. For example, a^* and b^* are estimated to in the range of 0.99-0.97 and 0.27-0.36, respectively, for the benzene·I_2 complex.[9] Most strong UV absorption bands peak around 250-300 nm (Fig. 5.2) and the excitation energy (Fig. 5.3) can be approximated by the following equality

$$\begin{aligned} h\upsilon &= \Delta H + I_D - E_A^v - (E_C - R_E) \\ &\approx I_D - E_A^v - E_C \quad , \end{aligned} \tag{5.4}$$

where ΔH is the binding energy of the complex in the ground state, I_D is the ionization potential of the donor, E_A^v is the vertical electron affinity of the acceptor, E_C is the Coulomb energy (e^2/R) and R_E is the resonance energy. Usually, the CT excitation energy can be estimated by $I_D - E_A^v - E_C$ because ΔH and R_E are very small comparing with the other three terms. Spectroscopic studies of a variety of electron donor-acceptor systems have in many cases confirmed this correlation of the CT band energy with the I_D and

E_A^v.[4,6-9,31-34] The UV absorption using I_2 as the electron acceptor ($E_A^v \approx 1.0$ eV)[47] peaks at 290 nm[35,40,48] for diethylsulfide·I_2 (I_D =8.7 eV), 270 nm[48] for *p*-dioxane·I_2 (9.13 eV) and 242 nm[46] for acetone·I_2 (9.7 eV). For the benzene·ICl complex, the CT absorption peak is located at ~282 nm[49] (I_D =9.24 eV) but with a larger E_A^v (~1.5 eV).[50,51]

The ground-state complex structure can be obtained by measurements of the vectorial correlation between the direction of the recoil and the CT transition dipole moment. The electronic transition dipole moment corresponding to the CT excitation is given by

$$\mu_{CT} = \langle \Psi_E | \hat{\mu} | \Psi_N \rangle = a^* b \mu_{11} - a b^* \mu_{00} + (a a^* - b b^*) \mu_{10} \quad , \tag{5.5}$$

μ_{00} and μ_{11} are simply the static dipole moments of the no-bond and dative-bond configurations, and μ_{10} is the transition dipole moment between them. The μ_{11} is approximately about e**R** and for typical vdW separations, the magnitude is on the order of 20 D and the direction points from the "center of charge" of D^+ to that of A^-. On the other hands, μ_{00} is nearly zero or very small (≤4D).[9] For example, the magnitude of the μ_{00} is about 4.0 D for diethylsulfide·I_2[52] and 1.0 D for *p*-dioxane·I_2.[39,53,54] Thus, equation (5.5) reduces to

$$\mu_{CT} \approx a^* b \mu_{11} + a a^* \mu_{10} \quad . \tag{5.6}$$

The CT transition dipole moment is dominated by the two major components. The magnitude of μ_{10} has been shown by Mulliken[4] to be roughly proportional to the spatial overlap of the donating and accepting orbitals and the direction is determined by the

group theory and the CT-state symmetry. Since D and A are in a vdW contact, this component is expected to be small.

For the strong nσ-complex, since b is large enough the μ_{CT} is dominated by the μ_{11} component. Thus, for diethylsulfide·I_2, *p*-dioxane·I_2 and acetone·I_2 complexes, the transition dipole moment μ_{CT} points from the heteroatom (S, O) to the center of I_2. For the weak πσ-complexes, it is difficult to judge the relative importance of the two components due to the small mixing coefficient b and it might differ from case to case. However, the μ_{10} component alone is certainly not enough to explain the observed strong CT transition in the πσ-complex and it turns out that the μ_{11} term also makes a major contribution to the CT transition in most cases. For the benzene·I_2 and benzene·ICl complexes, the μ_{11} points from the center of charge of benzene to that of I_2 or ICl, and the μ_{10} is determined from the point group and the CT-state symmetry, as analyzed in detail in the previous benzene·I_2 studies; see Chapter 4.[14] Experimentally, by measuring the vector correlation between μ_{CT} and the recoil velocity of the I-atom (v_I) in term of the anisotropy parameter (β), the ground-state complex structure is deduced.

Figure 5.4 shows the *ab initio* structures[55-58] for the different complexes we studied, except for the *p*-dioxane·I_2 geometry which is taken in a analogy from the X-ray crystal structure of *p*-dioxane·I_2.[59] The isolated 1:1 complex geometries predicted from recent *ab initio* calculations[57,58,60] are found to be very similar to the early X-ray crystal structures[61] and most geometries can be rationalized by a mutual orientation between D and A to reach a maximum overlap of the donating and accepting orbitals. For the large size of the I-atom, the electrostatic effect also plays an important role in forming the ground-state complex. All structures have a C_s symmetry. For the diethylsulfide·I_2

complex,[55] the binding energy is predicted to be -6.18 kcal/mol stabilizing by the interaction of the π-type lone-pair electrons ($3p^2$) on sulfur with the I-I σ^* orbital. For the acetone·I_2 complex,[56] the binding energy is calculated to be -5.08 kcal/mol with the sp^2-type lone-pair electrons on oxygen interacting with the σ^* orbital of I-I. The benzene·ICl complex[57] has a binding energy of -3.19 kcal/mol with the I-atom facing the C-atom or the C-C bond center. The *ab initio* predication of the stabilization energy for the *p*-dioxane·I_2 complex is not available yet, but an estimated value is around -4.0 kcal/mol with interaction of the sp^3-type lone-pair electrons on oxygen with I-I (σ^*), and should be close to the case of the acetone·I_2 complex.

5.3. Experimental

All experiments were performed in a two-chamber molecular-beam apparatus integrated with a tunable femtosecond laser system. Most details have been described in Chapter 2[14,29] and only a brief description related to this work is given here.

The fs laser pulses from the oscillator were passed through a home-build four-stage pulsed dye amplifier to reach an energy of 300-400 μJ/pulse and were tuned to be centered at ~609 nm typically with ~3-4 nm full width at half-maximum (fwhm). The 277-nm pump pulse (~5-10 μJ/pulse) was obtained by focusing 80% of the amplified beam into a D_2O solution to generate a white-light continuum, selecting the wavelength from the continuum, reamplifing through another three-stage pulsed dye amplifier and then frequency-doubling through 0.5-mm KDP nonlinear crystal. The remaining 20% of the 609-nm laser beam was sent to a double-passed single-stage dye amplifier and then delayed in time by a retroreflector mounted on a computer-controlled translation stage. A

0.5-mm KDP crystal was used for frequency doubling to obtain the probe beam at around 304.5 nm (~20 μJ/pulse) for 2+1 resonance-enhanced multiphoton ionization (REMPI) detection of free iodine atoms. Finally, the pump and probe pulses were recombined collinearly, focused and spatially overlapped in the extraction field region of the TOF mass spectrometer.

A supersonic molecular beam containing the species of interest was generated in the first chamber, skimmed and intersected by the fs laser beams in the extraction region of a two-stage linear TOF-MS housed in the second chamber. The molecular beam, TOF-MS axis and the fs laser beams were orthogonal to one another. For all results reported here, the pump laser polarization was orthogonal to the probe laser one and either parallel or at an angle of 54.7^0 to the TOF-MS axis (z). The TOF-MS was also used as a kinetic-energy spectrometer, as described in Chapter 2, to resolve the speed and angular distributions of reaction products. The pump-probe cross correlation was typically 400±50 fs fwhm. Although a much shorter probe pulse can be easily reached, the resulting broader spectrum leads to the loss of tunability for the iodine-atom REMPI detection. All transients reported here result from one-photon excitation as checked by the pump power dependence of the observed signal.

Molecules of interest were seeded in ~800 Torr of He and were expanded through the pulsed valve. The mixture was made by flowing the He over the donors and acceptors separately far away from the nozzle and then combining two gas lines together in front of the nozzle. To avoid larger cluster formation except 1:1 D·A binary complex, the condition was carefully controlled in two ways: sampling the different portion of the gas pulse by varying the delay time between the fs laser pulses and the pulsed valve opening,

and keeping the low vapor pressure of the samples by maintaining them at low temperatures.

All samples were purchased from Aldrich. For donors, the diethylsulfide (DS, ≥98% pure), *p*-dioxane (DO, ≥99%), acetone (AO, ≥99.5%) and benzene (Bz, ≥99.9%) were cooled down to -54 ^{0}C, -20 ^{0}C, -68 ^{0}C and -45 ^{0}C, providing 0.45 Torr, 2.8 Torr, 0.6 Torr and 0.5 Torr of vapors, respectively. For acceptors, the iodine (I_2, 99.999%) was used at room temperature (vapor pressure ~1 Torr). The iodine monochloride (ICl) was sublimated from the iodine trichloride (ICl_3) crystal in order to eliminate the contamination because the vapor above the ICl crystal contains I_2.[62] The existence of excess Cl_2 vapor above the ICl_3 crystal suppresses the I_2 formation due to the reaction of Cl_2 and I_2. The crystalline ICl_3 (≥97%) was cooled to -12 ^{0}C, giving an estimated ICl vapor of ~2-3 Torr.[62]

The TOF mass spectra are shown in Figure 5.5. Note that only 1:1 donor-acceptor binary complex was formed under the well-controlled conditions and the D·A complex ion fragmentation is server for most cases, as seen from the small D·A complex TOF signal and broad distributions of fragment mass peaks. Especially for the benzene·ICl, the 1:1 complex ion nearly goes to complete fragmentation. Experimentally, when the donors were added into the I_2/He mixture, the I-atom *transient* intensities were enhanced by a factor of ~14, 4, 5 for diethylsulfide, *p*-dioxane and acetone, respectively. For the reaction of benzene with ICl, the I-atom *transient* signal was enhanced by a factor of ~7. The observed enhancement indicates a direct CT excitation and excludes the contributions from the locally excited D^*·A and D·A^* reactions, in accord with the much

stronger absorption of the D·A complex than those of donors[35,46,49,63-65] and acceptors[66,67] alone, as illustrated in Figure 5.2 for the case of the diethylsulfide/I_2 mixture.

The fragment mass peak, D·I, resulting from the 1:1 complex (D·I_2) ion fragmentation, reflects the nature of the bonding between D and I_2/I. As mentioned in section II, the binding energies for diethylsulfide·I_2, acetone·I_2, *p*-dioxane·I_2 and benzene·ICl are -6.2 kcal/mol, -5.1 kcal/mol, ~-4.0 kcal/mol and -3.2 kcal/mol, respectively. As shown in Figure 5, the D·I peak is very large for diethylsulfide·I_2 (DS·I), small for acetone·I_2 (AO·I) and hardly seen for *p*-dioxane·I_2 and benzene·ICl, consistent with the D·I_2 (D·I) complex binding energies. An attempt was made to study the much strong complex reactions of pyridine·I_2 and diethylsulfide·ICl, but it didn't work because some chemical reactions between the donor and the acceptor occur in the mixing line before expansion.

5.4. Results

5.4.1. Time and Velocity Correlations

The angular-resolved I-atom KETOF distributions (χ-KETOF) for three different pump polarizations are shown in Figure 5.6 for the three nσ-complexes at a fixed delay time of 7.0 ps. The data were taken very carefully: (1) the pump and probe intensities were kept as low as possible to reduce the space-charge effect and minimize the KETOF broadening, and (2) the I-atom transient KETOF distributions from the background I_2 dissociation in the molecule beam, which account for 7% of the total signal for diethylsulfide·I_2, 25% for *p*-dioxane·I_2 and 20% for acetone·I_2, were subtracted out from each measurement. The iodine molecule was found to have a pure perpendicular

transition at 277 nm (C←X)[68] and the KETOF shape[69-72] (β~-1.0) is totally different from those shown in Figure 5.6, especially at $\chi=0^0$. No noticeable change was found for all KETOF distributions (Fig. 5.6) after 7 ps delay time. These distributions ($\chi=0^0$) clearly suggest that two distinct velocity components are present, especially clear for the diethylsulfide·I_2 complex. All three systems show a parallel transition and their different shapes reflect the different translational energy and anisotropy distributions of the I atom release.

In order to reveal the dynamic behavior of the two velocity distributions, the temporal evolution of the KETOF distributions was measured and for each measurement, the background I-atom transient KETOF distribution was subtracted out. Figure 5.7 shows the fs-resolved KETOF distributions at the parallel ($\chi=0^0$) and magic angle ($\chi=54.7^0$) polarizations for the diethylsulfide·I_2 complex. Clearly, two distinct velocity distributions, fast and slow, show a dramatic difference in the temporal behavior. At early times, only the fast I-atoms appear and the distribution reaches a plateau value after 1.75 ps. However, the slow ones show up only after ~900 fs and gradually buildup until 7 ps, and also have a higher anisotropy than the fast ones, as clearly seen from the growth of the two components at $\chi=0^0$.

The fs-resolved KETOF distributions for the *p*-dioxane·I_2 and acetone·I_2 complexes are shown in Figure 5.8 at $\chi=54.7^0$. Once again, two velocity distributions, fast and slow, are present and have different time behavior. For *p*-dioxane·I_2, the fast I-atoms were released quickly and after 2.26 ps, the signal ($v_z \geq 800$ m/s) stays constant but the slow distribution keeps growing until 7 ps. For acetone·I_2, although the two

distributions overlap heavily, the fast distribution at $v_z \geq 800$ m/s shows a constant after 3.03 ps under a careful examination and the slow I-atom signal still increases up to 7 ps.

In Figure 5.9, the two velocity distributions are clearly revealed in the speed distributions, derived from the magic-angle ($\chi=54.7^0$) data (Fig. 5.7 and 5.8). The corresponding translational energy distributions of I-atoms are shown in Figure 5.10. The high-speed (v≥800 m/s) components of three complexes are very similar whereas the three slow-speed distributions are very different. For diethylsulfide·I_2, the two speed distributions are well separated at v=800 m/s (E_T=3420 cm^{-1}). For the oxygen-containing donors, the two distributions overlap in the range of 750-850 m/s (E_T=3000-3860 cm^{-1}). The dramatic difference in the temporal behavior for the two speed distributions observed here for all three complexes clearly shows that the two types of I-atoms are *from two different dynamic processes of the reaction, not resulting from the parallel reaction pathways involving the two spin-orbit states of I and I** (separated by 7600 cm^{-1}), *e.g.,* for the covalent channel I/I^*+D·I/D·I^*. Analyses of the two translational energy distributions, as discussed below, also support this conclusion.

The high-speed component is centered at ~1030 m/s (5700 cm^{-1}) and extends to ~1300 m/s (10000 cm^{-1}) for all three complexes. This fast component *is unambiguously assigned to the exterior I-atom released through the dissociative covalent channel*, based on the following energetics consideration. For example, the maximum CT absorption of the diethylsulfide·I_2 complex in the gas phase is at 290 nm[35,40,48] (Fig. 5.2) and recent *ab initio* calculations[55] give an equilibrium distance of 3.32 Å between S and I, and a binding energy of -6.2 kcal/mol. For a complete ET, the DS^+I^- equilibrium distance is derived to be 3.7 Å.[14] To account for a fraction ET, we take the range of 2.7-3.7 Å,

predicting that the lower limit of the zero-point energy of DS^+I^- is ~2.1 eV above its ground state. Therefore, the upper limit of the available energy for the ionic exit channel is ~0.6 eV at 277 nm excitation and the maximum translational energy of the released exterior I-atoms, based on the kinematics, is ~3000 cm^{-1}, much smaller than our observed 10000 cm^{-1} of the fast I-atom. Similar considerations are applied to the other two oxygen-containing complexes. Thus, the presence of such covalent channel indicates that RET must occur and is responsible for the high speed distribution acquired by the fragment I-atom; much higher than that from the ionic exit channel.

For the diethylsulfide·I_2 complex, the slow distribution is centered at a final speed of v=500 m/s (1335 cm^{-1}) but terminates at 300 m/s (480 cm^{-1}). Furthermore, the peak shifts (Fig.5.9A) from the maximum of v=620 m/s at early times to v=500 m/s after 7 ps, indicating the degree of inelastic energy transfer from the atomic motion to the donor molecule. *The slow I-atom release is also from the dissociative covalent channel and any contribution from the ionic one must be negligible.* This is supported by our *five* observations: (1) the branching ratio of the fast I-atoms to slow ones, (2) the difference in coherent caging time from the fast I-atom distribution, (3) the difference in anisotropy of the two I-atoms (1-3 as shown below), (4) the shift of the entire distribution with time (shown above) and (5) the fact that the I-atom distribution observed here did not extend to zero speed, typically observed in many harpoon reactions.[73,74] Accordingly, this slow component results from the interior I-atoms, released from the dissociative covalent channel after collisions with diethylsulfide in a *one-molecule caging.*

For the oxygen-containing donor complexes, although the slow distribution is not well separated from the fast one, similar dynamic processes of the one-molecular caging

for the slow I-atoms are observed. The slow distribution for *p*-dioxane·I_2 is centered at the final speed of 500 m/s, similar to the diethylsulfide·I_2 complex, and also changes with time: at the early delay time it terminates at ~200 m/s and at the later delay time (7 ps) extends to 0. The slow component for acetone·I_2 peaks at the final speed of ~600 m/s (1925 cm^{-1}) and gradually extends to 0 with time. Although the contribution from the ionic exit channel for the two oxygen-containing donor complexes could not be exclusively ruled out, it should be negligible based on the following measurements on the branching ratios of the slow I-atoms to fast ones and the difference in anisotropy for the fast and slow components.

5.4.2. Femtosecond Transients and Branching Ratios

The temporal behavior of the two dynamic processes is also revealed clearly by gating of the fast and slow components (using v=800 m/s as the dividing line of the two distributions for the oxygen-containing complexes). The transients are shown in Figure 5.11, together with the experimental transients while collecting all I-atoms (the background I-atom transient from the I_2 monomer has been subtracted out). The slow I-atoms show a dramatic different time evolution from the fast ones for all cases studied here.

The total I-atom transients give time constants of τ=850, 1200 and 1200 (±50) fs for the overall reactions of diethylsulfide·I_2, *p*-dioxane·I_2 and acetone·I_2, respectively. The fast components, however, give rises of 510, 860 and 830 fs all with a ~150 fs coherent delay from the time zero, whereas the slow components show rise times of 1.15, 2.23 and 2.1 ps, but with a ~800 fs coherent shift for diethylsulfide·I_2 and only a ~150 fs

coherent delay, similar to the fast I-atom transients, for both oxygen-containing complexes.

The reaction time of the exterior I-atom (fast component) represents the bond rupture in the $D{\cdot}I_2$ system, *i.e.*, the dative-bonding TS lifetime of $D^+\text{-}^-I\cdots I^\ddagger$. Specifically, the observed 510, 860 and 830 fs reaction times are the entire complex lifetimes of $DS^+\text{-}^-I\cdots I^\ddagger$, $DO^+\text{-}^-I\cdots I^\ddagger$ and $AO^+\text{-}^-I\cdots I^\ddagger$, receptively. Since RET is responsible for the extinction of the dative bonding and the birth of the covalent bonding, *the observed complex lifetime here is actually the time of the overall RET process, of the dative bonding of the complex in the transition state and of the dissociative covalent bonding formation.* The coherent shift of 150 fs observed for all three complexes indicates the nature of the coherent reaction trajectories and is the shortest time for some trajectories moving from the initial *well-localized* configuration to the product of D···I+I. This coherent delay equals to the typical I-I bond breaking time on a repulsive potential surface.[29] Thus, after the dative wave-packet preparation at t=0, some trajectories quickly hop to the dissociative covalent exit channel by RET and the dative bonding promptly switches to the covalent bonding.

The reaction times of the interior I-atoms (slow component) represent the entire dynamic processes of the CT reactions including the one-molecule caging of the D···I complexes. Specifically, the observed 1.15, 2.23 and 2.1 ps contain the entire complex evolution time and the collision complex lifetimes of DS·I, DO·I and AO·I, respectively. The observed large coherent shift (800 fs) from DS·I indicates that the interior I-atom was *trapped* in the force field of the donor (DS) during the collision. The 150 fs coherent delay for both DO·I and AO·I gives the shortest time for the interior I-atom to liberate from the force field of both the donor and the fast exterior I-atom. This time equals to the

observed coherent shift of the fast exterior I-atom, implying that some trajectories coherently evolve along the three-body pathway to D+I+I after RET.

Since the exterior I-atoms are released from the covalent channel, the interior I-atoms, facing to the donor, proceed to an inelastic collision with the donor. For an ideal case in which the interaction between the I-atom and the donor is very weak, the interior I-atoms should be completely liberated and the branching ratio of the slow I-atoms to fast ones is 1. Experimentally, we obtained the branching ratios (after 7 ps in Fig. 5.11) of 55:100 for diethylsulfide·I_2, 65:100 for *p*-dioxane and 88:100 for acetone·I_2. These ratios are all less than 1 and also indicate that the I-atoms from the ionic exit channel should be negligible.

As much as 45% of the caged interior I-atoms are not liberated from the collision complex of DS·I, consistent with the strong binding energy, ~-6 kcal/mol, between diethylsulfide and the I-atom.[75] Further evidence of the speed cut-off at 300 m/s (Fig. 5.9) for the interior I-atoms indicates that some interior I-atoms with the low translational energy are trapped in the force field of diethylsulfide and there exists a barrier for dissociation to DS+I. It is surprising that as much as 35% of the caged I-atoms are trapped in the DO·I collision complex even though the binding energy is not so strong, only -4 kcal/mol. For the AO·I collision complex, only 12% of the interior I-atoms are trapped though the binding energy (-5.1 kcal/mol) is larger than that of the DO·I complex.

5.4.3. Recoil Anisotropy and Initial Complex Structure

Since the dynamic processes of CT reactions occur at the fs time scale, the rotation motion is negligible and therefore the measured recoil anisotropy of I-atoms reflects the vectorial correlation (φ, $\beta=2P_2(\cos\varphi)$) between the recoil direction (recoil velocity **v**) and the initial transition dipole moment (μ_{CT}). The final recoil anisotropy distributions $\beta(v)$ and the corresponding angles are shown in Figure 5.12 from a satisfied fitting of both the parallel and perpendicular polarization KETOF distributions (at $\chi=0^0$ and 90^0) according to the procedure described in Chapter 2, using the derived speed distributions (Fig. 5.9). Figure 5.13 shows the typical results of the fits for the three complexes at $\chi=0^0$.

For a given value of β, the derived angle could be two values, φ or 180^0-φ, depending on the relative recoil directions of the two I-atoms. Note that the angle between the recoil velocity of the exterior I-atom and μ_{CT} is always less than 90^0 (φ). However, the recoil direction of the interior I-atom relative to μ_{CT} could be either φ or 180^0-φ depending on the interior I-atom recoil direction relative to the exterior one. After RET, if most available energy is stored in the I-I bond (potential energy) the interior I-atom will move away from the exterior one and the angle derived from the anisotropy should be 180^0-φ (larger than 90^0), and if the D-I bond obtains most available energy (translational) the two I-atoms will move the same side away from the donor by three-body dissociation and the corresponding angle should be φ (less than 90^0).

The observed *fastest* exterior I-atoms (v~1250-1300 m/s and E_T~8360-9040 cm^{-1}) indicate most available energy is deposited in the I-I bond after RET according to the energy conservation and there are no other significant vibrations to alter the structure on this initial fs time. Therefore, it is reasonable to consider the complex structure, which

releases the fastest exterior I-atoms, as the initial one. From the measured β's of the fastest exterior I-atom release we obtain the angles of the I-I bond orientation (recoil velocity) relative to μ_{CT} in the range of 0^0-10^0 (Fig. 5.12) for all three systems.

As discussed in Sec.5.2, the overall transition dipole moment μ_{CT} in the strong nσ-complex is dominated by the CT-state dipole moment μ_{11} and the direction points from the donor atoms (S, O) to the center-of-mass of the iodine molecule. Thus, the corresponding angles derived from the β distributions are the relative direction of μ_{11} and the recoil speed v_I. The observed initial angles, 0^0-10^0, of the fastest exterior I-atoms indicate a nearly linear configuration of S(O)-I-I for all three complexes, consistent with recent *ab initio* predictions for the ground-state structures.[55,56] This linear interaction orientation is a perfect geometry for the maximum overlap between the donating orbital (lone-pair electron, p-type) and the accepting orbital (σ^*). The experimental structures of the three complexes are depicted in Figure 5.14 based on the *ab initio* predicted interaction scheme.

The β(v) distributions of the fast exterior I-atoms for the three systems have the similar trend, monotonically decreasing from the same higher value (~1.9) to a lower one. This observation indicates the dynamic structural changes with the energy release. For each system, the two components, naked exterior and caged interior I-atoms, have different anisotropy distributions. Specifically, for diethylsulfide·I_2 (Fig. 5.12(A)), the anisotropy β for the fast component monotonically decreases from 1.9 to -0.5 and has an average value of ~0.48 and the corresponding angle is 45^0, *i.e.*, 35^0 difference away from the μ_{CT} direction compared with the initial one. However, the slow I-atoms have a higher, nearly *constant* β's~0.9, indicating that all interior I-atoms are released nearly along the

same direction. For *p*-dioxane·I_2 (Fig. 5.12(B)), the β distribution shows monotonic decreasing from 1.9 to -0.5. The average β for the fast I-atoms is ~1.25 and the corresponding angle is 30^0. The slow I-atoms have an average β of ~1.0. For acetone·I_2 (Fig. 5.12(C)), the β distribution for the fast component monotonically decreases 1.95 to 1.25 with an average of 1.7 and the corresponding angle of ~18^0. The slow I-atoms shows monotonic decreasing anisotropy from 1.25 to 0 and have an average of ~1.0. These correlations of the structure evolution with the energy release for each CT complex will be discussed in detail in Sec. 5.5.

5.4.4. Benzene·ICl: A Direct Examine of Structure and Mechanism

The CT reactions of the 1:1 weak πσ-complexes of benzene (and its deuterated and methyl-substituted species) with I_2 have been previously studied in great detail; see Chapter 4.[14] The results are similar to those observed for the three nσ-complexes presented in the above. Basically, two speed distributions, fast and slow, were observed and the fast one is from the exterior I-atoms, released from the dissociative covalent channel and the slow one is liberated mainly from the one-molecule caging of the interior I-atoms after RET. The contribution of the ionic exit channel to the slow component is minor. The recoil anisotropy for the fast exterior I-atoms was about ~1.0 and the corresponding angle is 35^0, indicating that the recoil direction is tilted away from the initial transition dipole, which is also supported by recent ab initio calculations[58] (Fig. 5.4). For the slow interior I-atoms, the anisotropy shows a monotonic decreasing from 0.6 to 0.1.

Compared with the benzene·I_2 complex, the study of the benzene·ICl complex is unique. Using ICl as the electron acceptor instead of I_2, only one I-atom is observed and therefore only one speed distribution is expected. If the I-atom faces the benzene molecule in the complex, no I-atoms will be observed from the ionic channel in the fs time scale because the Bz^+I^- exciplex usually has ns lifetime as many rare-gas halide exciplexes have,[76] but for the dissociative covalent pathway after RET, a slow speed distribution will be expected. If the Cl-atom faces the benzene ring, the exterior I-atom is released from the ionic exit channel with a slow speed distribution but a fast distribution is expected from the covalent channel. Recent *ab initio* calculations[57] predict a C_s-symmetry structure, similar to the benzene·I_2 one,[58] with the I-atom facing the benzene ring (Fig. 5.4). Thus, only the slow speed distribution of interior I-atoms will be expected from the dissociative covalent channel and the ionic channel is not detectable in the fs range. In the following, the results from both reactions of benzene with ICl and I_2 are presented together for comparison.

The angular-resolved KETOF distributions for three pump polarizations are shown in Figure 5.15 at a delay time of 7 ps. After 7ps, the distributions stay unchanged and the CT reaction is complete. The three I-atom KETOF distributions from the benzene·ICl complex are surprisingly similar, indicating that the overall anisotropy is very small, close to 0. The much narrower distribution is due to the less total available energy (the strong I-Cl bond) and the dissociation kinematics of ICl, in which the Cl-atom takes more translational energy away. The background I-atom transient KETOF distribution, 15% of the total signal resulting from the ICl molecules alone in the molecular beam, has been subtracted out. The ICl molecule at 277 nm has a pure parallel

transition and exclusively dissociates into I^*+Cl/Cl^*,[77,78] and the I-atom KETOF distributions[78,79] (β~2.0) is totally different from those shown in Fig. 15, especially at $\chi=0^0$ and 54.7^0.

Comparing the two distributions at $\chi=0^0$ in Fig.5.15, the fast distribution from the benzene·ICl complex is dramatically reduced and the slow one dominates. The whole distribution shows no significant time dependence, indicating that *all I-atoms are from one dynamic process.* By gating the total I-atoms, the fs transient is shown in Figure 5.16(A) with a 950 fs rise time by a single exponential fit. The KETOF distribution from the benzene·I_2 complex shows two components, fast and slow, with different time behavior (not shown). The fast I-atoms have a 450 fs rise time and the slow ones with 1.4 ps (Fig. 5.16(B)). The branching ratio of the slow I-atoms to the fast ones is ~100:100, implying that a small percentage of the slow I-atoms is from the exterior ones of the ionic exit channel if accounting for some trapped interior I-atoms of the covalent channel. All transients have a ~150 fs coherent delay from time zero, similar to that observed in the three nσ-complexes, indicating the coherent nature in the CT reactions and that some trajectories after CT excitation promptly hop into the covalent channel by RET. The 150 fs coherent shift is simply the bond breaking time of I-Cl on a repulsive potential energy surface.

The final speed distributions derived from the magic angle data (Fig. 5.15) are shown in Figure 5.17, together with the corresponding translational energy distributions. The whole speed and translational energy distributions for the benzene·ICl complex shifts to the low values as expected. The distribution consists of a major peak centered at v~170 m/s and a tail peaking at v~585 m/s and extending to ~830 m/s. The major peak

accounts for ~75% of the total signal and the tail for 25%. This tail distribution is only from the covalent channel because the ionic channel, even though the Cl-atom faces the benzene ring, could not produce this high-speed I-atom according to the following energetics. The maximum CT absorption is at ~282 nm[49] and the complex binding energy is assumed to be -3.2 kcal/mol with a distance of 3.0 Å between benzene and Cl.[57] For a complete ET, the Bz^+Cl^- equilibrium distance is derived to be 3.26 Å. To account for a fraction ET, a range of 2.7-3.26 Å is used and the predicted low limit of the zero-point energy of Bz^+Cl^- is ~1.92 eV above its ground state. Therefore, the upper limit of the available energy for the ionic channel is ~0.27 eV at 277 nm excitation and the maximum translational energy of the released I-atom, based on the kinematics, is ~1025 cm^{-1}, much smaller than our observed ~3700 cm^{-1} for the high-speed component. Excluding the high-speed I-atoms from the ionic channel, the slow ones therefore are also from the covalent channel based on two key observations: (1) the high- and low-speed I-atoms show no dramatic temporal difference, thus all I-atoms are released from one dynamic process of the covalent exit channel (shown above); and (2) the anisotropy measurement in the following shows no dramatic difference for the whole I-atoms, indicating that all I-atoms are from the same channel.

The anisotropy distributions by fitting both the parallel and perpendicular KETOF profiles are given in Figure 5.18, together with the corresponding angles. The typical theoretical simulation of the KETOF distributions is shown in Figure 5.19 for $\chi=0^0$. The anisotropy distributions show a monotonic decreasing from 0.5 to 0 and surprisingly have the similar values of the caged interior I-atoms from the benzene·I_2 complex (Fig. 5.18), implying that both structures are nearly the same, consistent with the *ab initio* predictions

(Fig. 5.4).[57,58] This observation indicates that *the I-atom faces the benzene ring in the complex structure and all interior I-atoms result from the one-molecule caging of the covalent channel through RET.*

Finally, the two distributions of the major peak and small tail result from the parallel reaction pathways involving two spin-orbit states of I^* and I (7605 cm^{-1} separation) in the dissociation of ICl. The tail component is centered at ~1830 cm^{-1} and the major peak at ~155 cm^{-1}. The energy difference is ~1675 cm^{-1} and this value is the same *translational* energy separation of I and I^* from the dissociation of ICl ($E_{I*}=m_{Cl}/m_{ICl}E_{avl}$, $E_I=m_{Cl}/m_{ICl}(E_{avl}+7605)=E_{I*}+1673$ cm^{-1}). This observation is very surprising in that during the inelastic collision between I/I^* and benzene, the amount of the transferred atomic translational energy to the benzene moiety is the same for both I and I^*. Assuming that the total available energy is deposited in the I-Cl bond after RET, the I-atom acquires 3955 cm^{-1} translational energy and the I^*-atom gets 2329 cm^{-1}, and the amount of the energy loss from both I and I^* is ~2150 cm^{-1}, an upper limit of energy transferred to the benzene molecule (C-C motion and molecular rotation) during the collision. The electronic energy of I^* was found to be conserved during the collision.[15] The observed branching ratio of I^* to I is found to be 3:1 and represents a lower limit because most trapped iodine-atoms are from the I^* pathway due to its small translational energy. However, it should be pointed out that this branching ratio of I^* to I (3:1) cannot be applied to the correction of the branching ratio of the slow I-atoms to the fast ones obtained from the $D{\cdot}I_2$ reactions (Sec. 5.4.2) because of the different nature of potential energy surfaces of ICl and I_2, and more trapped iodine-atoms in the benzene·ICl reaction than in the $D{\cdot}I_2$ reactions due to the different translational energy partition in the I^*

pathway. Actually, the percentage of the caged interior iodine-atoms from the I pathway (I+I) hidden in the fast distribution in the D·I_2 reactions is negligible, as discussed in the next section (Sec. 5.5.1).

5.5. Discussion

The experimental results presented above elucidate the temporal evolution of the strong nσ-complex CT reactions along the dissociative covalent exit channel exclusively by RET in the TS although the initial configuration is a dative character (most ionic). The two distinct translational energy distributions of the I-atom product, high and low, result from the two elementary dynamic processes involved in the covalent exit channel: The high translational energy distribution of the fast exterior I-atoms (I_f) reflects the energy dissipation in the dative-bonding TS of the supramolecular D^+-I^-···$I^{\ddagger}$ complex before RET and the low one of the slow interior I-atoms (I_s) indicates the energy transfer to the donor after the ensuing one-molecule caging (D···I collision) following RET. Thus, the reaction mechanism can be described by the following elementary steps

$$[D\cdot I_2]^{\ddagger} \xrightarrow{h\nu} [D^+\text{-}I^-\cdots I]^{*\ddagger} \rightarrow [D\cdots I\cdots I]^{*\ddagger} \rightarrow D\cdot I + I_f \quad , \tag{5.7a}$$

$$\rightarrow D\cdots I + I_f \rightarrow D + I_s + I_f \quad . \tag{5.7b}$$

Reaction (5.7a) indicates a "two-body" (D·I and I_f) dissociation process and some interior I-atoms are trapped in the force field of the donor during the inelastic collision between I and D. Reaction (5.7b) is a complete "three-body" (D, I_s and I_f) decomposition process including both the two-body (D···I and I_f) dissociation and the subsequent atom-molecule collision process. The temporal behavior of the fast exterior I-atom (I_f) gives the dative-

bonding dynamics in the TS from the initial dative configuration to RET, leading to a two-body dissociation of D·I+I_f or D···I+I_f. The time evolution of the slow interior I-atom (I_s) integrates the entire dynamic process (reaction 5.7b) of most CT reaction trajectories from t=0 to the final three-body dissociation of D+I_s+I_f, including the one-molecule caging process. The measured anisotropy distributions give the initial complex structures and the geometric change with the energy release. For the weak πσ-complex of benzene·ICl, the observations elucidate the initial complex structure and the reaction mechanism.

In the following, we discuss the two dynamic processes of the dative-bonding TS before RET and the one-molecule caging after RET in detail.

5.5.1. Dative-bonding Transition States

At the time zero, the complex in the ground state is excited to the first dative-bonding CT state with most ionic character and launched at a well-localized nonequilibrium configuration. The initial photon energy is stored mainly in D^+-I_2^- and I-I^- bonds and starts to dissipate into other vibrational modes. Figure 5.20 represents three simplified ground-state, ionic and covalent PESs, constructed on the two reactive D···I and I···I coordinates, and Figure 5.21 is the contour maps of the ionic and covalent PESs with a typical trajectory by MD simulations. The prepared wave packet moves toward the dative-bonding TS region after t=0 and the entire complex begins the nuclear motion to search for the new stable structure or the exit channels (Figs. 5.1, 5.20 and 5.21). At our excitation energy (36100 cm^{-1}), two exit channels, ionic and covalent, are mainly considered. The ionic channel finishes with D^+I^-+I and the covalent channel ends up with

two types: $D{\cdot}I_2^*$ and $D^*{\cdot}I_2$. For the covalent channel, RET must occur from the acceptor to the donor.

After the vertical fs excitation at t=0, the I-I bond is weakened (σ^*) and I_2 anion is produced in high vibrational levels, around the dissociation limit.[47] For the ionic channel to release the exterior I-atom, as studied by MD simulations,[14] it takes several ps because of the nature of the attraction in both D^+-I^- and I-I^- bonds, indicating that the entire complex is initially trapped in the dative-bonding region. However, in the dative-bonding TS, an electron from the filled orbital of I_2^-, different from the initial electron from the donor, can jump back to the HOMO orbital of the donor to form $D{\cdot}I_2^*$, leaving I_2 still with one electron in the σ^* orbital (repulsive excited states) and releasing the exterior I-atom in ~150 fs.[29] Clearly, this process is much faster than the ionic one to liberate the exterior I-atom as long as the initial dative-bonding structure takes less than ps to encounter the covalent configuration.

For the covalent channel of $D^*{\cdot}I_2$, although some probability exists for one electron from I_2^- (σ^*) to hop into the excited orbital of the donor,[15] leaving I_2 in the ground state and the donor in the excited state (D^*), the chance for this process is minor because of the large change of the I-I configuration and the less overlap of σ^* and the donor excited orbital. Furthermore, the first electronic excited states of diethylsulfide and *p*-dioxane lie above our excitation energy (36100 cm^{-1}),[63,64] indicating that at least the covalent $D^*{\cdot}I_2$ channel is not available to these two complexes.

The occurrence of RET in the dative-bonding TS to form $D{\cdot}I_2^*$ depends on the overlap between one filled orbital of I_2^- and the unpaired HOMO orbital of D and the wavefunction overlap (Franck-Condon factor) between I_2^- and I_2^*. Thus, the I_2^* states are

likely the same states accessed by the optical excitation. Near our excitation energy of 36100 cm^{-1}, there is *only one* optically accessible $C\,^3\Sigma_{1u}^+$ state, which correlates to I+I*.[68] The electronic configuration of the ground state I_2^- is $\sigma_g^2\pi_u^4\pi_g^4\sigma_u^1$ (2441) and the C state belongs to $\sigma_g^1\pi_u^4\pi_g^4\sigma_u^1$ (1441). During RET, since the σ_g and σ_u orbitals of I_2 have the same symmetry in the entire complex and can interact similarly with the HOMO orbital of the donor one electron from the σ_g orbital promptly returns back to the donor (charge recombination).

There are some optically forbidden, repulsive excited states with the vertical energies close to our excitation energy but the probability to form these states through RET is negligible. Specifically, the $^1\Sigma_g^+$ and $^1\Delta_g$ states of the (2422) configuration, which correlate to I*+I* and I*+I, respectively, are not only optically forbidden (g symmetry) but also involving two electron transfer to two different moieties, one π_g electron to the donor and the other π_g electron to the σ_u orbital. These states are highly unfavored. The other optically forbidden repulsive states are three $^1\Pi_g$, $^3\Pi_{0^+g}$ and $^3\Pi_{0^-g}$ states from the (2341) configuration, which all correlate to I*+I, and one $^3\Sigma_{0^-u}^+$ state of the (1441) configuration, which correlates to I+I, and RET involves one electron transfer of I_2^- (π_u or σ_g) to the donor. Even though there is a very small probability to form these states after RET, most states correlate with a product asymptote yielding I*+I, the same as that of the optically allowed $C\,^3\Sigma_{1u}^+$ state. Thus, no interior I-atoms are produced from the I pathway (I+I) after RET, also proving that no interior I-atom distribution is located at the high-speed region under the fast exterior I-atom distribution, as mentioned in Sec.5.4.4.

We did observe the CT reaction to evolve *only* along the I^* pathway after RET from the translational energy distribution of the fast exterior I-atom. The distribution does reach the speed limit of the $I+I^*$ pathway determined by the total available energy; see Figure 5.22. However, the average translation energy of the exterior I-atoms is about 5670 cm^{-1} (~1030 m/s), lower than the expected value estimated from the total available energy and indicating that some energy is channeled into the donor "substrate" before RET. Assuming that the I-atoms corresponding to the average translational energy result from the two-body dissociation ($D{\cdot}I+I_f$), the average total translational energy of the entire complex after RET is in the range of 8990-11340 cm^{-1} for diethylsulfide$\cdot I_2$, 9020-11340 cm^{-1} for *p*-dioxane$\cdot I_2$ and 9560-11340 for acetone$\cdot I_2$ with two extreme conditions, strong interaction between D and I or no interaction between them, during the I-I dissociation. For the first extreme, we assume that the dissociation first produces an I-atom and a D·I complex and then the complex subsequently falls apart without significant translational energy change, whereas for the second extreme, we assume that D is simply a spectator and there is no interaction between D and I. Thus, the amount of energy dissipated into the internal modes of the donor substrate before RET is 4680-7030 cm^{-1} for diethylsulfide$\cdot I_2$, 4680-7000 cm^{-1} for *p*-dioxane$\cdot I_2$ and 4680-6460 cm^{-1} for acetone$\cdot I_2$.

If considering the three-body dissociation ($D{\cdots}I+I_f$), the derived internal energy from the extreme condition of strong interaction between D and I is an upper limit for the donor because the three-body dissociation requires more translational energy to produce the exterior I-atoms with 5670 cm^{-1} translational energy. The total energy stored in the first CT excitation state is our excitation energy, 36100 cm^{-1}. Therefore, the percentage of the energy flowing into the donor before RET is 13%-19.5% for diethylsulfide$\cdot I_2$, 13%-

19.4% for dioxane·I_2 and 13%-17.9% for acetone·I_2. We conclude that an upper limit of about 19% of the total excitation energy, ~6860 cm^{-1}, is channeled into the donor substrate before RET. Thus, in the dative-bonding TS, the chemical reaction competes with the energy dissipation to the donor substrate and the time scales of RET and the energy redistribution are critical to determine the final outcome of the CT reaction. Probably, there is a small portion of CT reaction trajectories trapped in the TS well (Fig.5.21) because the energy in the reactive coordinates (D^+-I^- and I-I^-) after the energy dissipation becomes lower than the required energy for forming $D{\cdot}I_2^*$. This energy-transfer process is very similar as found in many surface studies and surface-aligned photochemical reactions.[80-82]

The time scale of the RET process was obtained from the detection of the exterior I-atoms and is less than 1 ps for all systems reported here (Fig. 5.11). On this ultrafast time scale, there is no enough time to reach complete energy redistribution in the entire complex and the dissipated energy probably activates only several internal coordinates of the donor, such as the C-O or C-S motion. The temporal evolution of the dative-bonding TS is illustrated in Figure 5.20 and 5.21. At each crossing point, the wave packet bifurcates: One part hops into the covalent exit channel by RET and the other remaining one continues on the dative (most ionic) surface and is trapped in the TS well to search another crossing and RET. Basically, there are two crossing areas: One is in the range of the smaller r(I-I) and the other is with the larger r(I-I) and r(D-I); see Fig. 5.21. The r(D-I) for the latter crossing area is larger than its initial distance. The exterior I-atoms at the higher speed come from the crossing with the smaller r(I-I) because most available energy is transferred into the potential energy in the I-I bond after RET. The lower-speed

exterior I-atoms are mainly from the crossing area with the larger r(I-I) because some energy is transferred into the translational energy in the D-I bond. With the energy dissipation, there is a high crossing probability at the beginning with the smaller r(I-I) and in the later time with the larger r(I-I) because the potential energy is larger at the smaller r(I-I). Our observed broad energy distribution of the exterior I-atoms (~7.5 kcal/mol at FWHM) is basically due to the distribution of multiple crossings (Fig. 5.21) and the energy dissipation. The fate of each trajectory to evolve to two- or three-body dissociation depends on how much translational energy is stored in the D-I bond during RET and the nature of the interaction between the interior I-atom and the donor, which is discussed in Sec. 5.5.2.

The covalent PES of $D{\cdot}I_2^*$ is the same for all CT systems and most ionic PESs have the similar shape and the difference is only a constant in energy due to the different ionization energy (I_D) of the donor; see equation (5.4). Although the crossing configurations are different for each CT complex, the time for the wave packet to be trapped in the dative-bonding TS well would not be dramatic different as long as the total energy in the reactive coordinates before RET is higher than that at the crossing positions. However, the time highly depends on the initial configuration of r(D-I) and the shape of the ionic PES (driving force, similar for most complexes). Experimentally, we observed the survival times of 450 fs, 510 fs, 860 fs and 830 fs for Bz^+-I···$I^‡$,[14] DS^+-I···$I^‡$, DO^+-I···$I^‡$, AO^+-I···$I^‡$, respectively. Note that for the two oxygen-containing complexes, the initial configuration of r(O-I) is nearly the same, ~2.8 Å[55,56] thus the same lifetimes of the dative-bonding TS are expected, ~850 fs. The initial configurations of r(S-I) for diethylsulfide·I_2 is 3.27 Å and r(Bz-I) is 3.2 Å for bezene·I_2 thus the observed similar

lifetime, ~500 fs, is expected. MD simulations do indicate that the lifetime of the dative-bonding TS is sensitive to the initial configuration of r(D-I).[14] It should be noted that although the lifetimes are different the dissipated energies into the donor are similar due to the similar accepted modes of the C-O and C-S motions. The slight difference of some higher translational energy distribution of the exterior I-atoms from the acetone·I_2 complex, compared with the other two nσ-complexes, is probably due to the stiff bond of C=O.

For the πσ-benzene·ICl complex, the electronic configuration of ICl is similar as the I_2 molecule but there are four optically allowed-transition states near our excitation energy and three ones can be accessible during RET process. The $^1\Sigma^+_{0^+}$ state of the (2422) configuration, although it is optically allowed, is highly unfavored because of the involvement of two-electron transfer. The one $^1\Pi_1$ state, correlating to I+Cl*, and other two $^3\Pi_{0^+}$ and $^3\Pi_1$ states, which correlate to I+Cl, are all from the (2341) configuration and involve one electron transfer from the π_u orbital to the donor HOMO orbital. However, the largest absorption $^3\Pi_{0^+}$ state at our excitation energy strongly couples to the $^3\Sigma^-_{0^+}$ state of the (2422) configuration, which correlates to I*+Cl. Thus, both I and I* pathways are involved after RET, as observed in Fig. 5.17, unlike the I_2 case in which only the I* pathway is formed. The formation of the I* pathway in the CT benzene·ICl reaction implies that in the RET process one π_u electron of ICl^- transfers into the donor HOMO orbital and during the ICl dissociation, two π_g electrons of ICl in the (2341) configuration moves into its π_u and σ_u orbitals, respectively, to form I*+Cl as asymptotic products from the (2422) configuration.

The vertical electron attachment to ICl at t=0 produces the ICl anion above the dissociation limit. Thus, the dynamics in the dative-bonding TS are different from the $Bz{\cdot}I_2$ case because of the nature of the large repulsion in the anion I-Cl bond. The TS lifetime of Bz^+-$I^-\cdots Cl^{\ddagger}$ is expected to be much shorter than that obtained for Bz^+-$I^-\cdots I^{\ddagger}$, 450 fs, and the branching ratio of the ionic channel (Bz^+I^-+Cl) is increased. On the other hand, the observed interior I-atoms indicates that the coupling to the covalent channel is so prompt and efficient in such a short time.

The observed ~150 fs coherent delay time of the fast exterior I-atoms for all systems reported here indicates that the reaction trajectories are coherent. This robust observation originates from the initial well-defined localized wave-packet preparation. The observed time is simply the direct bond-breaking time of I_2 on the repulsive surface. Thus, some trajectories after the CT excitation promptly hop into the covalent channel through RET and all available energy is channeled into the I-I bond (potential energy) before any energy dissipation to the donor substrate, as depicted in Figs.5.20-5.22. Meanwhile, from the anisotropy of the fastest exterior I-atom (~1250-1300 m/s), we deduced the structure as the initial ground-state one, as shown in Fig. 5.14.

For the fast exterior I-atoms of the three nσ-complexes a strong correlation is observed between β and v (Fig. 5.12): the lower the speed, the smaller the anisotropy and the larger the corresponding angle, *i.e.*, the less translational energy the exterior I-atom is released with, the larger angle it is tilted away from $\mathbf{u}_{CT}$. This dynamic correlation with the molecular structure is elucidated from the following three facts. First, after the wave packet experiences the first crossing (smaller r(I-I) in Figs. 5.20 and 5.21) and moves into the dative-bonding TS, RET occurs at the larger r(I-I) and r(D-I). For a given total energy

in the reactive coordinates (D^+-I^- and I-I), if more translational energy is deposited in the D-I bond and less energy in the I-I bond, the D-I bond stretches longer and the exterior I-atom acquires less translational energy with a lower speed. The longer the D-I bond distance extends, the larger the angle of the I-I bond orientation is altered away from $\mathbf{u}_{CT}$. This correlation is illustrated in Figure 5.23.

Second, with the energy dissipation to the donor, the C-S(O) motion of the donor is probably activated and the stretching of the C-S(O) bond makes the I-I bond orientation tilted away from $\mathbf{u}_{CT}$. The more the energy flows into the C-S(O) motion, the larger the angle of the I-I orientation is tilted. Consequently, the exterior I-atom is released with less translational energy and a larger tilted angle after RET. Finally, the anisotropy distributions of the exterior I-atoms for three complexes show a robust monotonic decreasing from 1.9 to a lower value, indicating that a bending motion of S(O)-I-I is probably involved after the initial CT excitation. This observation is especially clear for the diethylsulfide·I_2 complex and the I-I bond orientation changes from 10^0 to 60^0, relative to $\mathbf{u}_{CT}$, in the dative-bonding TS. Thus, with the bending-angle increase and the more energy dissipated to the donor, the released exterior I-atom after RET has a larger tilted angle but with a lower speed.

5.5.2. One-molecule Caging

In the crossing area with the smaller r(I-I), the total energy is mainly deposited in the I-I bond (Fig. 5.21) after RET and the ensuing dynamics of the entire complex can be understood on the basis of the isolated I_2^* dissociation and subsequent one-molecule caging. After the direct I-I bond rupture and the releasing of the exterior I-atom, the

caged interior I-atom recoils away from the exterior I-atom (180^0-θ), as shown in Fig. 5.21(a). The initial incident angles of the interior I-atom can be obtained from the recoil direction of the exterior I-atom. The remaining dynamic process is an atom-molecule collision (one-molecule caging) and is determined by the relative collision energy between D and I, the impact parameter and the binding energy of the D·I complex.

If assuming all exterior I-atoms are from this crossing area, the initial incident angles of the interior I-atoms are ~170^0-120^0 (relative to $\mathbf{u}_{CT}$), 170^0-150^0 and 175^0-150^0 and the initial distributions of the collision energies are 4.1-10.7 kcal/mol (average~6.7 kcal/mol), 4.0-10.6 kcal/mol (6.6 kcal/mol) and 3.1-8.1 kcal/mol (5.1 kcal/mol) for diethylsulfide, *p*-dioxane and acetone, respectively. The binding energies of the D·I complexes have been shown in general to be the similar as their corresponding molecular I_2 complexes[83] thus they are 6.2 kcal/mol, ~4.0 kcal/mol and 5.1 kcal/mol for DS·I, DO·I and AO·I , respectively.[55,56] The equilibrium distance between S(O) and I in D·I is slightly larger than that in D·I_2[58] but the orientation of the I-atom to the donor could be very different from that in the D·I_2 complex. Clearly, the D·I complexes are launched at a repulsive, anisotropic PES between D and I in both azimuthal and radial directions. Based on the collision energies and the binding energies, some D·I complexes are trapped in the potential well and never escaped.

In the crossing area with the larger r(I-I), the molecular configuration is complicated. In Fig. 5.21, four typical crossings (b-e), assuming a linear configuration, is considered to illustrate the different collision processes between the interior I-atom and the donor after RET. These crossings occur at the larger r(D-I) and r(I-I) than their equilibrium distances. At the 4-5 Å distance of I-I, the repulsive potential energy of the

$I_2(C^3\Sigma_{1u}^+)$ state is very small and most available energy has been transformed into the translational energy in both D-I and I-I bonds after RET.

In case (b), both D^+-I^- and I-I^- bonds stretch toward the outer turning point and more translational energy is stored in D-I bond after RET. Both I-atoms moves in the same direction (φ) and this is a typical three-body dissociation. Case (c) shows the accelerated attraction interaction in both bonds after hitting the outer turning point and the D-I bond acquires more translational energy after RET. The interior I-atom first collides with the donor, flips the direction and then has a head-on collision with the coming exterior I-atom. Both I-atoms exchange the momentum and flip the direction, and the interior I-atom flies away from the exterior I-atom, having a corresponding angle of 180^0-φ (Fig. 5.12). If the interior I-atom is trapped during the first collision with the donor, the exterior I-atom will collide with the D·I complex. In case (d), the D^+-I^- bond has an accelerated attraction interaction and the I-I^- bond stretches towards the outer turning point. The interior I-atom has a head-on collision with the donor, flips the direction with a corresponding angle of φ. Case (e) is opposite to case (d) and the interior I-atom collides with the exterior I-atom, switches the momentum and moves toward the donor with a corresponding angle of 180^0-φ (Fig. 5.12). Thus, the recoil direction of the interior I-atom is φ or 180^0-φ depending on the relative motion of D-I and I-I during RET. In addition, it should be pointed out that the crossing probability is higher with the smaller r(I-I) and lower with the larger r(I-I) at the beginning and only when the total energy starts to dissipate into the donor and the total available energy in the reactive coordinates decreases, the crossing at the larger r(I-I) becomes significant. Also, it should be mentioned that although the exterior I-atoms even after RET are still involved in the

one-molecule caging such as in case (c) and (e), this period of time is very short (~150 fs) and the observed formation time of the exterior I-atom mainly represents the dynamic process in the dative-bonding TS before RET.

Besides the kinematics consideration in the above, during the collision some available energy can be channeled into the internal modes of D's, reducing the energy available for dissociation of the D·I complex. Although the T-V process is expected to be slow and rather inefficient owing to the weak coupling between the D internal modes and the D-I intermolecular vdW mode, the D-I collision, due to its large binding energy, can result in a collision complex of new chemical identity as an intermediate toward chemical reactions and the energy can be transferred to the internal modes of D in a short period of time through a much stronger chemical interaction. This consideration is supported by the results of a cross-beam experiment on Br+chlorotoluene reactions,[84] for which the collision complex was found to have a lifetime shorter than a rotational period (~5 ps) at collision energies of 20-35 kcal/mol and most available energy is channeled into the internal vibrational modes of the aromatic ring.

For the DS·I complex, we observed that 45% of the interior I-atoms could not be liberated from the force field of DS and the trapped I-atom may form a new "chemical" species with DS, such as an inner-sphere CT supramolecule.[85] The anisotropy distribution (Fig. 5.12(A)) of the escaped interior I-atoms is very striking with a nearly constant value (0.85), indicating that the interior I-atoms are "bound" to DS for certain time and then are released along the same direction. The observed ~800 fs coherent delay time reflects this trapping process and indicates that the fastest trajectories of the escaped interior I-atoms take 800 fs to reach the final D+I. A similar time behavior was also observed for the

$CH_3I{\cdot}I$ collision complex with a 1.4 ps coherent delay time.[86] The temporal evolution (1150 fs lifetime) of the escaped interior I-atoms integrates the entire dynamic process including the time behavior in the dative-bonding TS and the subsequent one molecule caging after RET. The first dynamic process takes 510 fs (lifetime) from the detection of the exterior I-atoms and the entire process needs 1150 fs, indicating that the one-molecule caging finishes in 1-2 ps. From the translational energy distribution of the interior I-atoms, the fraction of the interior I-atom energy transferred in the caging is ~80% (5133 cm^{-1}) and 47% of the transferred energy (2400 cm^{-1}) goes to the internal energy and 53% (2733 cm^{-1}) to the translational energy of diethylsulfide, assuming the crossing at the smaller r(I-I) during RET. The energy transfer is very efficient in such a short time, supporting the new chemical species involved. This is further supported by the observation of the speed cut-off at 300 m/s, indicating a new chemical species with a dissociation barrier of ~3.7 kcal/mol (upper limit). This inelastic energy transfer is also evident in the temporal shift of the slow speed component with the time in Fig. 5.9(A).

For the two oxygen-containing CT complexes, the anisotropy distributions of the caged I-atoms are very similar for both complexes and show a monotonic decreasing, indicating that the I-atoms are scattered by the donor away from the incident angles (Fig. 5.23), quite different from the DS·I complex. Although the binding energy for the DO·I complex is smaller than that for the AO·I one, the energy transfer must be more efficient because 35% of the interior I-atoms are trapped for DO·I, whereas only 12% for AO·I. The energy distributions of the escaped interior I-atoms support the observed branching ratios. Assuming that RET occurs at the smaller r(I-I), for the DO·I complex the fraction of the interior I-atom energy transferred in the caging is ~78% (4785 cm^{-1}) and 50% of

the transferred energy (2393 cm^{-1}) is channeled into the internal modes of *p*-dioxane and the other 50% into its translational energy. This efficient energy-transfer process is very similar to the DS·I complex, but the temporal behavior is different. The escaped I-atoms only have a ~150 fs coherent delay, similar to that of th exterior I-atoms, indicating no significant trapping time during the caging and the involvement of three-body dissociation such as case (b) in Fig.5.21. The dynamic process in the dative-bonding TS shows a lifetime of 860 fs and the entire time evolution from the escaped interior I-atoms has a 2.23 ps lifetime. Thus, the caging takes about 2-3 ps. For the AO·I complex, the fraction of the interior I-atom energy transferred in the caging is ~66% (3748 cm^{-1}) and 56% of the transferred energy (2089 cm^{-1}) is coupled into the internal modes of acetone and the other 44% (1659 cm^{-1}) into its translational energy. Compared with the DO·I complex, less translational energy of the caged I-atoms is transferred to acetone, which is probably due to the stronger C=O bond. The temporal evolution of the caging is very similar to that in the DO·I complex (2-3 ps) whereas the entire complex has a lifetime of 830 fs and the whole dynamic process of the escaped interior I-atoms has a 2.1 ps lifetime. Nevertheless, the T-V energy transfer is so efficient in such a short time for these two complexes thus this process must involve some "loose" new chemical species.

For the benzene·ICl weak complex, the entire dynamic process of the escaped interior I-atoms has a 950 fs lifetime, shorter than that for the benzene·I_2 complex (1.4 ps). This observation results from two facts: The initial interior I-atoms after RET have much lower translational energy than that from the benzene·I_2 complex and more caged I-atoms are expected to be trapped; the first dynamic process in the dative-bonding TS is much shorter for the benzene·ICl complex because of the nature of repulsion in the I-Cl^-

bond, as discussed in Sec. 5.5.1. Comparing the weak benzene·I_2 complex with the oxygen-containing complexes, the entire dynamic process for benzene·I_2 (1.4 ps lifetime) is faster than for *p*-dioxane·I_2 (2.23 ps) and acetone·I_2 (2.1 ps) and this is totally due to the shorter dynamic process in the dative-bonding TS (450 fs lifetime) whereas the lifetime of the first dynamic process is 860 fs for *p*-dioxane·I_2 and 830 fs for acetone·I_2. In fact, the caging takes nearly the similar time, 2-3 ps.

5.6. Conclusion

The *time, speed* and *orientation* resolution of dynamics of CT reactions is a powerful approach for dissecting the different elementary dynamic processes, elucidating the mechanism and determining the molecular structure. The CT supramolecular complex exclusively evolves along the dissociative covalent channel by RET and the reaction includes two dynamic processes: The first dynamic process of the entire complex in the dative-bonding TS region before RET includes the energy dissipation to the donor substrate and the searching for the exit channel. This process takes less than 1 ps by monitoring the release of the exterior I-atom; the second dynamic process after RET is one-molecule caging and takes more than 1 ps to liberate the interior I-atom. The energy transfer of the atomic motion to the donor substrate in this process is very efficient, which implies that a new "chemical" species is probably formed during this inelastic collision. The correlation of the dynamics and the structural evolution during the entire process is also elucidated by the measurement of the recoil speed and its direction relative to the initial fs complex alignment.

These studies emphasize several concepts. First, the *reversibility* of ET, which leads to a dominant covalent pathway, is an important mechanism and could be general in the so-called harpoon reaction mechanism.[20] Second, the separation of time scales for the two dynamic processes by RET indicates the *non-concertedness* between RET and the chemical bond breakage, a point of debate in many areas of studies. Moreover, the appearance of *coherent* reaction trajectories is evidence of the localized nuclear wave packet motion. Third, the dynamics of *energy dissipation* to the donor substrate in the dative-bonding TS critically depends on the time scales of RET and bond breakage. On the ultrashort time scale, this energy dissipation is not dominant. In the cases reported here, an upper limit of ~19% of the *total* excitation energy dissipates as internal energy of the donor substrate. Thus only few internal coordinates can be activated since there is no enough time to reach complete energy redistribution. This concept is important in studies of surface-aligned photochemical reactions.[80-82]

The interplay between the structure and the ensuing dynamics is rationalized with the help of LUMO-HOMO interactions. As depicted in Figs 5.1, 5.20 and 5.21, the initial structure, corresponding to the wave packet at zero time, has most ionic character with the transferred electron being in the σ^* LUMO of the I-I bond. When the trajectory of the motion reaches the seam and an electron goes back to the donor, the I_2 (or ICl) system is in an equivalent structure to that of an σ^* repulsive potential. Thus, the reason for the dominance of trajectories on the covalent potential by RET can now be understood. The trapping in the Coulomb potential (ionic channel) takes much longer time than the rupture on the repulsive surface (covalent channel) to release the exterior I-atom, and

hence it is the time scale of the nuclear motion which shifts the dominance toward the covalent bond breakage following RET.

5.7. References

1. G.N. Lewis, *Valence and the Structure of Atoms and Molecules* (The Chemical Catalog Co., New York, 1923).
2. L. Pauling, *The Nature of the Chemical Bond* (Cornell University Press, New York, 1939).
3. R.S. Mulliken, J. Am. Chem. Soc. **72** (1950) 610; **74** (1952) 811.
4. R.S. Mulliken and W.B.Person, *Molecular Complexes: A Lecture and Reprint Volume* (Wiley-Interscience, New York, 1969).
5. H.A. Benesi and J.H. Hildebrand, J. Am. Chem. Soc. **71** (1949) 2703.
6. G. Briegleb, *Elektronen-Donor-Acceptor-Komplexe* (Springer, Berlin, 1961).
7. *Spectroscopy and Structure of Molecular Complexes,* ed. by J. Yarwood (Plenum, New York, 1973).
8. *Molecular Complexes*, ed. R. Foster (Elek Science, London, 1973).
9. E.N. Gur'yanova, I.P. Gol'dshtein and I.P. Romm, *Donor-Acceptor Bond* (John Wiley, New York, 1975).
10. C.A. Langhoff, K. Gnädig and K.B. Eisenthal, Chem. Phys. Lett. **46** (1980) 117.
11. E.F. Hilinski and P.M. Rentzepis, J. Am. Chem. Soc. **107** (1985) 5907.
12. E. Lenderink, K. Duppen and D.A. Wiersma, Chem. Phys. Lett. **211** (1993) 503; E. Lenderink, K. Duppen, F.P.X. Everdij, J. Mavri, R. Torre and D.A. Wiersma, J. Phys. Chem. **100** (1996) 7822; F.P.X. Everdij, D.A. Wiersma, D.V. Spoel and J. Mavri, in: *Femtochemistry and Femtobiology: Ultrafast Reaction Dynamics at Atomic-scale Resolution,* ed. V. Sundström (Imperial College Press, Singapore, 1997).

13. S. Pullen, L.A. Walker II and R.J. Sension, J. Chem. Phys. **103** (1995) 7877; L.A. Walker II, S. Pullen, B. Donovan and R.J. Sension, Chem. Phys. Lett. **242** (1995) 177.

14. P.Y. Cheng, D. Zhong and A.H. Zewail, J. Chem. Phys. **103** (1995) 5153; **105** (1996) 6216.

15. G. DeBoer, J.W. Burnett, A. Fujimoto and M.A. Young, J. Phys. Chem. **100** (1996) 14882; G. DeBoer, J.W. Burnett and M.A. Young, Chem. Phys. Lett. **259** (1996) 368.

16. A.W. Castleman, Jr. and K.H. Bowen, Jr., J. Phys. Chem. **100** (1996) 12911; A.W. Castleman, Jr., (ed.) J. Phys. Chem. A **102,** No.23 (1998).

17. W.C. Lineberger, M. Nadal, S. Nandi, P. Wenthold, J.B. Kim, L.H. Andersen, Y. Ozaki and D.W. Boo, in: *Femtochemistry and Femtobiology: Ultrafast Reaction Dynamics at Atomic-Scale Resolution,* ed. V. Sundström (Imperial College Press, Singapore, 1997).

18. B.J. Greenblatt, M.T. Zanni and D.M. Neumark, Science **276** (1997) 1675; B.J. Greenblatt, M.T. Zanni and D.M. Neumark, J. Chem. Soc. Faraday Discuss. **108** (1997) 101; M.T. Zanni, B.J. Greenblatt and D.M. Neumark, J. Chem. Phys. **109** (1998) 9648.

19. P. Ayotte, C.G. Bailey, G.H. Weddle and M.A. Johnson, J. Phys. Chem. A **102** (1998) 3067; P. Ayotte, G.H. Weddle, J. Kim, J. Kelley and M.A. Johnson, J. Phys. Chem. A **103** (1999) 443.

20. M. Boivineau, J. Le Calvé, M.C. Castex and C. Jouvet, J. Chem. Phys. **84** (1986) 4712; Chem. Phys. Lett. **128** (1986) 528; **130** (1986) 208; C. Jouvet, M. Boivineau, M.C. Duval and B. Soep, J. Phys. Chem. **91** (1987) 5416.

21. T.O. Nelson, D.W. Setser and J. Qin, J. Phys. Chem. **97** (1993) 2585; F. Huang, D.W. Setser and B.S. Cheong, Israel J. Chem. **34** (1994) 127.

22. X.Y. Chang, R. Ehlich, A.J. Hudson, J.C. Polanyi and J.-X. Wang, J. Chem. Phys. **106** (1997) 3988; M.S. Topaler, D.G. Truhlar, X.Y. Chang, P. Piecuch and J.C. Polanyi, J. Chem. Phys. **108** (1998) 5378.

23. R. Zadoyan and V.A. Apkarian, Chem. Phys. Lett. **206** (1993) 475; M.H. Hill and V.A. Apkarian, J. Chem. Phys. **105** (1996) 4023.

24. L. Eberson, *Electron Transfer Reactions in Organic Chemistry* (Springer, Berlin, 1987).

25. J.M. Savéant, Adv. Phys. Org. Chem. **26** (1990) 1.

26. R.A. Marcus, Angew. Chem. Int. Ed. Engl. **32** (1993) 1111.

27. M.A. Fox, (ed.) Chem. Rev. **92**, No.3 (1992).

28. A.H. Zewail, *Femtochemistry: Ultrafast Dynamics of the Chemical Bond* (World Scientific, Singapore, 1994), and references therein.

29. D. Zhong and A.H. Zewail, J. Phys. Chem. A **102**, 4031 (1998).

30. D. Zhong and A.H. Zewail, Proc. Natl. Acad. Sci. USA **96** (1999) 2602.

31. L.J. Andrews, Chem. Rev. **54** (1954) 713; McGlynn, Chem. Rev. **58** (1958) 1113.

32. L.A. Andrews and R.M. Keefer, *Molecular Complexes in Organic Chemistry* (Holden-Day, San Francisco, 1964).

33. J. Rose, *Molecular Complexes* (Pergamon Press, Oxford, 1967).

34. C.N.R. Rao, S.N. Bhat and P.C. Dwivedi, Appl. Spectrosc. Rev. **5** (1971) 1.

35. M. Tamres and J.M. Goodenow, J. Phys. Chem. **71** (1967) 1982; J. Chem. Phys. **43** (1965) 3393.

36. H.B. Friedrich and W.B. Person, J. Chem. Phys. **44** (1966) 2161.

37. N. Ogimachi, L.J. Andrews and R.M. Keefer, J. Am. Chem. Soc. **77** (1955) 4202.

38. I. Drepaul, V. Fagundez, F. Guiterrez, E.H. Lau and J.A. Joens, J. Org. Chem. **61** (1996) 3571.

39. S.N. Bhat and C.N.R. Rao, J. Am. Chem. Soc. **90** (1968) 6008.

40. M. Koll, J. Am. Chem. Soc. **90** (1968) 1097.

41. M. Tamres and S.N. Bhat, J. Am. Chem. Soc. **94** (1972) 2577.

42. A.F. Garito and B.B. Wayland, J. Phys. Chem. **71** (1967) 4062.

43. J.D. McCullough and I.C. Zimmermann, J. Phys. Chem. **65** (1961) 888.

44. S.N. Bhat and C.N.R. Rao, J. Am. Chem. Soc. **88** (1966) 3216.

45. P. Klaboe, J. Am. Chem. Soc. **89** (1967) 3667.

46. D. Wobschall and D.A. Norton, J. Am. Chem. Soc. **87** (1965) 3559.

47. E.C.M. Chen and W.E. Wentworth, J. Phys. Chem. **89** (1985) 4099; J.G. Dojahn, E.C.M. Chen and W.E. Wentworth, J. Phys. Chem. **100** (1996) 9649.

48. C.N.R. Rao, G.C. Chaturvedi and S.N. Bhat, J. Mol. Spectrosc. **33** (1970) 554.

49. L.J. Andrews and R.M. Keefer, J. Am. Chem. Soc. **74** (1952) 4500; **72** (1950) 5170.

50. M.M. Hubers, A.W. Kleyn and J. Los, Chem. Phys. **17** (1976) 303; D.J. Auerbach, M.M. Hubers, A.P.M. Baede and J. Los, *ibid.* **2** (1973) 107.

51. W.B. Person, J. Chem. Phys. **38** (1963) 109.

52. I.P. Gol'dshtein, E.N. Kharlamova and E.N. Gur'yanova, Zhurn. Obshch. Khim. **38** (1968) 1984.

53. Y.K. Syrkin and K.M. Anisimova, Dokl. Akad. Nauk. **59** (1948) 1457; A.H. Price and V.L. Brownsell, in: *Molecular Relaxation Processes, Chemical Society Special Publication No. 20* (Academic Press, Washington DC, 1966).

54. F. Fairbrother, J. Chem. Soc. (1948) 1051; S.N. Bhat and C.N.R. Rao, J. Am. Chem. Soc. **90** (1968) 6008.

55. S.S.C. Ammal, S.P. Ananthavel, J. Chandrasekhar, P. Venuvanalingam and M.S. Hegde, Chem. Phys. Lett. **248** (1996) 153.

56. O. Setokuchi and Y. Shimizu, J. Mol. Struct. (Theochem) **281** (1993) 67.

57. S.S.C. Ammal, S.P. Ananthavel, P. Venuvanalingam and M.S. Hegde, J. Phys. Chem. A **102** (1998) 532.

58. J.T. Su and A.H. Zewail, J. Phys. Chem. A **102** (1998) 4082.

59. O. Hassel, Acta Chem. Scand. **19** (1962) 2259.

60. S. Reiling, M. Besnard and P.A. Bopp, J. Phys. Chem. A **101** (1997) 4409.

61. O. Hassel, Proc. Chem. Soc. (1957) 250; O. Hassel and K.O. Stromme, Acta Chem. Scand. **12** (1958) 1146; O. Hassel, C. Romming and T. Tufte, *ibid.* **15** (1961) 967.

62. R.H. Lamoreaux and W.F. Giauque, J. Phys. Chem. **73** (1969) 755.

63. C. H. Hearn, E. Turcu and J.A. Joens, Atmospheric Environment **24A** (1990) 1939; S.D. Thompson, D.G. Carroll, F. Watson, M. O'Donnell and S.P. McGlynn, J. Chem. Phys. **45** (1966) 1367.

64. G.J. Hernandez and A.B.F. Duncan, J. Chem. Phys. **36** (1962) 1504; T.J. Cornish, T. Baer and L.G. Pedersen, J. Phys. Chem. **93** (1989) 6064; P.O. Moreno, Q.Y. Shang and E.R. Bernstein, J. Chem. Phys. **97** (1992) 2869.

65. J.G. Calvert and J.N. Pitts, *Photochemistry* (Wiley, New York, 1966); E.K.C. Lee and R.S. Lewis, Adv. Photochem. **12** (1980) 1; M. Baba, I. Hanazaki and U. Nagashima, J. Chem. Phys. **82** (11985) 3938.

66. M. Tamres, W.K. Duerksen and J.M. Goodenow, J. Phys. Chem. **72** (1968) 966; A.A. Passchier and N.W. Gregory, J. Phys. Chem. **72** (1968) 2697.

67. D.J. Seery and D. Britton, J. Phys. Chem. **68** (1964) 2263.

68. R.S. Mulliken, J. Chem. Phys. **55** (1971) 288.

69. R.D. Clear and K.R. Wilson, J. Mol. Spectrosc. **47** (1973) 39.

70. H. J. Hwang and M.A. El-Sayed, J. Phys. Chem. **95** (1991) 8044.

71. The dissociation of I_2 at 277 nm exclusively leads to form I and I^* with an anisotropy close to -1 by the χ-KETOF measurements of I-atoms. Besides that, a broad peak, ~30-40% of the total signal, near zero velocity with an isotropic distribution (β~0) was observed with a slow dissociation process and this is attributed to a dissociative autoionization from a long-lived Rydberg state reached by two-photon absorption.[72]

72. M.S. de Vries, N.J.A. van Veen, T. Baller and A.E. de Vries, Chem. Phys. **56** (1981) 157.

73. K. Tamagake, J.H. Kolts and D.W. Setser, J. Chem. Phys. **71** (1979) 1264.

74. R.J. Donovan, P. Greenhill, M.A. MaDonald, A.J. Yencha, W.S. Hartree, K. Johnson, C. Jouvet, A. Kvaran and J.P. Simon, J. Chem. Soc. Faraday Discuss. **84** (1987) 221.

75. The binding energy of DS·I is taken to be similar to that of DS·I_2, similar to the results in Ref. 58. The bonding in DS·I is not pure van der Waals in nature, probably including a mixture of ionic and covalent characters.

76. T.H. Dunning and P.J. Hay, J. Chem. Phys. **66** (1977) 1306; K. Hakuta, M. Fujino, K. Nakayama and H. Takuma, Jpn. J. Appl. Phys. **29** (1990) 1194; E. Quinones, Y.C. Yu, D.W. Setser and G. Lo, J. Chem. Phys. **93** (1990) 333.

77. C. Ni and G.W. Flynn, Chem. Phys. Lett. **210** (1993) 333; K. Tonokura, Y. Matsumi, M. Kawasaki, H.L. Kim, S. Yabushita, S. Fujimura and K. Saito, J. Chem. Phys. **99** (1993) 3461; L.J. Rogers, M.N.R. Ashfold, Y. Matsumi, M. Kawasaki, B.J. Whitaker, Chem. Phys. Lett. **258** (1996) 159.

78. K.W. Jung, T.S. Ahmadi and M.A. El-Sayed, J. Phys. Chem. A **101** (1997) 6563.

79. The dissociation of ICl at 277 nm leads to a dominant channel of I^* + Cl/Cl^* (≥90% branching ratio) with an anisotropy close to ~2 and a minor channel of $I+Cl/Cl^*$ (≤10%) with β~-1 by the χ-KETOF measurements of iodine-atoms. Similar to the I_2 case,[71] another additional broad peak, ~30-40% of the total intensity, near zero velocity with an isotropic distribution (β~0) was observed with a slow dissociation process probably due to a dissociative autoionization of a long-lived Rydberg state reached by two-photon absorption.

80. S.J. Garrett, D.V. Heyd and J.C. Polanyi, J. Chem. Phys. **106** (1997) 7847.

81. W. Ho, Surf. Sci. **299/300** (1994) 996.

82. L. Hellberg, J. Strömquist, B. Kasemo and B.I. Lundqvist, Phys. Rev. Lett. **74** (1995) 4742.

83. G. Porter and J.A. Smith, Proc. R. Soc. London, Ser.A **261** (1961) 28; R.L. Strong, J. Phys. Chem. **66** (1962) 2433.

84. G.N. Robison, R.E. Continetti and Y.T. Lee, J. Chem. Phys. **89** (1988) 6226.

85. A. Hörmann, W. Jarzeba and P.F. Barbara, J. Phys. Chem. **99** (1995) 2006; W. Jarzeba, K. Thakur, A. Hörmann and P.F. Barbara, *ibid*, **99** (1995) 2016.

86. D. Zhong, P.Y. Cheng and A.H. Zewail, J. Chem. Phys. **105** (1996) 7864.

5.8. Figure Captions and Figures

Figure 5.1. A schematic representation of the multi-dimensional adiabatic ionic potential energy surface (the elliptic paraboloid) for the supramolecular $D{\cdot}I_2$ complex with one cut on the PES along I^--I coordinate for the ionic exit channel. The other cut on the PES results from the crossing with one of the dissociative covalent potential surfaces (the repulsive curve), leading to a nonadiabatic transition to the covalent exit channel along I-I coordinate. At zero time, the initial wave packet is launched at the dative configuration (most ionic) by an fs electron jump from the ground-state structure, $R_2S{\cdots}I_2$ ($R=CH_3CH_2$) at a vdW distance. The four snapshots show the reaction at $t<0$, after the electron transfer in the dative-bonding TS region ($t=t^{\ddagger}$), and after reaching the final ($t=t_f$) products along either the neutral, dissociative covalent channel or the ionic path. The simplified three-dimensional PES and the corresponding contour maps are depicted in Figs. 5.20 and 5.21, respectively.

Figure 5.2. Typical UV absorption spectra of gas phase diethylsulfide, iodine and diethylsulfide/I_2 mixtures at a temperature of 373 K (adapted from Ref. 35). Note the large enhancement around 290 nm in the gas mixture. The excitation wavelength (277 nm) used in this work is shown by the arrow.

Figure 5.3. Schematic potential energy levels of Mulliken's resonance theory for a donor-acceptor complex. R_E and R_N are the resonance energies and E_C is the Coulomb

attraction energy. D···A stands for "no-bond" configuration and D^+-A^- for "dative-bond" configuration.

Figure 5.4. Molecular structures of 1:1 donor-acceptor complexes based on the recent results of *ab initio* calculations: (A) diethylsulfide·I_2,[55] $R_{S\text{-}I}$=3.3 Å, $\theta_{S\text{-}I\text{-}I}$=175^0 and $\theta_{C\text{-}S\text{-}I}$=97^0; (B) *p*-dioxane·$I_2$,[59] $R_{O\text{-}I}\approx$2.8 Å, $\theta_{O\text{-}I\text{-}I}\approx$180^0 and $\theta_{C\text{-}O\text{-}I}\approx$116^0; (C) actone·$I_2$,[56] $R_{O\text{-}I}$=2.8 Å, $\theta_{O\text{-}I\text{-}I}$=180^0 (fixed) and $\theta_{C\text{-}O\text{-}I}$=132^0. Two minimum structures were found for benzene·ICl and benzene·I_2, C-atom centered or C-C bond centered, and only carbon-centered structures are shown here: (D) benzene·ICl,[57] $R_{C\text{-}I}$=3.03 Å, $\theta_{C\text{-}I\text{-}Cl}$=177.5^0; (E) benzene·$I_2$,[58] $R_{C\text{-}I}$=3.15 Å, $\theta_{C\text{-}I\text{-}I}$=175^0. Note that the structures of D and E are nearly the same.

Figure 5.5. TOF mass spectra under the 1:1 donor-acceptor complex conditions. The delay time between fs laser pulses and the pulse valve opening and the sample temperature were carefully varied. Note that no larger cluster traces except the 1:1 binary complexes were found even though the fragmentation is server. The donor structures are also shown on the right side. DS stands for diethylsulfide, DO for *p*-dioxane, AO for acetone and Bz for benzene.

Figure 5.6. Angular-resolved KETOF distributions for the three different χ's, as indicated, at a fixed delay time of 7.0 ps. All three complexes show a parallel transition at 277-nm excitation. Note that for each case two velocity distributions are presented. The

open circles are the experimental data and the smoothed solid lines are shown only for guidance of the eyes.

Figure 5.7. Fs-resolved KETOF distributions at two different χ's ($\chi=0^0$ and 54.7^0) for diethylsulfide·I_2. Note the different temporal behavior for the two velocity distributions. The open circles are the experimental data and the smoothed solid lines are shown for guidance of the eyes.

Figure 5.8. Fs-resolved KETOF distributions at $\chi=54.7^0$ for (A) *p*-dioxane·I_2 and (B) acetone·I_2. Note that the different time evolution of the two velocity distributions. The open circles are the experimental data and the smoothed solid lines are shown only for guidance of the eyes.

Figure 5.9. The fs-resolved speed distributions of the I-atoms obtained from $\chi=54.7^0$ magic-angle data of Fig. 7 and 8 for (A) diethylsulfide·I_2, (B) *p*-dioxane·I_2 and (C) acetone·I_2. The two speed distributions are clearly revealed and the slow component shows a dramatic difference in the temporal behavior from the fast one. Note the shift of the slow component with time and the lack thereof in the fast component, as clearly shown in the case of (A). Also in (A), the slow speed distribution terminates at v=300 m/s.

Figure 5.10. The corresponding translational energy distributions of the I-atoms obtained from the speed distributions (Fig. 5.9) for (A) diethylsulfide·I_2, (B) *p*-dioxane·I_2

and (C) acetone·I_2. Note that the two distributions are well separated at $E_T \approx 3500$ cm^{-1} for (A) but the two are heavily overlapped for (C).

Figure 5.11. Fs-gating of different speed distributions. Total iodine atom transients (open circle) and the gated transients (solid circle) of the fast and slow components are shown for the different systems studied: (A) diethylsulfide·I_2, (B) *p*-dioxane·I_2 and (C) acetone·I_2. The branching ratios of the slow to the fast are 55:100, 65:100 and 88:100 for (A), (B) and (C), respectively. The solid lines are the theoretical results using a coherent delay and exponential rise describing the time evolution (see text). Note that the slow I-atom component of (A) has an 800 fs coherent delay and all other fs transients with 150 fs coherent shift.

Figure 5.12. The final (≥7 ps) I-atom speed distributions, anisotropy distributions and corresponding angles between the recoil direction (the bond orientation) and the initial transition dipole moment μ_{CT} for (A) diethylsulfide·I_2, (B) *p*-dioxane·I_2 and (C) acetone·I_2. Note the different anisotropy distributions for the naked exterior (fast) and caged interior (slow) I-atoms for each system. The initial angles of the naked exterior I-atoms and the angle changes of the caged interior I-atoms are marked by the dashed lines; see the text for detail.

Figure 5.13. Typical results of the nonlinear least square fit of the parallel polarization KETOF distributions for three systems. The open circles are the experimental data and the solid lines are the results of the theoretical simulation. The simulation procedure[29]

only uses the first half ($v_z \leq 0$) of the KETOF distribution; because of symmetry, the second half ($v_z \geq 0$) of the data here is the replica of the first half.

Figure 5.14. The 1:1 donor-acceptor complex structures based on the derived angles between μ_{CT} and the initial recoil direction v_I, and recent *ab initio* predicted interaction schemes of the donor and the acceptor for (A) diethylsulfide·I_2 (R=CH_3CH_2), $\theta_{S\text{-}I\text{-}I}=165^0$, (B) *p*-dioxane·$I_2$ (R=CH_2), $\theta_{O\text{-}I\text{-}I}=172.5^0$ and (C) acetone·I_2 (R=CH_3), $\theta_{O\text{-}I\text{-}I}=165^0$. Both directions of μ_{CT} and the initial v_I are shown by arrows.

Figure 5.15. The angular-resolved KETOF distributions of I-atoms for the three different χ's at a fixed delay time of 7.0 ps for benzene·ICl (A). The results from the benzene·I_2 complex (B) are also shown for comparison.[14] Note that the three velocity distributions of (A) are very similar, narrower and sharper.

Figure 5.16. Total iodine atom transients (open circle) and the gated transients (solid circle) of the fast and slow components. Note that only one temporal evolution of I-atoms was observed for benzene·ICl (A). All transients have a ~150 fs coherent shift from the time zero. The branching ratio of the slow to the fast is 100:100 for benzene·I_2 (B). The solid lines are the theoretical results using a coherent delay (~150 fs) and an exponential rise describing the time evolution (see text).

Figure 5.17. The speed distributions derived from the magic-angle ($\chi=54.7^0$) data shown in Fig.5.15, together with the corresponding translational energy distributions for

(A) benzene·ICl and (B) benzene·I_2. Note the dramatic difference in the high translational energy distributions of both cases.

Figure 5.18. The final (≥7 ps) I-atom speed distributions, anisotropy distributions and corresponding angles between the recoil direction (the bond orientation) and the initial transition dipole moment μ_{CT}. (A) benzene·ICl: Only caged interior I-atoms were detected because the I-atom faces the benzene ring in the complex structure. The anisotropy monotonically decreases from 0.5 to 0. (B) benzene·I_2: The anisotropy for all I-atoms shows a monotonic decreasing from the initial 1.0 to the final 0. The initial angle is about 35^0 and the angle changes of the caged interior I-atoms are marked by the dashed lines. Note the similarity of the anisotropy distributions of the caged I-atoms for both cases, reflecting the similar complex structures and caging dynamics.

Figure 5.19. Typical results of the nonlinear least square fit of the parallel polarization KETOF distributions for (A) benzene·ICl and (B) benzene·I_2. The open circles are the experimental data and the solid lines are the results of the theoretical simulation. The simulation procedure[29] only uses the first half ($v_z \leq 0$) of the KETOF distribution; because of symmetry, the second half ($v_z \geq 0$) of the data here is the replica of the first half. Note the dramatic difference in the shapes of the two complexes.

Figure 5.20. The simplified three-dimensional PESs of the supramolecular complex, constructed on the two reactive coordinates, D···I and I···I, for the neutral ground state, the first CT state and one of the excited dissociative covalent states (I_2^* is in the C state).

The CT PES is drawn for a fraction ET of 89%, which determines the equilibrium position of the well; see the text. The seam, the crossing of the ionic and covalent PESs, is shown by the thick solid line. Two trajectories, the result of the bifurcation from the first crossing, represent two typical dissociation routes by RET in the dative-bonding TS: One is from the crossing at the smaller r(I-I) and the other results from the electron hopping at the larger r(I-I).

Figure 5.21. (A) The energy contour map of the ionic PES of Fig.5.20. The crossing seam (thick solid line) of the ionic and covalent PESs is also shown. A typical ionic trajectory (dashed line) takes more than 1 ps to reach a distance of 8 Å for r(I-I˙). The reactive trajectory (gray solid line) finally evolves along the covalent potential with the multiple crossings in the dative-bonding TS region and this route is the dominant pathway of the CT reactions. Also shown are the three snapshots of the structure, assuming a linear configuration, at t=0 (initial wave packet, solid oval), at the seam and in the final ionic product channel if possible. (B) The energy contour map of the covalent PES of Fig. 5.20 with the crossing seam (thick solid line) and a reactive trajectory (dashed line) in the dative-bonding TS. The potential energy curves (ionic and covalent) cut along the reaction pathway at five typical crossing points, one (a) with the smaller r(I-I) and the other four (b-e) with the larger r(I-I), are shown on the right side. (C) The energy contour map of the covalent PES of Fig. 5.20 with the crossing seam (thick solid line) and the subsequent moving directions after RET at the five crossings. The corresponding relative motions of D-I and I-I are shown in the five panels on the right.

Figure 5.22. The final (≥7 ps) speed distributions of the three complexes: (A) diethylsulfide·I_2, (B) p-dioxane·I_2 and (C) acetone·I_2. The maximum speeds from the two extreme conditions (see the text) for the exterior and interior I-atoms are shown. Also marked are the average speeds for the both I-atoms of the three complexes and the cut-off speed of the interior I-atom from diethylsulfide·I_2.

Figure 5.23. The correlation of the dynamics and the structural evolution illustrated by the measurement of the exterior I-atom recoil speed and its direction relative to the initial fs alignment, $\mathbf{u}_{CT}$. (A) RET occurs at the smaller r(I-I) and all available energy is deposited in the I-I bond (potential energy), resulting in the largest speed (v_I) with the smallest tilted angle. (B) and (C) RET occurs at the larger r(I-I) with most available energy transformed into the translational energy in both D-I and I-I bonds. In case (B), more translation energy in the I-I bond results in the larger speed with the smaller tilted angle whereas in case (C) more translational energy in the D-I bond results in the smaller speed with the larger tilted angle. Note that the interior I-atom is more scattered away from $\mathbf{u}_{CT}$ than the exterior I-atom by the collision with the donor (D).

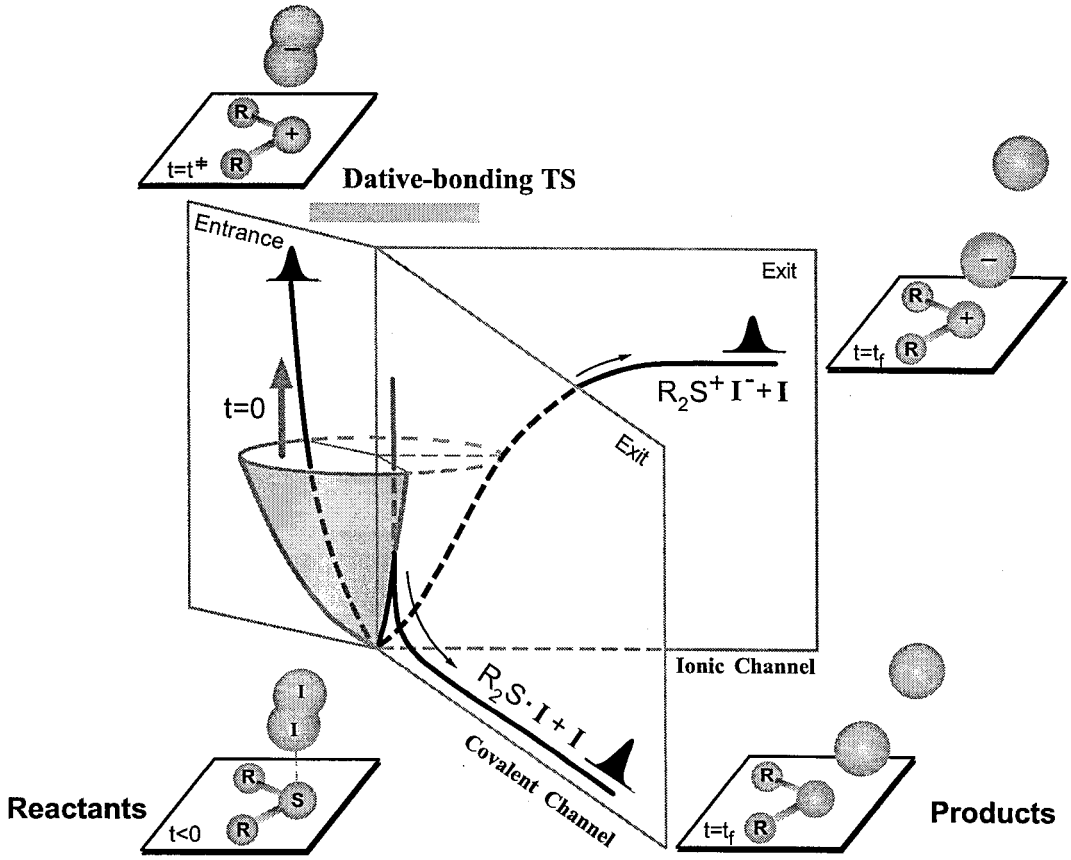
Dative-bonding TS
Entrance
Exit
t=0
$R_2S^+I^-+I$
Exit
Ionic Channel
$R_2S\cdot I+I$
Covalent Channel
Reactants
Products
t<0
$t=t_f$
$t=t_f$
$t=t^{\neq}$

Figure 5.1

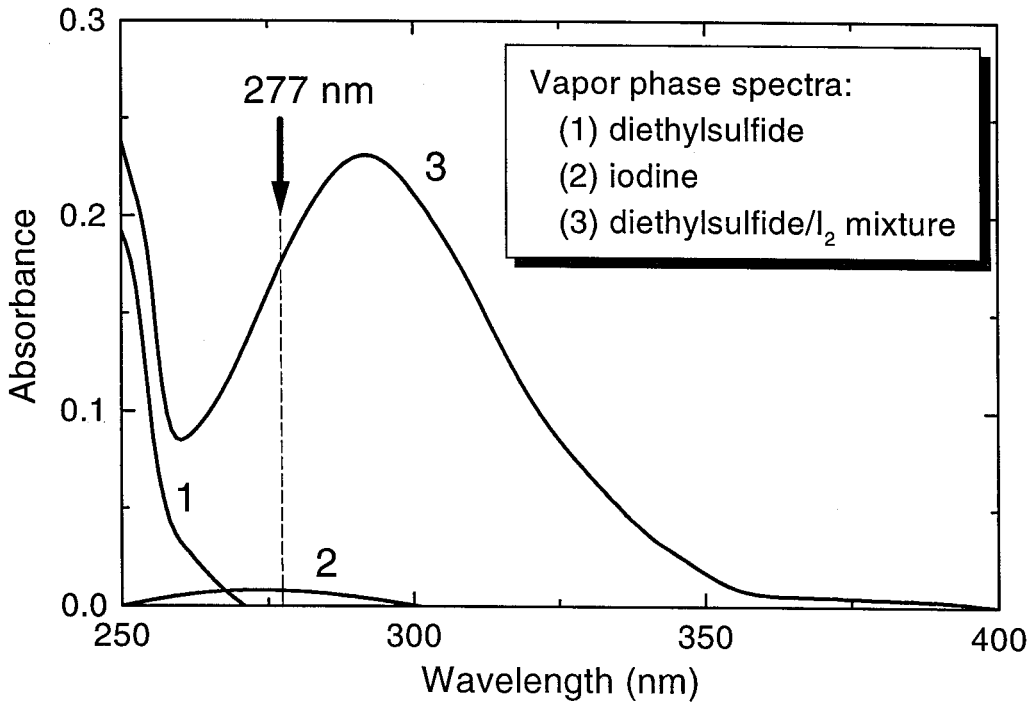
0.3
0.2
0.1
0.0
Absorbance
277 nm
3
1
2
Vapor phase spectra:
(1) diethylsulfide
(2) iodine
(3) diethylsulfide/I_2 mixture
250
300
350
400
Wavelength (nm)

Figure 5.2

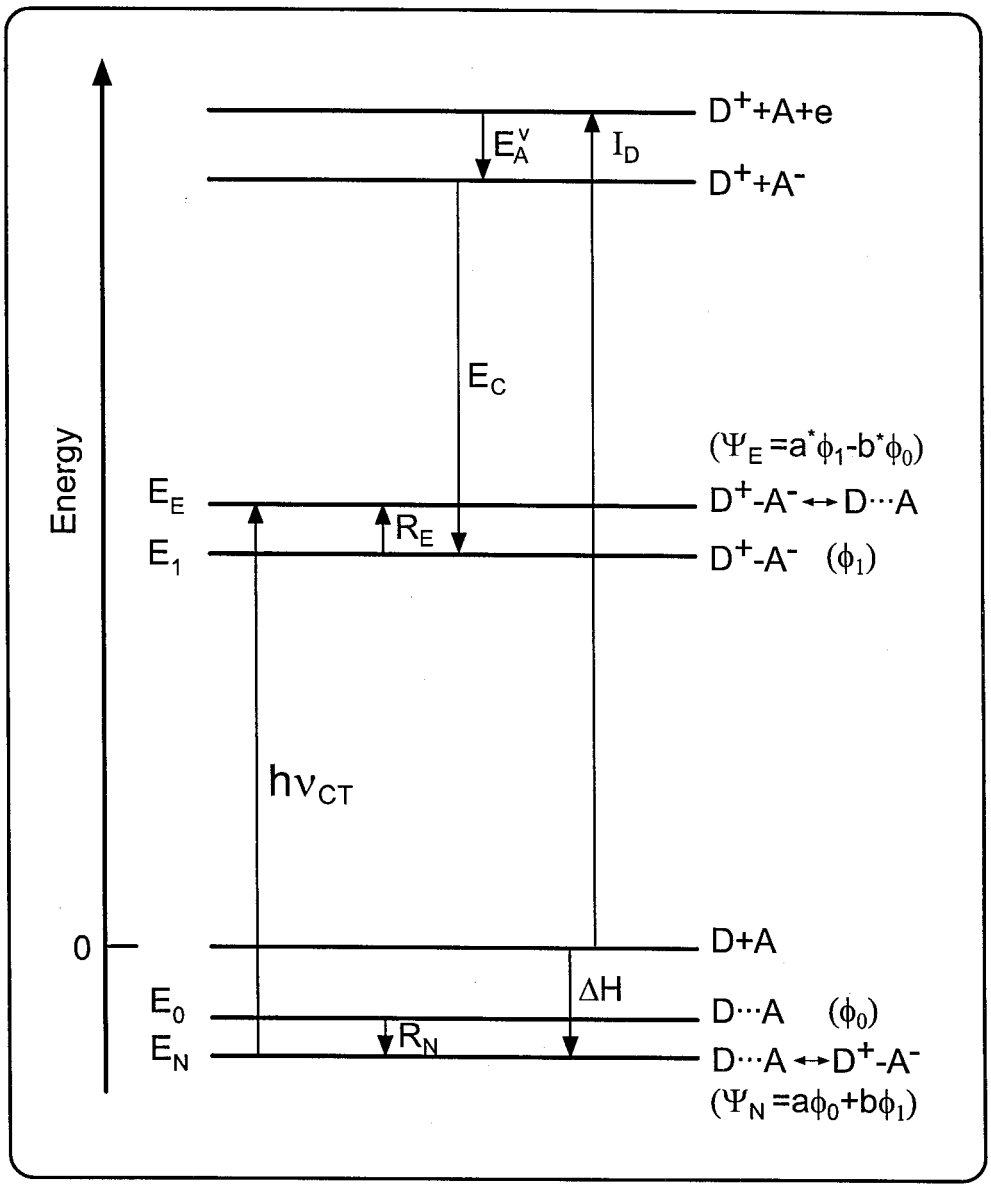
Energy
$D^+ + A + e$
E_A^v
I_D
$D^+ + A^-$
E_C
$(\Psi_E = a^*\phi_1 - b^*\phi_0)$
E_E
$D^+ - A^- \leftrightarrow D \cdots A$
R_E
E_1
$D^+ - A^-$ (ϕ_1)
$h\nu_{CT}$
0
D+A
ΔH
E_0
$D \cdots A$ (ϕ_0)
R_N
E_N
$D \cdots A \leftrightarrow D^+ - A^-$
$(\Psi_N = a\phi_0 + b\phi_1)$

Figure 5.3

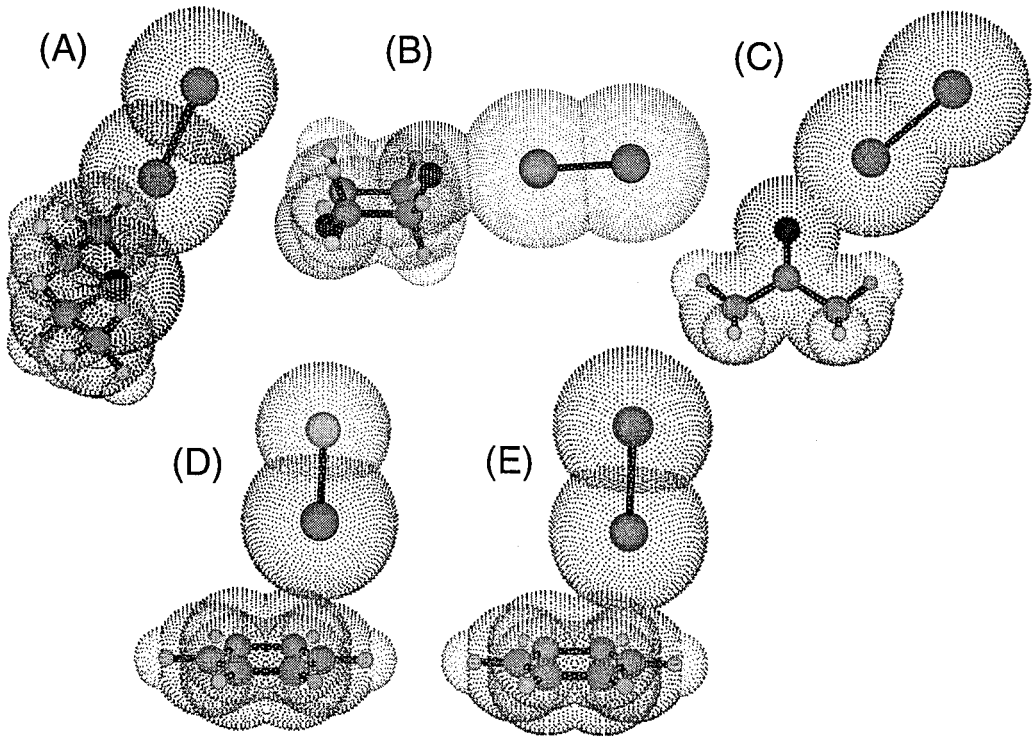

Figure 5.4

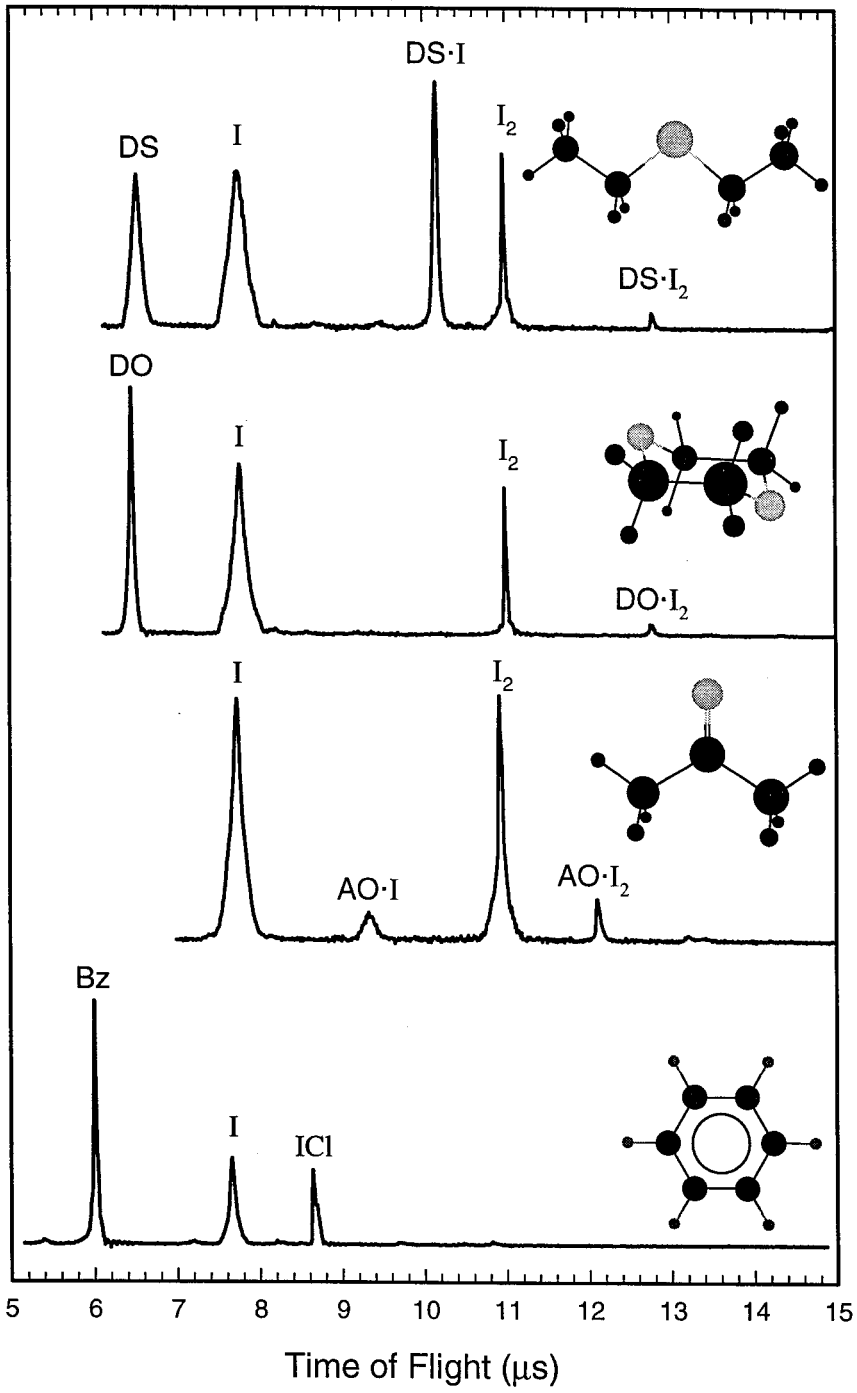
DS·I
DS
I
I2
DS·I2
DO
I
I2
DO·I2
I
I2
AO·I
AO·I2
Bz
I
ICl
5
6
7
8
9
10
11
12
13
14
15
Time of Flight (μs)

Figure 5.5

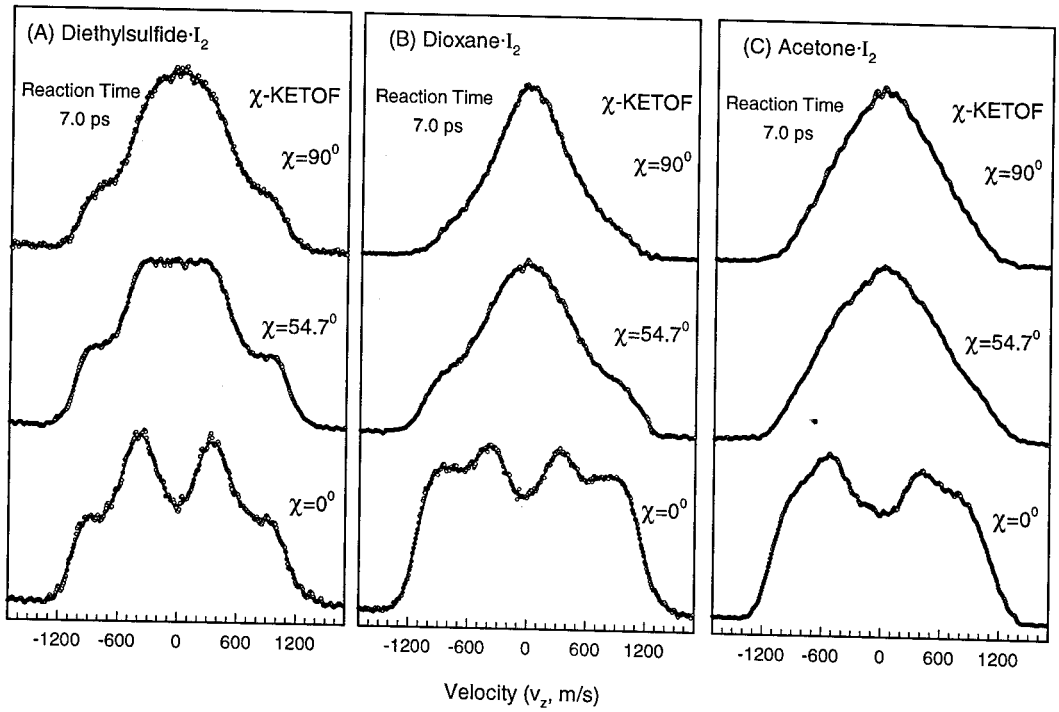
(A) Diethylsulfide·I_2
Reaction Time
7.0 ps
χ-KETOF
χ=90°
χ=54.7°
χ=0°
-1200 -600 0 600 1200
(B) Dioxane·I_2
Reaction Time
7.0 ps
χ-KETOF
χ=90°
χ=54.7°
χ=0°
-1200 -600 0 600 1200
(C) Acetone·I_2
Reaction Time
7.0 ps
χ-KETOF
χ=90°
χ=54.7°
χ=0°
-1200 -600 0 600 1200
Velocity (v_z, m/s)

Figure 5.6

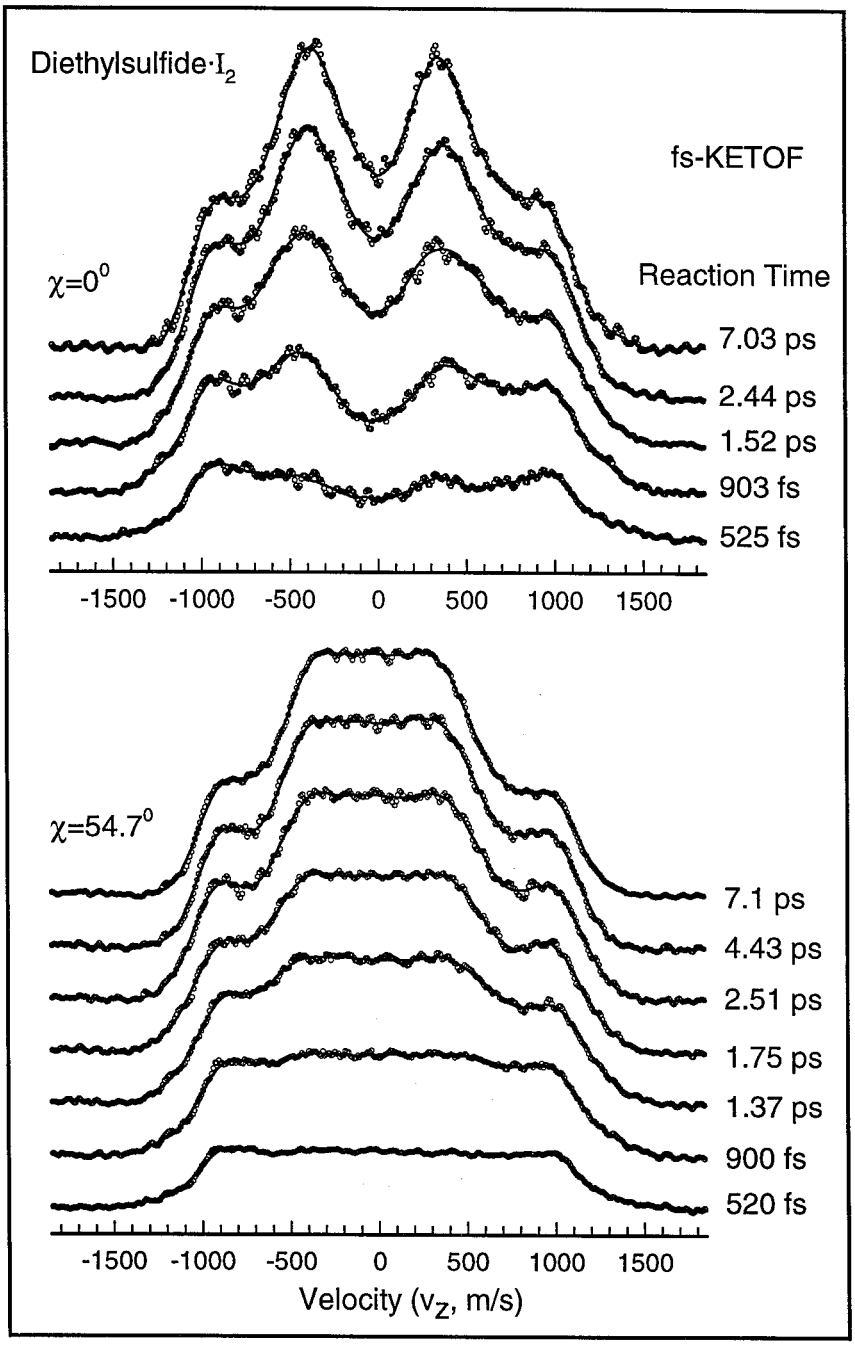
Diethylsulfide·I2
fs-KETOF
χ=0°
Reaction Time
7.03 ps
2.44 ps
1.52 ps
903 fs
525 fs
-1500 -1000 -500 0 500 1000 1500
χ=54.7°
7.1 ps
4.43 ps
2.51 ps
1.75 ps
1.37 ps
900 fs
520 fs
-1500 -1000 -500 0 500 1000 1500
Velocity (vZ, m/s)

Figure 5.7

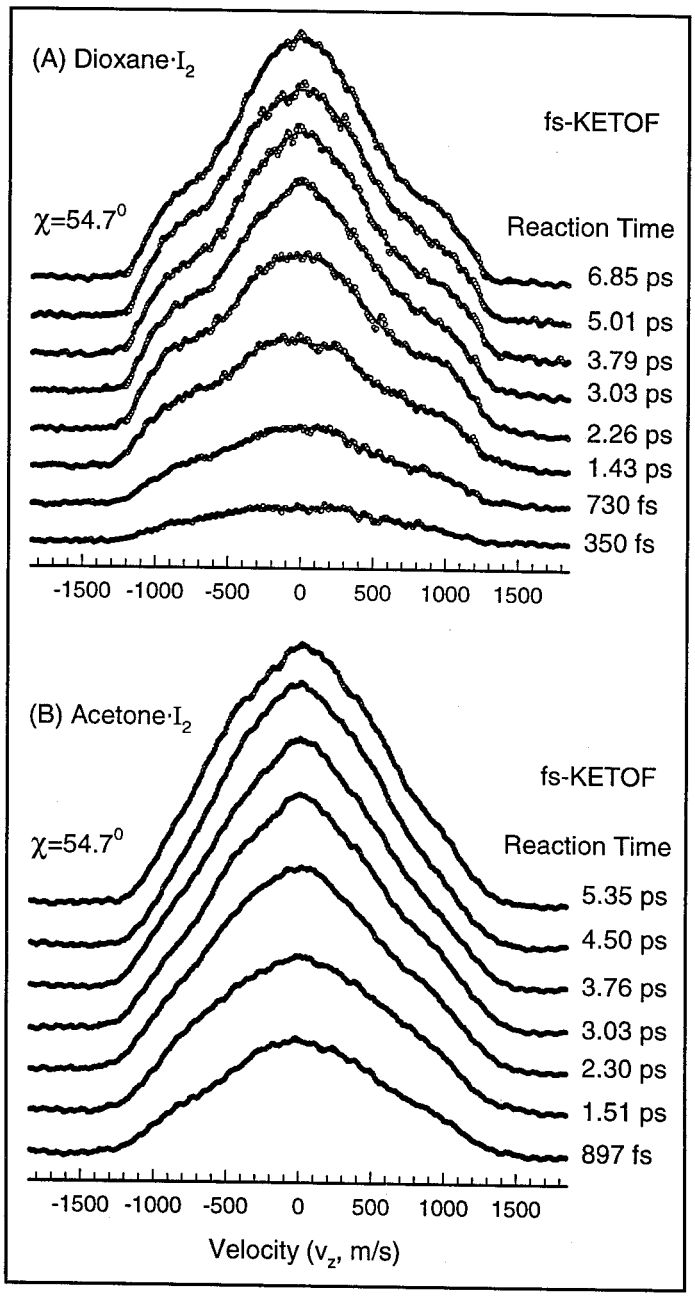
(A) Dioxane·I_2
fs-KETOF
χ=54.7^0
Reaction Time
6.85 ps
5.01 ps
3.79 ps
3.03 ps
2.26 ps
1.43 ps
730 fs
350 fs
-1500 -1000 -500 0 500 1000 1500
(B) Acetone·I_2
fs-KETOF
χ=54.7^0
Reaction Time
5.35 ps
4.50 ps
3.76 ps
3.03 ps
2.30 ps
1.51 ps
897 fs
-1500 -1000 -500 0 500 1000 1500
Velocity (v_z, m/s)

Figure 5.8

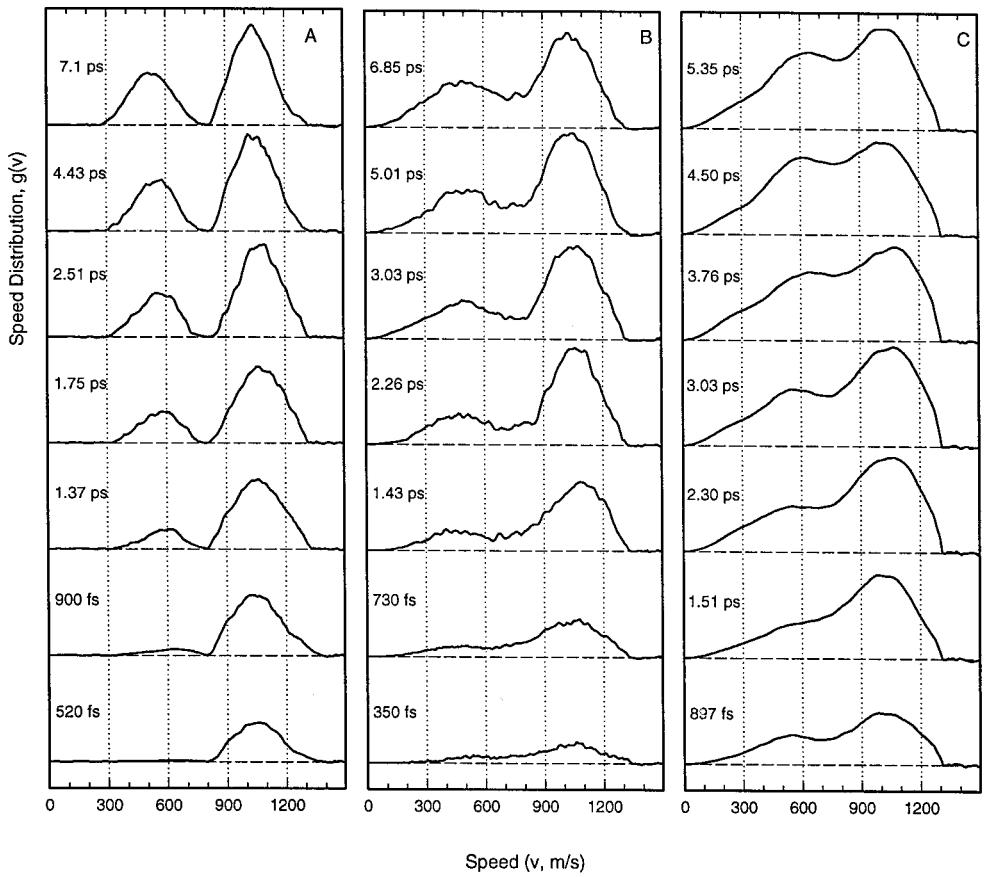
A
B
C
7.1 ps
4.43 ps
2.51 ps
1.75 ps
1.37 ps
900 fs
520 fs
6.85 ps
5.01 ps
3.03 ps
2.26 ps
1.43 ps
730 fs
350 fs
5.35 ps
4.50 ps
3.76 ps
3.03 ps
2.30 ps
1.51 ps
897 fs
0
300
600
900
1200
Speed Distribution, g(v)
Speed (v, m/s)

Figure 5.9

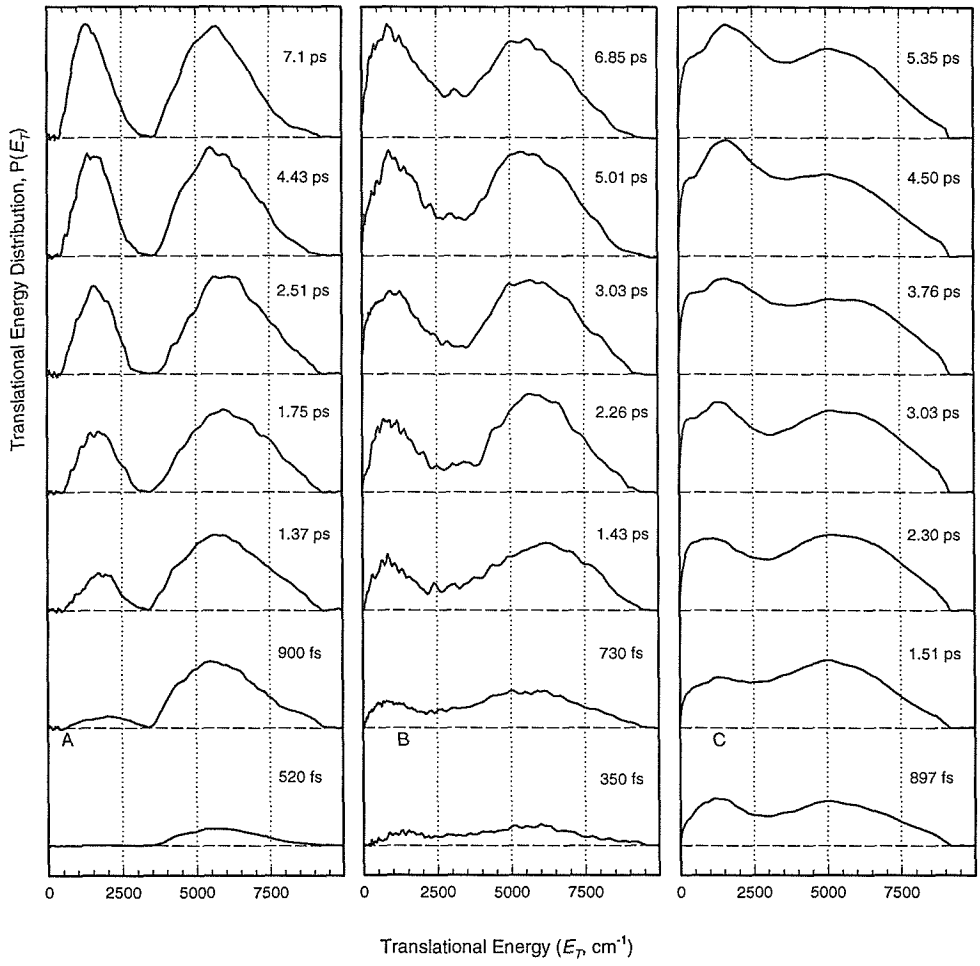
Translational Energy Distribution, P(E_T)
7.1 ps
4.43 ps
2.51 ps
1.75 ps
1.37 ps
900 fs
520 fs
A
6.85 ps
5.01 ps
3.03 ps
2.26 ps
1.43 ps
730 fs
350 fs
B
5.35 ps
4.50 ps
3.76 ps
3.03 ps
2.30 ps
1.51 ps
897 fs
C
0
2500
5000
7500
Translational Energy (E_T, cm^{-1})

Figure 5.10

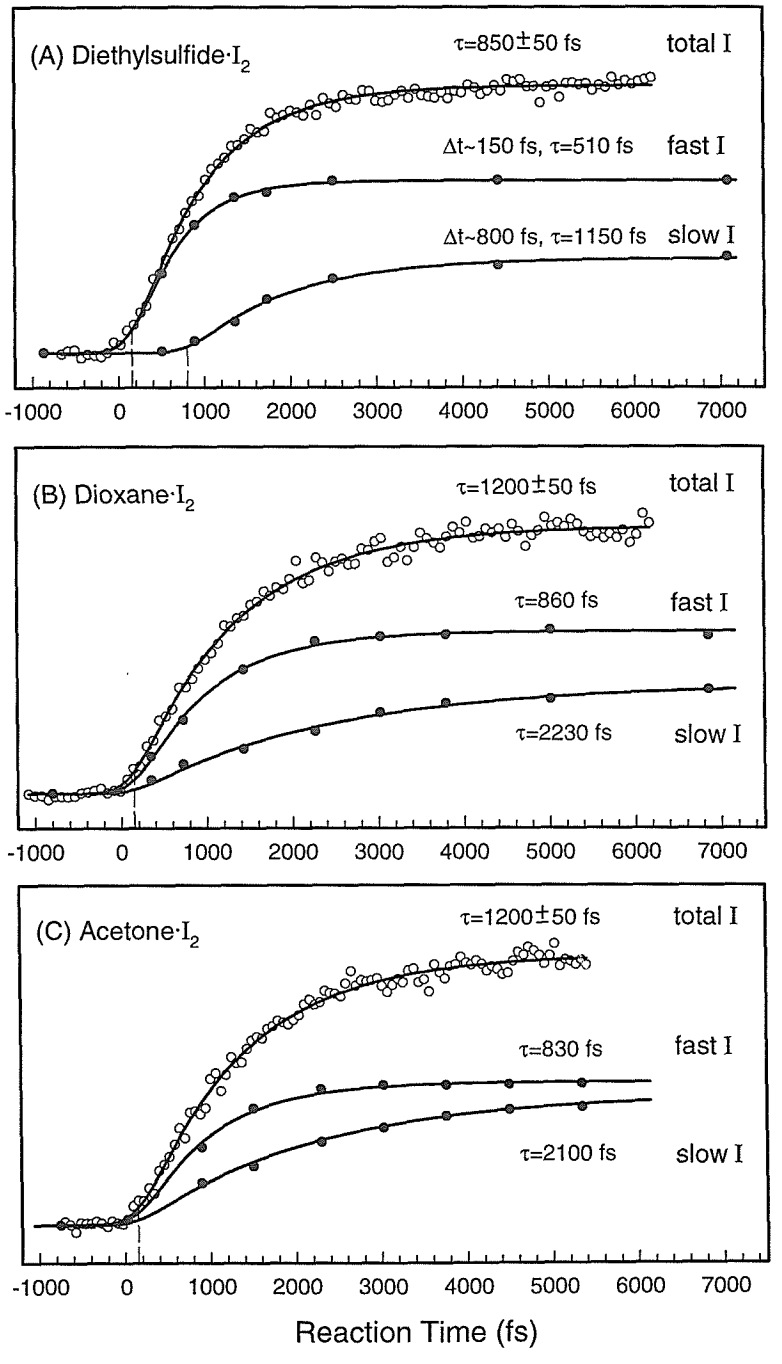
(A) Diethylsulfide·I_2
τ=850±50 fs
total I
Δt~150 fs, τ=510 fs
fast I
Δt~800 fs, τ=1150 fs
slow I
-1000 0 1000 2000 3000 4000 5000 6000 7000
(B) Dioxane·I_2
τ=1200±50 fs
total I
τ=860 fs
fast I
τ=2230 fs
slow I
-1000 0 1000 2000 3000 4000 5000 6000 7000
(C) Acetone·I_2
τ=1200±50 fs
total I
τ=830 fs
fast I
τ=2100 fs
slow I
-1000 0 1000 2000 3000 4000 5000 6000 7000
Reaction Time (fs)

Figure 5.11

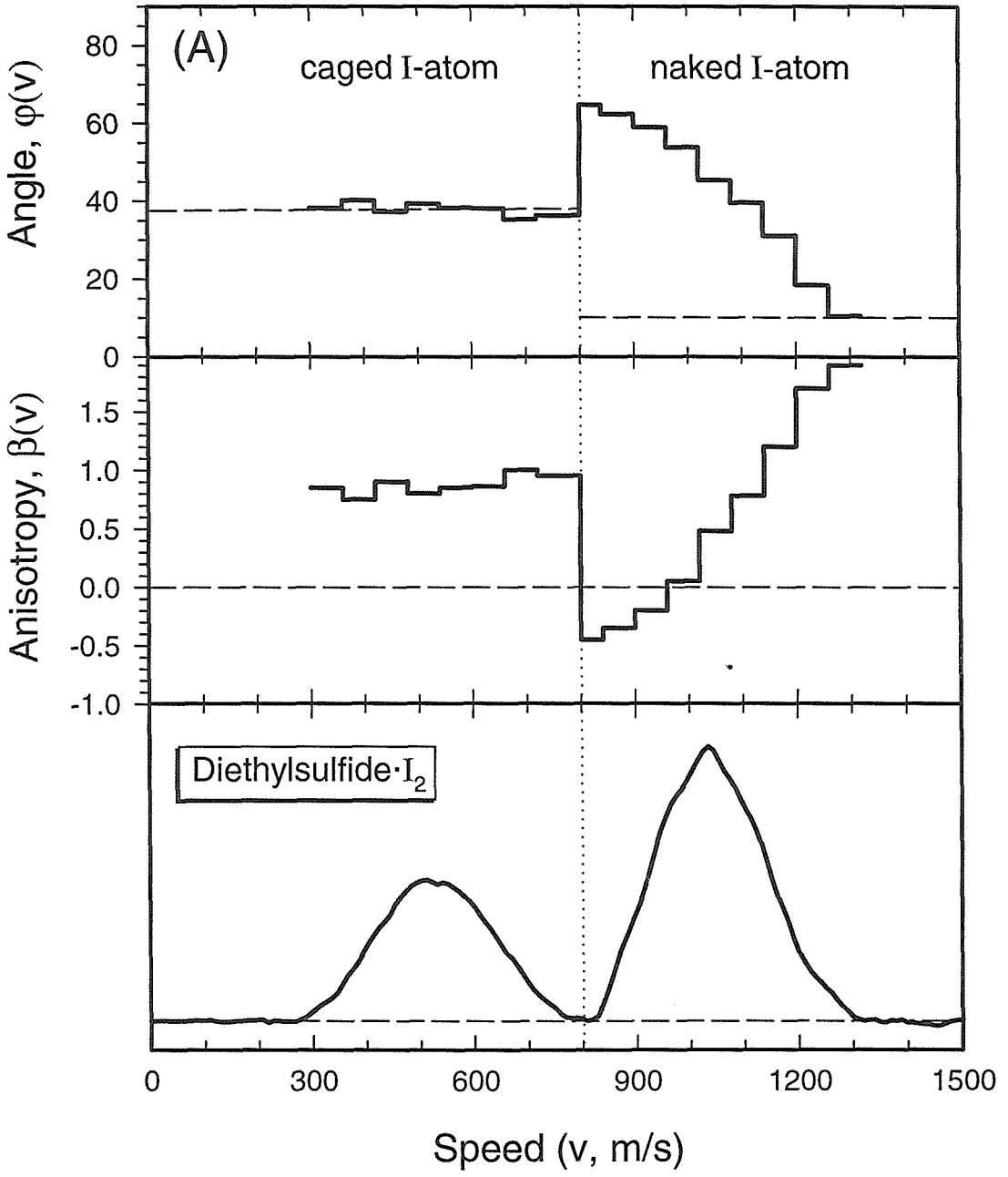
(A)
caged I-atom
naked I-atom
Angle, φ(v)
80
60
40
20
0
Anisotropy, β(v)
1.5
1.0
0.5
0.0
-0.5
-1.0
Diethylsulfide·I2
0
300
600
900
1200
1500
Speed (v, m/s)

Figure 5.12A

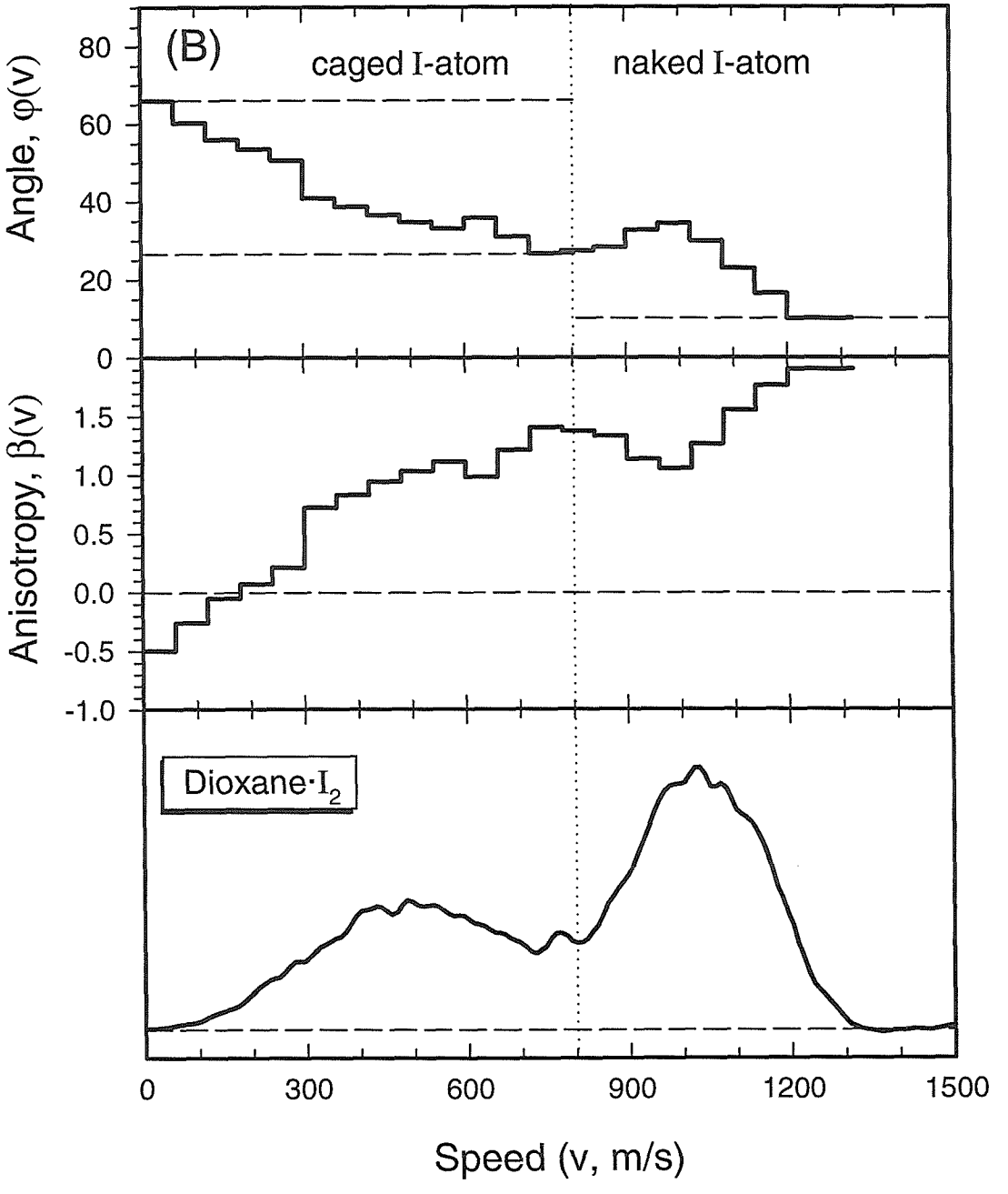
(B)
caged I-atom
naked I-atom
Angle, φ(v)
80
60
40
20
0
Anisotropy, β(v)
1.5
1.0
0.5
0.0
-0.5
-1.0
Dioxane·I2
0
300
600
900
1200
1500
Speed (v, m/s)

Figure 5.12B

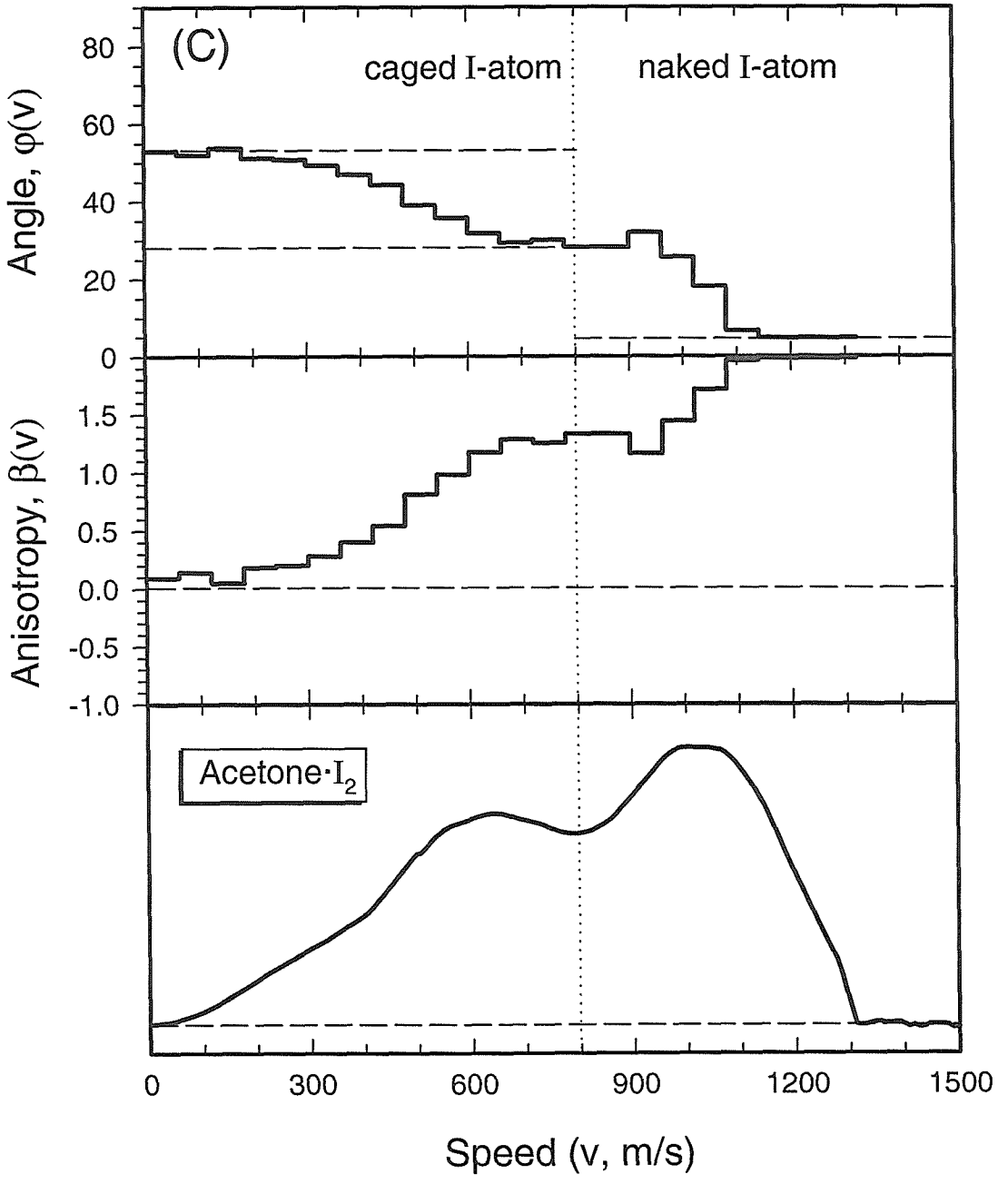
(C)
caged I-atom
naked I-atom
Angle, φ(v)
80
60
40
20
0
Anisotropy, β(v)
1.5
1.0
0.5
0.0
-0.5
-1.0
Acetone·I2
0
300
600
900
1200
1500
Speed (v, m/s)

Figure 5.12C

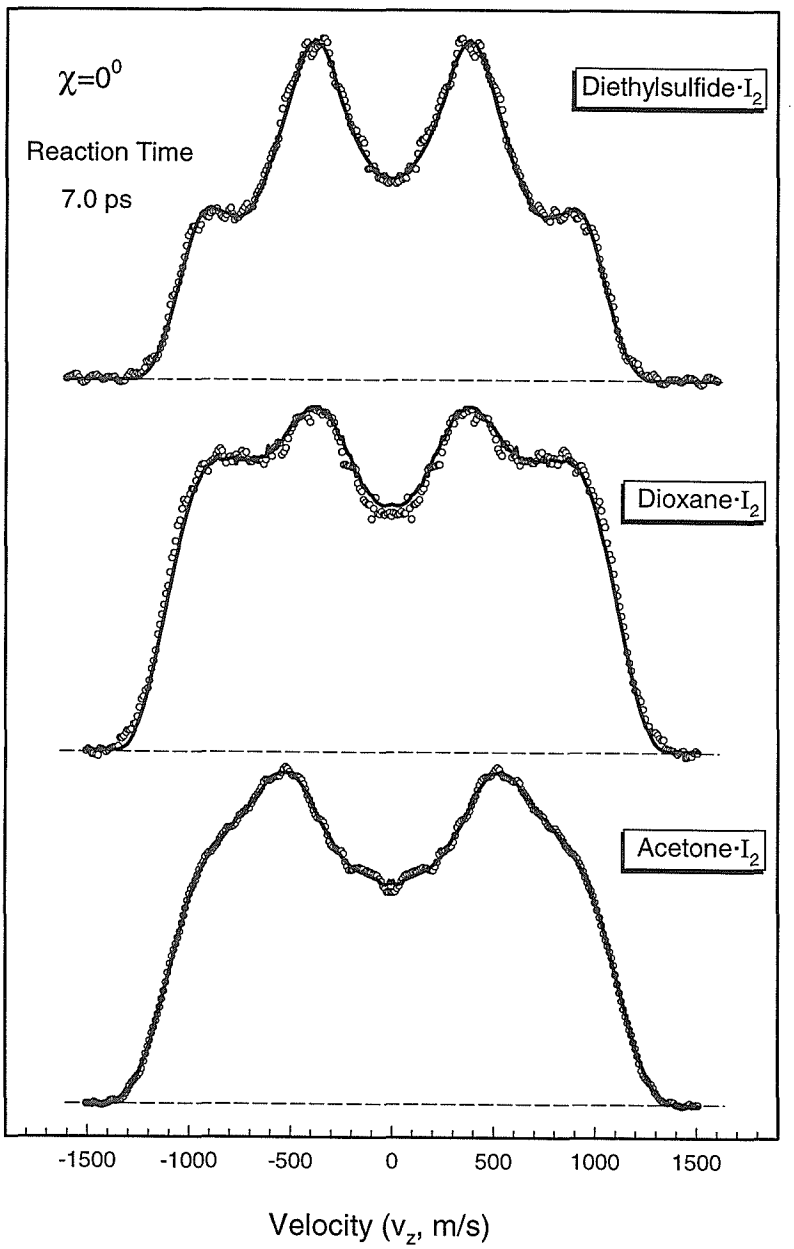
χ=0⁰
Reaction Time
7.0 ps
Diethylsulfide·I2
Dioxane·I2
Acetone·I2
-1500
-1000
-500
0
500
1000
1500
Velocity (vz, m/s)

Figure 5.13

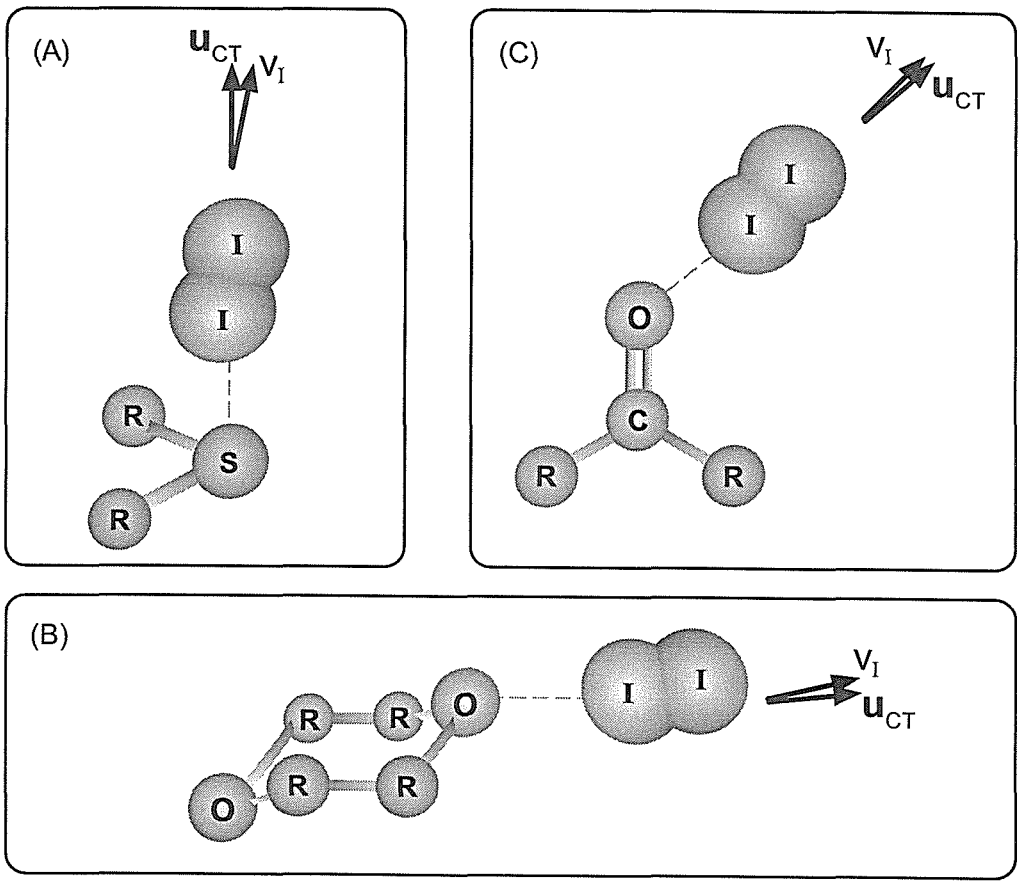

Figure 5.14

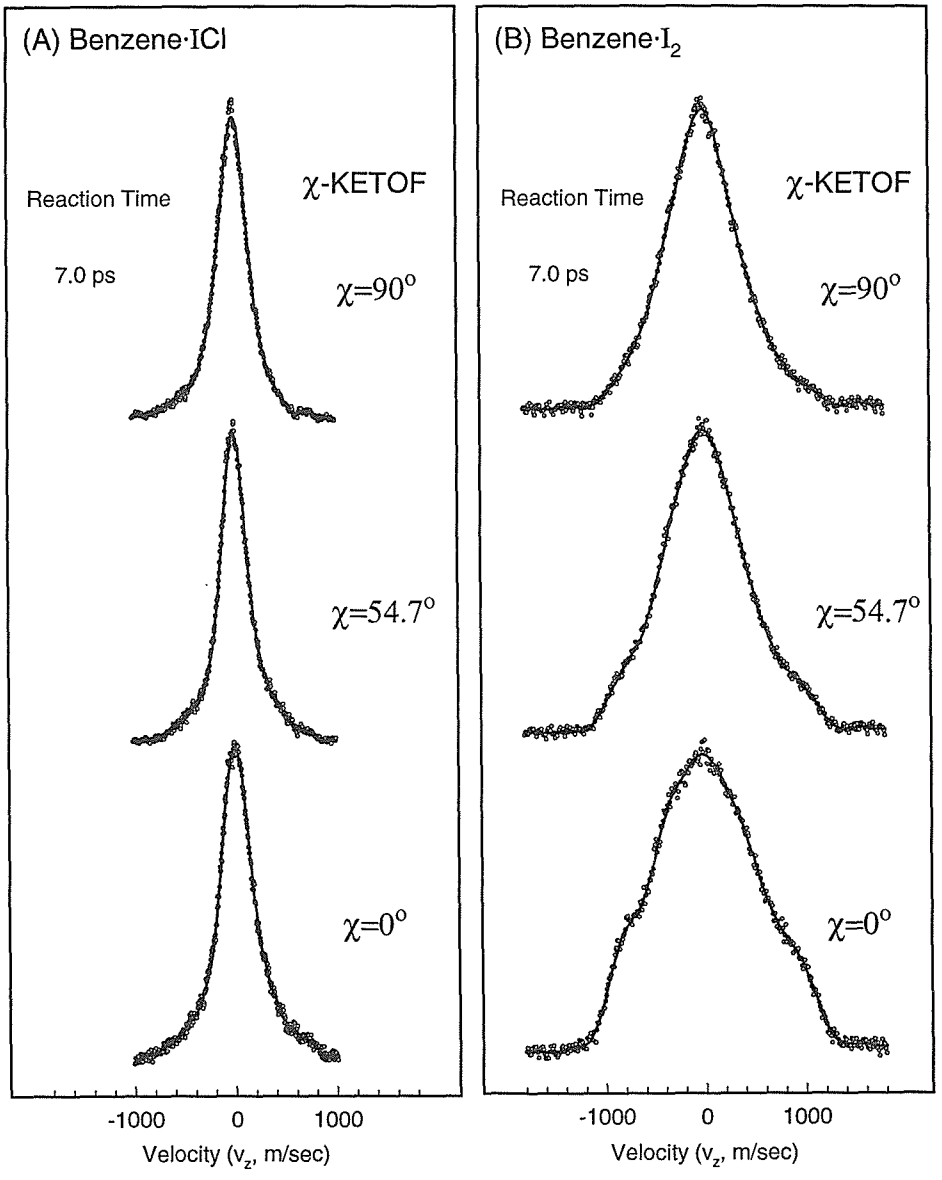
(A) Benzene·ICl
Reaction Time
7.0 ps
χ-KETOF
χ=90°
χ=54.7°
χ=0°
-1000
0
1000
Velocity (v_z, m/sec)
(B) Benzene·I_2
Reaction Time
7.0 ps
χ-KETOF
χ=90°
χ=54.7°
χ=0°
-1000
0
1000
Velocity (v_z, m/sec)

Figure 5.15

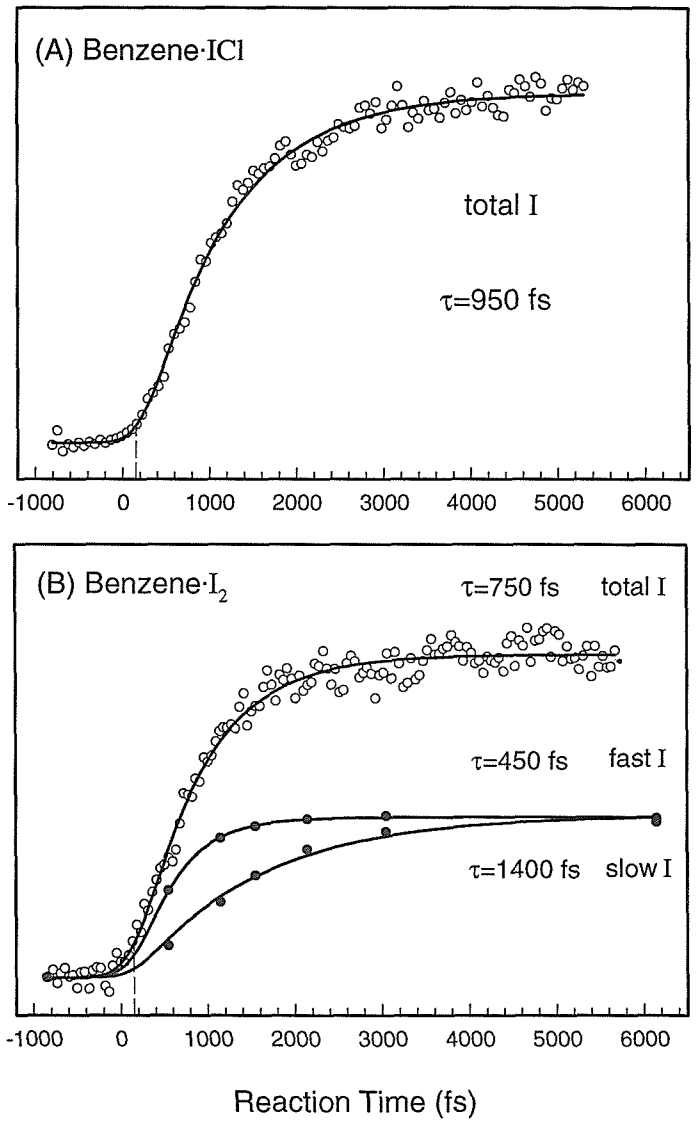
(A) Benzene·ICl
total I
τ=950 fs
-1000
0
1000
2000
3000
4000
5000
6000
(B) Benzene·I2
τ=750 fs
total I
τ=450 fs
fast I
τ=1400 fs
slow I
-1000
0
1000
2000
3000
4000
5000
6000
Reaction Time (fs)

Figure 5.16

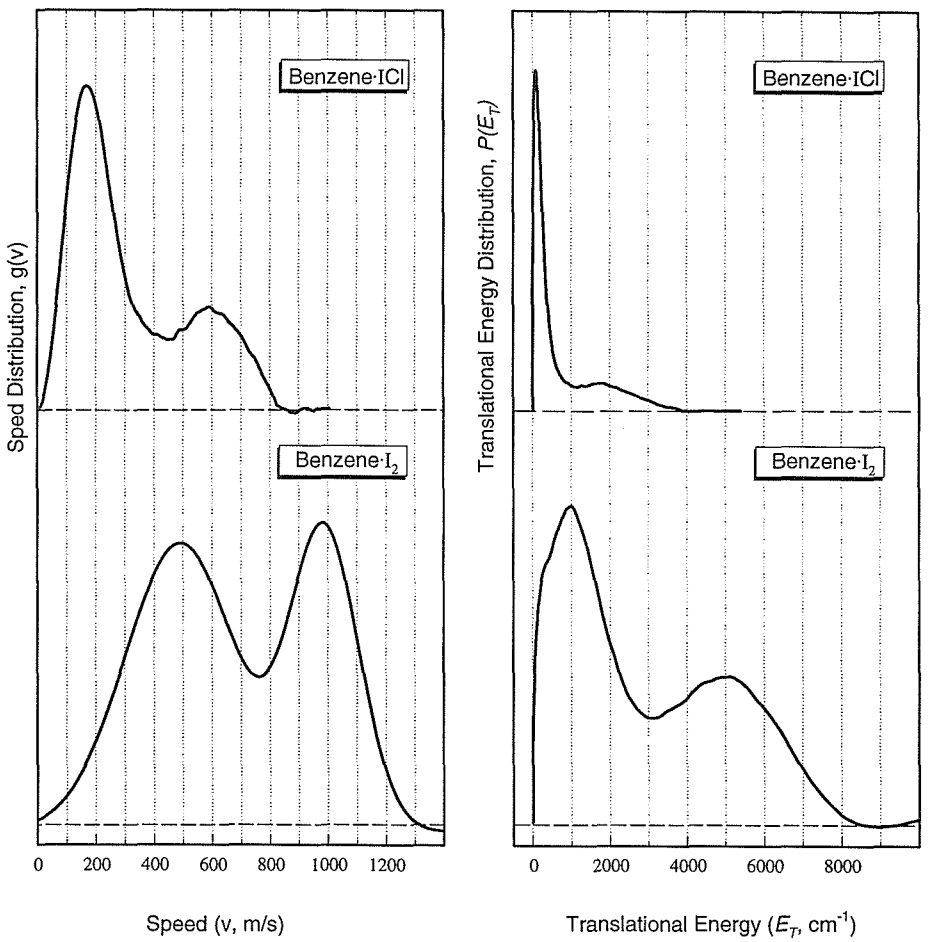
Benzene·ICl
Benzene·I2
Sped Distribution, g(v)
0 200 400 600 800 1000 1200
Speed (v, m/s)
Translational Energy Distribution, P(ET)
Benzene·ICl
Benzene·I2
0 2000 4000 6000 8000
Translational Energy (ET, cm-1)

Figure 5.17

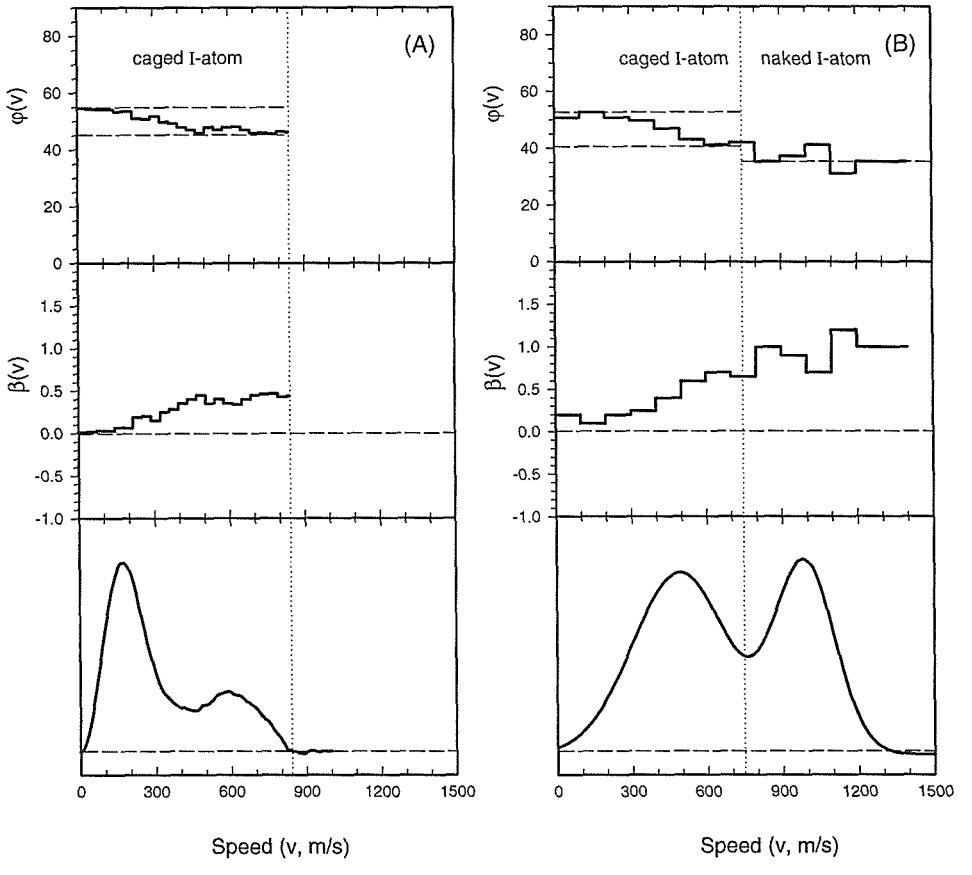
caged I-atom
(A)
caged I-atom
naked I-atom
(B)
φ(v)
β(v)
80
60
40
20
0
1.5
1.0
0.5
0.0
-0.5
-1.0
0
300
600
900
1200
1500
Speed (v, m/s)
Speed (v, m/s)

Figure 5.18

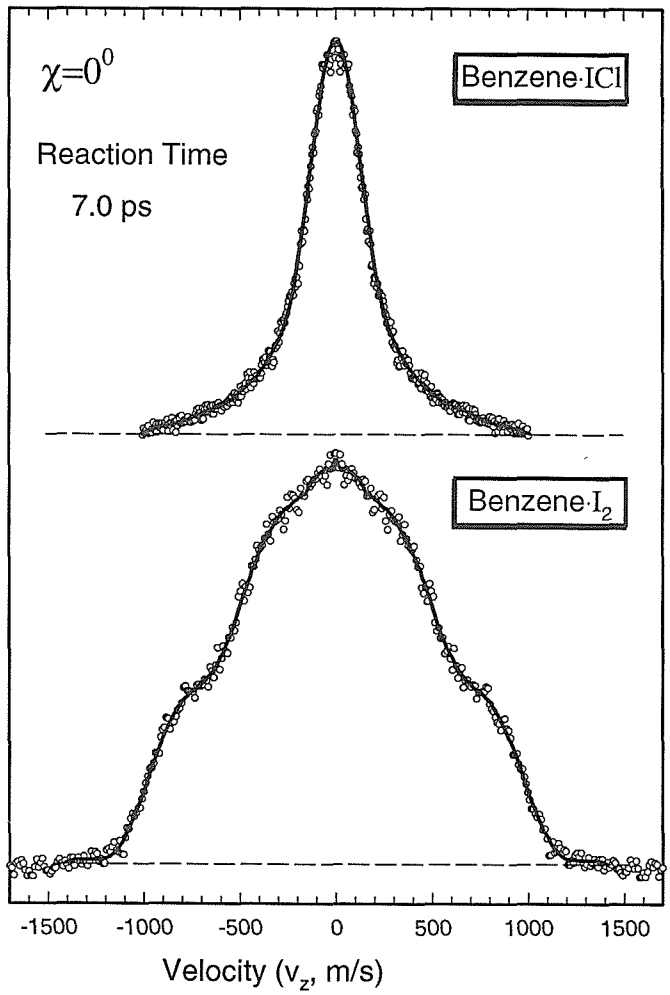
χ=0⁰
Reaction Time
7.0 ps
Benzene·ICl
Benzene·I2
-1500
-1000
-500
0
500
1000
1500
Velocity (vz, m/s)

Figure 5.19

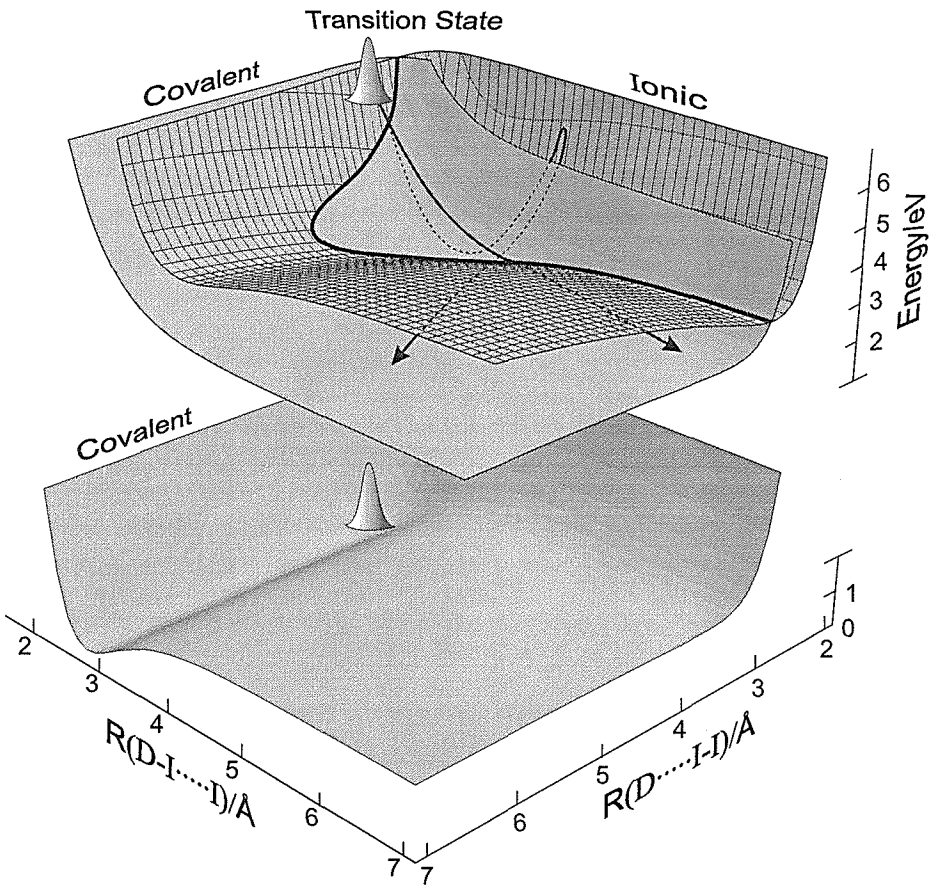
Transition State
Covalent
Ionic
Covalent
Energy/eV
6
5
4
3
2
1
0
2
3
4
5
6
7
R(D-I.....I)/Å
R(D.....I-I)/Å

Figure 5.20

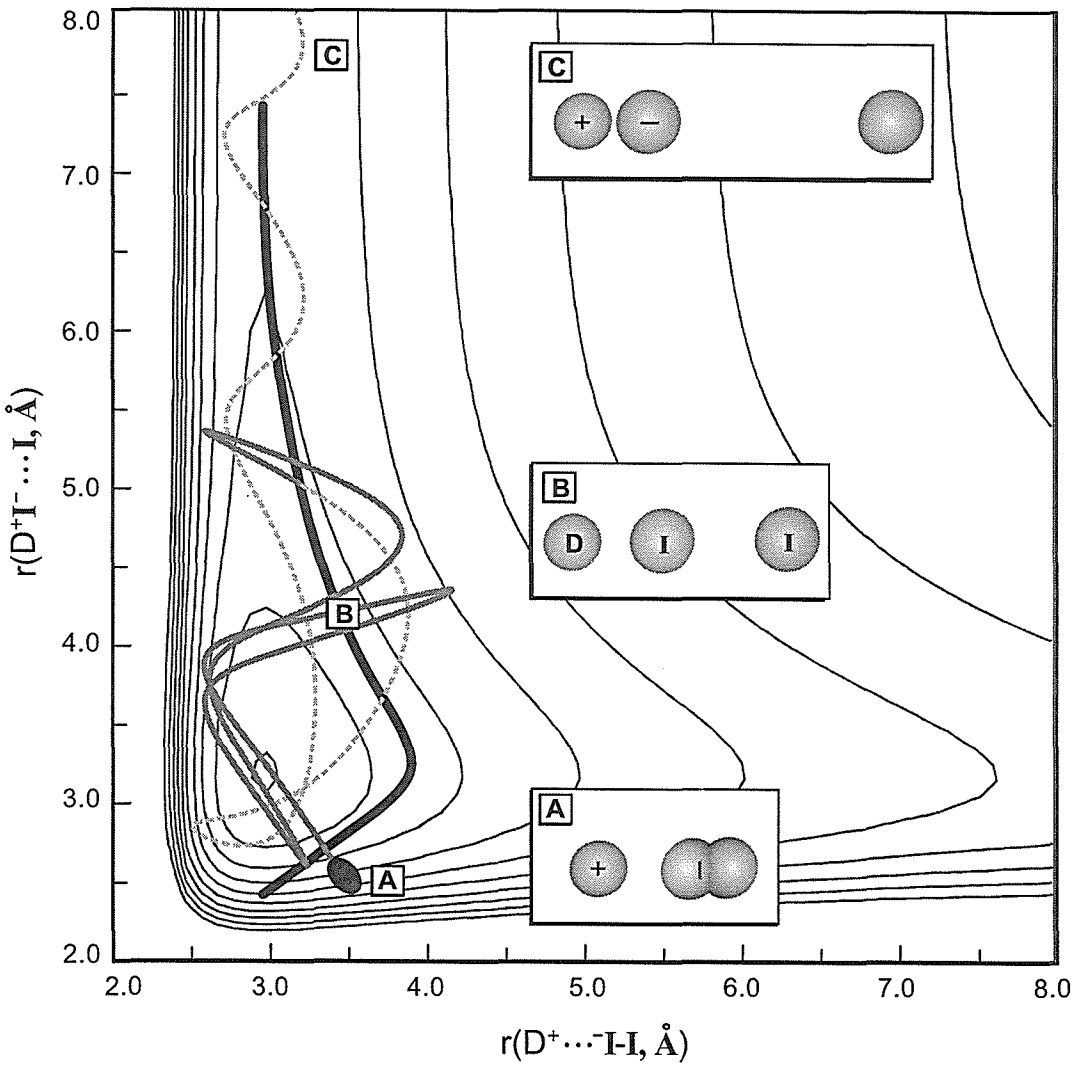

Figure 5.21A

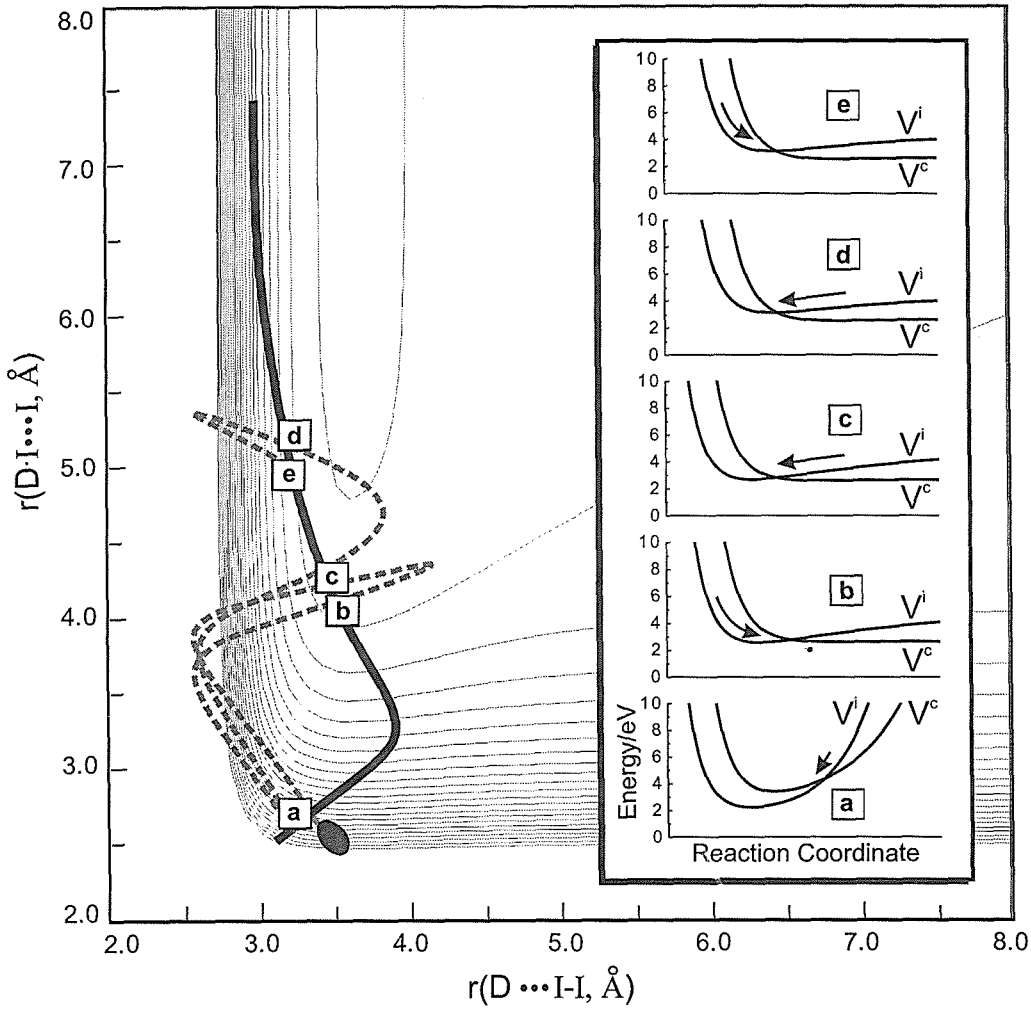
8.0
7.0
6.0
5.0
4.0
3.0
2.0
r(D-I•••I, Å)
2.0
3.0
4.0
5.0
6.0
7.0
8.0
r(D •••I-I, Å)
a
b
c
d
e
Energy/eV
Reaction Coordinate
V^i
V^c

Figure 5.21B

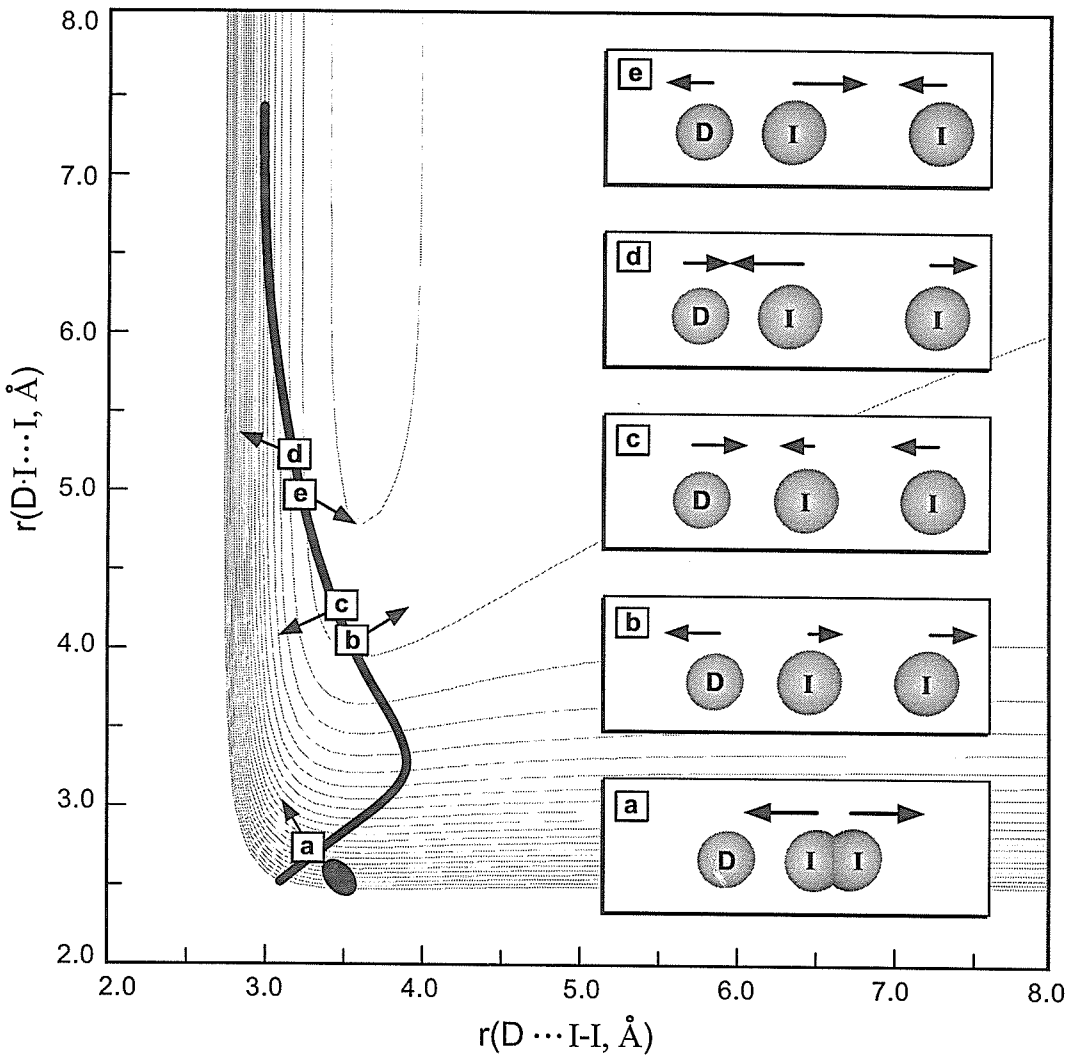

Figure 5.21C

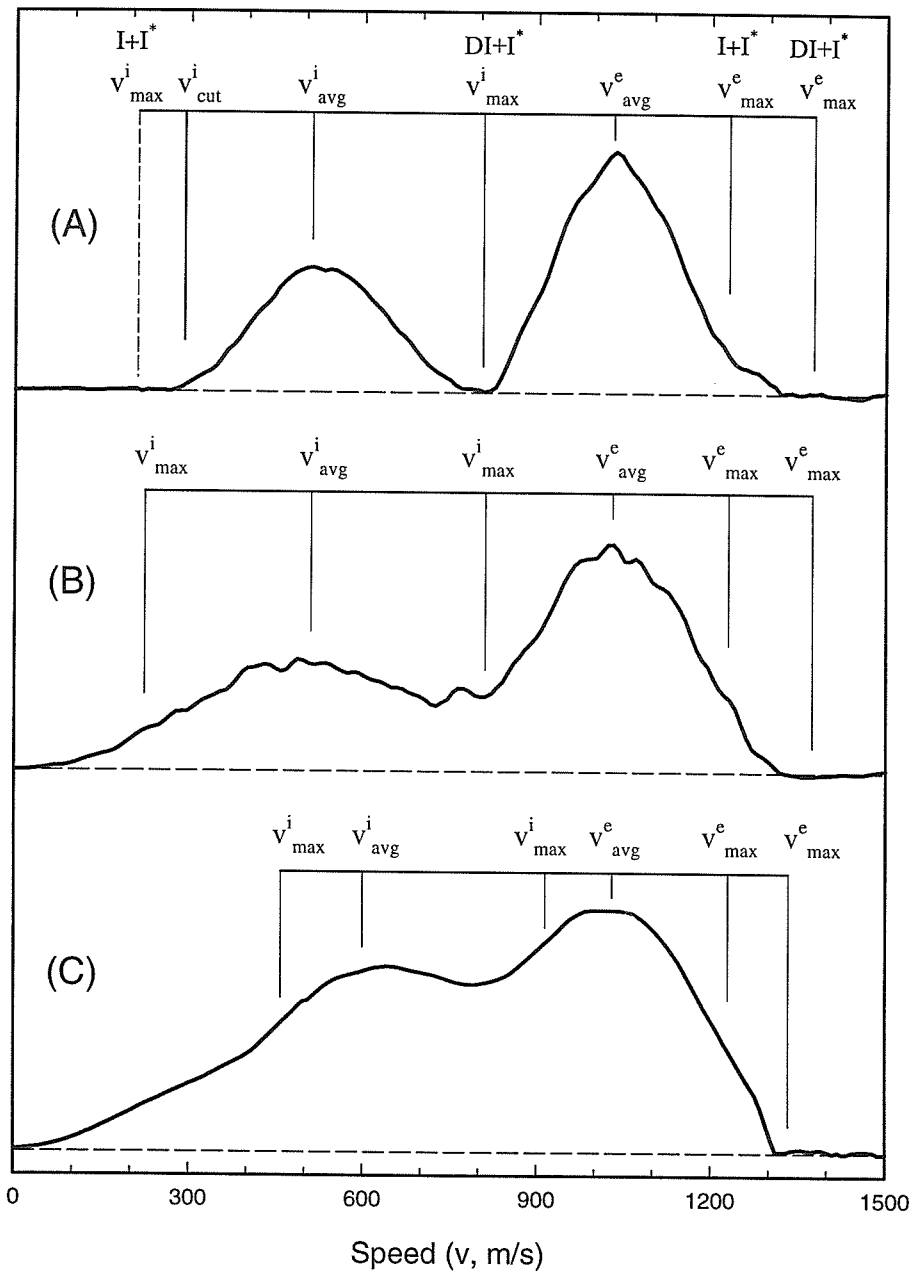
I+I*
DI+I*
I+I*
DI+I*
v^i_max
v^i_cut
v^i_avg
v^i_max
v^e_avg
v^e_max
v^e_max
(A)
(B)
(C)
0
300
600
900
1200
1500
Speed (v, m/s)

Figure 5.22

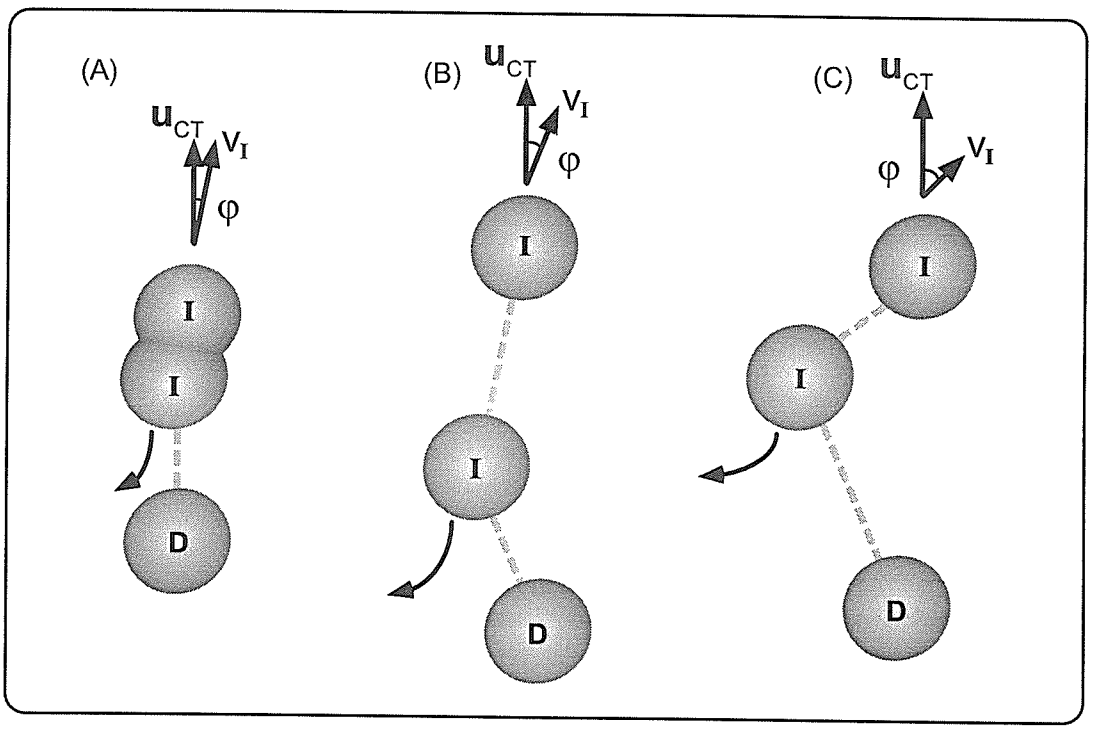

Figure 5.23

Chapter 6

Femtosecond Real-Time Probing of Bimolecular Reactions: Dynamics of Aromatic Nucleophilic Substitution, Inelastic Collision and Four-Center Cooperative Reaction[‡]

[‡] Adapted from: D. Zhong, S. Ahmad, P.Y. Cheng and A.H. Zewail, J. Am. Chem. Soc. **119** (1997) 2305-2306; D. Zhong, P.Y. Cheng and A.H. Zewail, J. Chem. Phys. **105** (1996) 7864-7867.

6.1. Nucleophilic Substitution Reaction

A general class of reactions termed aromatic nucleophilic substitution (S_NAr) reactions is central to organic syntheses, reaction mechanisms, and electron transfer processes.[1] A textbook example is the following reaction:

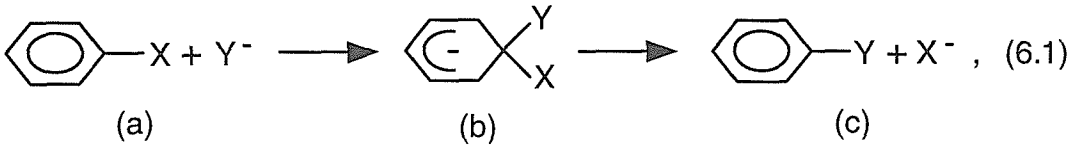

which is generally considered as a two-step process, the addition of the nucleophile (a→ b) and the elimination to form final products (b→c). However, if the processes of addition and elimination are concerted, the so-called σ-complex (b) becomes a transition state, similar in nature to S_N2 reactions.[2]

The dynamics of this elementary nucleophilic process is of great interest for a number of reasons. First, the potential energy surface[3] defines regions of transition states and complex intermediates, and these intermediates have been the subject of many experimental studies.[4] Second, the process involves both *electronic* and *nuclear* rearrangements and these occur on the femtosecond (fs) to picosecond (ps) time scale, hitherto unresolved. Third, the true lifetime of the intermediate determines the exact mechanism for the addition and elimination and reflects the nature of energy redistribution, statistical or not.[4a,5]

Here, our first study of S_NAr reactions with fs resolution is presented. The system of particular interest here is the reaction of a chlorine atom anion (Cl^-, nucleophile) with an iodobenzene cation (IBz^+, substrate) to form product chlorobenzene and iodine. The

concept of the experiment can be described as follows (Fig. 6.1). In a molecular beam, a fs pulse is used at time zero to create the charge separation in the van der Waals IBz·Cl_2 complex. In this way, the transition-state region, where the reagents are angstroms apart, is directly entered[6] and because of the limited impact parameters the barrier is minimally governed by centrifugal effects. The Cl_2^- is formed above the dissociation limit[7] and breaks up leaving the Cl^- to attack the most electron-deficient *i*-carbon of the cation.[8] Hence, a σ-complex can be formed but in contrast to (b) in (1), in this case, it is a delocalized *i*-cyclohexadienyl radical.[9] The activated σ-complex is probed with a second fs pulse by monitoring in time the liberated I atom and the kinetic energy-resolved time-of-flight (KETOF) distribution. These reaction steps are illustrated in Figure 6.1,[10] and the energetics is shown in Figure 6.2. The experimental apparatus is described in Chapter 2 and the mixing of Cl_2 and IBz was in front just before the gas expansion.

As shown in Figure 6.3, the mass spectra and KETOF distributions clearly show features of the reaction products. Without Cl_2 in the beam, only two peaks (>15 μs) of IBz^+ and I^+ appear in the mass spectrum. With a controlled concentration of Cl_2, a large enhancement of the I^+ signal and two new mass peaks, $ClBz^+$ and $IBzCl^+$, become evident. This enhancement is from the charge-transfer (CT) initiation at t=0.[6b] Indeed the initial excitation is confirmed to be a one-photon process (277 nm) and the I detection is by the known 2+1 REMPI (304.6 nm). The product formation of I and the nucleophilic substitution of Cl^- were consistent with the following observations: (1) as with the Bz·I_2 system (also see Chapter 4),[6] the CT absorption of the IBz·Cl_2 complex is much larger than that of IBz[13] and hence the observed enhancement, even though the total complex concentration is only a few percent of that of IBz, is from the CT excitation; (2) the Cl_2

absorption is very weak at 277 nm,[14] which again is consistent with the minor role of the radical substitution reaction (Cl+IBz); (3) the I^+ KETOF distributions are very different with and without Cl_2, and the enhanced part is a broad distribution, unlike the typical KETOF distribution observed from iodobenzene;[15,17] and finally (4) we have also monitored the temporal behavior of reaction constituents $IBzCl^+$ and $ClBz^+$ to check for consistency with the product I^+ transient.

We observed (Fig. 6.4) a 880 fs reaction time, orders of magnitude longer than the vibrational periods of the C-I and C-Cl bonds (~60 fs). Since the entrance channel involves Coulomb interaction, the addition process takes place in the first 100 fs; our MD simulations give 50 fs for the Cl^- to approach the IBz^+ at 2.45 Å separation, similar in magnitude to the result for $Cl_2^-+Xe^+$.[18] Accordingly, the observed 880 fs reaction time describes the elimination process, a rate-determining step for a highly non-concerted reaction. This indicates that a σ-complex is formed during the reaction. Along the one-dimensional reaction path of Fig. 6.2, it is expected that the elimination occurs on the fs time scale if electronic structural changes are controlling the process. However, intramolecular vibrational energy redistribution (IVR) must be involved in determining the effective dimensionality of the PES --- energy must flow from the site of the nucleophilic attack to the reaction coordinate. Furthermore, steric effects during the attack will slow the rates.

Consistent with the observations are the broad KETOF distributions which indicate vibrational energy involvement in *some* selective modes. In this regard, our results support the theoretical studies of S_N2 reaction lifetimes (multiexponential)[5a,b], consistent with nonconcerted S_N2 picture,[5c] and the experimental observation of

vibrational excitation in products.[4a,19] Crossed beam studies of radical substitution reactions have been performed by Lee's and Grice's groups.[21] It is interesting that for F+BzX (X=Br, I), a downhill reaction, the complexes' lifetimes were deduced to be longer than the rotational period.[21b] We have also studied other systems such as the reactions of Br^- with IBz^+ and Cl^- with *p*-iodotoluene cation and obtained similar findings. These results elucidate general features of the approach and these reactions.

The dynamics of the complex reflects the nature of bond making and bond breaking. From a frontier-orbital point of view, the interaction of the HOMO of the nucleophile with the σ^* LUMO of the C-I bond is critical for the formation of final products. Unlike the conventional S_N2 reaction, in this case the orbitals are orthogonal and with time must change configuration to allow for better interactions. The slower (than electron hybridization) nuclear motions determine the extent of IVR and its influence on the reaction rates. Simple MNDO MO calculations of OH^- reaction with *p*-nitrochlorobenzene[22] and *ab initio* electronic structure calculations[8a] of $:NH_3$ reaction with $C_6H_5Cl^+$ support the above picture.

The approach presented here to prepare and study the important nucleophilic substitution reactions is novel in its direct view of the dynamics of the transition-state region and with minimum impact parameter averaging. There are numerous extensions which include studies of other ion-molecule reactions, solvation effects and different orientations.

6.2. Bimolecular Inelastic Collision

Here, we present our first direct study of the femtosecond dynamics of the inelastic collision processes in bimolecular reactions. The bimolecular complex RX·M (R=H or CH_3, X=halogen-atom and M=molecule) is used as the precursor, formed in a supersonic molecular beam by the vdW interaction. A fs pulse is used to detach the H or CH_3 in ~100 fs, leaving the collision complex X·M in the ground-state surface with certain collision energy. The second fs pulse probes the liberated X-atoms. By delaying the fs probe pulse relative to the fs detaching pulse, the collision process is clocked. In this way, a variety of atom-molecule collision processes can be directly studied.

6.2.1. $CH_3I{\cdot}I^{\ddagger}$

The first system explored in this direction is the collision of I-atom with methyl iodide:

$$RI{\cdot}IR + h\nu \rightarrow [RI{\cdot}I]^{\ddagger} + R \rightarrow RI + I + R \ (R=CH_3), \quad \text{(inelastic collision)} \qquad (6.2)$$

a general class of halogen-atom reactions with alkyl halides or hydrocarbons; see, *e.g.*, refs. 23-29. The structures of $CH_3I{\cdot}ICH_3$ and $CH_3I{\cdot}I$ are shown in Figure 6.5.[30] In our experiments, the entire system is prepared on the reactive, *ground state* potential energy surface by direct launching of the wave packet of the collision complex $CH_3I{\cdot}I^{\ddagger}$ at time zero. The concept is illustrated in Figure 6.6. The translationally hot I atom is formed in 150 fs by detaching the CH_3 group in the direct dissociation of the moiety CH_3I (see Chapter 3). The reaction of CH_3I + I is observed from the van der Waals (vdW) geometry of the dimer at the I···I and C···I internuclear distances of the transition state (TS). The product I atom is then monitored with a series of probe pulses, delayed from t=0, and by

gating the different product velocities. As with other real-time studies of bimolecular reactions,[29, 31-34] the approach allows for direct clocking of the complex with a limited impact parameter and relatively well-defined energy.

The potential energy surface (PES) has a late TS[35] for CH_3I + I with a ~19 kcal/mol reaction barrier to form CH_3 + I_2.[26-28] Depending on the translational energy of the I atom, the complex may be trapped in the vdW potential well in the transition state region, exchanges the energy between I and CH_3I, and finally decomposes into the CH_3I + I. Thus by monitoring the I atom buildup, the temporal behavior will reflect the nature of the transition state of the $CH_3I{\cdot}I^{\ddagger}$ complex. This *inelastic* dynamical process is illustrated in Figure 6.6 by the trajectory reflection.

The fs laser system and the molecular beam apparatus used have been described in Chapter 2. The pump laser pulses (277 nm) initiate the CH_3I dissociation and the probe pulses (around 304 nm), delayed in time, detect the free iodine atoms (2+1 REMPI). For KETOF experiments, the pump laser polarization was fixed parallel to the TOF-MS (z) axis and perpendicular to the probe laser polarization. We performed the time resolved experiments by gating the velocity range of interest.[36] Calibration of t=0 and system response function was *in situ* made.[34] The molecular beam conditions were established by varying the time delay between the fs laser pulses and the pulsed valve opening. A gas mixture expansion containing methyl iodide vapor (-25°C, ~40 Torr) with He gas (~800 Torr) was made and, as shown in Figure 6.7, the leading edge only contains the monomer mass peak and the one which is slightly behind includes the monomer and *only* the dimer mass peak. We have studied the mass spectra for variety of concentrations and these studies will be detailed elsewhere.

The I^+ KETOF distributions at $\chi=0^0$ for a fixed delay time of 10 ps are also shown in Figure 6.7 under monomer and dimer conditions. When the slow-velocity z-component ($0 \leq v_z \leq 250$ m/s) of I^+ KETOF distribution (dimer) is gated (Fig. 6.8 (B)), and when the monomer contribution is subtracted (Fig. 6.8(A)), the transient, shown in Fig.6.8(C), exhibits a delayed, slow-rise behavior. The delay time is ~1.4 ps and the rise time is ~1.7 ps. This transient was repeated many times and is very reproducible. The observed ~1.4 ps delay time is striking and indicates that a coherent wave packet motion well persisted in the entrance channel during the inelastic collision between CH_3I and I.

For the minimum energy dimer geometry calculated by Zeigler,[30a] with reference to the crystal structure,[37] the I-I separation is estimated to be 3 Å and the structure is about 115^0 L-shaped with the two I atoms in proximity. The minimum energy structure of the collision complex is accordingly $CH_3I\cdots I$ (the I-I distance is > 3 Å); generally for these types of systems, one expects two minima as, *e.g.*, in the case of Cl+HCl and $I\cdots CH_3I$ complexes.[38,30b] Hence, the initial fs pulse, which detaches the CH_3 group, suddenly turns the vdW attractive $CH_3I\cdots ICH_3$ force into a repulsive interaction on the ground state PES of CH_3I + I. The entire complex of $CH_3I{\cdot}I^{\ddagger}$ recoils away from the CH_3 group. In the complex, the velocity of the I atom relative to the CH_3I molecule is small with an upper limit of 400 m/s, which corresponds to a maximum of 1.29 kcal/mol of collision energy.

As depicted in Figure 6.6, the I-atom first decelerates and then exchanges energy with CH_3I, and finally sticks to or separates from CH_3I depending on the strength of the repulsion and the initial translational energy. The latter, due to the large amplitude bending motion, could become less than the maximum available value. We have carried

out preliminary MD simulations. Considering the large amplitude motion, a linear geometry was involved for simplicity. The $CH_3I{\cdot}I^{\ddagger}$ vdW ($CH_3I{\cdots}I$) potential well is 1000 cm^{-1} deep and the equilibrium distance is 3.5 Å. These MD simulations show that the I-atom takes ~2 ps to separate from the CH_3I moiety with a 8 Å I-I distance. The center-of-mass of $CH_3I{\cdot}I^{\ddagger}$ moves ~5 Å, and because it has opposite velocity direction from the I atom (repulsive force) velocity in the complex the entire inelastic process slows down.

The 1.7 ps rise time of I atoms directly measures the lifetime of the $CH_3I{\cdot}I^{\ddagger}$ complex trapped in the potential well (low v trajectories). It manifests any resonance motion in the $CH_3I{\cdot}I^{\ddagger}$ complex during the energy redistribution. Molecular beam scattering experiments by Grice[26] and Ross[27] have shown a predominantly backscattered CH_3I from the reaction $CH_3+I_2 \rightarrow CH_3I + I$ (at 2-3 kcal/mol collision energy), indicating a rebound repulsive release with the lifetime of the complex being comparable to or less than the rotational period. Our real-time results show the formation of a long-lived complex and indicate that the beam experiments were only sensitive to the short-lived, high-energy states of the complex. Syage's observed broad (I recoil) angular distribution is consistent with a long-lived complex.[39] The formation of a complex in the inelastic E $\rightarrow$V process of HI + I (from HI dimers) has been shown recently by detecting the translational energy distributions of H atoms.[40] This is consistent with the above picture (CH_3I + I). It is interesting to note that the lifetimes of excited-state complexes ($Hg^{*}{\cdot}N_2$) in vdW wells have been reported to be of similar magnitude (2-5 ps).[41]

It should be pointed out that the gated transient (small v_z in Fig. 6.8(B)) includes the contributions from both I-atoms in dimer (Fig. 6.5). However, the I_b-atom is expected to be liberated very promptly, similar to the monomer dissociation, because of its

geometric position and the less energy exchange with CH_3I. Thus, the resulting transient (Fig. 6.8(C)) reflects the temporal behavior of the low-v I_a-atoms, which directly face the CH_3I moiety after the detachment.

6.2.2. $I{\cdot}C_6H_5I^{\ddagger}$

We extended the study to another more complex system, a collision process of I-atom with iodobenzene:

$$RI{\cdot}RI + h\nu \rightarrow R{+}[I{\cdot}RI]^{\ddagger} \rightarrow R + I + RI \quad (R{=}C_6H_5). \quad \text{(inelastic collision)} \qquad (6.3)$$

The possible structure of iodobenzene dimer is shown in Figure 6.9. As shown in Chapter 3, the first absorption band of iodobenzene (320-240 nm) is composed of two types of transitions: One is the (n, σ^*) excitation, localized along the C-I bond, and the other is the (π, π^*) excitation of the benzene ring system.[42,43] The dissociation dynamics following excitation in this wavelength region is complicated by the severe spectral overlaps of these two transitions. The (n, σ^*) states are similar to those of the A-band continuum observed in alkyl iodides which lead to a direct dissociation of the C-I bond in less than 400 fs.[44] The (π, π^*) states are expected to exhibit predissociative behavior due to mixing with the isoenergetic (n, σ^*) states.

With the fs time-resolved KETOF technique with a small aperture placed in front of the MCP assembly, we have characterized the I-atom velocity distributions at various delay times following the t=0 excitation in Chapter 3. A typical I atom KETOF distribution observed at ~10 ps is shown in Figure 6.10. A narrow high-velocity distribution and a broad low-velocity one are clearly observed. Transients obtained by

gating the high- and low-velocity distributions reveal markedly different temporal behaviors, as shown in Chapter 3. The high-velocity I atoms clearly exhibit a *coherent* wave packet motion manifested by the 400 fs delayed rise, consistent with the direct dissociation mechanism. Whereas, the low-velocity I atom transients are characterized by an exponential rise of about 600 fs, indicating an indirect predissociative process.

Slightly behind the leading edge of the pulse (monomer condition), there exists a region where only the iodobenzene monomer and dimer can be seen in the mass spectra (Fig. 6.10). The KETOF distribution observed in this monomer/dimer region is mostly from the monomer, but is distorted due to the presence of the dimer. In order to avoid collecting the I-atoms from the (π, π^*) excitation, we only gated the highest velocity component under this condition and the resulting transient is shown in Fig. 6.11. The initial rise is identical to the I-atom transient obtained in the monomer region. A second component, delayed by ~ 1.4 ps from the zero-of-time, is also observed due to the iodobenzene dimers. This observation indicates that the coherent wave packet motion of the C-I direct dissociation observed in the iodobenzene monomer remains intact in the dimer, but is greatly slowed down by the presence of the other iodobenzene molecule.

In the monomer, the appearance of the free I atom is governed by the relative velocity of the two fragments falling apart. We have shown that it takes 400 fs for the two fragments to escape from the long-range vdW interaction such that the free I atoms can be detected (Chapter 3). For the iodobenzene dimer, the further delayed appearance of the free I atom can be rationalized by the following two effects. Firstly, the relative velocity of the two dissociating fragments can be slowed down due to the additional vdW potential originating from the undissociated iodobenzene (Fig. 6.9). Secondly and more

importantly, the relative velocity between the departing I atom and the undissociated iodobenzene is now much slower, making it spend more time to escape from the vdW potential of the undissociated iodobenzene (Fig. 6.9).

The two systems studied here, $CH_3I{\cdot}I^{\ddagger}$ and $I{\cdot}C_6H_5I^{\ddagger}$, represents two extremes. For the former, we detected the low-v I-atoms from the "head-on" collision between I and CH_3I, but for the latter, we collected the high-v I-atoms from the "fly-by" collision between I and C_6H_5I. Both collision processes probably include the bending motion between I and the other undissociated moiety because of the different minimum structures of dimer and I·monomer as shown in Fig. 6.5.

6.3. Four-center Bimolecular Reaction

For the inelastic-collision dynamics described in Sec. 6.2.1., at the translational energy of our experiments, the wave packet cannot cross the barrier to $CH_3 + I_2$ formation. By using 304 nm as a pump, this reactive channel is still *not* open even for two-photon excitation, where the C-I bond breakage is still on the fs time scale.[45] This is because the detached CH_3 takes up most of the available energy ($m_I E_{avl}/m_{CH3I}$) either for the $I(^2P_{3/2})$ or $I(^2P_{1/2})$, as mentioned before. The reaction of $CH_3I + I(^2P_{3/2}) \rightarrow I_2 + CH_3$ is endothermic by 17.5 kcal/mol. (The channel of $CH_3I + I(^2P_{1/2})$, although exceeds the endothermicity, is shown to proceed through the inelastic collision by E→V transfer to form $CH_3I(v) + I(^2P_{3/2})$.[46]) The fact that we do observe the I_2 formation under the dimer condition, indicates a "four-center" mechanism. As shown in Figure 6.12, the build up of I_2 is very fast, in less than 500 fs. With a 304-nm pump pulse (two photons), the I_2 molecule can be formed in the electronically excited B state and detected by a 1+1

REMPI process (277 nm). Indeed the power dependence of the pump shows a quadratic behavior. No attempt yet was made to examine the ground state I_2 formation, observed in one-photon A-band promotion.[47]

The key for the formation of I_2 is the *cooperative* nuclear motion of both C-I bonds in the four-center reaction:

$$RI{\cdot}IR + h\nu \rightarrow [R\cdots I\text{-}I\cdots R]^{*\ddagger} \rightarrow 2R + I_2 \quad (R=CH_3), \qquad \text{(four-center reaction)} \quad (6.4)$$

a Bodenstein-type reaction.[48] Because the equilibrium distance of I_2 is 2.6 Å and the separation of I-I in the dimer is already about 3 Å, the I_2 molecule is formed promptly. Such I_2 formation has been studied in CW experiments[30a,47,49] and with 10 ps resolution.[50] The fs I_2 dynamics reported here can be rationalized using frontier orbitals. The initial fs one-electron promotion makes the LUMO/HOMO interaction effective to create an I-I bond with the in-phase σ^* orbital ($n\rightarrow\sigma^*$ excitation) or s or p orbital (Rydberg excitation) combination on the two I atoms. Donaldson and coworkers[47] proposed a modified exciton model. After the excitation of a CH_3I moiety to the A continuum or to the Rydberg state, a partial charge transfer occurs from one I end to the other. This process results in some anion-type character with the C-I bond now experiencing a repulsive force.

The consequence of the orbital interactions is to form the I-I bond on the time scale of the C-I breakage which as reported in Chapter 3 is 125 fs (for Rydberg excitation is similar),[45] consistent with the results in Figure 6.12 for I_2 production. The I_2 formation, which may be coherent, as shown in the case of molecular photodissociation (CH_2I_2),[51] has also been observed in the photodissociation of the HI dimer,[52,53] and again is a four-center reaction. Polanyi's group[54] observed the formation of Cl_2 and Br_2 by

photoinitiating reactions of 2HX (X=Cl and Br) on LiF surfaces. This surface aligned formation of X_2 is a four-center reaction. The chemistry in these aligned complexes and surfaces is novel and the method should be extended to other systems.

6.4. References

1. L. Eberson, *Electron Transfer Reactions in Organic Chemistry* (Springer-Verlag, New York, 1987); S.S. Shaik, H.B. Schlegel and S. Wolfe, *Theoretical Aspects of Physical Organic Chemistry: The S_N2 Mechanism* (Wiley, New York, 1992); A. Pross, *Theoretical & Physical Principles of Organic Reactivity* (Wiley, New York, 1995).

2. See: *e.g.,* E.B. Gluz, M.N. Glukhovtsev, B.Y. Simkin and V.I. Minkin, J. Org. Chem. (Russia) **28** (1992) 1798; J. March, *Advanced Organic Chemistry* (Wiley, New York, 1992), 4th ed., Ch. 13.

3. W.E. Farneth and J.I. Brauman, J. Am. Chem. Soc. **98** (1976) 5546; K. Hirao and P. Kebarle, Can. J. Chem. **67** (1989) 1261; J. Cornelisse, G. Lodder and E. Havinga, Rev. Chem. Intermediat. **2** (1979) 231.

4. (a) S.T. Graul and M.T. Bowers, J. Am. Chem. Soc. **113** (1991) 9696; (b) D.M. Cyr, L.A. Posey, G.A. Bishea, C.C. Han and M.A. Johnson, J. Am. Chem. Soc. **113** (1991) 9697; (c) J.L. Wilbur and J.I. Brauman, J. Am. Chem. Soc. **113** (1991) 9699; and references therein.

5. (a) S.R.V. Linde and W.L. Hase, J. Chem. Phys. **93** (1990) 7692; (b) W.L. Hase, Science 266 (**1994**) 998, and references therein; (c) J. Chandrasekhar and W.L. Jorgensen, J. Am. Chem. Soc. **107** (1985) 2974.

6. (a) A.H. Zewail, J. Chem. Phys. **100** (1996) 12701, Centennial Issue; (b) P.Y. Cheng, D. Zhong and A.H. Zewail, J. Chem. Phys. **105** (1996) 6216.

7. E.C.M. Chen and W.E. Wentworth, J. Chem. Phys. **89** (1985) 4099.

8. (a) B. Wassermann and B. Brutschy, J. Mol. Struct. (Theochem) **284** (1993) 107; (b) Y. Hu, W. Lu and S. Yang, J. Chem. Phys. **105** (1996) 5305.

9. (a) S.W. Benson, J. Am. Chem. Soc. **115** (1993) 6969; (b) P.S. Skell, H.N. Baxter III, J.M. Tanko and V. Chebolu, J. Am. Chem. Soc. **108** (1986) 6300; (c) S.K. Dotterer and R.L. Harris, J. Org. Chem. **53** (1988) 777.

10. The σ-complex energetics is estimated by considering the exothermic addition of Cl atom to a carbon double bond, -21 kcal/mol[11] and an endothermic disruption of the π electron framework of the ring (resonance stabilization energy), 11 kcal/mol.[12] This places the σ-complex below the Cl+IBz by -10 kcal/mol, and the products, ClBz+I, by -30 kcal/mol (exothermic). There may be a small barrier for the σ-complex to decompose into the products. The ionic state (IBz^+Cl^-) is estimated to be ~ 30 kcal/mol above the Cl+IBz and the total available energy for the σ-complex is ~ 45 kcal/mol.

11. H.B. Schlegel and C. Sosa, J. Phys. Chem. **88** (1984) 1141.

12. G.L. James and R.D. Stuart, Trans. Faraday Soc. **64** (1968) 2752.

13. R.M. Keefer and L.J. Andrews, J. Am. Chem. Soc. **72** (1950) 4677.

14. D.J. Seery and D.J. Britton, *J. Chem. Phys.* **68** (1964) 2263.

15. It is known that a new compound of iodobenzene dichloride is formed due to the mixing of Cl_2 with IBz. However, the absorption cross section is similar to IBz.[16] Furthermore, we observed that the enhancement of KETOF disappears when Cl_2 was shut off. If the compound is statically formed in the line, such change will not occur.

16. M.A.A. Beg and Y.Z. Abbasi, Pak. J. Sci. Ind. Res. **12** (1969) 12.

17. P.Y. Cheng, D. Zhong and A.H. Zewail, Chem. Phys. Lett. **237** (1995) 399.

18. F. Huang, D.W. Setser and B.S. Cheong, Isr. J. Chem. **34** (1994) 127.

19. It should be mentioned that after the CT excitation of the IBz·Cl_2 complex, the back electron transfer could in principle occur to form IBz*·Cl_2 or IBz·Cl_2^*. The IBz*·Cl_2 channel is minor based on the observed broad I^+ KETOF distribution.[17] If some trajectories evolve along the other back electron transfer channel (IBz·Cl_2^*),[20] similar to the Bz^+·I_2^- system,[6b] a radical substitution reaction (IBz·Cl) may occur. The resulting reaction route and dynamics (a slow-step elimination) will be the same as for the S_NAr reaction, as discussed above.

20. Because there are only fewer repulsive states of Cl_2^* in our energy region, this back electron transfer channel may be less important. See S.D. Peyerimhoff and R.J. Buenker, Chem. Phys. **57** (1981) 279 for the states of Cl_2.

21. (a) G.N. Robinson, R.E. Continetti and Y.T. Lee, J. Chem. Phys. **89** (1988) 6226; (b) J.J. Wang, D.J. Smith and R. Grice, J. Phys. Chem. **100** (1996) 16169.

22. S. Yamabe, T. Minato and Y. Kawabata, Can. J. Chem. **62** (1984) 235.

23. Y.T. Lee, Science **236** (1987) 793; J.M. Farrar and Y.T. Lee, J. Chem. Phys. **63** (1975) 3639.

24. D.M. Golden and S.W. Benson, Chem. Rev. **69** (1969) 125; D.F. McMillen and D.M. Golden, Annu. Rev. Phys. Chem. **33** (1982) 493; J. Berkowitz, G.B. Ellison and D. Gutman, J. Phys. Chem. **98** (1994) 2744, and references therein.

25. R.F. Varley and P.J. Dagdigian, J. Phys. Chem. **99** (1995) 9843; W.R. Simpson, T.P. Rakitzis, S.A. Kandel, T. Lev-On and R.N. Zare, J. Phys. Chem. **100** (1996) 7938.

26. C.F. Carter, M.R. Levy and R. Grice, Faraday Discuss. Chem. Soc. **55** (1973) 357.

27. J.A. Logan, C.A. Mims, G.W. Stewart and J. Ross, J. Chem. Phys. **64** (1976) 1804.

28. L.J. Kovalenko and S.R. Leone, J. Chem. Phys. **80** (1984) 3656.

29. N.F. Scherer, L.R. Khundkar, R.B. Bernstein and A.H. Zewail, J. Chem. Phys. **87** (1987) 1451; **92** (1990) 5239; I.R. Sims, M. Gruebele, E.D. Potter and A.H. Zewail, J. Chem. Phys. **97** (1992) 4127.

30. (a) P.G. Wang, Y.P. Zhang, C.J. Ruggles and L.D. Ziegler, J. Chem. Phys. **92** (1990) 2806; (b) C.C. Arnold, D.M. Neumark, D.M. Cyr and M.A. Johnson, J. Phys. Chem. **99** (1995) 1633.

31. S.I. Ionov, G.A. Brucker, C. Jaques, L. Valachovic and C. Wittig, J. Chem. Phys. **99** (1993) 6553.

32. R.D. van Zee and J.C. Stephenson, J. Chem. Phys. **102** (1995) 6946; C. Dedonder-Lardeux, M. Berdah, C. Jouvet, S. Martrenchard-Barra, J.M. Mestdagh, D. Solgadi and J.P. Visticot, J. Chem. Phys. **104** (1996) 2740.

33. S.A. Wright, M.F. Tuchler and J.D. McDonald, Chem. Phys. Lett. **226** (1994) 570.

34. P.Y. Cheng, D. Zhong and A.H. Zewail, J. Chem. Phys. **103** (1995) 5153.

35. J.C. Polanyi, Acc. Chem. Res. **5** (1972) 161.

36. P.Y. Cheng, D. Zhong and A.H. Zewail, J. Phys. Chem. **99** (1995) 15733.

37. T. Kaweguchi, M. Hijikigawa, Y. Hayafuji, M. Ikeda, R. Fukishima and Y. Tomiie, Bull. Chem. Soc. Jpn. **46** (1973) 53.

38. M. Dubernet and J.M. Hutson, J. Phys. Chem. **98** (1994) 5844.

39. J.A. Syage, Chem. Phys. **207** (1996) 411.

40. J. Zhang, M. Dulligan, J. Segall, Y. Wen and C. Wittig, J. Phys. Chem. **99** (1995) 13680.

41. L. Krim, P. Qiu, N. Halberstadt, B. Soep and J.P. Visticot, in: *Femtosecond Chemistry*, eds. J. Manz and L. Wöste (VCH, Weinheim, 1994), p. 433.

42. T.M. Dunn and T. Iredale, J. Chem. Soc. (1952) 1592.

43. A. Freedman, S.C. Yang, M. Kawasaki and R. Bersohn, J. Chem. Phys. **72** (1980) 1028.

44. J.L. Knee, L.R. Khundkar and A.H. Zewail, J. Chem. Phys. **83** (1985) 1996.

45. M.H.M. Janssen, M. Dantus, H. Guo and A.H. Zewail, Chem. Phys. Lett. **214** (1993) 281; H. Guo and A.H. Zewail, Can. J. Chem. **72** (1994) 947.

46. C. Fotakis and R.J. Donovan, J. Chem. Soc. Faraday Trans. 2 **74** (1978) 2099.

47. Y.B. Fan and D.J. Donaldson, J. Phys. Chem. **96** (1992) 19; J. Chem. Phys. **97** (1992) 189; Y.B. Fan, K.L. Randall and D.J. Donaldson, J. Chem. Phys. **98** (1993) 4700.

48. M. Bodenstein, Z. Physik. Chem. **13** (1894) 56.

49. S.P. Sapers, V. Vaida and R. Naaman, J. Chem. Phys. **88** (1988) 3638.

50. J.A. Syage and J. Steadman, Chem. Phys. Lett. **166** (1990) 159.

51. U. Marvet and M. Dantus, Chem. Phys. Lett. **256** (1996) 57.

52. M.A. Young, J. Phys. Chem. **98** (1994) 7790; J. Chem. Phys. **102** (1995) 7925.

53. K.L. Randall and D.J. Donaldson, J. Phys. Chem. **99** (1995) 6763.

54. C.-C. Cho, J.C. Polanyi and C.D. Stanners, J. Chem. Phys. **90** (1989) 598.

6.5. Figure Captions and Figures

Figure 6.1. Five snapshots of schematic structures to illustrate the preparation and evolution of the nucleophilic substitution reaction. Emphasis is on the structural change prior to the fs preparation (t_-), when separation of charges occurs (t_0), in the transition-state region ($t_1^{\ddagger}$, $t_2^{\ddagger}$) and for final products (t_f). The initial structure is assumed in analogy with Bz/X_2 systems.[6b]

Figure 6.2. Shown are the energetics and reaction path.[10] The initial wavepacket in the transition-state region is displayed at the available energy. Note that for the neutral Cl + IBz reaction, the collision energy will be less than the ~35 kcal/mol value (~10 kcal/mol) because of Cl_2 direct dissociation.

Figure 6.3. Upper panel: TOF mass spectra without (dotted) and with (solid line) Cl_2 under the same conditions. Lower panel: The corresponding I^+ KETOF distributions taken at a ~ 6 ps delay time. The enhancement of the I^+ KETOF signal is also shown (heavy solid line).

Figure 6.4. The experimental fs transient, which is well simulated by a single exponential rise with τ=880 fs (solid line), obtained by gating the central part of the I^+ KETOF distribution with 60 ns gatewidth. The temporal response of the system is also indicated (dashed line). The KETOF resolution is not optimum because a small aperture arrangement was not used in order to observe the entire velocity distribution.[17]

Figure 6.5. The structures of $CH_3I\cdots ICH_3$ and $CH_3I\cdots I$.[30]

Figure 6.6. A contour PES map for the full-collision, bimolecular $CH_3I + I$ reaction (schematic). An inelastic scattering trajectory is shown, together with the initial wave packet (black oval) at I···I and I···C distances of 3 Å and 2.1 Å, respectively. The three panels illustrate snapshots of the complex in the transition state ($t^{\ddagger}$), as final products of the inelastic channel, $CH_3I + I$ (t_f), or final products of the reactive channel, $CH_3 + I_2$ (t_f).

Figure 6.7. Upper panel: TOF mass spectra obtained for two conditions, the monomer (dotted line) and the monomer/dimer condition (solid line). The mass spectrum under the dimer condition is shown only for arrival times longer than 20 μs and the monomer signal (not shown) is about 25 times larger than the dimer signal. Both 277 nm and 304 nm fs lasers were used near time zero. Lower panel: The corresponding I^+ KETOF distributions for the two cases. The dimer contribution is clearly pronounced in the small v_z region. The I^+ KETOF distributions were taken at a pump-probe delay time of ~600 ps.

Figure 6.8. (A) Femtosecond I^+ transient taken by gating I^+ signal for the slow-velocity z-component ($0 \le v_z \le 250$ m/s) under the monomer condition. The overall I^+ transient was best fitted by two components (dashed lines): a peak at time zero, from the fragmentation of CH_3I^+, and a shifted (125 fs) step-function rise from the dissociation product. (B) Femtosecond I^+ transient obtained under the same conditions as in (A) except for the dimer condition. The dashed lines (peak + plateau), similar to A, are the

contributions from the monomer dissociation. The apparent rise signal at longer times, which is absent in A, therefore gives the dimer transient contribution (the inelastic channel). (C) The transient response of $(CH_3I)_2$, after correction for the monomer in B. The signal was best fitted by a delayed (Δt ~1.4 ps) single exponential rise (τ ~ 1.7 ps) convoluted with the experimental response function, and the theoretical fit is displayed as a solid line.

Figure 6.9. The possible structure of dimer, $C_6H_5I\cdots C_6H_5I$.

Figure 6.10. Upper panel: TOF mass spectra obtained for two conditions, the monomer (dotted line) and the monomer/dimer condition (solid line). The mass spectrum under the dimer condition is shown only for arrival times longer than 20 μs. Lower panel: The corresponding I^+ KETOF distributions for the two cases. The KETOF distribution under monomer/dimer condition is broader because of the dimer contribution.

Figure 6.11. I-atom transient obtained in the monomer/dimer condition by gating the highest velocity component in the I^+ KETOF distribution. The data are fitted to the sum of two-delayed step functions convoluted with the pump-probe correlation. The first rise is due to the monomer (n=1) and is found to be identical to the transient obtained in the monomer condition. The second rise due to the dimer (n=2) is delayed from the first one by ~1 ps. The second delayed rise is reproducible.

Figure 6.12. Femtosecond I_2^+ transient obtained under only the dimer condition $(CH_3I)_2$, detecting the I_2^+ signal. The corresponding reaction mechanism is sketched on the top by the structure changes during the reaction.

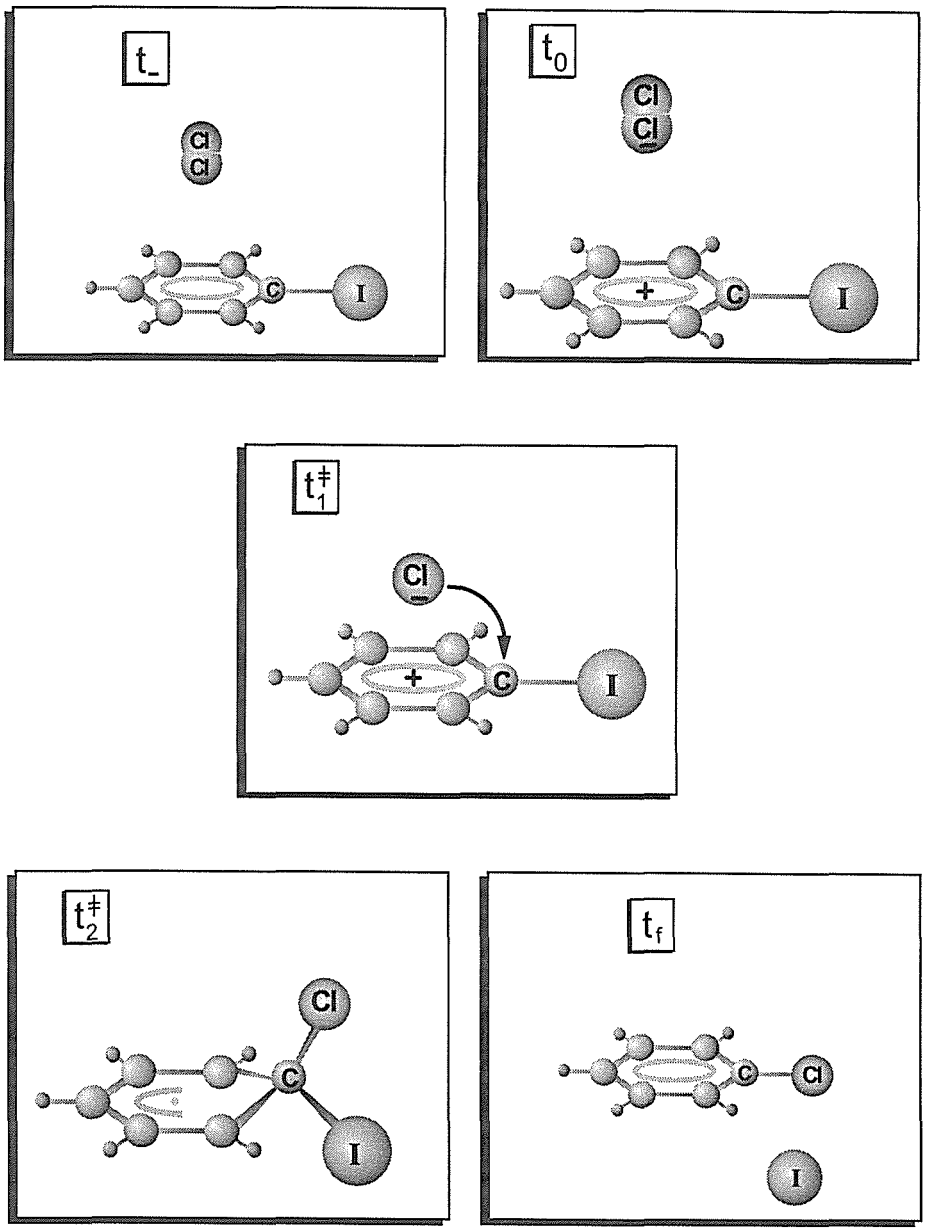

Figure 6.1

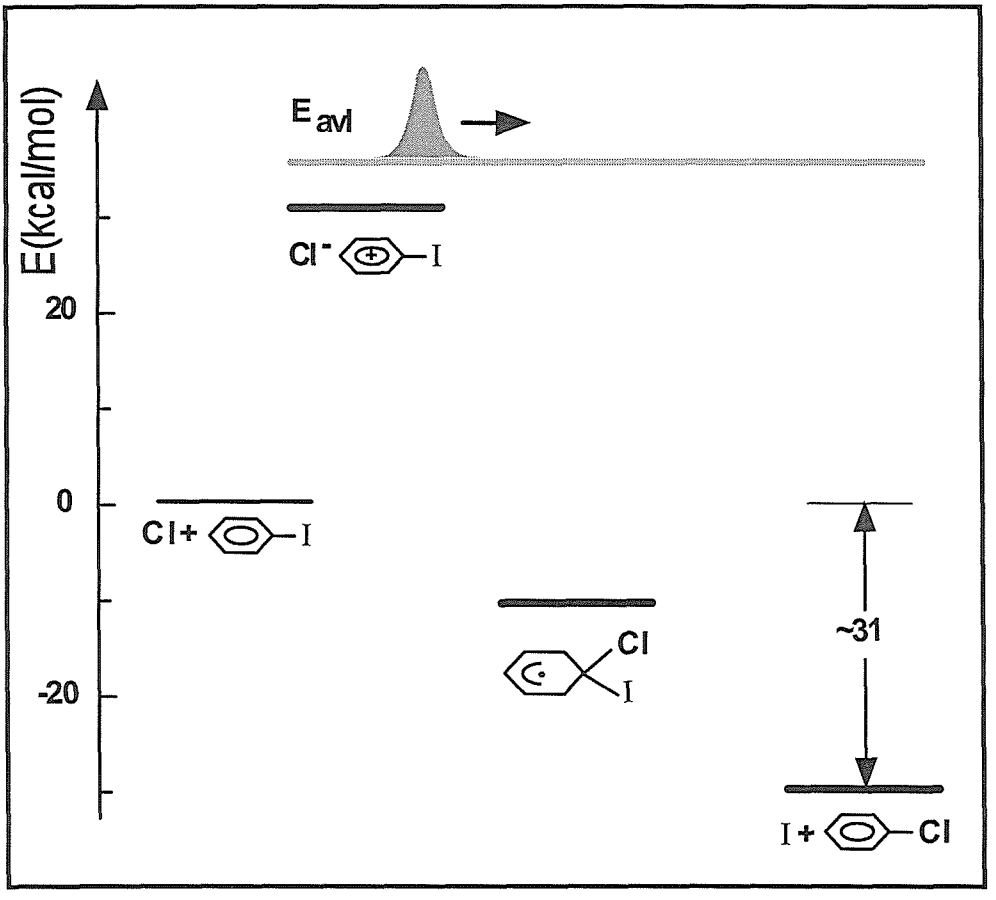

Figure 6.2

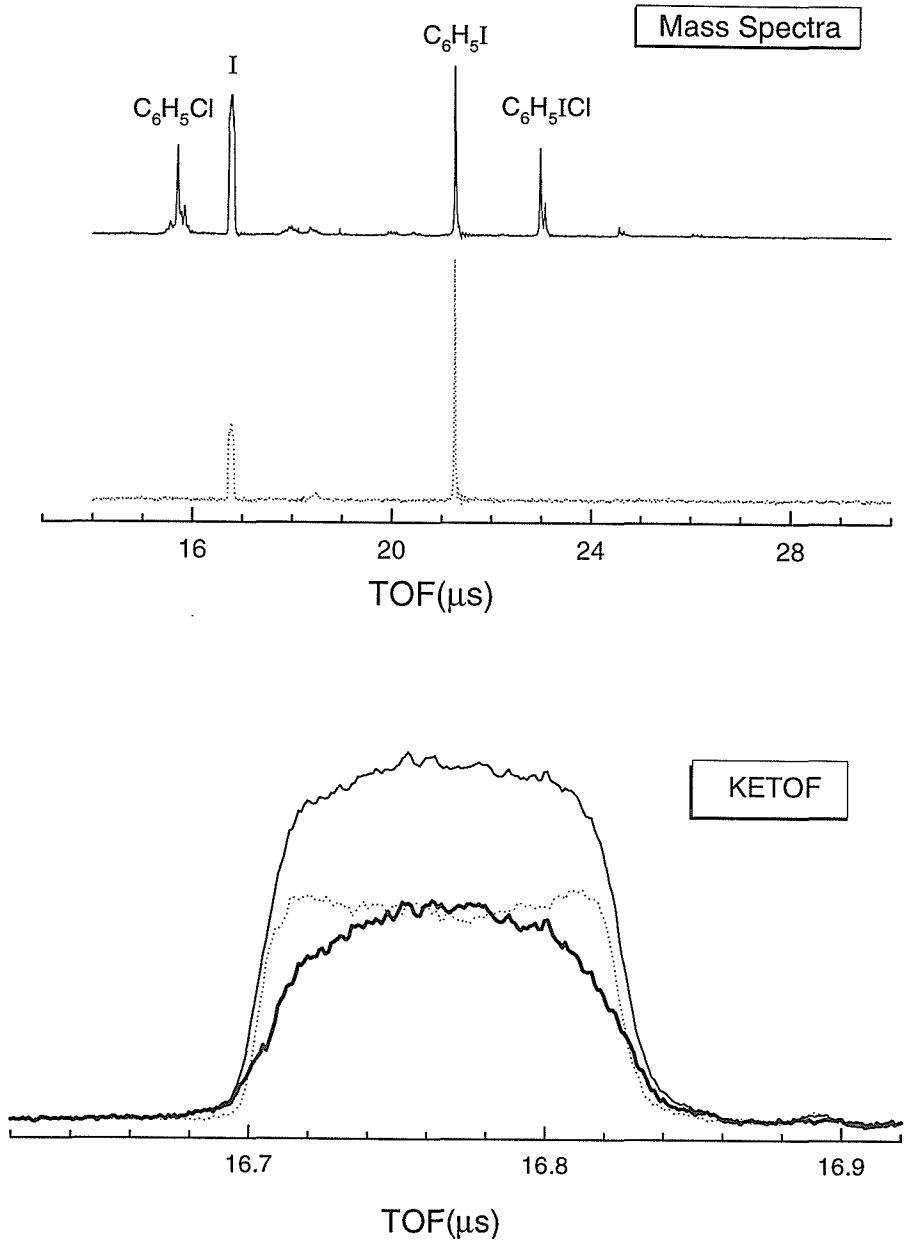
Mass Spectra
C_6H_5I
I
C_6H_5Cl
C_6H_5ICl
16
20
24
28
TOF(μs)
KETOF
16.7
16.8
16.9
TOF(μs)

Figure 6.3

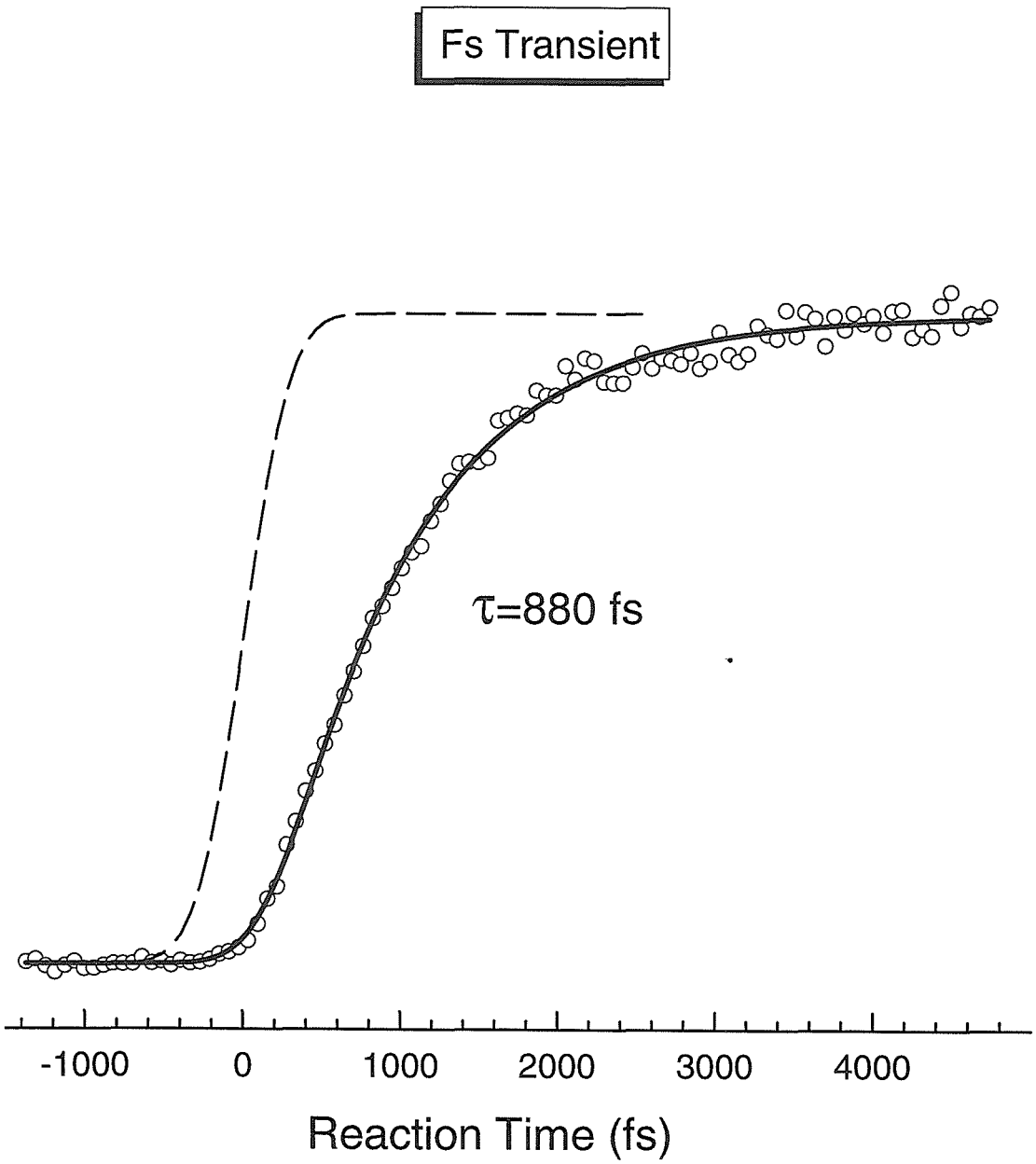
Fs Transient
τ=880 fs
-1000
0
1000
2000
3000
4000
Reaction Time (fs)

Figure 6.4

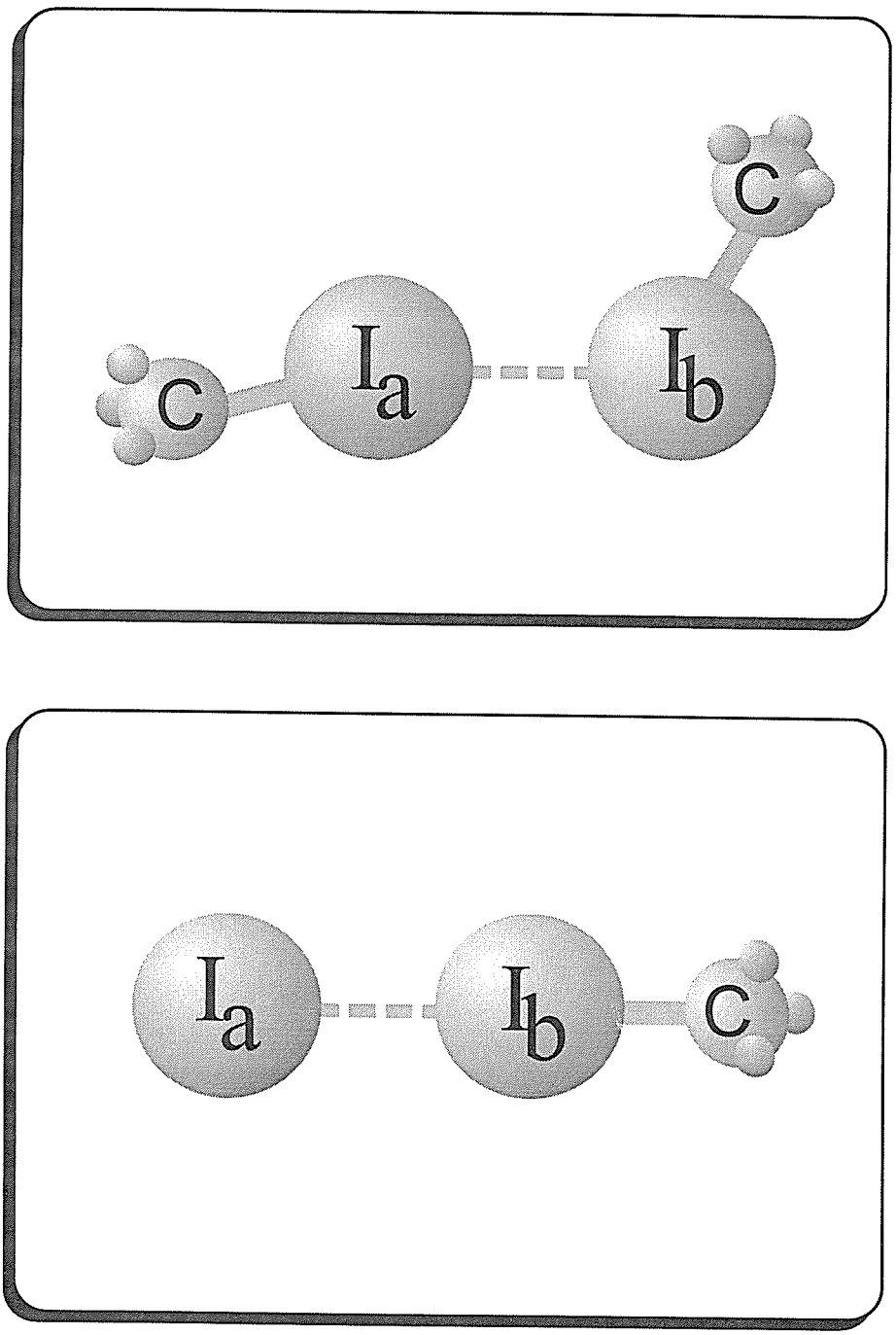

Figure 6.5

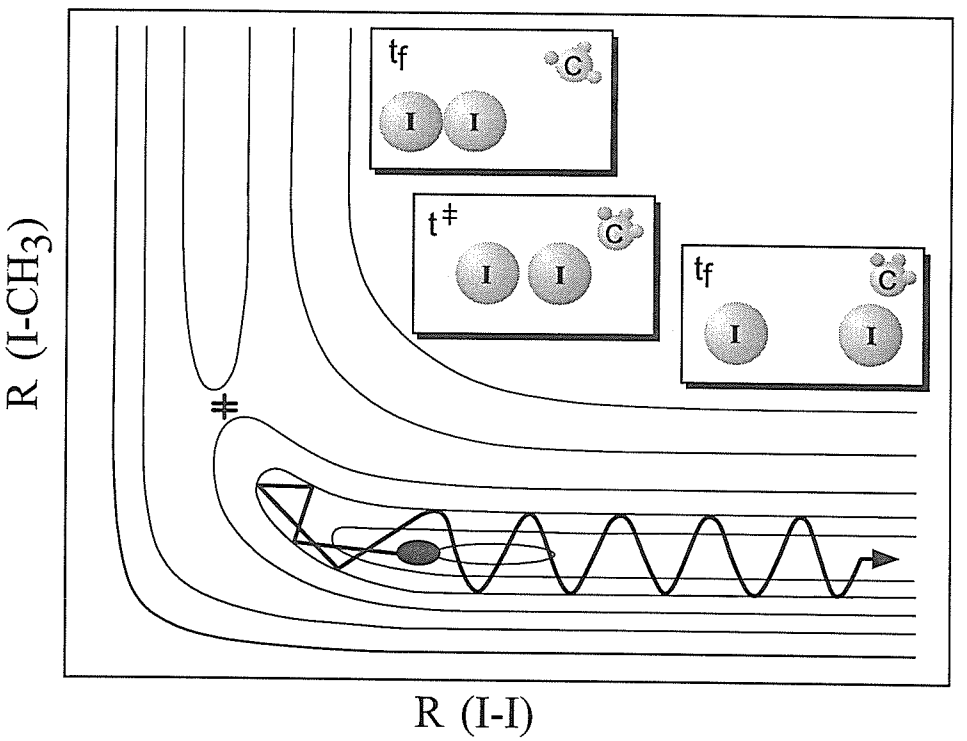

Figure 6.6

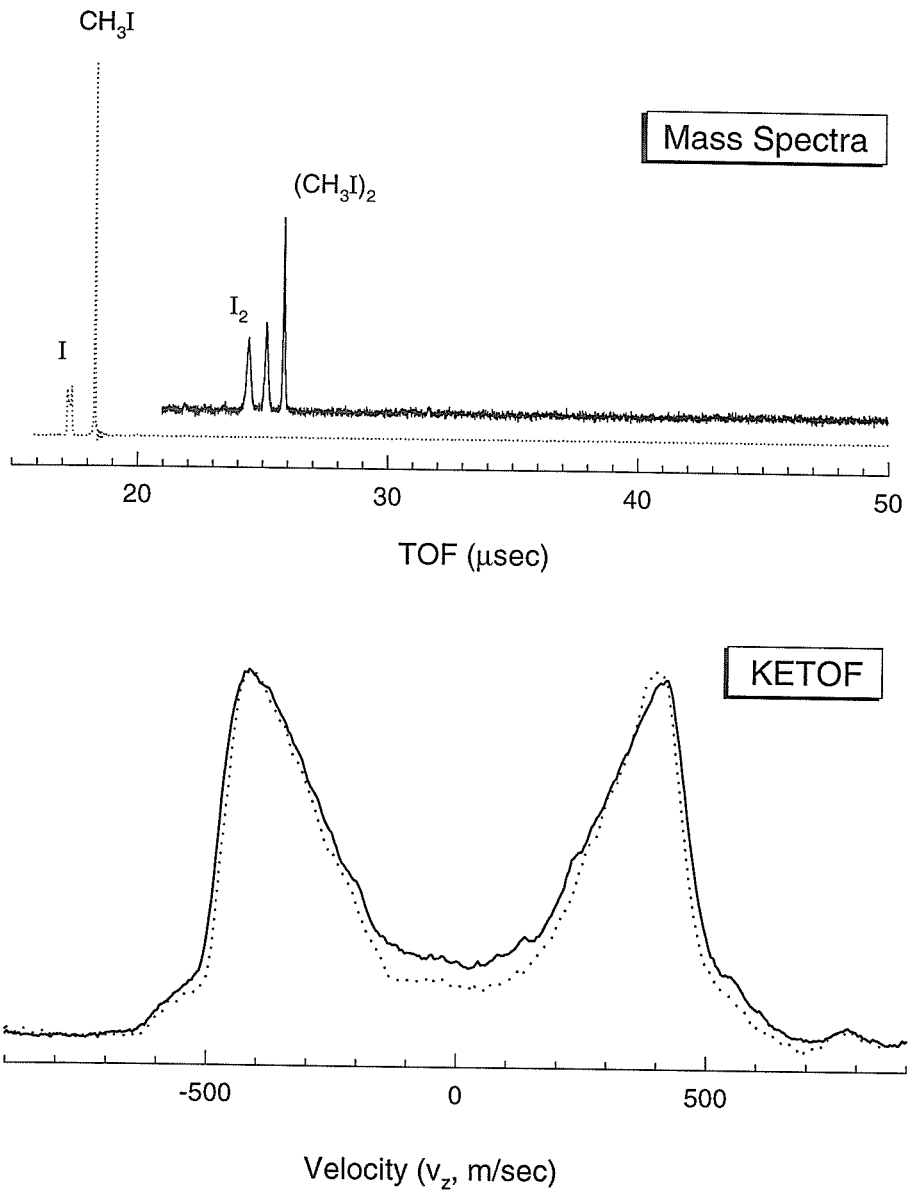
CH3I
Mass Spectra
(CH3I)2
I2
I
20
30
40
50
TOF (μsec)
KETOF
-500
0
500
Velocity (vz, m/sec)

Figure 6.7

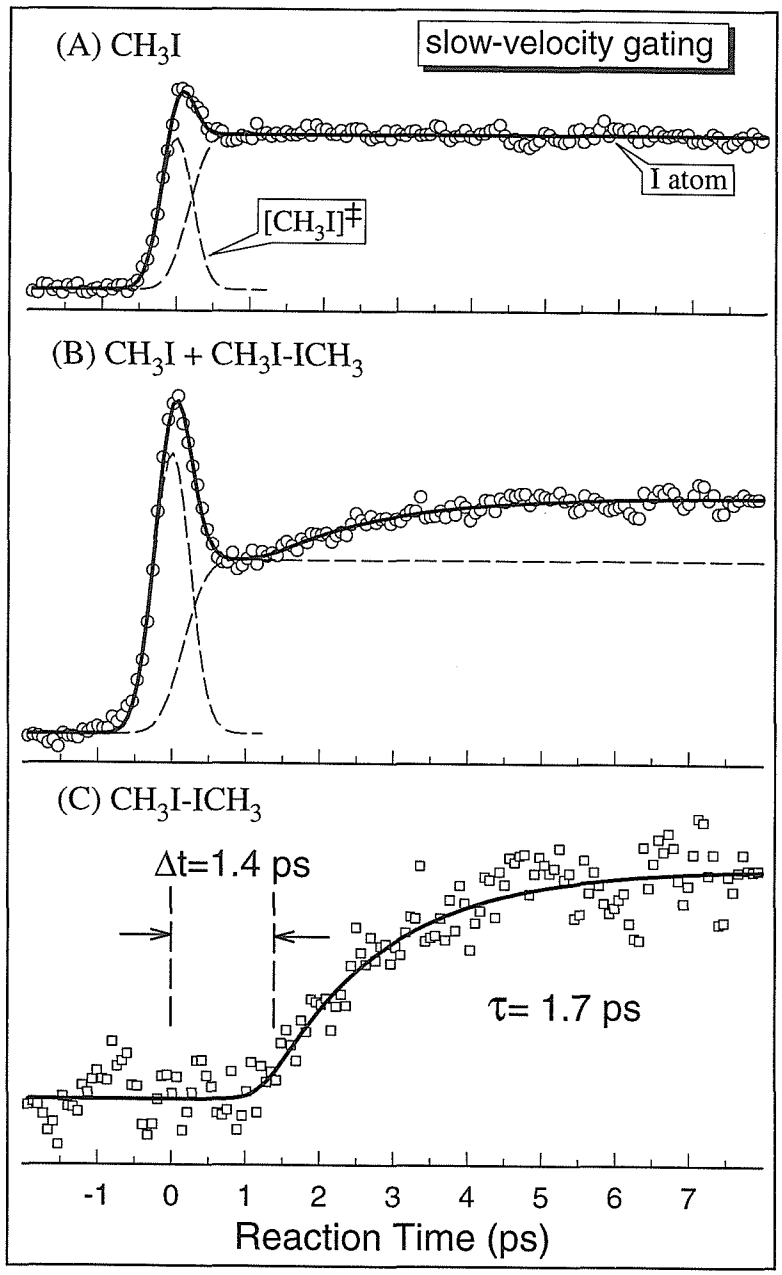
(A) CH_3I
slow-velocity gating
I atom
$[CH_3I]^{\ddagger}$
(B) $CH_3I + CH_3I\text{-}ICH_3$
(C) $CH_3I\text{-}ICH_3$
Δt=1.4 ps
τ= 1.7 ps
-1
0
1
2
3
4
5
6
7
Reaction Time (ps)

Figure 6.8

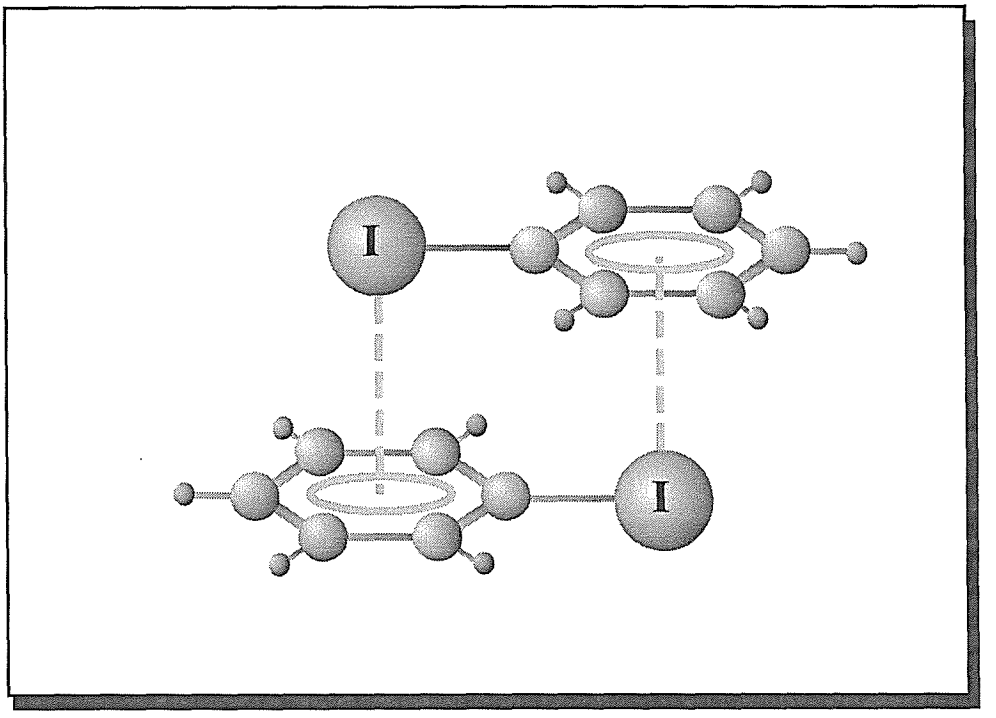

Figure 6.9

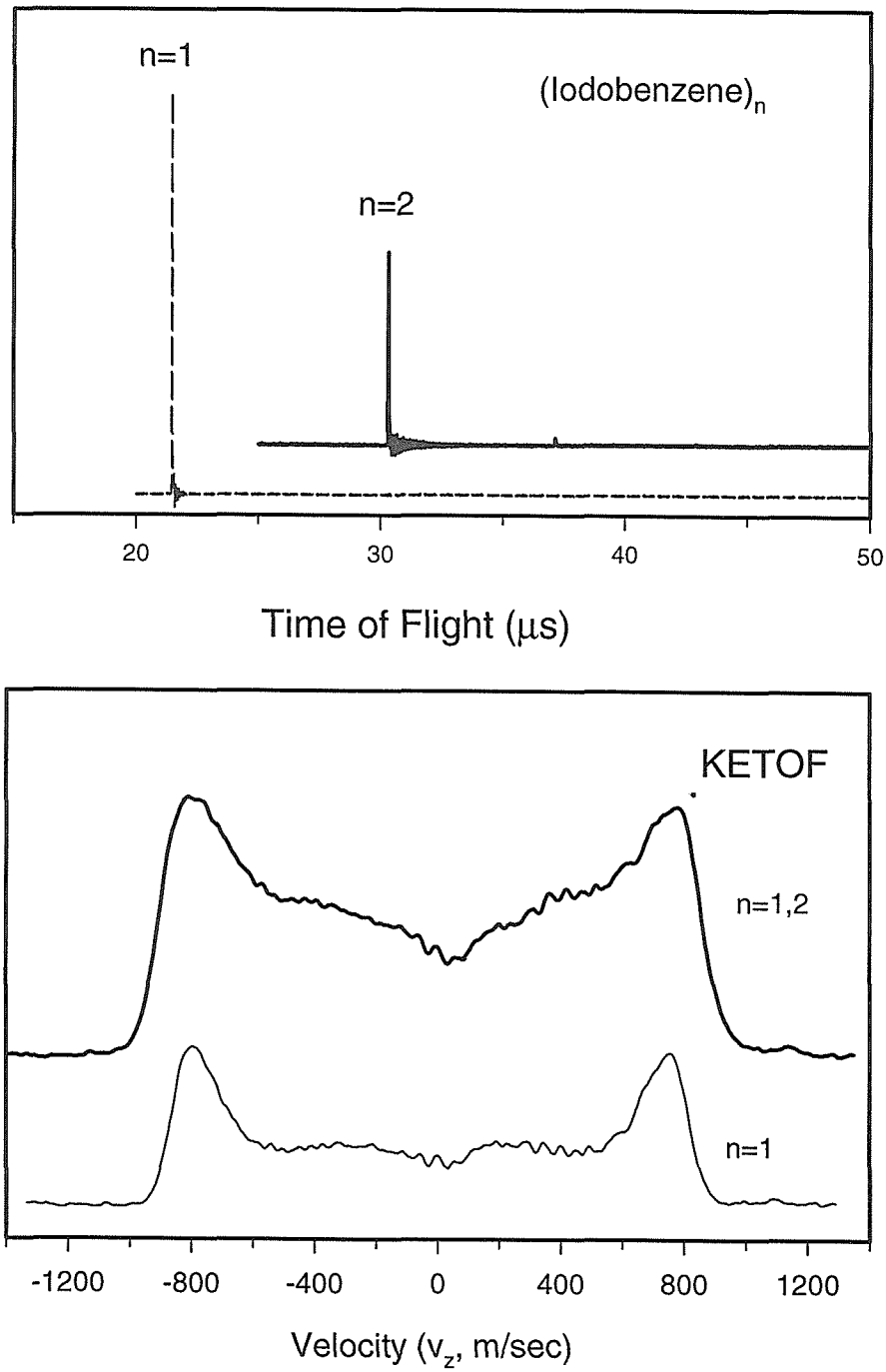
n=1
(Iodobenzene)n
n=2
20
30
40
50
Time of Flight (μs)
KETOF
n=1,2
n=1
-1200
-800
-400
0
400
800
1200
Velocity (vz, m/sec)

Figure 6.10

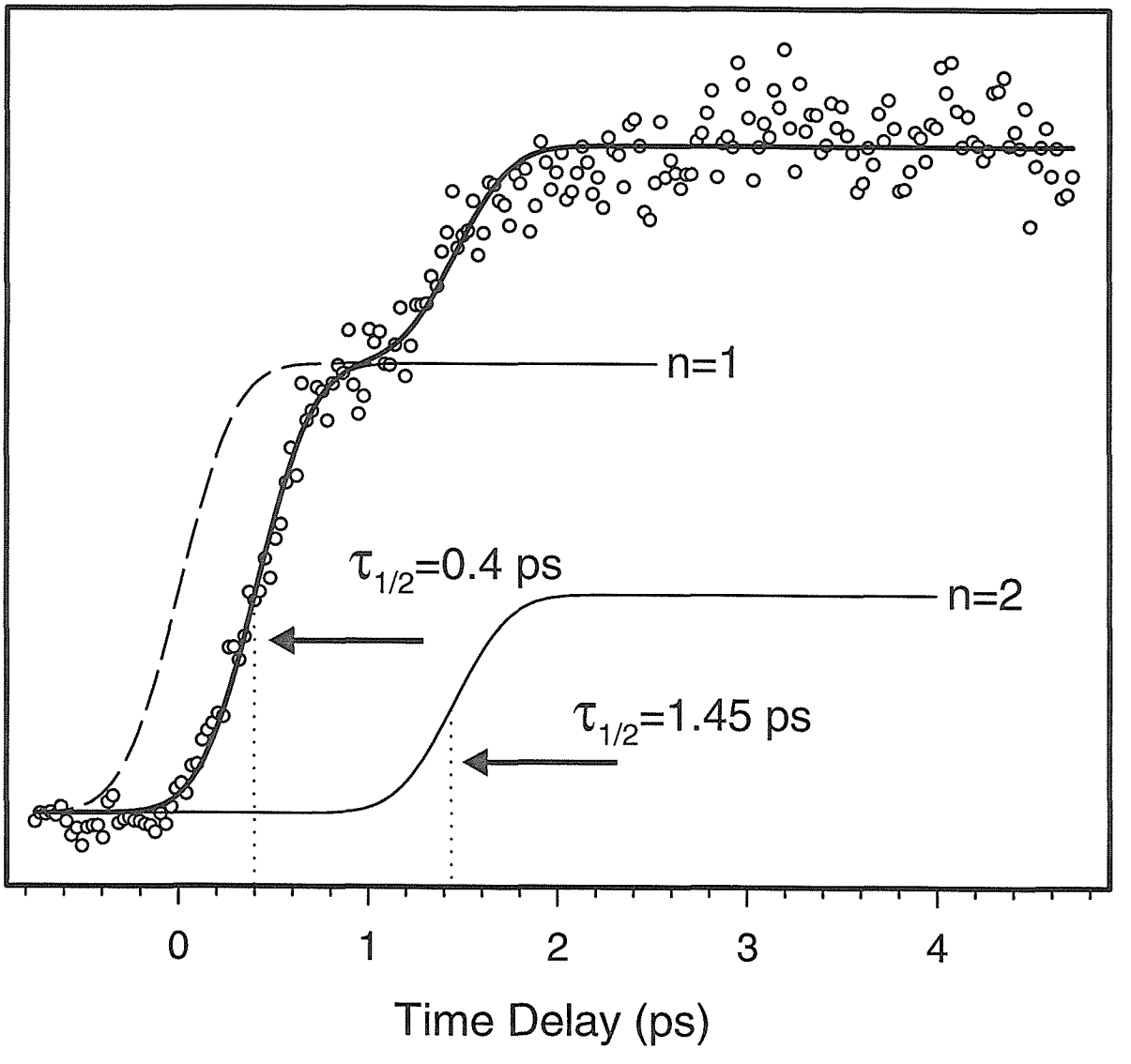

Figure 6.11

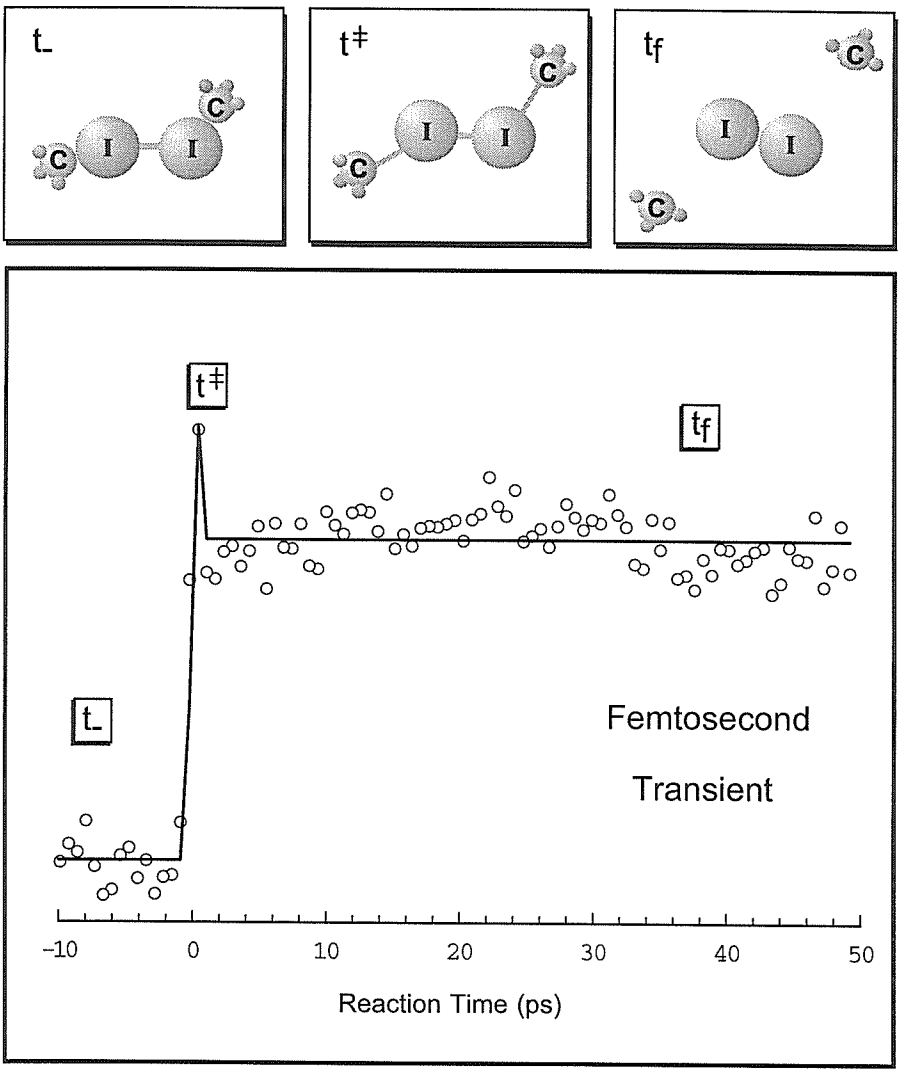
t_
t‡
tf
C
I
I
C
C
I
I
C
C
I
I
C
t‡
tf
t_
Femtosecond
Transient
−10
0
10
20
30
40
50
Reaction Time (ps)

Figure 6.12

Chapter 7

Femtosecond Real-Time Probing of Solvation Dynamics: Cage Exit and Solvent Structures[‡]

[‡] Adapted from: P.Y. Cheng, D. Zhong and A.H. Zewail, J. Phys. Chem. **99** (1995) 15733-15737; Chem. Phys. Lett. **242** (1995) 369-379.

7.1. Introduction

Photofragment translational spectroscopy, which measures product kinetic-energy distribution, provides valuable information on the nature of the exit channel and energy disposal in reactions (see, for example, reviews in ref. 1 and 2). More recently, this approach has been applied to the photoinitiated dissociation and reactions in molecular clusters,[3-6] demonstrating its potential in these systems. These studies have shown that the product kinetic-energy distributions from clusters are in general broader and less anisotropic than those from the monomers and are shifted to much lower energies. The behavior has been attributed to the collisional relaxation of the photoproducts escaping from the clusters, or the condensed-phase analogy of the "cage effect." Molecular dynamics simulation studies have elucidated this picture.[7-9]

As detailed in Chapter 2, the femtosecond kinetic-energy resolved time-of-flight (fs-KETOF) mass spectrometry provides a two-dimensional, *time-velocity correlation* method in which the product kinetic-energy distribution measurements are made with femtosecond (fs) time resolution.[10] Here, the ultrafast solvation dynamics in iodobenzene clusters are elucidated as a demonstration, illustrating the power of the time resolution in identifying the caging dynamics and the solvent structures. Dissociation of pure iodobenzene clusters yields product kinetic-energy distributions which are broader, less structured, and lower in energy. Temporal evolution of these distributions from the clusters is clearly revealed and two vastly different channels are separated: One in which dissociation occurs in few picoseconds (ps) and the other in which dissociation takes up to hundreds of ps. We relate these two distinct channels to two different solvation

structures and we systematically use the velocity gating to examine the nature of caging in the different-sized structures.

7.2. Experimental

The molecular beam apparatus and the fs laser system have been described in Chapter 2. Briefly, the molecular beam was produced by expanding iodobenzene vapor (70^0C, ~ 10 Torr) with He gas (~ 800 Torr) through a pulsed valve, and was skimmed before the intersection with the fs laser pulses in the extraction region of a TOF-MS. The pump laser pulse (275 nm) initiated the reaction and the probe laser pulse (304.7 nm), delayed in time, *resonantly* ionized the free I atom products through 2+1 REMPI. A discrimination aperture (5 mm diameter) is placed right in front of the MCP detector.

Different regions of the gas pulse were sampled by varying the time delay between the fs laser pulses and the pulsed valve opening. This allows for selective excitation of different cluster-size distributions without changing the beam conditions. Usually, the monomer dominates the leading edge of the gas pulse, whereas the central region of the gas pulse contains significant amount of large clusters, as shown in Figure 7.1 of mass spectra. This selective excitation is also supported by the dramatic differences in the I-atom velocity distributions and their temporal behaviors observed in these two regions of the gas pulse, as discussed below.

7.3. Results and Discussion

The first absorption band of iodobenzene (320-240 nm) is composed of two types of transitions: One is the (n, σ^*) excitation, localized along the C-I bond, and the other is

the (π, π^*) excitation of the benzene ring system.[11,12] The dissociation dynamics following excitation in this wavelength region is complicated by the severe spectral overlaps of these two transitions. The (n, σ^*) states are similar to those of the A-band continuum observed in alkyl iodides which lead to a direct dissociation of the C-I bond in less than 400 fs.[13] The (π, π^*) states are expected to exhibit predissociative behavior due to mixing with the isoenergetic (n, σ^*) states.

With the fs time-resolved KETOF technique, we have characterized the velocity distributions of I-atoms under the monomer condition at various delay times following the t=0 excitation in Chapter 3. The I^+ KETOF distributions have a narrow high-velocity distribution and a broad low-velocity one (Fig. 7.2(a)). Transients obtained by gating the high- and low-velocity distributions reveal markedly different temporal behaviors. The high-velocity I-atoms clearly exhibit a *coherent* wave packet motion manifested by the 400 fs delayed rise, consistent with the direct dissociation mechanism. Whereas, the low-velocity I atom transients are characterized by an exponential rise of about 600 fs, indicating an indirect predissociative process (Fig. 7.3.(a) and Fig. 7.4(a)).

When the fs lasers are moved from the leading edge toward the central region of the gas pulses, iodobenzene cluster ions gradually appear in the mass spectra (Fig. 7.1(b)). In the mean time, the I^+ KETOF distributions also gradually become less structured and finally turn into those shown in Fig. 7.2(b) when the fs laser pulses reach the central region of the gas pulse. Between the leading edge and the central region of the gas pulse, the KETOF distributions exhibit mixed characteristics of the two extreme conditions. The change in KETOF distributions is related to the iodobenzene clusters as it is clearly accompanied with the appearance of the cluster peaks in the mass spectra.

Fig. 7.2(b) shows the KETOF distributions observed in the cluster-rich region. The mass spectra observed in this region indicate that a broad distribution of iodobenzene clusters (n=2-8) is sampled. Comparison with the monomer KETOF distribution suggests that the monomer contribution is quite small. Also shown in the same figure is the dramatic temporal evolution of the KETOF distributions as the pump-probe delay time increases. Two distinct types of distributions are readily identified from this time-resolved KETOF experiment. One is a high-velocity bifurcated distribution similar in shape to the monomer KETOF distribution, but is broader and less structured. By gating the peak region of this distribution, while the pump-probe delay is scanned, we obtained transients that are dominated by this distribution. As shown in Fig. 7.3 (b), this cluster high-velocity distribution grows in rapidly and can be characterized by a *delayed* single exponential rise of 1.4 ps.

The similarities between this cluster high-velocity component and the monomer in terms of their velocity distributions and temporal behaviors suggests that some monomer-like "uncaged" I atoms are present in the clusters. These I-atoms dissociate from the clusters without direct interactions with the rest of the system, and are expected to result in a rapid escape and little translational energy loss. The velocity distributions, although less structured, clearly reveal that the averaged kinetic energy of the I-atoms released from the clusters is comparable to that from the monomer. This indicates that the initial kinematics does not change significantly for these uncaged I atoms and the gated signal is mostly due to the direct dissociation channel. The additional vdW potentials in the clusters are expected to decrease the available energy for the dissociation, consistent with

the slightly lower peak velocity (smaller splitting) observed in the cluster KETOF distributions.

The presence of the additional vdW potential also slows down the I-atom departure in time, as already shown for the dimer case in Sec. 6.2.2 of Chapter 6. In larger clusters (n>2), the uncaged I atoms are expected to be further slowed down because of the deeper vdW wells and different structures. We extrapolate that the delayed exponential rise of 1.4 ps observed in the cluster high-velocity I atom transient shown in Fig. 7.3(b) is an averaged result of several delayed rises originating from various sizes of clusters (n=2-8).

At long pump-probe delay times, an additional component is clearly observed in the KETOF distributions (Fig. 7.2(b)). Subtraction of the early time (~ 5 ps) distributions from the later ones reveals a Gaussian-like distributions centered at v_z=0. Transients obtained by gating this general region exhibit bi-exponential behaviors with the slower rise being as long as 365 ps (Fig. 7.4(b)). By analogy the initial fast rise (2.3 ps) is due to the predissociation of uncaged I atoms in the clusters following the (π, π^*) excitation. Again, the dissociation is slowed down because of the presence of the additional vdW potential. Nevertheless, the much slower rise of the Gaussian-like velocity distribution centered at v_z=0 is a strong indication that a very different form of I-atoms are also present in the clusters.

We consider this much slower component as evidence to "caged" I-atoms that immediately undergo collisions with other iodobenzene molecules following dissociation. A rough calculation shows that ~ 95% of the translational energy of an iodine atom can be lost by a single collinear collision with a point mass having the mass of an

iodobenzene molecule. Therefore, even though it may depend on the impact parameters, because of the finite size of the iodobenzene molecule, the collisional translational energy relaxation of the I-atom in the clusters should be facile. In larger clusters, these caged I atoms can be trapped for long periods of time, allowing the kinetic energy of the I-atoms to be distributed among the cage modes. The energy transfer can soften the solvent cage and leads to the escape of I atoms with very low kinetic energy. These qualitative descriptions in terms of the product velocity distribution and its temporal behavior are in complete accord with the cluster low-velocity distribution.

Upon reducing the degree of clustering, the slower component gradually decreases and its rise time becomes shorter. We have taken two low-velocity I-atom transients somewhere between the cluster-rich and the monomer/dimer regions and obtained rise times of 160 and 55 ps. At the leading edge of the gas pulse, the low-velocity I-atom transient becomes eventually identical to the monomer transient shown in Fig. 7.4(a). These observations indicate that the residence times of the caged I atoms are longer in larger clusters, consistent with the caging dependence on size. Moreover, they also suggest that the fraction of the caged I atoms increase with the cluster size. The latter conclusion provides important implications to the structures of the iodobenzene clusters.

The two structural forms of I atoms present in the iodobenzene clusters can be rationalized by the fact that the dispersive interaction between I-I, I-phenyl, and phenyl-phenyl are relatively strong and comparable. The relatively large dipole moment of iodobenzene[14] (~ 1.7 D) may also play an important role through electrostatic interactions. In an iodobenzene cluster of a certain size, some C-I bonds may point directly toward a phenyl ring or an I-atom, while some may not (Fig. 7.5). Isomeric

structures may also exist because of the comparable interaction energies between the three pairs mentioned above.

7.4. Conclusion

The results presented here demonstrate the usefulness of adding a new dimension (time) to translational spectroscopy. Reaction dynamics can be examined not only by the analysis of product kinetic-energy distributions but also by their temporal evolution for a specific velocity distribution.

The reverse method of gating at different times allows one to separate the dynamics of different structures. It was shown here that two structural forms of I-atoms are present in the iodobenzene clusters (n=2-8). The uncaged I-atoms exhibit slightly perturbed monomer-like dynamics and reflect the effect of the vdW forces to the departing fragments. On the other hand, the caged I atoms show dramatically different dissociation dynamics due to a caging structure. Such distinct structures have also been found in the theoretical study of HF in Ar.[9] Further theoretical studies of the molecular dynamics in different-sized structures are needed to compare with the experimental observations.

7.5. References

1. S.J. Riley and K.R. Wilson, Faraday Discuss. Chem. Soc. **53** (1972) 132.
2. A.M. Wodtke and Y.T. Lee, in: *Molecular Photodissociation Dynamics,* eds. M.N.R. Ashfold and J.E. Baggott (Royal Society of Chemistry, London, 1987).
3. J. Segall, Y. Wen, C. Wittig, A. Garcia-Vela and R.B. Gerber, Chem. Phys. Lett. **207** (1993) 504; C. Jaques, L. Valachovic, S. Ionov, E. Bohmer, Y. Wen, J. Segall and C. Wittig, J. Chem. Soc. Faraday Trans. **89** (1993) 1419.
4. M.A. Young, J. Chem. Phys. **102** (1995) 7925.
5. R. Ogorzalek Loo, G.E. Hall, H.P. Haerri and P.L. Houston, J. Phys. Chem. **92** (1988) 5.
6. J.A. Syage, Chem. Phys. Lett. **245** (1995) 605.
7. R. Alimi and R.B. Gerber, Phys. Rev. Lett. **64** (1990) 1453.
8. A. Garcia-Vela, R.B. Gerber, D.G. Imre and J.J. Valentini, Chem. Phys. Lett. **202** (1993) 473.
9. T. Schröder, R. Schinke, S. Liu, Z. Bacic and J.W. Moskowitz, J. Chem. Phys. **93** (1997) 1459.
10. P.Y. Cheng, D. Zhong and A.H. Zewail, Chem. Phys. Lett. **237** (1995) 399.
11. T.M. Dunn and T. Iredale, J. Chem. Soc. (1952) 1592.
12. A. Freedman, S.C. Yang, M. Kawasaki and R. Bersohn, J. Chem. Phys. **72** (1980) 1028.
13. J.L. Knee, L.R. Khundkar and A.H. Zewail, J. Chem. Phys. **83** (1985) 1996.
14. E.C. Hurdis and C.P. Smyth, J. Am. Chem. Soc. **64** (1942) 2212.

7.6. Figure Captions and Figures

Figure 7.1. TOF-MS spectra obtained in two regions of the gas pulse: (a) the leading edge and (b) central region of the gas pulse. In the *case a* spectrum, the 275-nm fs laser is used as the ionization laser. In the *case b* spectrum, the laser wavelength was tuned to 285 nm to minimize ionic fragmentation. The reduction of the monomer intensity in the *case b* spectrum is due to the lowering of the photon energy. The TOF-MS was optimized for the dimer in the spectra shown in the lower panel, but was optimized for larger clusters in the spectrum taken under the *case b* condition shown in the upper panel.

Figure 7.2. (lower panel) I^+ KETOF distribution arising from the dissociation of iodobenzene monomer at a pump-probe delay time of ~ 10 ps. (upper panel) I^+ KETOF distributions observed in the cluster-rich region (*case b*) of the gas pulse at various pump-probe delay times.

Figure 7.3. I-atom transients obtained by gating the high-velocity component of the I^+ KETOF distribution under the monomer (*case a*) and cluster-rich (*case b*) conditions. Note the different time scales in the two long-time transients.

Figure 7.4. I-atom transients obtained by gating the low-velocity component of the I^+ KETOF distribution under the monomer (*case a*) and cluster-rich (*case b*) conditions. Note the different time scales in the two long-time transients.

Figure 7.5. The sketch of the iodobenzene cluster structure, illustrating the two-type I atoms observed in the experiments.

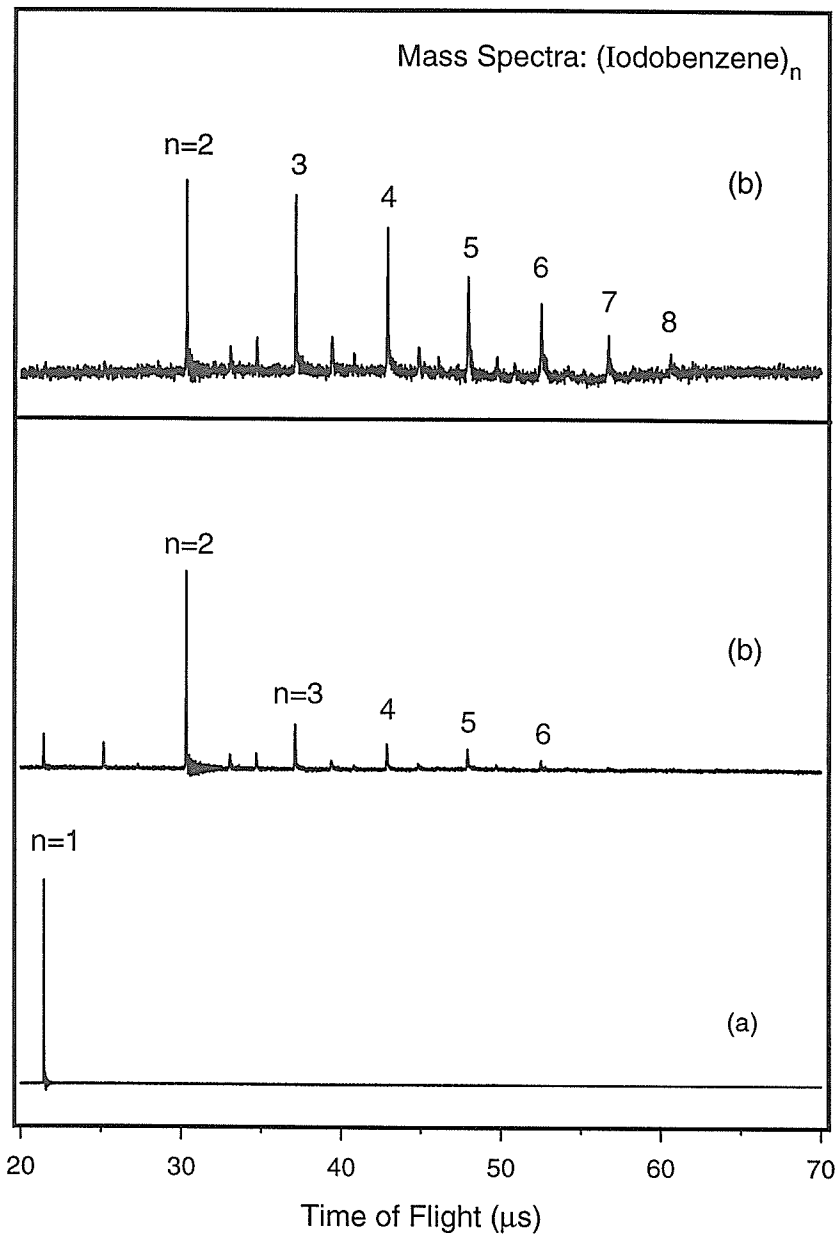
Mass Spectra: (Iodobenzene)n
n=2
3
4
5
6
7
8
(b)
n=2
n=3
4
5
6
(b)
n=1
(a)
20
30
40
50
60
70
Time of Flight (μs)

Figure 7.1

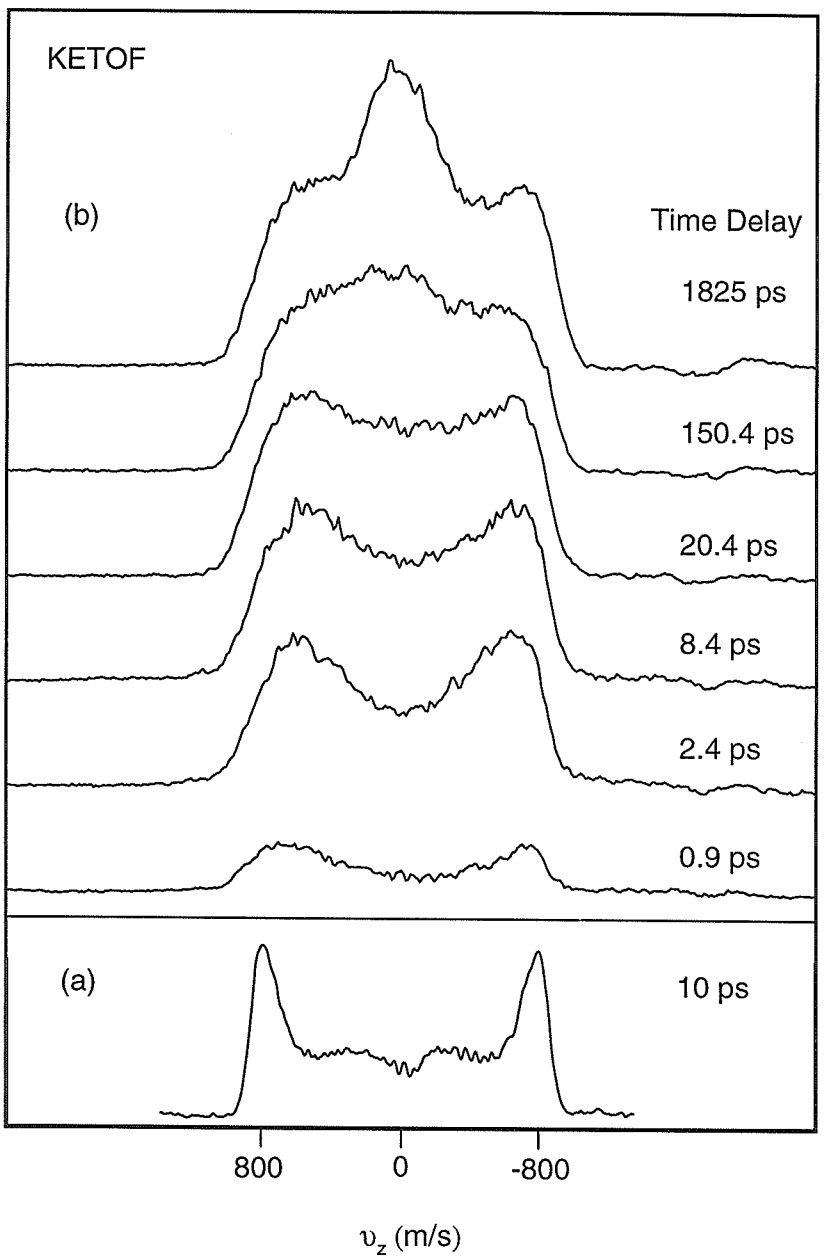
KETOF
(b)
Time Delay
1825 ps
150.4 ps
20.4 ps
8.4 ps
2.4 ps
0.9 ps
(a)
10 ps
800
0
-800
v_z (m/s)

Figure 7.2

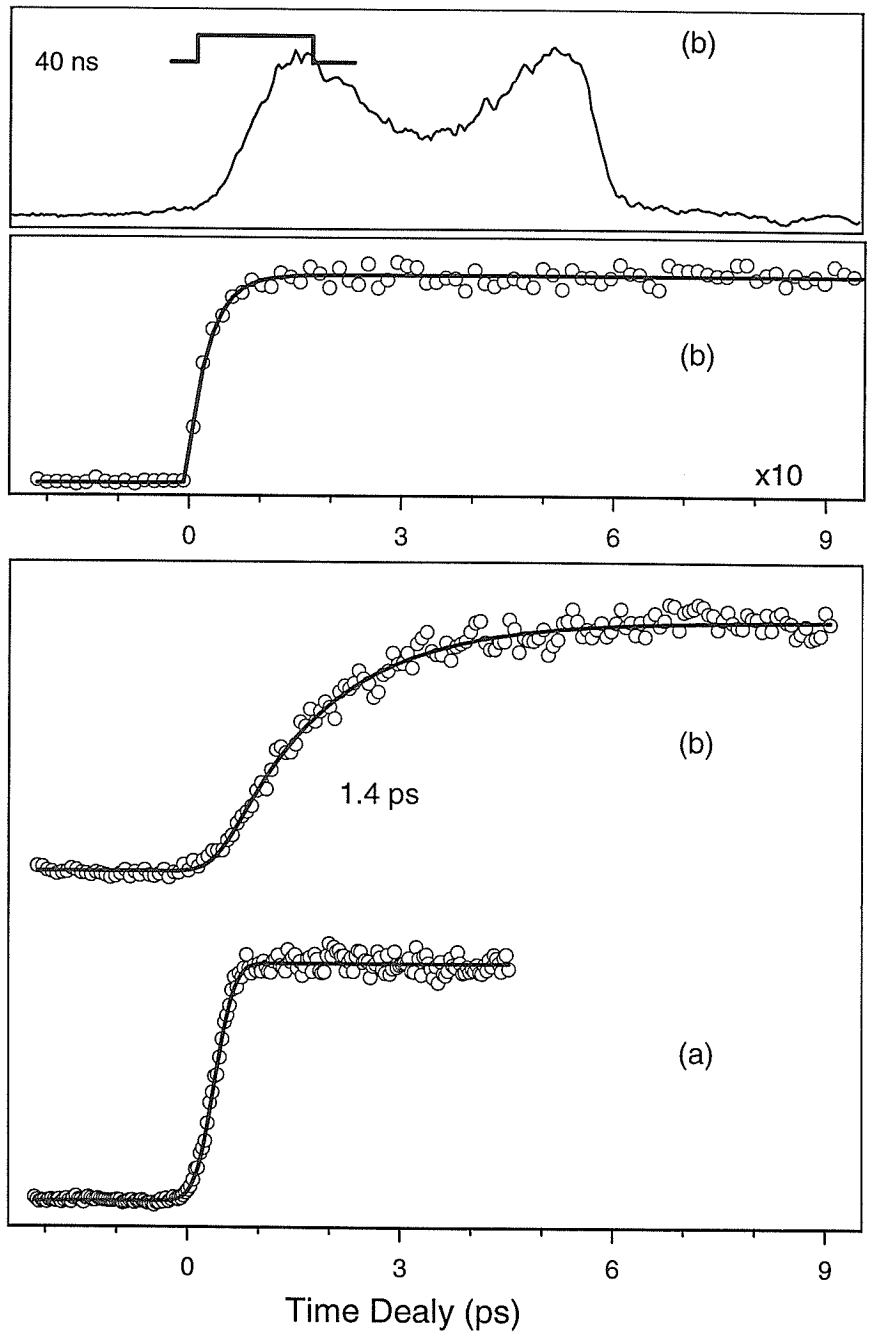

Figure 7.3

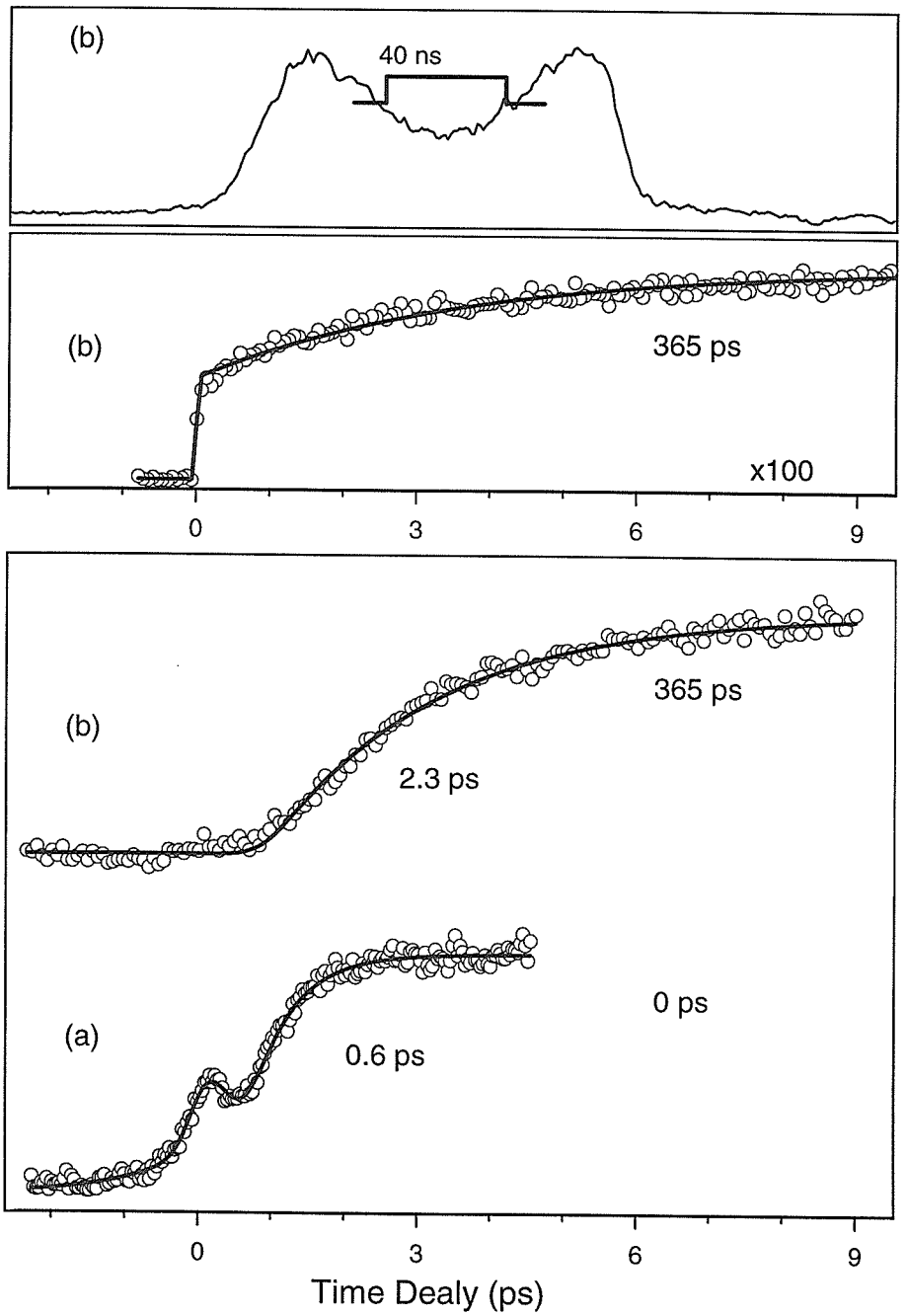
(b)
40 ns
(b)
365 ps
x100
0
3
6
9
(b)
365 ps
2.3 ps
(a)
0 ps
0.6 ps
0
3
6
9
Time Dealy (ps)

Figure 7.4

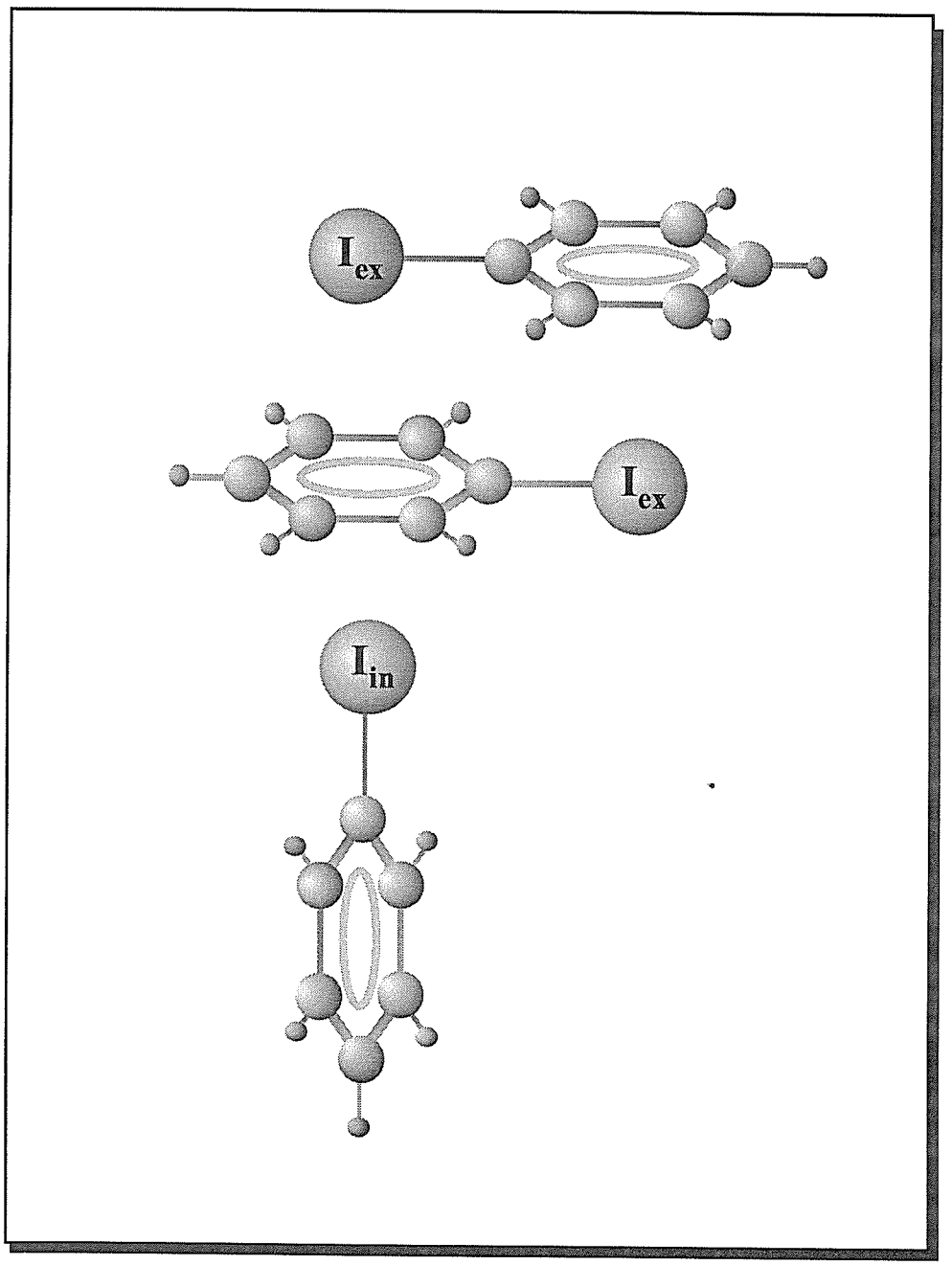

Figure 7.5

Chapter 8

Femtosecond Real-Time Probing of Nonradiative Dynamics: Transition States and Conical Intersections in Valence-Bond Isomers of Azines[‡]

[‡] Adapted from: D. Zhong, E.W.-G. Diau, T.M. Bernhardt, S.D. Feyter, J.D. Roberts and A.H. Zewail, Chem. Phys. Lett. **208** (1998) 129-140.

8.1. Introduction

Many chemical reactions having overall small energy changes are regarded as "forbidden" and have large energy barriers above the ground state. In the description of such reactions by the Woodward-Hoffmann rules, they exhibit unfavorable orbital symmetry correlations. The ground state of the reactants correlates with the excited state of the products, and vice versa. The barriers in such cases are, therefore, made by the "crossing" of two potential energy surfaces (PES) and the transition states are defined accordingly.

The crossing or near-crossing of PESs is a well-known problem in polyatomic molecules since the early work by Teller, Herzberg and others, and has become the subject of theoretical studies for many decades. In particular, the relevance of conical intersections (CI) to nonradiative relaxations and to photochemical and thermal reactions has been the focus of many articles and books [see, *e.g.*, refs 1-4, and references therein]. In all of these studies, one must consider the breakdown of the Born-Oppenheimer approximation as the nuclei make their nonadiabatic journey between reactants and products.

A classic problem, where conical intersections play a major role, is that of reactions involving the isomers of benzene and azines. Over a century, several valence structures for the ground state of benzene have been proposed: Kekulé, Dewar, Hückel (benzvalene type), Ladenburg (prismane type) and Thiele [see ref 5]. The well-established aromatic structures are represented by the electron-delocalized or resonance expression of the Kekulé formula, and isomers, such as the Dewar structures, have much higher energies. Thus, ground-state thermal reactions involve a high energy barrier to

reach any of the isomers. But, in addition, the conversion of benzene to Dewar benzene is formally considered as a disrotatory 4π-ring closure reaction, forbidden on the ground state. However, from the excited state it is possible to populate these isomers directly.

Experimentally, the exploration of the reaction dynamics is possible provided: (a) a wave packet is prepared in the reactant valley, prior to reaching the conical intersection, and (b) sufficient energy is supplied to cross over the forbidden region. Both requirements can be satisfied by femtosecond-resolved mass spectrometry as developed in this laboratory for studies of complex reactions.[6]

In this Chapter, we report studies of pyridine and its possible high-energy isomers, such as one of the two Dewar structures:

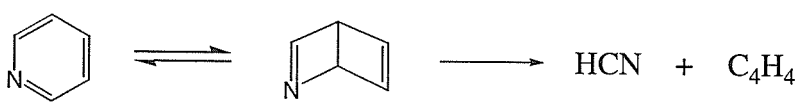

The energy change in this isomerization for one thing involves dearomatization, the loss of ~ 40 kcal/mol of resonance energy. Then, the net of making of σ and π bonds and breaking of two π bonds is expected to be –20 kcal/mol. Account must also be taken of strain energy of ~50 kcal/mol. Thus, as will be shown below, the overall energy of the pertinent Dewar structure would be ~70 kcal/mol above that of aromatic pyridine. The ring opening reaction of pyridine involves the C-N bond breakage (~70 kcal/mol); in contrast, C-C bond breakage requires ~85 kcal/mol.

By using femtosecond pulses, together with the mass spectra, we are able to observe the wave packet motion and examine the molecular changes involved in the isomerization. The crucial role of conical intersections (Figure 8.1) and their influence on the nonradiative processes are elucidated. In order to compare the experimental and

theoretical results of structures and rates, we have carried out DFT/*ab initio* calculations at G2M level. For comparison, we also studied other azines, namely, pyrimidine, triazine, and substituted (deuterium and methyl) pyridines. All these studies were made at total energies of 99 to 103 kcal/mol. At a higher energy (186 kcal/mol), we were able to study the ring-opening process.

8.2. Experimental

All experiments were performed in a two-chamber molecular beam apparatus integrated with femtosecond (fs) laser systems and a time-of-flight (TOF) mass spectrometer. For experiments at 277 nm (and 282 & 288 nm) excitation, a synchronously pumped dye laser was used. For the study of two-photon excitation of pyridine at 307 nm, we employed a colliding pulse mode-locked ring dye laser (CPM). The details of both fs laser systems have been previously described.[6] Typically the pulse width from the CPM is 90 fs and from the other system is 300 fs. All experiments were done for the monomer beam condition,[7] and all samples were purchased from Aldrich (purity ~99%). Care was taken in the analysis of all transients by scanning each for three different time scales. For example, for pyridine, three scans were made: short (~12 ps); intermediate (~40 ps) and long (~100 ps). This way we were able to determine accurately and with consistency the time constants and the amplitude of each component.

8.3. Theoretical Calculations

Calculations of the PES for the isomerization reaction path were performed at G2M(RCC6) level of theory.[8] First, the geometries of the pyridine molecule, isomers,

transition states and products were optimized at the B3LYP/6-311G(d,p) level. Then, vibrational frequencies of all species were calculated at the same level of theory in order to characterize the nature of the stationary points, determine the zero-point energy correction for the PES, and calculate the statistical (RRKM) microcanonical reaction rates. Second, a series of high-level *ab initio* calculations was carried out at the MP4/6-311G(d,p), CCSD(T)/6-31(d,p), and MP2/6-311+G(3df,2p) levels of theory. An additive scheme was implemented to determine more reliable energies using the modified Gaussian-2 (G2M) method to approximate the CCSD(T)/6-311+G(3df,2p) calculation.

The DFT/*ab initio* results are shown in Figure 8.2 and scheme 8.1. Because of the presence of nitrogen, the Hückel, Dewar and Ladenburg structures have three, two and one isomers, respectively. Two Dewar (D_1 and D_2) isomers lie at energies of 69 and 78 kcal/mol above the aromatic Kekulé structure (0 energy). The three Hückel (H_1, H_2 and H_3) isomers have energies of 62, 67 and 82 kcal/mol, respectively. The H_1 isomer has the lowest energy among all isomers and the Ladenburg isomer has the highest energy, 112 kcal/mol. On the isomerization pathway, the D_1 structure has the lowest isomerization barrier of 90 kcal/mol and the D_2 isomer has a higher barrier of 106 kcal/mol. The H_1, H_2 and H_3 isomers have barriers of 92, 94 and 101 kcal/mol, respectively. For the Ladenburg isomer, the barrier is the highest, 152 kcal/mol. On the decomposition side of the isomers, the D_1 structure has the lowest barrier, 111 kcal/mol, to form HCN and 1,3-cyclobutadiene, and all others have barriers of more than 115 kcal/mol. From our calculations, we can identify the structure of the transition state as having a "diradical" character for isomerization to the Hückel and to the Dewar. The structure of the transition state for the isomerization to the Hückel is similar to that what has been called

prefulvene,[9,10] but we have found that the TS in the lowest-energy path involves a twisted (five-atom nonplanar) geometry. The Hückel (benzvalene type) can also form tetrahedron C_4H_4 and HCN but this decomposition will involve a high-energy barrier.[11]

Similar DFT calculations were carried out for 2,6- and 3,5-dimethylpyridines at the B3LYP/6-31G(d) level. For pyridine-d_5, only the calculated zero-point energy was different from pyridine. We also made calculations for pyrimidine. For the ring-opening reaction of pyridine, the PES was calculated at the spin-unrestricted B3LYP/6-311G(d,p) level of theory because of the formation of an open-shell species, the ring-opened diradical intermediate.[12] All electronic structure calculations reported here were performed using G94 and G98 (Gaussian) packages.

8.4. Results and Discussion

The mass spectrum and transients are shown in Figures 8.3 and 8.4. The mass spectrum for pyridine (Fig. 8.3) only shows two peaks: the dominant parent (79 amu) and the C_4H_4 (52 amu). Transients were obtained for the individual mass peaks. For 277 nm excitation, the results are striking and exhibit both fs and ps dynamical processes. The C_4H_4 ion signal shows the same transient (not shown) as the parent, indicating its origin from the parent ion fragmentation. When the wavelength was changed to 282 nm, we observed similar behavior to the 277-nm case. For 288 nm excitation, *i.e.*, below the S_1 transition, the transient signal disappears, indicating the one-photon nature of the excitation to the well-known $^1n\pi^*$ transition [see, *e.g.*, refs 13,14]. This is confirmed by the lack of change of the general transient shape for pyridine when the pump energy (<5μJ) was attenuated by a factor of 2-3.

The total available energy in our experiment is 103 kcal/mol. Accordingly, only the isomerization pathways are possible (see Fig. 8.2). The transients exhibit a fast decay component of 400 fs and slower ones of 3.5 and 15 ps. All of the pyridine derivatives and deuteropyridine studied exhibit similar behavior, but the time constants increase (see Fig. 8.3 and 8.4). As discussed in Sec. 8.4.3, the non-aromatic structures are formed through the CI in less than 400 fs, and the time scales observed here are much shorter than the known spectroscopic lifetimes. In what follows, we discuss three major features of this work.

8.4.1. Dynamics of Dewar, Hückel and Other Structures

Among all isomers only D_1 and H structures allow for isomerization at our total energy of 103 kcal/mol (Fig. 8.2) and these are the isomers that give rise to the transient behavior. However, for all molecules studied, we observed a 10-25% non-decaying component on the ps time scale. This component reflects the contribution from the molecules on the upper surface that miss the conical intersection region and stay in the local minima of the S_1 or T_1 state (Sec. 8.4.3).

The Dewar and Hückel isomers are structurally different from the aromatic Kekulé structure, but they have the same mass. On rearomatization, they isomerize to a highly vibrationally excited pyridine and the effective ionization cross section becomes very small. The reverse process occurs on a much longer time scale in the μs to ms range because the barrier is very high. Accordingly, the observed decay components of the parent signal in the ps range directly reflect the isomerization rates from the distinct Dewar- and Hückel-type structures to the excited aromatic Kekulé structure. Note that the

Ladenburg structure can not be prepared at the available energies and neither is there enough energy to achieve any of the ring-opening processes (Fig. 8.2).

For pyridine-h_5, the transient in the ps range gives two apparent decay components, the 3.5 and 15 ps. From the DFT/*ab initio* calculations of the equilibrium energies and transition states, the faster decay is from the D_1 structure and the slower decay is from the H structures. Using our force field calculations, we obtained the total density and number of states and, thus, the statistical microcanonical rates. The RRKM calculations give the rates for the isomers in the ns range (1 ns for D_1, 29 ns for H_1, 17 ns for H_2 and 43 ns for H_3). The statistical RRKM rates differ from the experimental ones by three orders of magnitude. This is expected because, as discussed elsewhere,[15] the conical intersection is highly directional and on the fs time scale only selected vibrational modes are populated (non-statistical).[16] However, it is interesting to note that the calculations indicate the two distinct time scales of D and H isomers and give the order of magnitude trend for the ratios.

For pyridine-d_5, the overall decay clearly becomes slower (Fig. 8.3A). For D_1 upon deuteration, the decay time of 3.5 ps increases to 5.1 ps, and for the H isomers the time is nearly the same, ~16 ps. The statistical calculations predict that both reaction times should lengthen by a factor of 3 (4) for D_1 (H_1), contrary to the observed almost doubling of the reaction time for D_1 and almost lack of change for H. This reflects difference in the motion of nuclei to form the transition states during the isomerization process. For the Dewar structure, all five deuterium atoms are involved in the bending motions at the transition state, but for the Hückel structure the C-C twisting is relatively localized and only two deuterium atoms participates effectively.

Methyl-group substitutions similarly lead to slower dynamics (Fig. 8.4A). From our DFT calculations, we find that methyl groups located on a double bond stabilize the isomer equilibrium structure. The D_1 isomers for 2,6- and 3,5-lutidine are stabilized by 3-4 kcal/mol, relative to pyridine. For both molecules, the isomerization barrier increases by 1-2 kcal/mol. Therefore, the reaction rates are expected to decrease, and the RRKM calculations give a reaction time in the 20-30 ns range as compared to 1 ns for the unsubstituted molecule. Experimentally, we obtained a reaction time of 10 ps for 2,6-lutidine and 6.5 ps for 3,5-lutidine, 3 to 2 times slower than pyridine. The reaction rate of 2,6-lutidine is slower than that of 3,5-lutidine because the barrier for the former is a little higher.

For the H_1 structure, the stabilization energy for 2,6- and 3,5-lutidine is ~1-2 kcal/mol. For 2,6-lutidine, the reaction barrier increases by ~1 kcal/mol, but it decreases by ~1 kcal/mol for 3,5-lutidine. The transition state for 3,5-lutidine is looser than that of 2,6-lutidine and has more low-frequency modes. The RRKM calculation predicts rate ratios of 80 times slower for 2,6-lutidine, but only 10 for 3,5-lutidine. Experimentally, we observed a ratio of 33/3.5 ~10 for 2,6-lutidine, in the correct direction. For 3,5-lutidine, the long-decay component is not present, consistent with the predicted decrease of the ratio from 80 to 10 which will give time on the order of 6 ps. The reaction rates of 3,5-lutidine for both D and H structures are nearly the same, even though the Hückel isomer is more stable by ~5.5 kcal/mol and has a higher reaction barrier by ~6.5 kcal/mol. This can be ascribed to the loose nature of the transition state.

The general picture seen from the studies of pyridine was extended to other azines. For pyrimidine and triazine, the measured times are 113 ps and 106 ps,

respectively. The fs decay component is actually faster than pyridine, 200 fs (Fig. 8.4B). Our DFT calculations show that the isomers of pyrimidine have similar energies and barriers as those of pyridine. Because of the observation of the early fs dynamics of the wave packet, the long ps components arise from the isomerization, similar to that of pyridine. However, because in the case of pyrimidine, the time is 30-fold longer than pyridine we must also include the spectroscopic lifetimes, which are ~100 ps at our energies.[17] For triazine, the reported results (277 nm or longer) suggest no or little direct fragmentation into 3HCN, indicating that the recent photodissociation studies of translational energy distributions by the Huber group[18] may result from two-photon excitation.

8.4.2. The Ring Opening and Fulvene Channels

At the energy of 186 kcal/mol, the dynamics are drastically different although the mass spectrum is the same as that for 277-nm excitation. At the available energy of 193 nm (148 kcal/mol), the Lee group[11,19] observed several additional fragmentation channels, with the HCN plus C_4H_4 (believed to be 1,3-cyclobutadiene) being the major one.

The transient of mass 79 decays in 80 fs while that of mass 52 builds up in 80 fs and then disappears in 130 fs (Fig. 8.3B). Because the one-photon energy is below the S_1 transition, the results are from the two-photon excitation. The power dependence of the pump shows a close to quadratic behavior. The difference of the transients observed at 79 amu and 52 amu indicates that the signal at 52 amu is not due to ion fragmentation. The signal describes the dynamics of ring opening. The comparable times of the parent decay

and the diradical fragment rise reveal that the fragment formation is directly related to the disappearance of the parent.

According to the DFT calculations in Sec. 8.3, ring opening of pyridine requires ~110 kcal/mol to overcome the resonance energy and to break one C-N bond. This diradical (mass 79), originally in the "gauche" configuration, actually is near the energy of the trans geometry (Fig. 8.2A). To eliminate HCN and form the cis or trans butadienyl diradical (mass 52), the molecule requires another ~30 kcal/mol, breaking one C-C bond and forming a triple C-N bond. Thus, this transient species is formed in ~80 fs and then evolves in 130 fs to form the final products (Fig. 8.2A): two acetylenes by C-C bond breakage; 1,3-cyclobutadiene by C-C bond closure; vinylacetylene by one hydrogen migration; and/or butatriene by a two-hydrogen migration.

It should be noted that there are three fulvene-type isomers and the most stable structure has an energy of 23.5 kcal/mol, predicted at the G2M level of theory. However, in order to form a fulvene-type isomer from the aromatic Kekulé and Hückel structures, the molecule needs to cross over a high energy barrier and this process involves the carbene (or nitrene) and/or prefulvene type of intermediates. Those intermediates lie at an energy of 102-112 kcal/mol based on the unrestricted DFT predictions.

8.4.3. Wave-packet Motion: Into the Conical Intersection

Following the fs laser preparation (Fig. 8.1), the packet, whose vibrational composition depends on the total energy, proceeds with two different types of *trajectories*; the reactive ones which go through the intersection region ("funnel") and the unreactive which are trapped in the "spectroscopic" well. Accordingly, within the

bending vibrational motion (1/ν~80 fs), the valence structure is distorted and vibrationally hot isomers are formed. However, the initial energy is deposited in the optically-allowed modes and energy must redistribute to other modes for the molecule to reach the intersection. This IVR process takes hundreds of fs. The nuclear bending and twisting motions are critical in making the "forbidden" isomers. As the molecule bends or twists in the ground state, the energy rises because the motion is accompanied by strain and loss of the resonance energy--then new bond formation contributes to the total energy (see above). Concurrently, the upper surface lowers its energy (directly or through a barrier) as the molecule distorts its original structure, resulting in CI(s).[15,9]

The observed 200-700 fs component in all systems reported here reflects the initial displacement of the wave packet and IVR in the reactive channel. For pyridine-h_5 and -d_5, this takes ~400 fs. The decay time is not significantly different for both molecules because the bending and twisting motions, not the C-H motions, are mainly involved in the transformation; the excess energy in S_1 is ~1260 cm^{-1} (3.6 kcal/mol), much lower than the C-H(D) frequency. For the 2,6-, 3,5-dimethyl, the process slows down to ~650 fs (Fig. 8.4A). This is consistent with the fact that, on methylation, a blue shift takes place[20] and the available vibrational energy decreases. Also, the total number of vibrational degrees of freedom increases. On the other hand, for pyrimidine and s-triazine, the process becomes faster, ~200 fs (Fig. 8.4B), and this is because the S_1 state is red shifted, relative to pyridine, and the molecule (even with less vibrational modes) has more excess energy.

Evidence for the "bifurcation" of the wave packet motion comes from the following observations. First, our observed decay times in pyridine are much shorter than

all reported times of fluorescence and internal conversion; 0.4-15 ps as opposed to 30-60 ps.[17] As shown by Yoshihara's group,[17] the rates display an abrupt change with (small) excess vibrational energy; they suggest the importance of the isomerization channel of benzvalene form. Second, the effect of methyl substitution on the observed rates is contrary to that observed for fluorescence in azines. As shown by Lim and coworkers,[21] the proximity of the $n\pi^*$ to the $\pi\pi^*$ state leads to an enhanced internal conversion. Upon methylation, this conversion increases (not decreases) because of the decreased $n\pi^*$-$\pi\pi^*$ energy gap (~1800 cm^{-1} for 2,6-lutidine as opposed to 3600 cm^{-1} for pyridine[20]) and hence an increased overlap of wave functions S_1/S_0. In pyrazine, *e.g.*, the nonradiative rate increases considerably upon methylation.[21]

Third, all molecules studied show an underlying absorption continuum and some sharp bands; even in supersonic beams such continua do exist as shown in the careful study by Villa *et al.*[22] This indicates that the wave packet motion is recurring in certain vibrational coordinates,[23] but ultrafast dynamics due to the reactive channel must be part of the description. Even in three-atom systems, bifurcation of the wave packet from the transition state to final products is a general phenomenon due to the initial momenta and energy content of the packet.[24,7] It is interesting to note that the continuum absorption is present in many azines (Fig. 8.5) and that, in fact, the larger the sharp-band component, the more the non-reactive trapping. Spectral congestion is not the dominant factor, especially at higher energies. Note that excitation spectra would not display features of the continuum and that nanosecond pulse excitation will bias the process to a much less continuum excitation. Finally, our measurement of the transients with different polarizations did not result in a significant change in the time constants, consistent with

our picture; the inertial decay should be several ps. The above results are in agreement with product yield and species analysis.[25,26] They are also entirely consistent with photochemical experiments from Michl's group[27] involving the excitation of Dewar naphthalene and the conversion to naphthalene.

In concluding this section, we emphasize that elucidating the time scales observed for the different processes studied is the key for understanding the mechanism. We believe that such reactive pathways are general and important to many nonradiative processes in polyatomics. Bend motions promote the vibronic coupling as reported by Ito's group,[28] and the valence distortion is evident in the studies of the spectroscopy (see the discussion in ref. 22 for earlier relevant work, and ref. [29] for showing the quasiplanarity in S_1). As shown in Fig. 8.1, the degree of distortion is linked to the branching of trajectories; when the distortion reaches outside the bound region, the reactive trajectories through CI dominate. The cases studied here show that lack of chemical fragmentation may lead to erroneous conclusion about the absence of CI-induced nonradiative return to the ground state and that the yield of products[30,31] has to be examined carefully. As such, our findings are relevant to the mysterious channel-3 process of benzene [see refs: 10, 9 and 32]. The fs initial reaction preparation is a key to observing the ultrafast nonadiabatic processes through the conical intersection.[15,33]

8.5. References

1. M. Klessinger and J. Michl, *Excited states and photochemistry of organic molecules* (VCH, New York, 1995), and references therein.
2. F. Bernardi, M. Olivucci and M.A. Robb, Pure & App. Chem. **67** (1995) 17.
3. W. Domcke and G. Stock, Adv. Chem. Phys. **100** (1997) 1.
4. D.R. Yarkony, Acc. Chem. Res. **31** (1998) 511.
5. Y. Kobayashi and I. Kumadaki, Top. Curr. Chem. **123** (1984) 103.
6. A.H. Zewail, *Femtochemistry-ultrafast dynamics of the chemical bond* (World Scientific, Singapore, 1994), and references therein.
7. D. Zhong and A.H. Zewail, J. Phys. Chem. A **102** (1998) 4031, and references therein.
8. A.M. Mebel, K. Morokuma and M.C. Lin, J. Chem. Phys. **103** (1995) 7414.
9. A.L. Sobolewski and W. Domcke, Chem. Phys. Lett. **180** (1991) 381.
10. B.R. Smith, M.J. Bearpark, M.A. Robb, F. Bernardi and M. Olivucci, Chem. Phys. Lett. **242** (1995) 27.
11. K.A. Prather and Y.T. Lee, Isr. J. Chem. **34** (1994) 43.
12. A.A. Scala, E.W.-G. Diau, Z.H. Kim and A.H. Zewail, J. Chem. Phys. **108** (1998) 7933.
13. A. Bolovinos, P. Tsekeris, J. Philis, E. Pantos and G. Andritsopoulos, J. Mol. Spectrosc. **103** (1984) 240.
14. I.S. Walker, M.H. Palmer and A. Hopkirk, Chem. Phys. **141** (1989) 365.
15. E.W.-G. Diau, O.K. Abou-Zied, A.A. Scala and A.H. Zewail, J. Am. Chem. Soc. **120** (1998) 3245.

16. E.W.-G. Diau, J.L. Herek, Z.H. Kim and A.H. Zewail. Science **279** (1998) 847.

17. I. Yamazaki, T. Murao, T. Yamanaka and K. Yoshihara, Faraday Discuss. Chem. Soc. **75** (1983) 395.

18. T. Gejo, J.A. Harrison and J.R. Huber, J. Phys. Chem. **100** (1996) 13941.

19. J.D. Chesko and Y.T. Lee, in: *Highly Excited Molecules*, eds. A.S. Mullin and G. Schatz (ACS, Washington, DC, 1997), p107.

20. I. Yamazaki, K. Sushida and H. Baba, J. Chem. Phys. **71** (1979) 381.

21. E.C. Lim, Adv. Photochem. **23** (1997) 165, and references therein.

22. E. Villa, A. Amirav and E.C. Lim, J. Phys. Chem. **92** (1988) 5393.

23. R. Schinke, *Photodissociation Dynamics* (Cambridge, New York, 1993).

24. K. Möller and A.H. Zewail, Chem. Phys. Lett. **295** (1998) 1.

25. O.L. Chapman, C.L. McIntosh and J. Pacansky, J. Am. Chem. Soc. **95** (1973) 614.

26. D.E. Johnstone and J.R. Sodeau, J. Phys. Chem. **95** (1991) 165.

27. S.L. Wallace and J. Michl, in: *Photochemistry and Photobiology*, ed. A.H. Zewail, Vol. II (Harwood, Chur, Switzerland, 1983), p1191.

28. Y. Mochizuki, K. Kaya and M. Ito, J. Chem. Phys. **65** (1976) 4163.

29. J.P. Jesson, H.W. Kroto and D.A. Ramsay, J. Chem. Phys. **56** (1972) 6257.

30. K.E. Wilzbach and D.J. Rausch, J. Am. Chem. Soc. **92** (1970) 2178.

31. E. Ratajczak, B. Sztuba and D. Price, J. Photochem. **13** (1980) 233.

32. A.L. Sobolewski, C. Woywod and W. Domcke, J. Chem. Phys. **98** (1993) 5627.

33. S.A. Trushin, W. Fuβ, T. Schikarski, W.E. Schmid and K.L. Kompa, J. Chem. Phys. **106** (1997) 9386.

8.6. Figure Captions and Figures

Figure 8.1. Schematic representation of the two potential energy surfaces, illustrating ground-state reactions reached through conical intersections. The wave packet and its reactive and non-reactive trajectories are displayed. No recurrences on the upper surface are shown for simplicity.

Figure 8.2. Ground-state Density Functional Theory/*ab initio* calculations. (A) The energetics and abbreviation of several possible valence-bond pyridine isomers as indicated. The related energy barriers have also been displayed. The values shown here are the G2M energies except those for the ring opening channel which were obtained at the UB3LYP/6-311G(d,p) level. The energy of the ring-opening "gauche" structure (non-optimized geometry shown in bracket) is close to that of the trans structure. Two excitation energies (E) are indicated by thick dashed lines. The transition state structures for some species are shown in scheme I. For discussion of other products and fulvene, see text for details. (B) Two different reaction pathways for the Kekulé structure to form two Dewar isomers through the bending motion. The dissociative process for both reactions involves a higher energy barrier, see text.

Figure 8.3. (A) Transients of pyridine-h_5 and -d_5 (277 nm excitation) at short- and long-time ranges. A 10-20% non-decaying component (not shown) was present in the transients. (B) Mass spectrum of pyridine with fs laser ionization. The mass spectra are similar for both 277 nm and two-photon 307-nm excitation, and the parent signal is

dominant. Transients (307/2 nm excitation) are shown for the 79 and 52 masses. Note the difference in time scale between (A) and (B).

Figure 8.4. (A) Transients obtained for 2,6- and 3,5-lutidine on short- and long-time scales. A 10-20% non-decaying component (not shown) was present in the transients. (B) Comparison of transients for different nitrogen substitution, pyridine, pyrimidine and triazine on the long and short time scales.

Figure 8.5. Gas-phase absorption spectra of pyridine, pyrazine, pyrimidine and triazine (adapted form reference 13). Indicated in the spectra are the $S_1 \leftarrow S_0$ (0-0) transitions and the experimental excitation wavelengths used in the present investigation. The two-photon 307-nm excitation of pyridine is not shown here. For pyrazine, the spectrum beyond 4.1 eV was reproduced, according to ref 13, and at 277 nm excitation the absorption is not enough to give strong transients although we did observe the mass spectra, primarily from the probe pulse (304 nm; 4 eV).

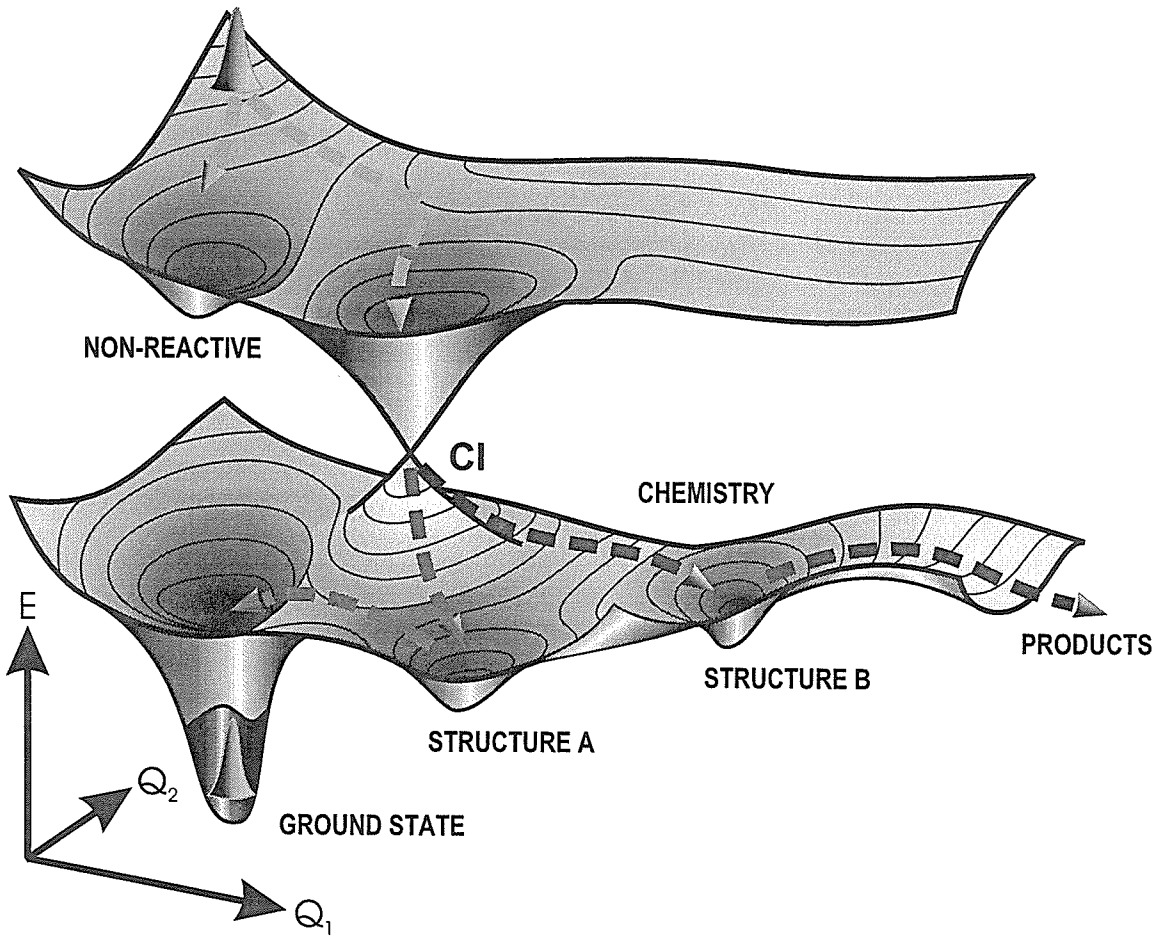
NON-REACTIVE
CI
CHEMISTRY
E
PRODUCTS
STRUCTURE B
STRUCTURE A
Q_2
GROUND STATE
Q_1

Figure 8.1

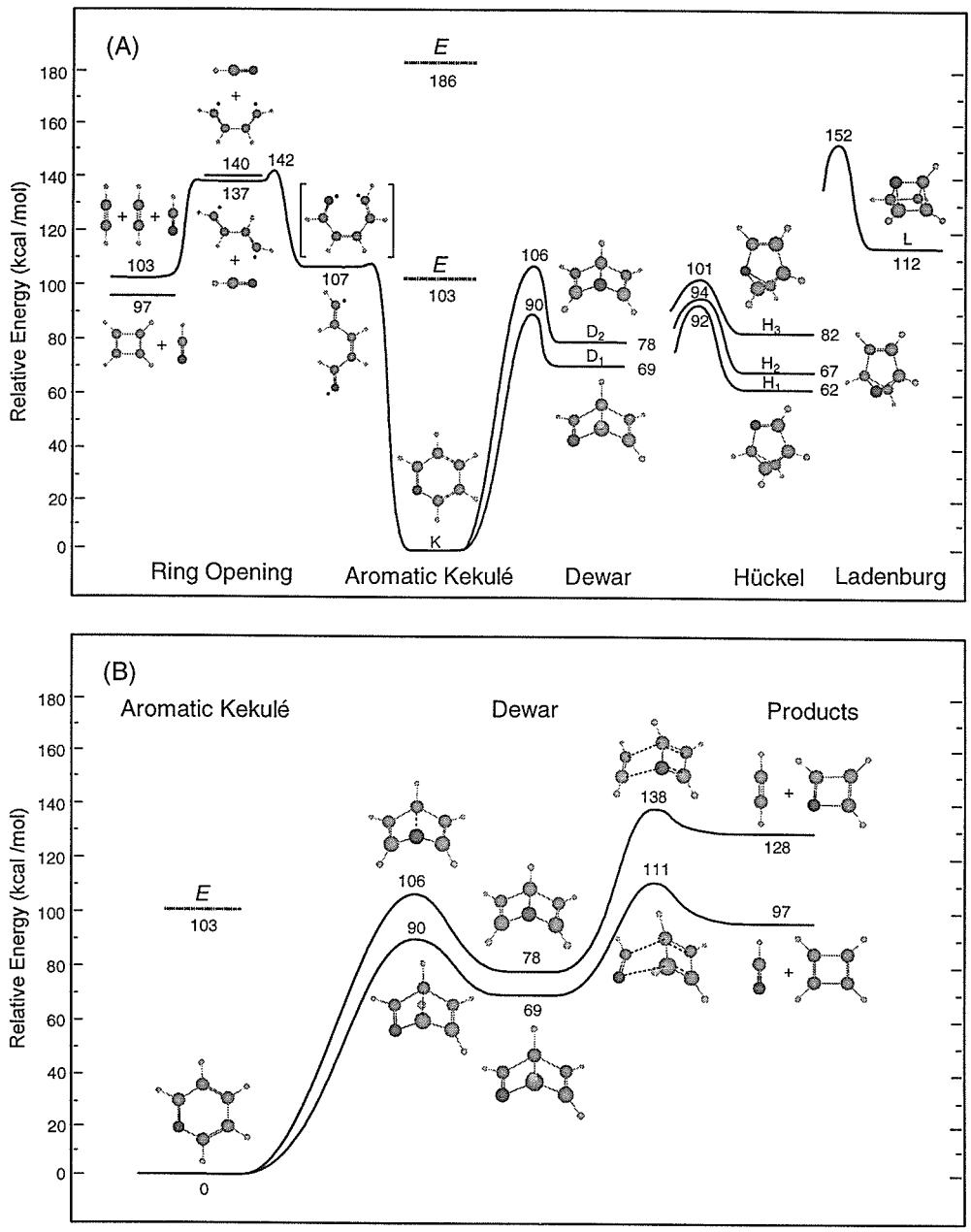
(A)
Relative Energy (kcal /mol)
180
160
140
120
100
80
60
40
20
0
E
186
103
97
140
142
137
107
E
103
106
90
D2
D1
78
69
101
94
92
H3
H2
H1
82
67
62
152
L
112
K
Ring Opening
Aromatic Kekulé
Dewar
Hückel
Ladenburg
(B)
Aromatic Kekulé
Dewar
Products
E
103
106
90
78
69
138
111
128
97
0

Figure 8.2

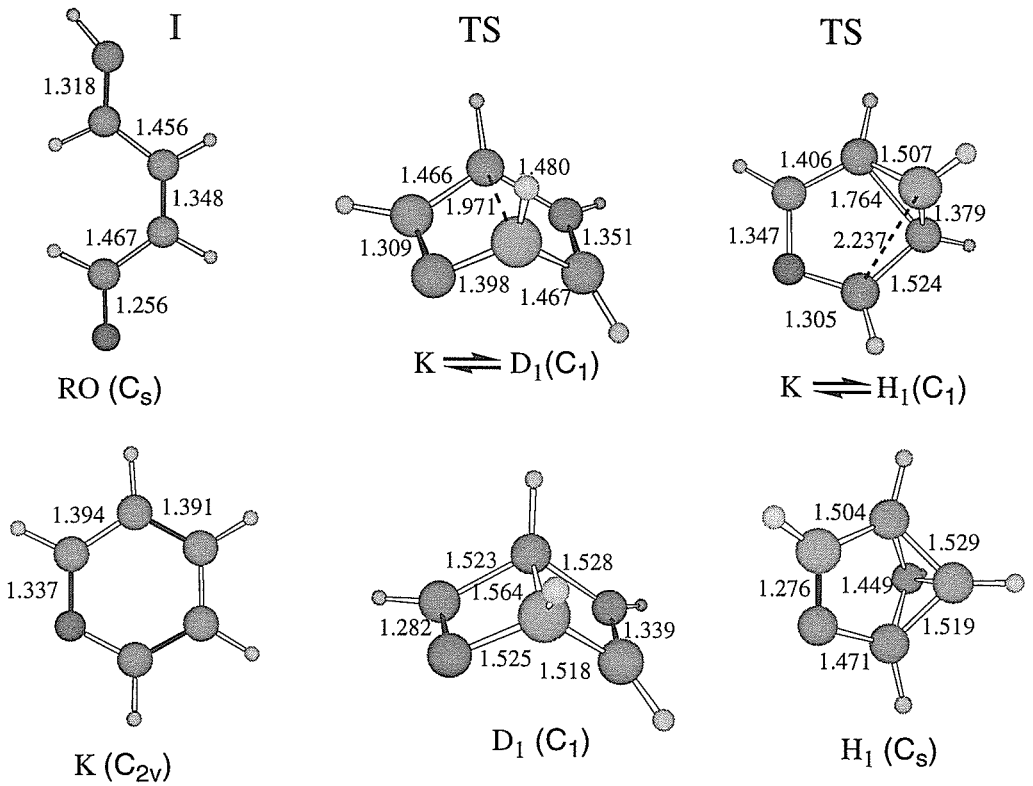

Scheme 1 : Structures of transition states (TS), intermediate (I) and isomers obtained from our DFT calculations for some of the reaction paths of Fig. 2. K stands for aromatic Kekulé; D for Dewar; H for Hückel; and RO for ring opening. Double bonds are indicated by solid lines.

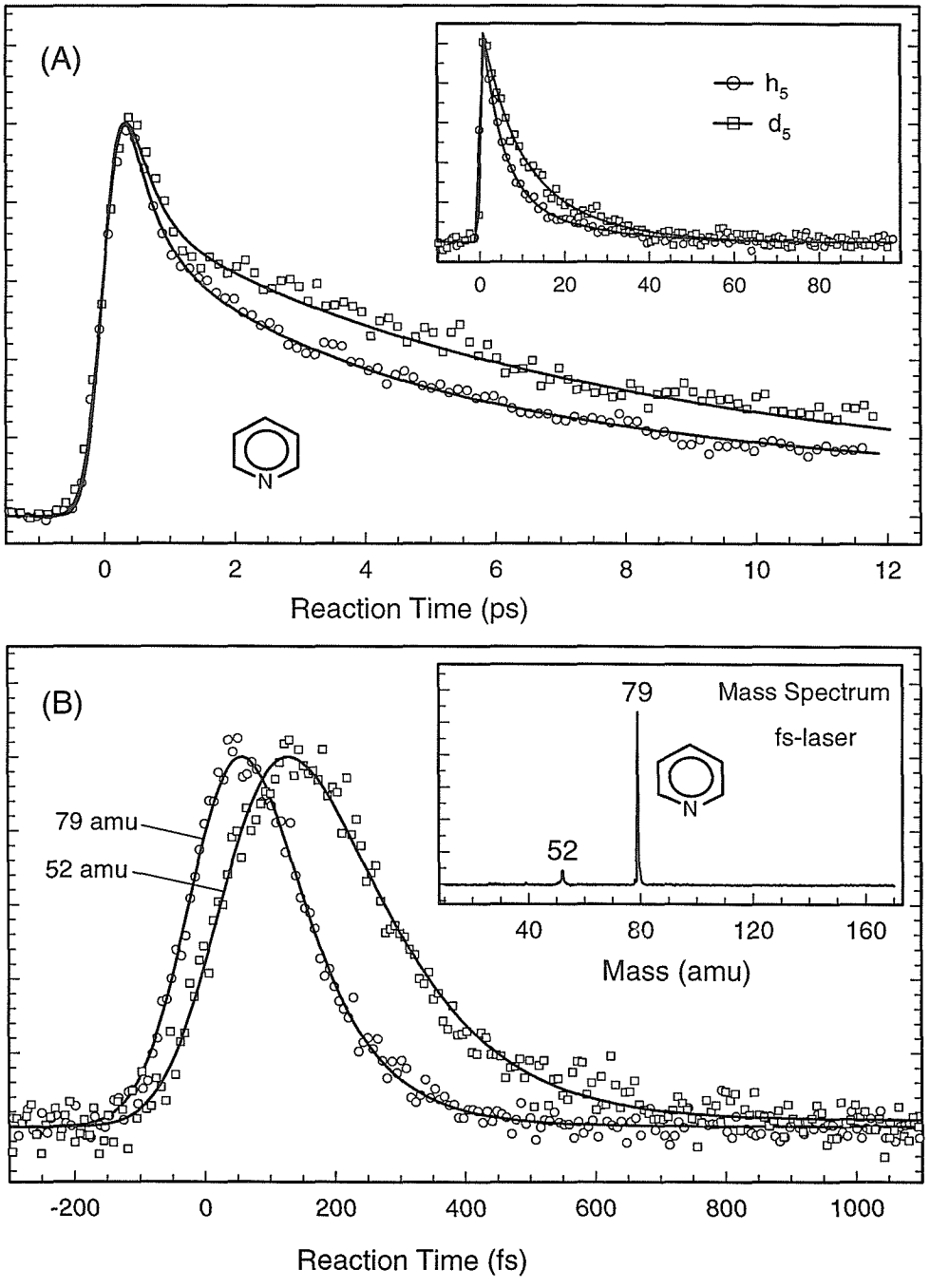
(A)
h5
d5
0
20
40
60
80
N
0
2
4
6
8
10
12
Reaction Time (ps)
(B)
79 amu
52 amu
79
Mass Spectrum
fs-laser
N
52
40
80
120
160
Mass (amu)
-200
0
200
400
600
800
1000
Reaction Time (fs)

Figure 8.3

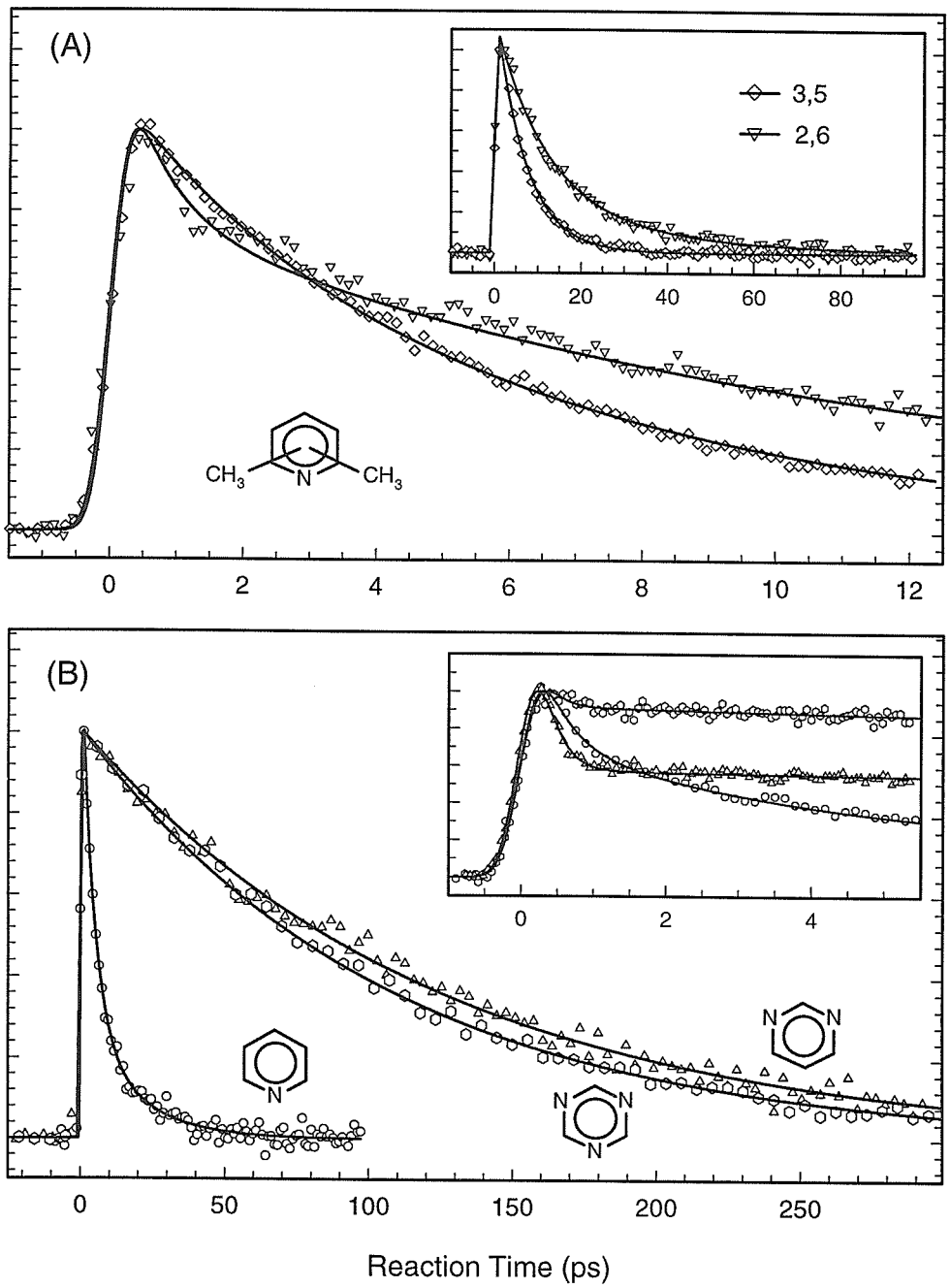
(A)
3,5
2,6
0
20
40
60
80
CH3
N
CH3
0
2
4
6
8
10
12
(B)
0
2
4
N
N
N
N
N
0
50
100
150
200
250
Reaction Time (ps)

Figure 8.4

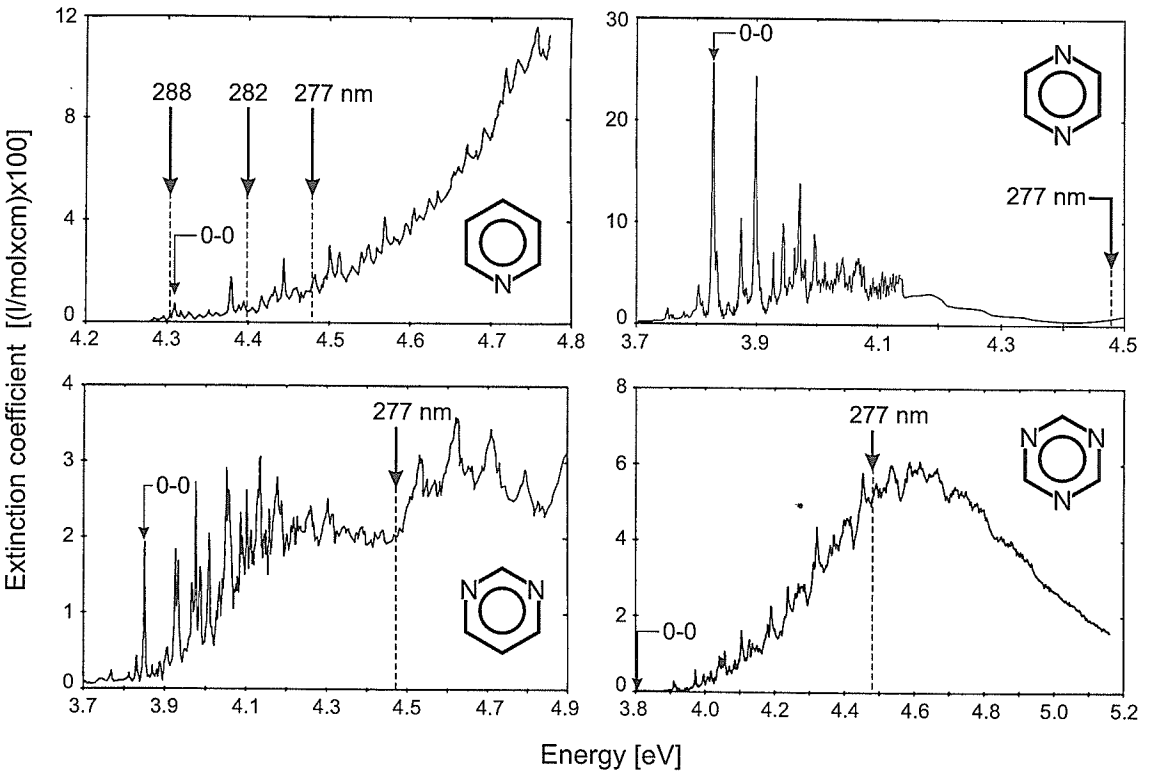
Extinction coefficient [(l/molxcm)x100]
288
282
277 nm
0-0
277 nm
0-0
277 nm
0-0
277 nm
0-0
Energy [eV]

Figure 8.5